Ecoulement des polymères à travers des milieux poreux : impact des effets viscoélastiques à l'échelle des pores sur les propriétés effectives à l'échelle de Darcy

Omar Mokhtari

THÈSE

En vue de l'obtention du

DOCTORAT DE L'UNIVERSITÉ DE TOULOUSE

Délivré par :

Institut National Polytechnique de Toulouse (Toulouse INP)

Discipline ou spécialité :

Surfaces Interfaces Continentales Hydrologie

Présentée et soutenue par :

M. OMAR MOKHTARI

le mardi 12 juillet 2022

Titre :

Ecoulement des polymères à travers des milieux poreux : impact des effets viscoélastiques à l'échelle des pores sur les propriétés effectives à l'échelle de Darcy

---

Ecole doctorale :

Sciences de l'Univers de l'Environnement et de l'Espace (SDU2E)

Unité de recherche :

Institut de Mécanique des Fluides de Toulouse (IMFT)

Directeurs de Thèse :

M. MICHEL QUINTARD

M. YOHAN DAVIT

Rapporteurs :

M. HUGUES BODIGUEL, INP GRENOBLE

M. PIERRE SARAMITO, CNRS SAINT MARTIN D'HERES

Membres du jury :

M. JACQUES MAGNAUDET, CNRS TOULOUSE, Président

M. JEAN-CLAUDE LATCHE, IRSN ST PAUL LES DURANCE, Invité

MME EDWIGE GODLEWSKI, UNIVERSITE SORBONNE, Membre

M. MICHEL QUINTARD, TOULOUSE INP, Membre

M. ROMAIN DE-LOUBENS, TOTAL, Invité

MI. SEBASTIEN BOYAVAL, ECOLE DES PONTS PARISTECH, Membre

M. YOHAN DAVIT, TOULOUSE INP, Membre

Aux femmes de ma vie : ma mère, mon épouse et ma fille...

Résumé

L'écoulement de solutions de polymères à travers des milieux poreux est un problème riche en mécanique des fluides qui combine la complexité des écoulements à travers des structures poreuses à celle de la rhéologie non linéaire du fluide. De tels écoulements peuvent présenter des comportements particuliers sur une large gamme d'échelles. Malgré des efforts continus, une compréhension claire des mécanismes à petite échelle impliqués et de leur lien avec les phénomènes à plus grande échelle fait toujours défaut. Dans ce travail, notre objectif est d'étudier certains des phénomènes physiques à l'échelle des pores et de les relier aux propriétés à l'échelle de Darcy. Pour ce faire, nous avons simulé l'écoulement de fluides viscoélastiques à travers des milieux poreux modèles, tels que des réseaux de cylindres en 2D ou des empilements de sphères en 3D, en résolvant, par des méthodes haute performance les modèles Oldroyd-B, FENE-P et FENE-CR.

Dans la première partie, nous présentons donc un nouveau schéma de projection à grille décalée pour les écoulements viscoélastiques, ainsi que sa validation dans les cas de la cavité entraînée et de l'écoulement autour d'un cylindre confiné. Nous montrons ainsi que ce schéma possède une semi-différenciation spatiale cohérente avec une estimation de l'énergie libre, maintient la positivité du tenseur de conformation, est bien adapté au calcul haute performance (HPC), montre une bonne précision et peut être facilement utilisé pour une variété de lois constitutives viscoélastiques. Dans la deuxième partie, nous utilisons cette approche numérique pour montrer que les zones localisées de grande contrainte polymérique, appelées brins biréfringents, pilotent l'écoulement d'un fluide Oldroyd-B à travers des réseaux de cylindres en 2D. Nous constatons que ces brins génèrent en effet une réorganisation complète de l'écoulement avec une augmentation des zones de stagnation, un renforcement des chemins préférentiels et une division des canaux d'écoulement. De plus, nous montrons que cette réorganisation génère une augmentation de la dissipation visqueuse du solvant et que l'étirement des molécules de polymère dans les brins est associé à une production d'entropie. Ces deux phénomènes conduisent ainsi à une augmentation globale de la dissipation qui peut être directement liée à l'augmentation de la résistance à l'écoulement.

Dans la troisième partie, nous étudions l'écoulement à travers un réseau hexagonal 2D de cylindres pour large une gamme de nombres de Weissenberg et différentes orientations du terme de forçage qui génère l'écoulement. Nous montrons que les brins biréfringents contrôlent la direction de l'écoulement moyen. Ces brins ont également tendance à adhérer aux cylindres voisins, ce qui conduit à des directions d'écoulement privilégiées et à une succession de bifurcations lorsque l'on fait varier l'angle du terme de forçage. L'effet le plus marquant est la présence d'une tristabilité associée à une hystérésis sur l'angle. Nous démontrons en outre que l'apparition d'un écoulement instationnaire est associée au mouvement des différents brins du réseau qui ouvrent et referment successivement les canaux d'écoulement. Ceci fournit une nouvelle perspective sur les écoulements viscoélastiques instationnaires à travers les milieux poreux et peut aider à comprendre la transition vers le chaos.

Dans la quatrième partie, nous dérivons une forme moyennée du modèle Oldroyd-B à l'échelle de Darcy. Pour ce faire, nous utilisons une forme de linéarisation du problème, en considérant une limite très diluée, et nous décomposons le problème initial en une séquence de problèmes à différents ordres. Cette limite est très différente de la limite du faible nombre de Weissenberg car elle peut capturer la formation de brins biréfringents. Nous procédons à la moyenne spatiale de chaque problème et dérivons le modèle moyen correspondant pour obtenir une forme modifiée de la loi de Darcy.

Les écoulements viscoélastiques en 2D dans des réseaux de cylindres ont suscité beaucoup d'intérêt, en particulier dans une série de travaux expérimentaux très récents, et nous ont aidés à comprendre les aspects fondamentaux de ces écoulements. Cependant, les écoulements à travers des structures 2D et 3D sont fondamentalement différents. Dans la dernière partie de ce travail, nous présentons donc des résultats préliminaires pour les écoulements viscoélastiques à travers des empilements 3D de sphères. De telles structures conduisent à des régions localisées de contrainte qui peuvent être considérées comme des brins 1D et des hyperplans 2D. Cela soulève donc des questions importantes sur la façon dont les écoulements viscoélastiques sont affectés par la dimensionnalité.

Abstract

The flow of polymer solutions through porous media is a rich problem in fluid mechanics, combining the complexity of flows through porous structures with the nonlinear rheology of the fluid. Such flows can display peculiar behaviours over a range of different scales. Despite continuous efforts, a clear picture of the small-scale mechanisms involved and their link with larger scale phenomena are still lacking. In this work, our goal is to study some of the physical phenomena at pore-scale and connect these to Darcy-scale properties. To do so, we simulated the flow of viscoelastic fluids through model porous structures, such as 2D arrays of cylinders or 3D packings of spheres, using high performance computations of Oldroyd-B, FENE-P and FENE-CR models.

In the first part, we present a new staggered projection scheme for viscoelastic flows, along with validation cases for the lid-driven cavity problem and flow around a confined cylinder. We show that this scheme has a space semi- discretization that is consistent with a free-energy estimate, maintains the positivity of the conformation tensor, is well suited to high-performance computing (HPC), shows good accuracy and can be readily used for a variety of viscoelastic constitutive laws.

In the second part, we use this numerical approach to show that localized zones of large polymeric stress, known as birefringent strands, drive the flow of an Oldroyd-B fluid through 2D arrays of cylinders. We found that these strands generate a complete reorganization of the flow with an increase of stagnation zones, a reinforcement of preferential paths and a splitting of flow channels. Furthermore, we showed that this reorganization is the source of an increase in the viscous dissipation of the solvent and also that the stretching of polymer molecules in the strands is associated with entropy production. Both these phenomena lead to a global increase in dissipation that can be directly linked with the increase of flow resistance.

In a third part, we study the flow through a 2D hexagonal lattice of cylinders for a range of Weissenberg numbers and different orientations of the forcing term generating flow. We show that birefringent strands control the direction of the average flow. These strands also tend to stick to neighbouring cylinders, leading to preferential flow directions and a succession of bifurcations when varying the angle of the forcing term. The most striking effect is tristability and hysteresis in the staggered configuration. We further demonstrate that the onset of unsteady flow is associated with movement of the different strands in the network that are successively opening and closing flow channels. This provides a new perspective on unsteady viscoelastic flows through porous media and may help in understanding the transition to chaos.

In the fourth part, we derive an average form of the Oldroyd-B model at Darcy-scale. To do this, we use some form of linearization of the problem, considering a highly diluted limit, and decompose the initial problem in a sequence of problems at different orders. This limit is very different from the low Weissenberg number limit because it can capture the formation of birefringent strands. We proceed to averaging each problem in space and deriving the corresponding average model to obtain a modified form of Darcy's law.

2D viscoelastic flows in arrays of cylinders have received a lot of interest, in particular in a series of recent experimental works, and they have helped us understand fundamental aspects of such flows. However, flows through 2D and 3D structures are fundamentally different. In the last part of this work, we thus present preliminary results for viscoelastic flows through 3D packings of spheres. Such structures lead to localized regions of stress that can be thought of as 1D strands and 2D hyperplanes. This raises important questions about how viscoelastic flows are affected by the dimensionality.

Table des matières

Chapter 1

Introduction

L'ajout d'une petite quantité de polymères à une solution aqueuse suffit à en modifier considérablement les caractéristiques et les propriétés d'écoulement. On passe ainsi d'un écoulement linéaire (newtonien) à un monde beaucoup plus complexe (non-newtonien). Les écoulements de solutions de polymères à travers des milieux poreux sont impliqués dans de nombreuses applications dans les domaines de l'énergie et de l'environnement, que ce soit dans des systèmes géophysiques, biologiques, microfluidiques ou industriels. A titre d'exemples, on peut citer la récupération assistée des hydrocarbures [187, 192] et l'assainissement des eaux souterraines [28, 104]. Dans les processus diphasiques, l'ajout de polymères au fluide de déplacement permet d'améliorer la récupération d'une phase liquide non-aqueuse en augmentant la traînée sur les ganglions piégés par capillarité et en réduisant la digitation visqueuse grâce à un rapport de mobilité plus favorable [4, 52, 112, 183, 71]. D'autres applications, telles que la filtration [11] ou la chromatographie [43], font également intervenir de tels écoulements.

Un milieu poreux est généralement constitué d'une matrice solide perméable caractérisée par un réseau de pores remplis de fluide et interconnectés par des gorges relativement resserrées. Les exemples de tels milieux poreux comme les roches, les milieux de filtration ou encore les tissus biologiques ne manquent pas. Lorsqu'on s'intéresse à la modélisation des écoulements dans de ces systèmes, on cherche souvent à obtenir une description macroscopique (continue) du transport des fluides dans ces milieux [11, 43] en utilisant des variables moyennées. Cependant, contrairement aux fluides simples, la mécanique des solutions de polymères se couple de manière non-linéaire à la déformation du fluide et, par conséquent, à la géométrie locale des pores. L'étude de tels écoulements constitue donc un problème riche, où la rhéologie non triviale du fluide se couple à la microstructure poreuse complexe pour conduire à des propriétés d'écoulement et de transport parfois surprenantes. Malgré des efforts continus depuis plusieurs décennies, une compréhension claire des mécanismes à petite échelle et de leur impact sur des échelles plus grandes fait toujours défaut.

Ce premier chapitre est organisé de la manière suivante. Après quelques généralités sur fluides non-newtoniens Section 1.1 et une rapide introduction sur les fluides viscoélastiques Section 1.2, on s'intéressera aux propriétés des solutions de polymères, notamment à leur rhéologie dans la Section 1.3. Le développement d'un modèle à l'échelle du pore constitue le point de départ nécessaire pour comprendre la physique de l'écoulement et éventuellement développer des modèles à une échelle plus grande, que ce soit par simulation numérique directe (DNS), modèles de type réseaux de pores ou passage à l'échelle par prise de moyenne volumique ou homogénéisation. Nous nous intéressons donc ensuite à la modélisation des solutions de polymères dans la Section 1.4. On y présente notamment la dérivation des systèmes d'équations modélisant les écoulements issus à la fois d'approches de mécanique continue et de modèles moléculaires. Dans la Section 1.5, on discute les différents phénomènes susceptibles d'intervenir dans les milieux poreux aux petites

échelles et la Section 1.6 se concentre sur les plus grandes échelles, en particulier l'échelle de Darcy. On conclue ce Chapitre avec une présentation des objectifs de la thèse et du plan du manuscrit dans la Section 1.7.

1.1 Généralités sur les écoulements non-newtoniens

Dans le cadre des méthodes de récupération améliorée du pétrole ou de remédiation des sols, l'effet principalement recherché par les ingénieurs lors de l'ajout des molécules de polymère à la solution injectée est d'en augmenter la viscosité. Ceci permet d'obtenir un rapport de mobilité plus favorable et donc d'améliorer le balayage. Quelques centaines de *ppm* suffisent à augmenter la viscosité "newtonienne" du liquide. Si l'idée est simple, la réalité de l'écoulement est bien plus complexe pour diverses raisons. L'aspect qui est peut-être le plus important est lié à une modification profonde de la rhéologie du fluide, le rendant non-newtonien.

Un fluide newtonien est caractérisé par une relation constitutive linéaire pour la contrainte, ce qui s'exprime généralement sous la forme

$$\boldsymbol{\tau} = 2\eta \mathbf{D}(\mathbf{u}), \tag{1.1}$$

où η est la viscosité dynamique, constante et uniforme, $\boldsymbol{\tau}$ le tenseur de contrainte et $\mathbf{D}(\mathbf{u}) = \frac{1}{2}\left(\boldsymbol{\nabla}\mathbf{u} + (\boldsymbol{\nabla}\mathbf{u})^{\mathsf{T}}\right)$ le tenseur du taux de déformation avec $\mathbf{u}$ le vecteur vitesse et $\boldsymbol{\nabla}\mathbf{u}$ son gradient. Lorsque la relation entre contrainte et taux de déformation n'est plus linéaire, on qualifie alors le fluide de non-newtonien. On trouve ainsi de nombreux exemples de fluides non-newtoniens dans la vie de tous les jours : de la crème anglaise à la pâte de dentifrice, en passant par la peinture ou le shampoing. Les exemples ne manquent pas ! Le but de la rhéologie en tant que discipline est de décrire et d'expliquer les propriétés de ces matériaux. Nombre d'ouvrages sont disponibles sur ce thème, dont [23, 174], et on ne s'aventurera pas ici à proposer une présentation exhaustive. On va donner sur quelques éléments de contexte sur les fluides non-newtoniens pour se concentrer ensuite sur la partie qui nous intéressera tout au long de cette thèse : les fluides viscoélastiques.

Parmi les comportements non-newtoniens, on différencie tout d'abord ceux qui dépendent ou non du temps. Dans les fluides dont le comportement dépend du temps, on distingue les fluides thixotropes qui, lorsqu'une contrainte constante leur est appliquée, voient leur viscosité diminuer au cours de temps [184]. C'est par exemple le cas de certaines peintures ou des sables mouvants. Ce comportement est dû à des restructurations au sein du fluide qui s'effectuent sur des temps comparables au temps de sollicitation. A l'inverse, les fluides anti-thixotropes voient leur viscosité augmenter avec le temps. Ces fluides sont plus rares mais on peut citer l'exemple de la crème fouettée [155].

Parmi les fluides dont le comportement est indépendant du temps, on compte les fluides quasi-newtoniens. On distingue les fluides rhéofluidifiant dont la viscosité diminue avec le taux de cisaillement. C'est généralement le cas des suspensions diluées telles que les encres, le sang et les solutions de polymères. A l'inverse, les fluides rhéoépaississants ont une viscosité qui diminue avec le taux de cisaillement. Tel est le cas, par exemple, des suspensions de verre et des suspensions concentrées en général. Ces fluides quasi-newtoniens peuvent être décrits par une relation du type

$$\boldsymbol{\tau} = 2\eta(\dot{\gamma}_D)\mathbf{D}(\mathbf{u}), \tag{1.2}$$

où la viscosité n'est cette fois plus constante et dépend du taux de cisaillement $\dot{\gamma}_D$ défini comme étant le second invariant du tenseur de déformation

$$\dot{\gamma}_D = \sqrt{2\mathbf{D}(\mathbf{u}) : \mathbf{D}(\mathbf{u})} = \sqrt{2\mathrm{tr}\left(\mathbf{D}(\mathbf{u})\right)}. \tag{1.3}$$

On parle aussi de fluides newtoniens généralisés. De nombreux modèles existent pour décrire cette dépendance, Figure 1.1(a). L'un des plus simples est le modèle en loi de puissance avec coupure (PLCO), pour lequel la viscosité s'écrit

$$\eta(\dot{\gamma}) = \begin{cases} \eta_0 & \text{si } \dot{\gamma} < \dot{\gamma}_c \\ \eta_0 \left(\frac{\dot{\gamma}}{\dot{\gamma}_c}\right)^{n-1} & \text{sinon,} \end{cases} \tag{1.4}$$

où η_0 est la viscosité newtonienne à faible cisaillement, $\dot{\gamma}_c$ le taux de cisaillement critique et $n > 0$ l'indice de puissance. Lorsque $n < 1$ le fluide est rhéofluidifiant, $n = 1$ correspond à un fluide newtonien et $n > 1$ à un fluide rhéoépaississant. La transition entre le plateau newtonien et la partie rhéofluidifiante n'est pas lisse avec ce modèle, on peut donc lui préférer des modèles plus complexes [27, 39, 228]. On trouve aussi souvent un plateau dans les forts taux de cisaillement, comme capturé par le modèle de Cross [39]

$$\eta(\dot{\gamma}) = \eta_\infty + \frac{\eta_0 - \eta_\infty}{1 + \left(\frac{\dot{\gamma}}{\dot{\gamma}_c}\right)^n} \tag{1.5}$$

où η_∞ correspond à un second plateau, à taux de cisaillement élevés. On peut également utiliser la loi de Carreau pour les solutions concentrées et les polymères fondus [27]

$$\eta(\dot{\gamma}) = \eta_\infty + (\eta_0 - \eta_\infty)\left(1 + \left(\frac{\dot{\gamma}}{\dot{\gamma}_c}\right)^2\right)^{\frac{n-1}{2}}, \tag{1.6}$$

que l'on peut généraliser par la loi de Carreau-Yasuda [228]

$$\eta(\dot{\gamma}) = \eta_\infty + (\eta_0 - \eta_\infty)\left(1 + \left(\frac{\dot{\gamma}}{\dot{\gamma}_c}\right)^a\right)^{\frac{n-1}{a}}, \tag{1.7}$$

où a est un paramètre. Cette dernière est assez populaire et est utilisée, par exemple, pour modéliser les écoulements sanguins [1, 12, 22].

Parmi les comportements non-newtoniens, on distingue ensuite les fluides à seuil qui, en deçà d'un certain seuil de contrainte, ont un comportement solide et s'écoulent comme un fluide visqueux au delà. On parle alors de comportement viscoplastique avec comme exemple courant le dentifrice ou bien le gel capillaire. Au delà du seuil d'écoulement, certains fluides comme la boue ou la mayonnaise ont un comportement linéaire (newtonien), on parle de fluides de Bingham [13].

1.2 Les fluides viscoélastiques

De nombreux fluides ont un comportement élastique et rentrent donc dans la catégorie des fluides viscoélastiques. Ce comportement peut être mis en évidence par des expériences de fluage [153] qui consistent à imposer une contrainte constante à un matériau et à suivre l'évolution temporelle de la déformation. Pour un matériau élastique, la réponse est instantanée et réversible alors que pour un matériau visqueux, elle croît linéairement en temps et est irréversible. Pour un matériau viscoélastique, on distingue trois phases : une déformation élastique, instantanée et réversible suivie d'un déformation croissante en temps mais réversible puis d'une déformation visqueuse, dépendante du temps et irréversible. On parle ainsi de fluide à mémoire déclinante ou évanescente [231]. On retrouve de nombreux exemples de fluides viscoélastiques dans l'industrie textile et alimentaire. Les solutions de polymères sont en général viscoélastiques du fait de la

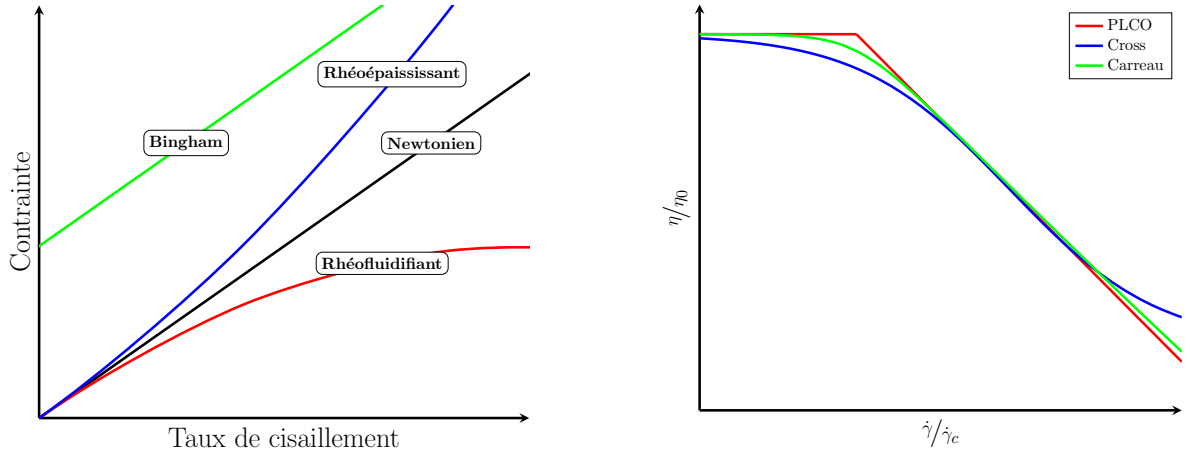

(a) (b)

Fig. 1.1 **Rhéologies non-newtoniennes.** (a) Exemples de comportements non-newtoniens. (b) Exemples de modèles pour la viscosité.

flexibilité des molécules de polymères pouvant, par déformation, stocker de l'énergie élastique, de même que les polymères fondus. Les effets élastique dans les fluides peuvent avoir des effets spectaculaires.

Parmi ces effets élastiques, on peut citer

- l'effet de Weissenberg où le fluide remonte le long d'une tige en rotation (Figure 1.2(a)),
- la détente élastique d'un matériau versé depuis un récipient qui, une fois coupé, peut remonter dans le récipient (Figure 1.2(b)),
- le siphon sans tube où, après avoir été initialisé, le siphonnage d'un bécher perdure sans avoir recours à un tuyau (Figure 1.2(c)),
- le gonflement à l'extrusion (Figure 1.2(d)) qui doit par exemple être pris en compte lors du moulage de pièce en plastique par injection.

Ces effets sont attribués soit à la différence de contraintes normales, induites par l'écoulement, et perpendiculaires aux surfaces sur lesquelles elles s'exercent (effet de Weissenberg et gonflement) soit à la très forte résistance du fluide à l'étirement (siphon ouvert et détente élastique). Cette résistance accrue à l'étirement se traduit par une viscosité, dite élongationnelle, bien plus élevée que celle observée en cisaillement et nécessite des techniques de mesure spécifiques [179], voir Section 1.3.3.

1.3 Solutions de polymères

On va maintenant s'intéresser plus spécifiquement aux propriétés des solutions de polymères, en commençant par quelques notions de base sur la caractérisation des écoulements fluides qui sont importantes pour définir la rhéologie des solutions de polymères.

1.3.1 Quelques rappels sur la caractérisation des écoulements

La topologie de l'écoulement a un impact important sur la déformation des polymères, qui peut elle même affecter la dynamique de l'écoulement [78, 213]. Les chaînes de polymères, soumises

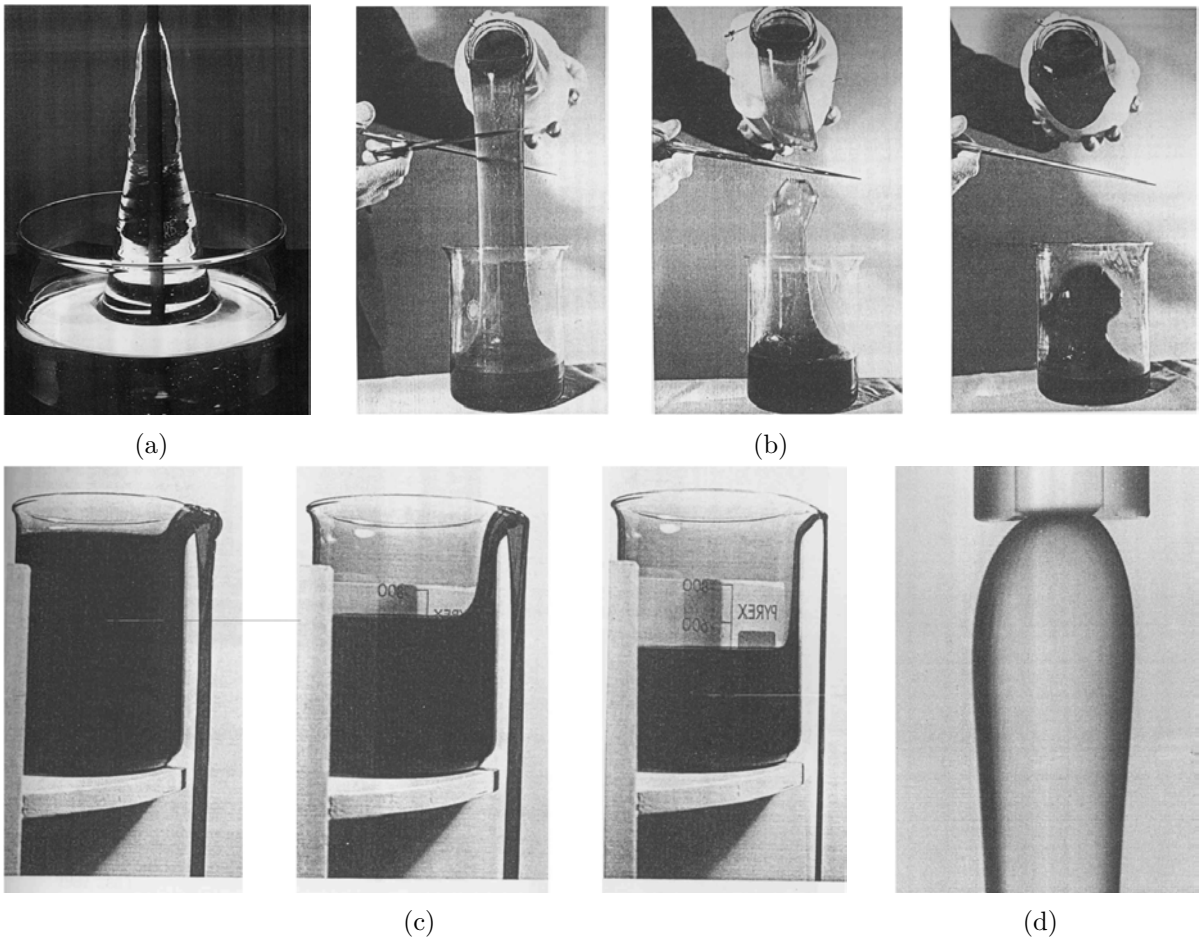

Fig. 1.2 **Exemple d'effets élastiques** [20]. (a) Effet de Weissenberg où le fluide remonte le long d'un axe tournant. (b) Détente élastique. (c) Siphon ouvert. (d) Gonflement à la sortie d'un tube de petit diamètre.

à un cisaillement, peuvent ainsi subir un culbutage [186] ou, lorsqu'elle sont soumises à un extension, subir une transition de déroulement ("coil-stretch") [86, 156], voir Figure 1.3. On distinguera donc principalement deux types d'écoulement que sont le cisaillement simple et l'élongation, le cisaillement étant la combinaison d'une rotation d'une élongation comme décrit ci-dessous

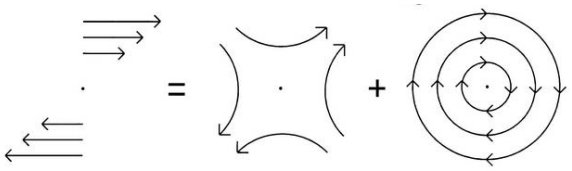

- Le cisaillement simple correspond à un gradient de vitesse transverse au sens d'écoulement. En $2D$, le champs de vitesse peut s'écrire $\mathbf{u} = \dot{\gamma} \begin{pmatrix} y & 0 \end{pmatrix}^{\mathsf{T}}$ où $\dot{\gamma}$ désigne le taux de cisaillement. Son gradient est donc

$$\boldsymbol{\nabla}\mathbf{u} = \begin{pmatrix} 0 & \dot{\gamma} \\ 0 & 0 \end{pmatrix}. \tag{1.8}$$

- L'élongation uniaxiale correspond à un étirement le long d'un seul axe et à une compression selon les autres axes. Le champs de vitesse prend la forme $\mathbf{u} = \dot{\epsilon} \begin{pmatrix} x & -y/2 & -z/2 \end{pmatrix}^{\mathsf{T}}$ pour une élongation selon l'axe $\mathbf{e}_x$, $\dot{\epsilon}$ désignant le taux d'élongation. Son gradient s'écrit alors

$$\boldsymbol{\nabla}\mathbf{u} = \begin{pmatrix} \dot{\epsilon} & 0 \\ 0 & -\dot{\epsilon} \end{pmatrix}. \tag{1.9}$$

Dans les écoulements mixtes, la déformation locale du fluide peut être caractérisée par le paramètre de type d'écoulement Λ défini par

$$\Lambda = \frac{|\mathbf{D}| - |\boldsymbol{\Omega}|}{|\mathbf{D}| + |\boldsymbol{\Omega}|}, \tag{1.10}$$

où $\mathbf{D}(\mathbf{u})$ est le tenseur de taux de déformation défini plus haut et $\boldsymbol{\Omega}(\mathbf{u}) = \frac{1}{2}\left(\boldsymbol{\nabla}\mathbf{u} - (\boldsymbol{\nabla}\mathbf{u})^{\mathsf{T}}\right)$ désigne le tenseur de vorticité. Par définition, on a $-1 \leq \Lambda \leq 1$, avec $\Lambda = 0$ pour un cisaillement, $\Lambda = 1$ pour une élongation et $\Lambda = -1$ pour une rotation. Ce paramètre pose parfois problème pour être déterminé [7, 87] même si sa définition peut être adaptée [6, 203]. Il est souvent utilisé dans l'étude des écoulements de solutions de polymères [79, 78, 81, 213].

1.3.2 Comportement des solutions de polymères en cisaillement

Considérant un écoulement 2D en cisaillement pur, la viscosité en cisaillement est définie par

$$\eta_c := \frac{\tau_{xy}}{\dot{\gamma}}, \tag{1.11}$$

où τ_{xy} est la contrainte tangentielle et $\dot{\gamma}$ le taux de cisaillement. On mesure la viscosité en cisaillement à l'aide de rhéomètres rotationnels classiques de type cône-plan ou plan-plan. Soumises à un cisaillement, les solutions de polymères ont généralement un comportement rhéofluidifiant. C'est ainsi le cas du xanthane [95] et du polyacrylamide partiellement hydrolysé (HPAM) [237] utilisés dans l'industrie pétrolière. Au niveau moléculaire, ce comportement

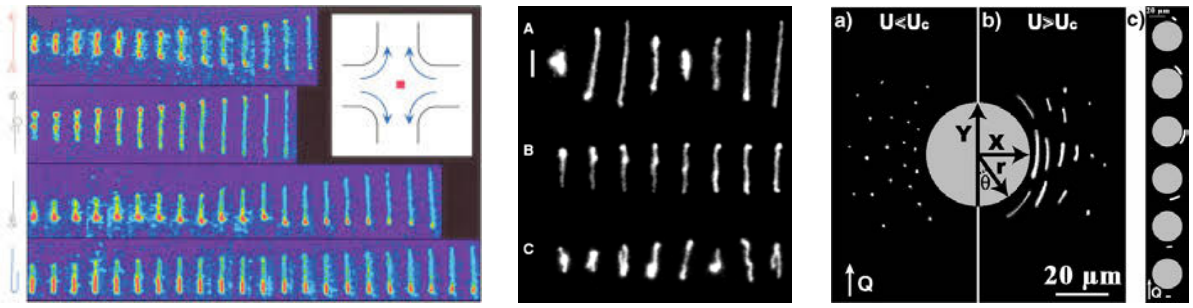

(**I**) (**II**) (**III**)

Fig. 1.3 **Déformation des chaînes de polymère individuelles dans différents type d'écoulements. (I)** Configurations moléculaires dans un écoulement élongationnel [156]. **(II)** Chaînes de polymère sous cisaillement constant [186]. (A) Cas d'une molécule passant par les états enroulé, étiré, enroulé, puis à nouveau étiré. (B) Cas d'une molécule partiellement étirée. (C) Cas d'une molécule repliée en U vers le haut, puis qui se défait comme une corde glissant sur une poulie avant de se retourner et se replier en U inversé. **(III)** Molécules d'ADN au voisinage d'un cylindre [63]. (a) Lorsque le débit est faible, les molécules restent en forme de pelote. (b) À débit plus élevé et en fonction de leur position, certaines molécules sont fortement étirées. (c) Séquence montrant l'approche et l'allongement et d'une molécule au voisinage du cylindre.

s'explique par un alignement des molécules de polymère avec l'écoulement qui opposent alors une résistance moins importante. La rhéofluidification d'une solution de polymère dépend de nombreux paramètres [222] tels que la taille des chaînes de polymère, leur flexibilité [171] et masse molaire [142], la qualité du solvant [171] mais également de la concentration en polymères. Dans les régimes semi-dilués, par exemple, l'alignement des molécules s'accompagne en plus d'un détachement des molécules qui glissent alors les unes sur les autres, amplifiant encore les caractère rhéofluidifiant. Lorsqu'on ignore le comportement élastique, la relation constitutive est donnée par

$$\boldsymbol{\tau} = 2\eta_c(\dot{\gamma})\mathbf{D}(\mathbf{u}), \tag{1.12}$$

où la viscosité $\eta_c(\dot{\gamma})$ peut alors par exemple être modélisée par une loi de Cross [142] ou par une loi de type PLCO [31, 181, 209, 234] qui convient aux solutions de polymère de type xanthane ou dextran.

1.3.3 Viscosité élongationnelle des solutions de polymère

Dans une élongation uni-axiale, la viscosité élongationnelle est définie par

$$\eta_e = \frac{\tau_{xx} - \tau_{yy}}{\dot{\epsilon}}, \tag{1.13}$$

où τ_{xx} et τ_{yy} correspondent aux contraintes normales et $\dot{\epsilon}$ au taux d'élongation. Pour un fluide newtonien en écoulement, le rapport de Trouton $Tr = \eta_e/\eta_c$ vaut 2 en $2D$ et 3 en $3D$. La mesure expérimentale de la viscosité élongationnelle est souvent difficile [94] et de nombreuses méthodes ont été développées. On notera en particulier des méthodes sans point de stagnation comme la contraction [18, 92, 89], la contraction hyperbolique (e-VROC™) [238], le filage [53], le siphon sans tube [138], la traction [99, 206] ou l'étirement [134, 204]. En ce qui concerne les méthodes avec point de stagnation, peut citer les méthodes par jets opposés [66], quatre rouleaux [64] CaBER™(Capillary Break-up Extensional Rheometer) [132] et la goutte tombante [212]. L'écoulement élongationnel de solutions diluées de polymère montre généralement un

caractère rhéoépaississant [32, 37, 226]. D'un point de vue moléculaire, ce comportement est souvent attribué à la transition de déroulement ("coil-stretch") [48] des molécules qui, étirée par l'écoulement, atteignent un degré élevé d'allongement associé à une augmentation marquée de viscosité apparente [32]. D'autres études attribuent plutôt ce comportement à une différence de contraintes normales $N_1 = \tau_{xx} - \tau_{yy}$ [91], mais une compréhension précise de ce phénomène semble encore faire défaut [214].

1.3.4 Les fluides de Boger

Comme on a pu le voir, les solutions de polymères ont souvent un comportement rhéofluidifiant en cisaillement et rhéoépaississant en élongation. Afin de pouvoir découpler ces deux comportements apparemment opposés, on utilise des fluides dits de Boger [90]. La viscosité de ces fluides est indépendante du taux de cisaillement ce qui permet de séparer les effets élastiques des effets purement visqueux. Ces fluides sont généralement des solutions de polymères diluées (voire très diluées) d'un polymère de poids moléculaire élevé, réalisées avec un solvant très visqueux comme le sirop de maltose, par exemple [90].

1.3.5 Les brins birefringents

Les écoulements de solutions de polymère font apparaître des régions localisées de grande déformation et de forte contrainte appelées "birefringent strands", dont une traduction possible est "brins biréfringents" [38, 76]. Cette dénomination vient de leur fine structure et de la propriété utilisée pour les observer, la biréfringence [198], Figure 1.4. Une méthode pour mesurer la biréfringence consiste à mesurer le retard $\mathcal{R}$ entre deux chemins optiques, provenant de la différence d'indice de réfraction dues aux molécules de polymère. Le changement local des propriétés optiques de la solution de polymère peut alors être relié à la contrainte locale par une relation linéaire entre le retard $\mathcal{R}$ et la différence de contraintes principales $\Delta\sigma$

$$\mathcal{R} = \frac{2\pi h C}{\Lambda}\Delta\sigma, \tag{1.14}$$

où C est le coefficient de contrainte optique, Λ la longueur d'onde de la lumière incidente et h l'épaisseur de la couche de fluide traversées par le lumière. Ces brins biréfringents ont ainsi pu être observés dans une très grande variété de systèmes [40, 80, 103, 123, 135, 144, 197]. Au niveau moléculaire, ces brins correspondent à des polymères fortement étirés par l'écoulement et qui ont alors tendance à s'aligner dans une fine zone optiquement anisotrope. En considérant la limite correspondant au régime très dilué, des approches théoriques permettent de déterminer la structure du champs de contrainte ainsi que ses échelles dans différentes configurations simplifiées [76, 164, 165, 163].

Le rôle précis de ces zones de fortes contraintes sur l'écoulement reste une question importante. Une des approches consiste à traiter le brin de polymères étendus comme une ligne de force plongée dans un fluide newtonien [76, 163]. Cette force qu'exercent les polymères sur le fluide se traduit par un saut du taux de cisaillement à travers le brin et conduit à une réduction de la vitesse autour du brin [76]. Cette approche a ainsi été utilisée dans diverses configurations modèles [76, 77, 114, 125]. Dans des écoulements plus complexes, la présence de ces brins soulève de nombreuses questions concernant notamment leur influence sur l'écoulement, leurs interactions mutuelles ou avec des obstacles ou encore leur effet à plus grande échelle.

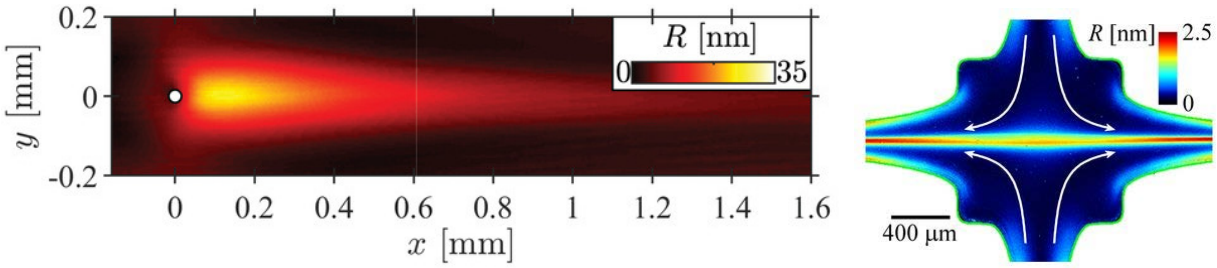

(a) (b)

Fig. 1.4 **Exemples d'observations expérimentales de brins biréfringents.** (a) Cas d'un cylindre dans un canal. On observe la formation d'une zone de forte contrainte dans le sillage du cylindre [85]. (b) Écoulement élongationnel de type "cross-slot". On observe la formation d'un brin à partir du point de stagnation [197].

1.3.6 Effets de concentration et transport de matière

Les propriétés statiques et dynamiques des polymères en solution sont très dépendantes de leur concentration. On distingue ainsi différents régimes de concentration, allant du régime dilué au régime concentré [56, 149, 168, 230]. A faible concentration, on peut considérer que les chaînes individuelles de polymère sont séparées les unes des autres et adoptent une conformation aléatoire tout en se déplaçant de manière indépendante. En augmentant la concentration, les molécules commencent à interagir entre elles, se chevauchent ou se lient les unes aux autres, devenant ainsi plus stable et se déplaçant moins facilement [141]. La transition est généralement caractérisée par une concentration critique, dite de chevauchement, notée c^* [49, 56, 216] où les bobines de polymère se retrouvent tassées [168].

Lorsque la concentration c en polymères est très inférieure à cette concentration critique, $c \ll c^*$, on parle de régime très-dilué. Dans ce cas, les molécules subissent tout simplement l'écoulement, sans avoir de rétroaction sur celui-ci. Comme on le verra, ce régime est particulièrement intéressant pour découpler l'écoulement de la rétroaction du polymère sur celui-ci et donc pour étudier précisément le couplage entre écoulement et contraintes induites par les polymères. Pour des concentrations légèrement plus élevés, pour lesquelles $c < c^*$, on parle de régime dilué, ce qui correspond à peu d'interactions entre chaînes de polymère. Lorsque $c^* < c$, on parle de régime semi-dilué. On peut observer une contraction des molécules en solution, les chaînes individuelles s'enchevêtrent, ce qui réduit considérablement leur mobilité. À de telles concentrations, la solution a généralement un comportement rhéofluidifiant marqué. Tel est par exemple le cas du HPAM ou du xanthane, particulièrement utilisés dans les applications pétrolières [192]. À partir d'une concentration critique d'agrégation, notée c^{**}, on distingue une autre transition, vers des régimes concentrés, où les polymères ne peuvent plus se contracter. Les molécules forment alors des agrégats [146] et une forme de gel [55, 201, 223]. Expérimentalement, la détermination de ces régimes et des concentrations critique se fait à l'aide d'analyses rhéologiques, de la diffusion dynamique de la lumière [146, 168] ou de la distribution du temps de relaxation [149].

Dans les régimes dilués et très dilués, qui vont nous intéresser dans le cadre de cette thèse, les chaînes peuvent être transportées par advection ou par diffusion. La diffusion est due aux mouvements browniens et dépend à la fois de la pression, de la température ou de la viscosité. Les processus de diffusion sont généralement assez rapides dans les gaz alors qu'ils sont beaucoup plus lents dans les liquides et les solides. Dans les solides, la gamme de valeurs du coefficient de diffusion peut-être très large, rendant son estimation théorique assez difficile [41]. Dans le cas des polymères, la diffusion est un processus particulièrement complexe avec des taux se situant entre ceux des liquides et ceux des solides. Le coefficient de diffusion montre également

de fortes variations avec une dépendance importante à la configuration des polymères et à leur concentration dont dépend leur mobilité [98, 116, 211]. Ceci étant, on peut en fait simplifier le problème en considérant les effets de la diffusion relativement à ceux de l'advection. Ceci est quantifié par le nombre de Péclet, $Pe = {}^{LU}/_{D}$, où D correspond au coefficient de diffusion. Bien que cette hypothèse pose question près de la paroi où les vitesses sont généralement faibles et la diffusion plus importante, on considère quasi-systématiquement que $Pe \gg 1$, en négligeant ainsi la diffusion.

Les solutions de polymères ne sont jamais complètement monodisperses. Le processus de polymérisation même conduit à une solution polydisperse de tailles de polymères. Par ailleurs, de nombreux mécanismes de dégradation tels que la biodégradation [127], la dégradation thermique [194, 195, 215] ou la dégradation mécanique [2, 108, 189] peuvent également modifier la distribution des tailles. Cette distribution de masse moléculaire peut également varier spatialement, nécessitant d'adopter une description de type multiconstituant du transport. L'équation de transport peut impliquer une cinétique de réaction associée à des modèles simples de dégradation [194]. Ces modèles restent cependant assez éloignés d'une description complète de création-dégradation prenant en compte l'ensemble des composants. Une modélisation stochastique des mécanismes de rupture de chaîne peut être envisagée [195] mais la dérivation de modèles réactifs basés sur des situations réelles reste un problème ouvert. A une échelle plus grande, la distribution de taille pose diverses difficultés, notamment dans la détermination des différentes zones de l'écoulement qui peuvent discriminer certaines tailles de molécule, voir Section 1.5. Le caractère multiconstituant peut également être à l'origine d'une non-linéarité des variables telles que la densité ou la viscosité et d'une complexification du couplage entre les mécanismes de transport scalaire et le bilan de quantité de mouvement.

1.4 Modélisation des écoulements viscoélastiques de solutions de polymères

Différentes échelles peuvent être considérées pour la modélisation des phénomènes physiques en milieu poreux (voir quelques exemples dans le cas des parois dans la Figure 1.7(b)). On peut considérer des approches moléculaires. Ces approches permettent de mieux comprendre les mécanismes en jeu à la très petite échelle [100, 147, 190, 191] mais le coût numérique est rapidement prohibitif, même pour des approches simplifiées où les macromolécules sont modélisées sous la forme de chaînes en haltères ou de réseaux de ressorts [14, 151, 157, 169]. On peut également considérer une échelle mésoscopique, qui correspond à une description moyenne du comportement des polymères. Ces modèles décrivent un comportement moyen des molécules, par exemple en utilisant des équations du type Fokker-Planck. De telles formulations permettent de simplifier la description mathématique, et de faciliter la résolution numérique et l'extrapolation à des échelles plus grandes. Cependant, la prise en compte de l'ensemble des caractéristiques des solutions de polymères présentes pose encore certaines difficultés. En particulier, l'équation d'évolution de la concentration dépend des interactions moléculaires et des effets stériques près de la paroi qui, par conséquent, varient localement avec la distance à celle-ci [224]. De plus, comme pour l'approche microscopique, la taille des volumes pouvant être considérés par une résolution numérique reste assez limitée. Ces deux échelles sont donc difficiles à utiliser pour une modélisation numérique sur un nombre de pores suffisamment grand.

On décrit dans cette section la dérivation de modèles viscoélastiques de solution de polymère. On cherche à modéliser le comportement d'un fluide qui, à l'échelle moléculaire, est constitué de longues chaîne de polymère en solution dans un solvant. Les modèles classiques proposent généralement une description continue qui néglige les effets de concentration, partant du principe que celle-ci reste uniforme, pour se concentrer sur le transport des contraintes et de la quantité

de mouvement. On distinguera en particulier deux approches. La première consiste à adopter d'emblée une description continue, c'est-à-dire à considérer les équations d'équilibre pour certaines quantités moléculaires moyennes et des équations constitutives pour la contrainte [15]. On verra ensuite qu'on peut dériver les modèles continues à partir de considérations moléculaires, ce qui permet d'avoir un lien plus claire entre les différentes échelles.

1.4.1 Approche de mécanique continue

Le bilan de quantité de mouvement s'écrit

$$\rho(\partial_t \mathbf{u} + \mathbf{u}\cdot\nabla\mathbf{u}) = \nabla\cdot\boldsymbol{\sigma} + \mathbf{F}, \tag{1.15}$$

où $\mathbf{u}$ est le vecteur vitesse, ρ la densité du fluide, que l'on suppose constante, et $\boldsymbol{\sigma}$ la contrainte totale. En supposant le fluide incompressible, l'équation de conservation de la masse totale s'écrit

$$\nabla\cdot\mathbf{u} = 0. \tag{1.16}$$

La contrainte $\boldsymbol{\sigma}$ peut être décomposée comme suit

$$\boldsymbol{\sigma} = -p\mathbf{I}_d + \boldsymbol{\tau}, \tag{1.17}$$

où $p = -\frac{1}{d}\mathrm{tr}(\boldsymbol{\sigma})$ désigne le champs de pression, le terme $-p\mathbf{I}_d$ correspondant donc à la pression isotrope, $\boldsymbol{\tau}$ le déviateur des contraintes totales et $\mathbf{F}$ une densité de force que l'on peut voir comme un terme source volumique de quantité de mouvement. Le tenseur $\boldsymbol{\tau}$ est généralement décomposé en

$$\boldsymbol{\tau} = \boldsymbol{\tau}_s + \boldsymbol{\tau}_p, \tag{1.18}$$

où $\boldsymbol{\tau}_s$ est la contrainte liée et $\boldsymbol{\tau}_p$ celle due au polymère. Le solvant est généralement un fluide newtonien dont la contrainte vérifie donc

$$\boldsymbol{\tau}_s = 2\eta_s\mathbf{D}(\mathbf{u}), \tag{1.19}$$

où η_s désigne la viscosité du solvant. Tout l'objet de ce qui suit est de déterminer l'équation constitutive pour la contrainte $\boldsymbol{\tau}_p$ associée au polymère.

1.4.1.1 Le modèle de Maxwell

Le point de départ de l'approche continue est le modèle proposé par Maxwell [131], qui consiste à modéliser le comportement viscoélastique du fluide en combinant celui d'un fluide visqueux $\boldsymbol{\tau}_p = 2\eta_p\mathbf{D}(\mathbf{u})$ et celui d'un solide élastique $\boldsymbol{\tau}_p = G\gamma$, avec $\boldsymbol{\tau}_p$ qui désigne la contrainte associée au polymère, η_p une viscosité polymérique qui provient de la friction entre le fluide et les longues chaînes de polymère, et G un module d'élasticité. On obtient ainsi l'équation constitutive suivante

$$\boldsymbol{\tau}_p + \lambda\dot{\boldsymbol{\tau}}_p = 2\eta_p\mathbf{D}(\mathbf{u}), \tag{1.20}$$

où $\lambda = \frac{\eta_p}{G}$ est un temps de relaxation. On note ici que la dérivée utilisée est la dérivée particulaire $\dot{\boldsymbol{\tau}}_p = \partial_t\boldsymbol{\tau}_p + \mathbf{u}\cdot\nabla\boldsymbol{\tau}_p$ qui a l'inconvénient majeur de ne pas être objective.

1.4.1.2 Notion d'objectivité

Le principe d'objectivité est fondamental en mécanique. Il exige que la réponse matérielle soit indépendante de l'observateur, c'est-à-dire invariante par translation et rotation (mouvement

rigide) [74, 126]. On retrouve par exemple cette exigence dans la théorie des structures lagrangiennes cohérentes [75]. Dans le cas d'une équation constitutive, une telle propriété est également requise, le comportement du fluide ne devant pas dépendre de l'observateur. D'un point de vue formel, considérant $\mathbf{x}$ et $\hat{\mathbf{x}}$ la position d'une particule matérielle dans deux repères différents en rotation $\mathbf{Q}(t)$ et translation $\mathbf{p}(t)$ l'un part rapport à l'autre, cette condition s'écrit

$$\hat{\mathbf{x}} - \mathbf{x} = \mathbf{Q}(t)\mathbf{x} + \mathbf{p}(t) \tag{1.21}$$

On peut montrer que la dérivée particulaire (ou Lagrangienne) n'est pas objective [174], d'où la nécessité de définir une nouvelle dérivée, objective, concept introduit par Oldroyd [148].

1.4.1.3 Dérivée de Gordon–Schowalter et cas particuliers

La dérivée de Gordon-Showalter [70] est définie par

$$\mathcal{D}_a\boldsymbol{\tau} = \partial_t\boldsymbol{\tau} + \mathbf{u}\cdot\nabla\boldsymbol{\tau} + \boldsymbol{\tau}\cdot\boldsymbol{\Omega}(\mathbf{u}) - \boldsymbol{\Omega}(\mathbf{u})\cdot\boldsymbol{\tau} - a\left(\mathbf{D}(\mathbf{u}) + \mathbf{D}(\mathbf{u})\right), \tag{1.22}$$

où $-1 \leq a \leq 1$ est un paramètre, $\mathbf{D}(\mathbf{u})$ et $\boldsymbol{\Omega}(\mathbf{u})$ désignent respectivement le taux de déformation et le taux de rotation, également appelé le tenseur de vorticité. On peut montrer que cette dérivée est objective [174]. Par ailleurs, elle généralise certaines dérivées connues dont, en particulier

- la dérivée convectée inférieur ou contravariante, correspondant à $a = -1$ et définie par

$$\overset{\triangle}{\boldsymbol{\tau}} = \partial_t\boldsymbol{\tau} + \mathbf{u}\cdot\nabla\boldsymbol{\tau} + \nabla\mathbf{u}\boldsymbol{\tau} + \boldsymbol{\tau}\left(\nabla\mathbf{u}\right)^{\mathsf{T}}, \tag{1.23}$$

- la dérivée de Jaumann ou corotationnelle, correspondant à $a = 0$ et définie par

$$\overset{\circ}{\boldsymbol{\tau}} = \partial_t\boldsymbol{\tau} + \mathbf{u}\cdot\nabla\boldsymbol{\tau} + \boldsymbol{\tau}\boldsymbol{\Omega}(\mathbf{u}) - \boldsymbol{\Omega}(\mathbf{u})\boldsymbol{\tau}, \tag{1.24}$$

- la dérivée convectée supérieur, correspondant à $a = 1$ et définie par

$$\overset{\triangledown}{\boldsymbol{\tau}} = \partial_t\boldsymbol{\tau} + \mathbf{u}\cdot\nabla\boldsymbol{\tau} - \nabla\mathbf{u}\boldsymbol{\tau} - \boldsymbol{\tau}\left(\nabla\mathbf{u}\right)^{\mathsf{T}}. \tag{1.25}$$

Depuis les travaux de Oldroyd [148], le choix de la valeur de a fait toujours débat [84, 174]. Par exemple, la dérivée de Jaumann ($a = 0$) apporte certaines simplifications mathématiques permettant d'avoir une preuve d'existence de solutions globales [118]. Dans notre étude, on considérera que la dérivée convectée supérieur est plus adaptée. D'abord, elle permet de retrouver un effet de Weissenberg positif tel qu'observé expérimentalement pour certaines solutions de polymère [111], Figure 1.2(a). D'autre part, la dérivée convectée supérieur permet de retrouver la limite élastique correspondant à $\lambda \to \infty$ [188]. Enfin, comme on la verra Section 1.4.2, cette dérivée découle naturellement de l'approche microscopique.

1.4.1.4 Le modèle Oldroyd-B

En remplaçant, dans l'équation (1.20), la dérivée Lagrangienne par la dérivée convectée supérieur, on obtient finalement le modèle Oldroyd-B qui s'écrit

$$\begin{cases} \rho\left(\partial_t \mathbf{u} + \mathbf{u}\cdot\nabla\mathbf{u}\right) = -\nabla p + \nabla\cdot\boldsymbol{\tau}, \\ \nabla\cdot\mathbf{u} = 0, \\ \boldsymbol{\tau} = \boldsymbol{\tau}_s + \boldsymbol{\tau}_p, \\ \boldsymbol{\tau}_s = 2\eta_s \mathbf{D}(\mathbf{u}), \\ \partial_t \boldsymbol{\tau}_p + \mathbf{u}\cdot\nabla\boldsymbol{\tau}_p = \nabla\mathbf{u}\cdot\boldsymbol{\tau}_p + \boldsymbol{\tau}_p\cdot\left(\nabla\mathbf{u}\right)^{\mathsf{T}} + 2\frac{\eta_p}{\lambda}\mathbf{D}(\mathbf{u}) - \frac{1}{\lambda}\boldsymbol{\tau}_p. \end{cases} \tag{1.26}$$

Ce modèle constitue le point de départ de nombreux calculs et analyses d'écoulements complexes de solutions de polymères dilués. Malgré sa simplicité, il permet de prédire, au moins qualitativement, des caractéristiques aussi complexes que les instabilités élastiques, la modification de la traînée turbulente et même la rhéologie effective de particules en suspension dans les solutions de polymères [182]. Par ailleurs la réponse en cisaillement est une viscosité constante $\eta_c = \eta_s + \eta_p$, ce qui correspond à un fluide de Boger et permet de distinguer les effets rhéofluidifiants des effets élastiques [90]. Ce modèle présente néanmoins certains défauts. Outre le fait qu'il ne permet pas de prendre en compte le caractère rhéofluidifiant des solutions de polymère, son défaut principal est que sa réponse en élongation fait apparaître une singularité. En effet, celle-ci est donnée par

$$\eta_e = 2(\eta_s + \frac{\eta_p}{1-2\lambda\dot{\epsilon}} + \frac{\eta_p}{1+2\lambda\dot{\epsilon}}), \tag{1.27}$$

et possède donc une asymptote verticale en $\dot{\epsilon} = \frac{1}{2\lambda}$. Cette singularité est due à une extensibilité infinie des chaînes de polymère (voir plus bas) et est accusée, parfois à tort, d'être à l'origine de difficultés numériques.

1.4.1.5 Premières extensions : les modèles de Giesekus, PTT et de White-Metzner

Certaines extensions permettent de pallier les défauts du modèle Oldroyd-B. Ainsi, on distinguera par exemple le modèle de Giesekus [69] dont la relation constitutive est donnée par

$$\boldsymbol{\tau}_p + \lambda \overset{\triangledown}{\boldsymbol{\tau}}_p + \alpha\frac{\lambda}{\eta_p}\boldsymbol{\tau}_p^2 = 2\eta_p\mathbf{D}(\mathbf{u}), \tag{1.28}$$

où $0 \leq \alpha \leq 1$ est un paramètre généralement pris égale à $1/2$, le cas $\alpha = 0$ correspondant au modèle Oldroyd-B. L'ajout du terme quadratique rend la relation non-linéaire mais permet de corriger la singularité rencontrée avec le modèle Oldroyd-B. De même, le modèle PTT (pour Phan-Thien-Tanner) [202], consiste à ajouter un terme non-linéaire à la relation constitutive

$$\boldsymbol{\tau}_p + \lambda \overset{\triangledown}{\boldsymbol{\tau}}_p \left(\exp\left(\frac{\lambda}{\eta_p}\mathrm{tr}\left(\boldsymbol{\tau}_p\right)\right)\right)\boldsymbol{\tau}_p = 2\eta_p\mathbf{D}(\mathbf{u}). \tag{1.29}$$

Ces deux modèles sont issus d'une modélisation de polymères enchevêtrés [200] et correspondent donc plutôt aux régimes semi-dilués [130, 205].

Finalement, le modèle de White-Metzner [220] consiste à généraliser le modèle Oldroyd-B en considérant un temps de relaxation et une viscosité non-constants

$$\boldsymbol{\tau}_p + \lambda(\dot{\gamma}_D) \overset{\triangledown}{\boldsymbol{\tau}}_p = 2\eta_p(\dot{\gamma}_D)\mathbf{D}(\mathbf{u}), \tag{1.30}$$

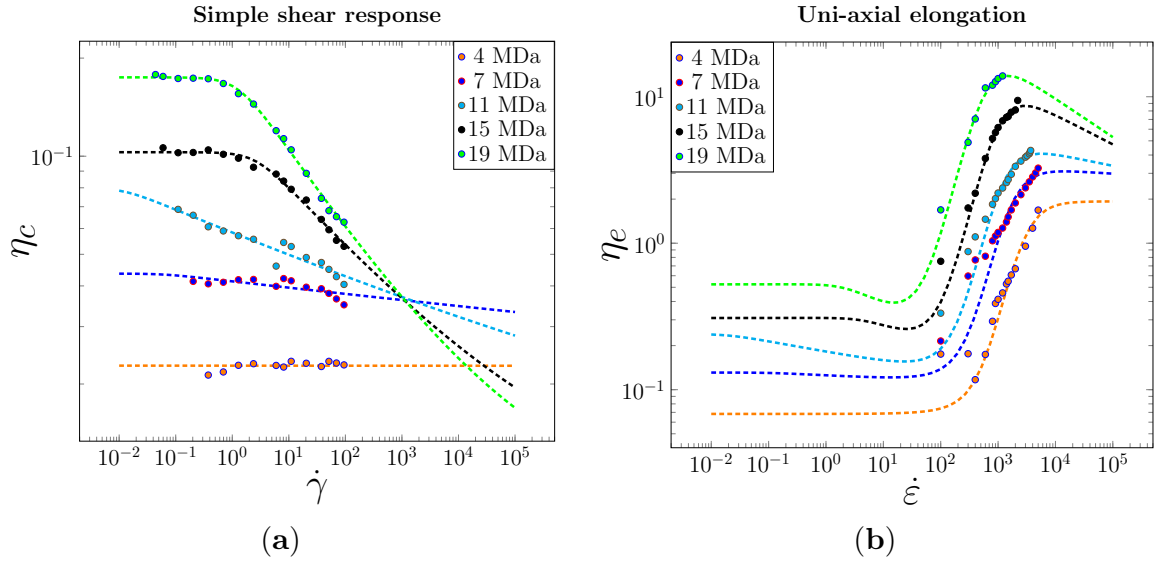

Fig. 1.5 **Exemples de réponse du modèle de White-Metzner.** Comparaison avec les données expérimentales (points) [67], pour le HPAM, obtenues (a) en cisaillement simple et (b) en élongation uni-axiale, pour différents poids moléculaire. Les données expérimentales en élongation ont été obtenues avec le rhéomètre e-VROC™. Les différentes réponses du modèle (traits) ont été obtenues avec les paramètres qui sont récapitulés dans le tableau 1.1.

où le taux de cisaillement $\dot{\gamma}_D$ est défini par (1.3). Plusieurs choix pour les fonctions $\lambda(\dot{\gamma}_D)$ et $\eta_p(\dot{\gamma}_D)$ sont alors possibles parmi lesquels, entre autres, le modèle de Carreau-Yasuda (1.7) [117, 228]. Le modèle de White-Metzner permet de modéliser les différents comportement rhéologiques des solutions de polymère. Il a ainsi pu être utilisé pour étudier l'effet du caractère rhéofluidifiant sur la transition vers l'instationnaire [17, 30]. On présente également, Figure 1.5, une comparaison entre les courbes rhéologiques expérimentales [67], et les réponses obtenues avec le modèle White-Metzner décrit par

$$\begin{cases} \eta_p(\dot{\gamma}_D) = \frac{\eta_{p0}}{(1+K\dot{\gamma}_D)^{1-n}}, \\ \lambda(\dot{\gamma}_D) = \frac{\lambda_0}{1+L\dot{\gamma}_D}, \end{cases} \tag{1.31}$$

où les valeurs des paramètres K, L, η_{p0}, et λ_0 sont données dans le tableau 1.1. On observe ainsi qu'un choix judicieux des paramètres permet de modéliser des fluides réels et d'éliminer la singularité présente dans le modèle Oldroyd-B. Néanmoins, outre la complexité due à l'ajout de paramètres supplémentaires, ce modèle présente l'inconvénient d'être issue d'une extension ad hoc du modèle Oldroyd-B qui ne semble être basée sur aucune théorie.

1.4.2 Dérivation des modèles continus à partir de modèles moléculaires

Dans cette section, on présente la dérivation les modèles de type haltère ("dumbbell") modélisant les solutions diluées de polymères [9, 14, 56, 113, 151, 157]. L'idée, en considérant ces haltères, est d'avoir une description qui soit à la fois suffisamment fine pour obtenir les caractéristiques essentielles d'une chaîne de polymère et permettre de capturer une rhéologie raisonnable mais suffisamment grossière pour que le modèle reste simple.

MDa	η_{p0}	K	n	λ_0	L
4	0.0136	66.6699	0.9999	0.0033	0.0039
7	0.0345	16.0077	0.9750	0.0051	0.0059
11	0.0713	85.1260	0.9186	0.0081	0.0094
15	0.0945	0.3824	0.7971	0.0147	0.0170
19	0.1662	0.7889	0.7364	0.0297	0.0344

Table 1.1 **Paramètres du modèle de White-Metzner**, pour différents poids moléculaires (en MDa), utilisés pour la comparaison avec les mesures expérimentales présentée Figure 1.5. La détermination de paramètre a été obtenue par fitting, en utilisant la routine *lsqnonlin* de Matlab®.

1.4.2.1 Représentation en haltères

La représentation en haltères correspond à une conceptualisation des molécules de polymère sous la forme de chaînes linéaires constituées de deux billes reliées entre elles par un ressort, Figure 1.6(II). Cette représentation est une version simplifiée de la représentation de Rouse [169] où chaque molécule est représentée par une chaîne constituée N sous-éléments de longueur fixe ℓ, en libre en rotation les uns par rapport aux autres, Figure 1.6(I). La grandeur importante est $\mathbf{R}$, le vecteur bout-à-bout reliant les deux billes. On peut définir la fonction densité de probabilité $\psi(\mathbf{R},\mathbf{x},t)$ pour $\mathbf{R}$ où $\psi(\mathbf{R},\mathbf{x},t)\,d\mathbf{x}d\mathbf{R}$ correspond à la probabilité au temps t pour le polymère d'être dans une configuration entre $\mathbf{R}$ et $\mathbf{R}+d\mathbf{R}$ à une position entre $\mathbf{x}$ et $\mathbf{x}+d\mathbf{x}$. À l'état d'équilibre, on a $\langle\mathbf{R}\rangle = 0$ et la densité de probabilité $\psi(\mathbf{R},\mathbf{x},t)$ peut être obtenue en considérant que chaque sous-élément est un marcheur aléatoire sur l'angle de rotation relatif aux sous-éléments voisins. On définit alors la moyenne statistique d'une quantité A par

$$\langle A\rangle_\psi = \int A\psi(\mathbf{R},\mathbf{x},t)\,d\mathbf{R},$$

avec par définition $\langle 1\rangle_\psi = 1$.

1.4.2.2 Bilan des forces et équations de Langevin

La première étape consiste à réaliser un bilan de forces sur les deux billes constituant l'haltère. En notant $\mathbf{x}_t^i$, la position de la bille i du temps t, la force de traînée sur chaque bille s'écrit

$$\mathbf{F}_{(h)}^i = \zeta\left(\mathbf{u}\left(t,\mathbf{x}_t^i\right) - d\mathbf{x}_t^i\right), \tag{1.32}$$

où ζ est le coefficient de traînée et $\mathbf{u}\left(t,\mathbf{x}_t^i\right)$ la vitesse du solvant en $\mathbf{x}_t^i$. Par ailleurs, la chaîne est soumise à une force de rappel entropique $\mathbf{F}_{(e)}$, dérivant d'un potentiel. On distinguera deux cas

- le cas linéaire (hookéen) où $\mathbf{F}_{(e)}(\mathbf{R}) = H\mathbf{R}$,
- le cas non-linéaire, $\mathbf{F}_{(e)}(\mathbf{R}) = \frac{H\mathbf{R}}{1-H|\mathbf{R}|^2/\ell^2}$, correspondant à une extensibilité finie ℓ des chaînes de polymère,

où $H = \frac{3kT}{Nb^2}$, k étant la constante de Boltzmann et T la température. Enfin, les billes sont chacune soumise à une force brownienne

$$\mathbf{F}_{(b)}^i = \sqrt{\frac{2kT}{\zeta}}\mathbf{W}^i, \tag{1.33}$$

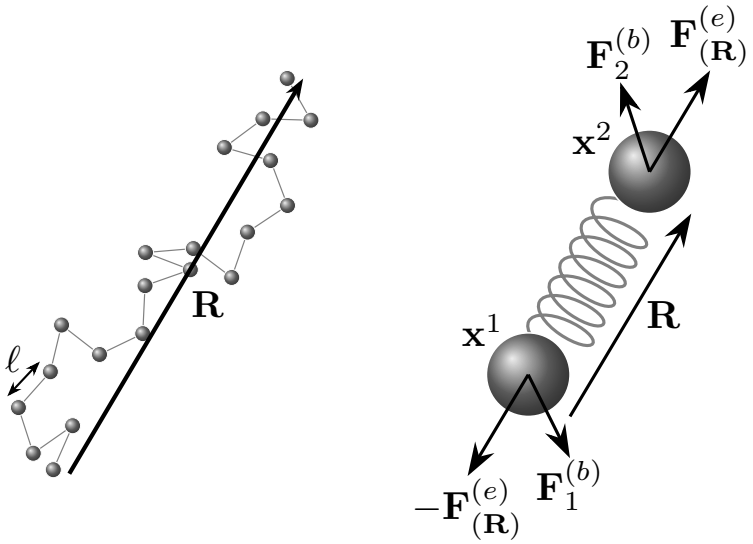

(**I**) Modèle de Rouse (**II**) Modèle dumbell

Fig. 1.6 **Représentations des molécules de polymère.** (I) Modèle de Rouse où la molécule est modélisée par une chaîne constituée de N sous-éléments de longueur b fixe, en libre rotation autour des points de jonction. (II) Modèle en haltère ("dumbell") où les chaînes sont représentées par deux billes reliées par un ressort entropique.

où $\mathbf{W}^i$, $i = 1, 2$ désigne des processus de Wiener indépendants. En faisant un bilan de force sur chacune des billes dont on néglige la masse, on obtient les équations de Langevin suivantes

$$\begin{cases} d\mathbf{x}^1 - \mathbf{u}\left(t, \mathbf{x}^1\right) dt = & \frac{1}{\zeta}\mathbf{F}_{(e)}(\mathbf{x}^2 - \mathbf{x}^1)dt + \sqrt{\frac{2kT}{\zeta}}d\mathbf{W}^1, \\ d\mathbf{x}^2 - \mathbf{u}\left(t, \mathbf{x}^2\right) dt = & \frac{1}{\zeta}\mathbf{F}_{(e)}(\mathbf{x}^1 - \mathbf{x}^2)dt + \sqrt{\frac{2kT}{\zeta}}d\mathbf{W}^2. \end{cases} \tag{1.34}$$

En remarquant que le vecteur "bout-à-bout" peut s'écrire $\mathbf{R} = \mathbf{x}^2 - \mathbf{x}^1$ on obtient, sous certaines approximations [113], l'équation d'évolution suivante

$$d\mathbf{R}(\mathbf{x}) + \mathbf{u}\left(t, \mathbf{r}\right) \cdot \nabla \mathbf{R}(\mathbf{x}) dt = \nabla \mathbf{u}\left(t, \mathbf{r}\right) \cdot \mathbf{R}(\mathbf{x}) dt - \frac{2}{\zeta}\mathbf{F}_{(e)}(\mathbf{R}(\mathbf{x}))dt + \sqrt{\frac{4kT}{\zeta}}d\mathbf{B}, \tag{1.35}$$

où $\mathbf{B} = \frac{1}{\sqrt{2}}\left(\mathbf{W}^2 - \mathbf{W}^1\right)$ correspond également un processus de Wiener.

Il reste à introduire un ingrédient important pour pouvoir compléter cette approche: la relation entre la contrainte et conformation des polymères. Celle-ci est donnée par la relation de Kramers [151]

$$\boldsymbol{\tau}_p(t, \mathbf{x}) = n_p \left(-kT\mathbf{I}_d + \left\langle \mathbf{R}\mathbf{F}_{(e)}\left(\mathbf{R}\right) \right\rangle_{\psi} \right), \tag{1.36}$$

où n_p correspond à la concentration en polymères.

1.4.2.3 Les modèles hybrides

On peut alors directement utiliser l'équation 1.35 pour obtenir le système

$$\begin{cases} \rho\left(\partial_t \mathbf{u} + \mathbf{u}\cdot\nabla\mathbf{u}\right) = -\nabla p + \eta_s \Delta\mathbf{u} + \nabla\cdot\boldsymbol{\tau}_p, \\ \nabla\cdot\mathbf{u} = 0, \\ \boldsymbol{\tau}_p = n_p\left(-kT\mathbf{I}_d + \left\langle \mathbf{R}\mathbf{F}_{(e)}\left(\mathbf{R}\right)\right\rangle_{\psi}\right), \\ d\mathbf{R} + \mathbf{u}\left(t,\mathbf{r}\right)\cdot\nabla\mathbf{R}dt = \left(\nabla\mathbf{u}\left(t,\mathbf{r}\right)\cdot\mathbf{R} - \frac{2}{\zeta}\mathbf{F}_{(e)}(\mathbf{R})\right)dt + \sqrt{\frac{4kT}{\zeta}}d\mathbf{B}. \end{cases} \tag{1.37}$$

Ce système correspond à un modèle hybride micro-macro [113] où l'équation constitutive n'est pas prise en compte et la contrainte est calculée à partir de la dynamique des chaînes de polymères. Cette approche combine donc à la fois des considérations issues de la mécanique des milieux continus et des considérations basées sur la théorie cinétique des polymères en solution. Ce système peut-être résolu à l'aide de méthodes de type CONNFFESIT [62] où la dynamique du polymère est calculée à partir de simulations browniennes qui sont réputées coûteuses du fait d'un taux de convergence faible et d'un grand nombre d'haltères nécessaires pour obtenir un calcul suffisamment précis (environ 10^5 par maille). Certaines techniques permettent néanmoins de rendre ce type de méthode plus efficace [21].

On peut aussi écrire une équation de Fokker-Planck [167] à partir de l'équation sur $\mathbf{R}$, ce qui amène à

$$\begin{cases} \rho\left(\partial_t \mathbf{u} + \mathbf{u}\cdot\nabla\mathbf{u}\right) = -\nabla p + \eta_s \Delta\mathbf{u} + \nabla\cdot\boldsymbol{\tau}_p, \\ \nabla\cdot\mathbf{u} = 0, \\ \boldsymbol{\tau}_p = n_p\left(-kT\mathbf{I}_d + \left\langle \mathbf{R}\mathbf{F}_{(e)}\left(\mathbf{R}\right)\right\rangle_{\psi}\right), \\ \partial_t\psi + \mathbf{u}\cdot\nabla_{\mathbf{x}}\psi = -\nabla_{\mathbf{R}}\cdot\left(\left(\nabla\mathbf{u}\mathbf{R} - \frac{2H}{\zeta}\mathbf{F}_{(e)}(\mathbf{R})\right)\psi\left(\mathbf{R}\right)\right) + \frac{2H}{\zeta}\Delta_{\mathbf{R}}\psi\left(\mathbf{R}\right). \end{cases} \tag{1.38}$$

Ce type de modèle est basé sur une description précise des polymères à l'échelle microscopique, permettant de mieux comprendre le lien entre le comportement microscopique des chaînes et le comportement macroscopique de la solution. Néanmoins, l'introduction de ces variables rend le coût l'implémentation de tels modèles prohibitif, restreignant l'utilisation de ceux-ci à des problèmes à petite échelle comme, par exemple, pour comprendre ce qui se passe près d'une frontière solide.

1.4.2.4 Retour aux modèles continus : cas linéaire

Pour retrouver les modèles continus, on commence par introduire le tenseur de conformation $\mathbf{c}$ défini par

$$\boxed{\mathbf{c} := \frac{H}{kT}\left\langle \mathbf{R}\mathbf{R}\right\rangle_{\psi}} \tag{1.39}$$

Comme on le verra, ce tenseur est essentiel dans la prise en compte de la configuration locale des polymères sur la rétroaction sur l'écoulement. A l'équilibre, toutes les orientations des chaînes sont équiprobables et $\mathbf{c} = \mathbf{I}_d$.

Dans le cas hookéen, $\mathbf{F}_{(e)}(\mathbf{R}) = H\mathbf{R}$, on peut montrer, en multipliant dans (1.38) l'équation de transport sur ψ par $\mathbf{R}$ et en intégrant, que le système précédent peut s'écrire

$$\begin{cases} \rho\left(\partial_t \mathbf{u} + \mathbf{u}\cdot\nabla\mathbf{u}\right) = -\nabla p + \eta_s \Delta\mathbf{u} + \nabla\cdot\boldsymbol{\tau}_p, \\ \nabla\cdot\mathbf{u} = 0, \\ \boldsymbol{\tau}_p = \frac{\eta_p}{\lambda}\left(\mathbf{c} - \mathbf{I}_d\right), \\ \partial_t \mathbf{c} + \mathbf{u}\cdot\nabla\mathbf{c} = \nabla\mathbf{u}\cdot\mathbf{c} + \mathbf{c}\cdot(\nabla\mathbf{u})^{\mathsf{T}} - \frac{1}{\lambda}\left(\mathbf{c} - \mathbf{I}_d\right), \end{cases} \tag{1.40}$$

avec $\lambda = \frac{\zeta}{4H}$ un temps de relaxation et $\eta_p = n_p kT\lambda$ la viscosité associée aux polymères. Par substitution, on retrouve l'équation de transport sur $\boldsymbol{\tau}_p$ suivante

$$\partial_t \boldsymbol{\tau}_p + \mathbf{u}\cdot\nabla\boldsymbol{\tau}_p = \nabla\mathbf{u}\cdot\boldsymbol{\tau}_p + \boldsymbol{\tau}_p\cdot(\nabla\mathbf{u})^{\mathsf{T}} + \frac{\eta_p}{\lambda}\left(\nabla\mathbf{u} + (\nabla\mathbf{u})^{\mathsf{T}}\right) - \frac{1}{\lambda}\boldsymbol{\tau}_p, \tag{1.41}$$

qui correspond exactement au modèle Oldroyd-B dérivé plus haut. Le fait que le modèle Oldroyd-B puisse découler de deux approches très différentes est particulièrement remarquable. Par ailleurs, une remarque importante est que la dérivée convectée supérieure qui apparaît dans les modèles continus découle naturellement d'une approche microscopique.

1.4.2.5 Cas d'une extensibilité finie

Dans le cas d'une extensibilité finie, $\mathbf{F}_{(e)}(\mathbf{R}) = \frac{H\mathbf{R}}{1 - H|\mathbf{R}|^2/\ell^2}$, le calcul de $\left\langle \mathbf{R}\mathbf{F}_{(e)}(\mathbf{R}) \right\rangle_\psi$ nécessite une approximation. L'approximation de Peterlin [158] consiste à supposer que

$$\left\langle \mathbf{R}\frac{H\mathbf{R}}{1 - H|\mathbf{R}|^2/\ell^2} \right\rangle_\psi \simeq \frac{H}{1 - H\langle\mathbf{R}\mathbf{R}\rangle_\psi/\ell^2}\langle\mathbf{R}\mathbf{R}\rangle_\psi, \tag{1.42}$$

dont on déduit le modèle FENE-SP (pour finite extendable non-linear elastic models)

$$\begin{cases} \rho\left(\partial_t \mathbf{u} + \mathbf{u}\cdot\nabla\mathbf{u}\right) = -\nabla p + \eta_s \Delta\mathbf{u} + \nabla\cdot\boldsymbol{\tau}_p, \\ \nabla\cdot\mathbf{u} = 0, \\ \boldsymbol{\tau}_p = \frac{\eta_p}{\lambda}\left(\frac{b}{b - \mathrm{tr}(\mathbf{c})}\mathbf{c} - \mathbf{I}_d\right), \\ \partial_t \mathbf{c} + \mathbf{u}\cdot\nabla\mathbf{c} = \nabla\mathbf{u}\cdot\mathbf{c} + \mathbf{c}\cdot(\nabla\mathbf{u})^{\mathsf{T}} - \frac{1}{\lambda}\left(\frac{b}{b - \mathrm{tr}(\mathbf{c})}\mathbf{c} - \mathbf{I}_d\right), \end{cases} \tag{1.43}$$

où $b = \frac{kT}{H}\ell$ correspond au maximum de $\mathrm{tr}(\mathbf{c})$. Ce modèle est en fait une version simplifiée du modèle FENE-P [14, 166]

$$\begin{cases} \rho\left(\partial_t \mathbf{u} + \mathbf{u}\cdot\nabla\mathbf{u}\right) = -\nabla p + \eta_s \Delta\mathbf{u} + \nabla\cdot\boldsymbol{\tau}_p, \\ \nabla\cdot\mathbf{u} = 0, \\ \boldsymbol{\tau}_p = \frac{\eta_p}{\lambda}\left(\frac{b}{b - \mathrm{tr}(\mathbf{c})}\mathbf{c} - \frac{b}{b - \mathrm{tr}(\mathbf{I}_d)}\mathbf{I}_d\right), \\ \partial_t \mathbf{c} + \mathbf{u}\cdot\nabla\mathbf{c} = \nabla\mathbf{u}\cdot\mathbf{c} + \mathbf{c}\cdot(\nabla\mathbf{u})^{\mathsf{T}} - \frac{1}{\lambda}\left(\frac{b}{b - \mathrm{tr}(\mathbf{c})}\mathbf{c} - \frac{b}{b - \mathrm{tr}(\mathbf{I}_d)}\mathbf{I}_d\right). \end{cases} \tag{1.44}$$

Le modèle FENE-P est rhéofluidifiant en cisaillement [199] et rhéoépaississant en élongation [207] et retrouve ainsi les principales caractéristiques rhéologiques des solutions de polymère, ce qui fait de lui un modèle particulièrement utilisé [47, 109, 160]. L'inconvénient est que la réponse prédite en cisaillement contient une région en loi de puissance où la pente et fixe égale à $-2/3$, rendant la comparaison avec des rhéologies réelles plutôt limitée.

Il existe de nombreux modèle de type FENE [57, 83]. Parmi ceux proposés dans la littérature, on distinguera en particulier l'approximation donnée par [33] qui correspond au modèle FENE-CR

$$\begin{cases} \rho\left(\partial_t \mathbf{u} + \mathbf{u}\cdot\nabla\mathbf{u}\right) = -\nabla p + \eta_s \Delta\mathbf{u} + \nabla\cdot\boldsymbol{\tau}_p, \\ \nabla\cdot\mathbf{u} = 0, \\ \boldsymbol{\tau}_p = \frac{\eta_p}{\lambda}\frac{b}{b-\mathrm{tr}(\mathbf{c})}\left(\mathbf{c}-\mathbf{I}_d\right), \\ \partial_t \mathbf{c} + \mathbf{u}\cdot\nabla\mathbf{c} = \nabla\mathbf{u}\cdot\mathbf{c} + \mathbf{c}\cdot\left(\nabla\mathbf{u}\right)^{\mathsf{T}} - \frac{1}{\lambda}\frac{b}{b-\mathrm{tr}(\mathbf{c})}\left(\mathbf{c}-\mathbf{I}_d\right). \end{cases} \tag{1.45}$$

Bien qu'il soit inconsistant avec la théorie cinétique du fait qu'elle modifie la relation de Kramers de manière ad hoc, ce modèle nous semble très intéressant car la viscosité en cisaillement reste constante. A l'image du modèle Oldroyd-B, il correspond donc à un fluide de Boger, permettant de découpler des effets rhéofluidifiants des effets élastiques. De plus, la réponse en élongation est identique à celle du modèle FENE-P et ne souffre pas de singularités, contrairement au modèle Oldroyd-B.

1.5 Physique des écoulements de solutions de polymères en milieux poreux

Comparé à un écoulement newtonien à travers une géométrie simple, l'écoulement d'un fluide complexe à travers un milieu poreux est considérablement plus complexe. Pour un écoulement newtonien, des caractérisation géométriques simples permettent d'estimer rapidement des propriétés importantes, telle que la perméabilité par exemple. Ceci n'est plus vrai pour des écoulements non-newtonien pour lesquels, même pour des géométries semblant très similaires, on peut observer des comportement très différents, voir opposés [78]. Dans un écoulement d'une solution de polymère, les longues chaînes polymériques vont avoir tendance à interagir avec la paroi. Elles sont par ailleurs transportées, déformées et parfois même dégradées par l'écoulement. En s'étirant fortement, le polymère crée des régions de forte contrainte allant jusqu'à générer des instabilités d'écoulement. Comme on le verra dans cette section, ce comportement microscopique semble être à l'origine d'un comportement macroscopique étrange qui reste encore inexpliqué.

1.5.1 Interaction des chaînes de polymère avec la paroi solide et zones d'exclusion

Les milieux poreux sont caractérisés par leur grande surface spécifique, rapport entre la surface de l'interface fluide-solide et le volume total. Les propriétés macroscopiques des écoulements à travers de tels milieux sont donc très sensibles aux phénomènes présents proches de la surface solide. Les solutions de polymères font preuve d'une grande variété de comportements proche de la paroi [8, 191] (zone notée b-phase Figure 1.7). On distingue principalement les mécanismes de sorption, où les chaînes de polymères flexibles adhèrent à la paroi [5, 68, 210], et les mécanismes de répulsion où, au contraire, les chaînes de polymère sont repoussées par la paroi, formant une couche dite de désorption où la concentration en polymère devient plus faible [54, 96]. On retrouve également des effets similaires au niveau de la surface libre du fluide ou à l'interface entre différentes phases pour des écoulements multiphasiques. De tels effets ont de multiples origines physiques et dépendent à la fois des propriétés de la molécule et de la surface mais également du régime d'écoulement.

La Figure 1.7 propose un découpage schématique en différentes zones de l'espace poral et des différentes approches de modélisation envisageables. Évidemment, beaucoup d'autres mécanismes sont envisageables et il ne s'agit ici que d'illustrer la complexité du problème. On peut imaginer que la b-phase modifie à la fois le transport de quantité de mouvement

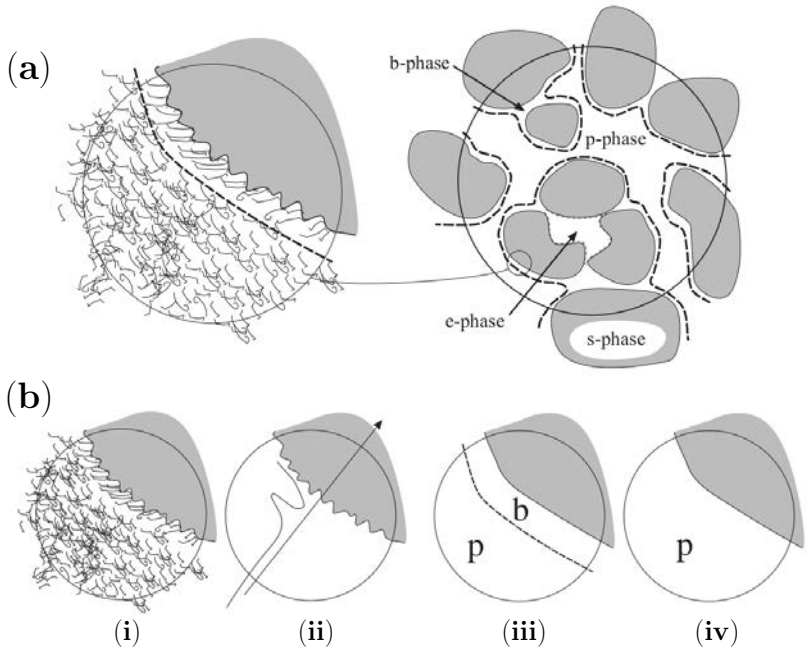

Fig. 1.7 **Ecoulement en milieu poreux à la petite échelle** [162]. (a) Différentes phases correspondant à la répartition des chaînes de polymère à l'échelle du pore. b-phase : zones de paroi où l'on peut observer des arrangements spécifiques des chaînes de polymères, e-phase : zones d'exclusion où les chaînes de polymères ne peuvent pas accéder, p-phase : correspond à la zone dite de bulk et s-phase : correspond à la phase solide. (b) Différentes modélisations du transport de polymère proche paroi. (i) chaque molécule de polymère est considérée, (ii) une description continue de la concentration en polymère où les chaînes sont considérée de manière statistique, (iii-iv) le concept de surface effective permet lisser la rugosité à petite échelle des interfaces, (iii) une description à la mésoéchelle est maintenue proche de paroi, (iv) la description continue est étendue à la paroi où l'on impose une certaine condition limite.

et de masse de polymère, ce qui peut être capturé par des concept de surfaces effectives ou une description multi-domaines de l'espace poral. Selon les tailles caractéristiques des milieux poreux, on peut également distinguer une autre zone, dite d'exclusion [58, 121], et notée e-phase. Contrairement à la b-phase où les molécules de polymère sont toujours présentes, la e-phase correspond à des zones d'inaccessibilité où les molécules, de part leur diamètre de giration, ne peuvent entrer. Elles sont difficiles à modéliser du fait que les macromolécules ne sont pas des sphères dures et que leur distribution de taille n'est pas forcément mono-disperse. Ces zones modifient également l'écoulement et le transport des polymères, tout en restant accessibles aux autres espèces chimique telles que le solvant ou le sel. Elle peuvent ainsi être représentées par une interface avec les autres zones avec un flux nul pour le polymère et une continuité pour les autres espèces. A l'extrême, pour certains milieu très peu perméables, la taille des polymères peut être similaire à celles des pores. Cela peut se mesurer à l'aide du nombre de Knudsen (K_n), qui représente le rapport entre le diamètre des particules et l'échelle de longueur caractéristique du milieu poreux. Lorsque $K_n \ll 1$ [115], on peut se poser des questions sur la pertinence des modèles continus.

1.5.2 Transport de matière : dégradation

Lors de l'écoulement dans un milieux poreux, les chaînes de polymère subissent de fortes contraintes mécaniques pouvant entraîner leur dégradation [124]. Cette dégradation, essentiellement due à l'étirement trop important des chaînes, dépend à la fois de la concentration en polymère, de la longueur du chemin d'écoulement ou du poids moléculaire du polymère [61, 140]. Elle a pour conséquence une modification du poids moléculaire et une redistribution des tailles de molécules. Les chaînes polymériques, plus petites, voient également leur élasticité diminuer. A l'échelle mésoscopique, cette dégradation entraîne entre autres une modification de la viscosité de la solution [180] et de sa rhéologie [170]. Dans le cadre des méthodes de récupération des huiles lourdes, par exemple, la dégradation des chaînes de polymère peut avoir et sur l'injectivité et l'efficacité du balayage [2, 124].

1.5.3 Effets inertiels

Le nombre de Reynolds, $Re = {}^{\rho UL}/_{\eta}$, représente le rapport entre forces d'inertie et forces visqueuses, où ρ, U, L et η sont respectivement la densité du fluide, une vitesse caractéristique, la taille caractéristique des pores et la viscosité du fluide. Dans les roches pétrolières, la taille caractéristiques des pores est généralement petite, de l'ordre de $0.1 - 50$ μm [16, 25] selon que l'on considère le diamètre des pores ou celui des gorges qui les relient. Les vitesses d'écoulement à l'intérieur de ces roches, imposées par un gradient de pression géothermique ou par l'injection d'un fluide de déplacement, sont également assez faibles de l'ordre de $0.01 - 100\,\mu m/s$ [36, 143]. Ainsi, le nombre de Reynolds dans ce type d'écoulement est de l'ordre de $10^{-11} - 10^{-3}$ [110], ce qui implique que l'inertie peut généralement être considérée comme négligeable. Ce régime d'écoulement, dit rampant, à faible nombre de Reynolds est caractéristique de nombreux écoulements en milieu poreux.

1.5.4 L'élasticité

L'ajout de longues chaînes de polymères confère à la solution une certaine élasticité, avec un temps de relaxation que l'on note généralement λ. L'importance relative de l'élasticité est quantifiée par différents nombres sans dimension. Le nombre de Weissenberg $Wi = {}^{\lambda U}/_{L_g}$, où L_g est le diamètre moyen des gorges quantifie le rapport entre les forces élastiques et les forces visqueuses. Le nombre de Deborah $De = {}^{\lambda U}/_{L_p}$, où L_p est le diamètre moyen des pore correspond

pour sa part au rapport entre le temps de relaxation et le temps d'advection sur une longueur caractéristique. Même à de faibles vitesses d'écoulement, les petites dimensions des tailles de pores et de gorges sont telles qu'elles génèrent des gradients de vitesse localement très élevés. Ainsi, pour les écoulements en sous-sol, les nombres de Weissenberg et de Deborah peuvent varier dans des plages de valeurs assez larges, $10^{-5} - 10^{5}$ et $10^{-6} - 10^{5}$, respectivement [110]. On peut également définir le nombre élastique $El = {Wi}/{Re} = {\lambda\eta}/{\rho L_g^2}$ comme étant le rapport entre les force élastiques et les forces inertielles. Il a l'avantage d'être indépendant de l'écoulement et de ne dépendre que des propriétés du fluide et du milieu poreux. En raison des très petites échelles de longueur présentes, on a généralement $El \gg 1$, les forces élastiques dominent ainsi les forces inertielles.

1.5.5 Les instabilités viscoélastiques et le turbulence élastique

Dans le cas $Wi > 1$, des instabilités élastiques peuvent apparaître. On peut, par exemple, les observer dans le cas d'un écoulement autour de deux cylindres [208] entre lesquels se forme une zone de recirculation (Figure 1.8(b)), de même qu'en entrée de contractions abruptes [19, 29, 221] (Figure 1.8(c)). Ces instabilités d'écoulement peuvent mener à de la turbulence, sans inertie, qui est alors dite élastique (voir [72] et Figure 1.8(d) pour la première mise en évidence et [196] pour une revue récente). Cette turbulence a des propriétés analogues à celle observée dans la turbulence inertielle, bien que les mécanismes physiques sous-jacents soient différents. Elle est, entre autre, caractérisée par une augmentation du facteur de friction, une efficacité de mélange plus importante (voir Figure 1.8(e)) et une décroissance rapide des fréquences de fluctuation élevées. Cette turbulence pourrait s'avérer intéressantes pour la récupération des huiles lourdes car elle permettrait d'induire un meilleur balayage en mobilisant l'huile piégée par capillarité [35, 137, 229].

Attribuée aux contraintes élastiques et à leur rétroaction sur l'écoulement, l'origine précise de ces instabilités reste une question importante. L'analyse de la dynamique non-linéaire de ces système montre que la transition spontanée vers un régime instationnaire se fait de manière sous-critique pour des écoulements parallèle [139] et supercritique lorsqu'une courbure est présente [154]. Celle-ci est souvent caractérisé par le critère de McKinley [133, 152]

$$\left[\frac{\lambda U}{\mathcal{R}}\frac{\tau_{11}}{\tau_c}\right]^{1/2} \geq M_{crit}, \tag{1.46}$$

où $\mathcal{R}$ est le rayon courbure d'une ligne de courant (Figure 1.8(a)), τ_{11} la contrainte de traction (tensile stress) dans le sens de l'écoulement, τ_c la contrainte de cisaillement et M_{crit} une constante dépendant de la géométrie. Le premier terme du membre de gauche représente la contribution de la géométrie à l'étirement du polymère à travers la ligne de courant. Le second terme est le rapport entre les contraintes d'extension et de cisaillement. Bien qu'heuristique, ce critère est très utilisé pour décrire la transition vers l'instationnaire. L'étude des instabilités viscoélastiques et de la turbulence élastique soulève de très nombreuses questions [44].

1.5.6 La turbulence élasto-inertielle

Pour une valeur de $Re \cdot De$ suffisamment élevée, un autre type de turbulence, dite élasto-inertielle, est observé [26, 172]. Celle-ci se produit à des nombres de Reynolds plus faibles que la turbulence newtonienne, avec des propriétés dynamiques significativement différentes. On constate en particulier que la traînée diminue avec la concentration en polymère et finit par approcher une limite empirique, l'asymptote de réduction maximale de la traînée. L'utilisation de polymères s'avère ainsi être une méthode particulièrement efficace pour réduire l'importante traînée observée

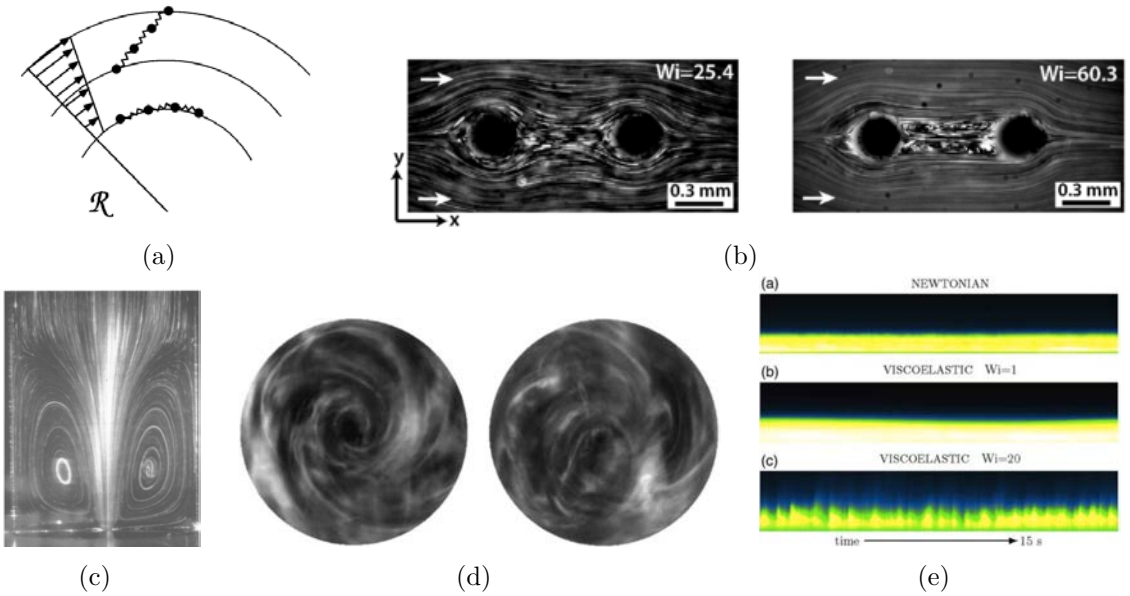

Fig. 1.8 **Instabilités et turbulence viscoélastique.** (a) Illustration du critère de McKinley, issue de [152]. Région représentative d'un écoulement d'une solution de polymère avec un rayon de courbure $\mathcal{R}$. Un faible écart par rapport à la ligne de courant engendre une extension non-linéaire de la molécule de polymère. (b) Écoulement rampant d'un fluide viscoélastique autour de deux cylindres [208]. On observe la formation d'une zone de recirculation entre les deux cylindres. (c) Recirculations à l'entrée d'une contraction [29]. (d) Mise en évidence historique de la turbulence élastique grâce à un écoulement rotatif entre deux plaques parallèles [72]. On observe la formation, sur les deux instantanées, la formation des patterns d'écoulement très irréguliers avec des structures de tailles assez différentes. (e) Flux spatio-temporel colorant dans un canal, en aval d'une perturbation de l'écoulement induite par une rangée de cylindres [161]. On observe, à nombre de Wi élevé, un mélange qui, pour un écoulement newtonien, est inexistant.

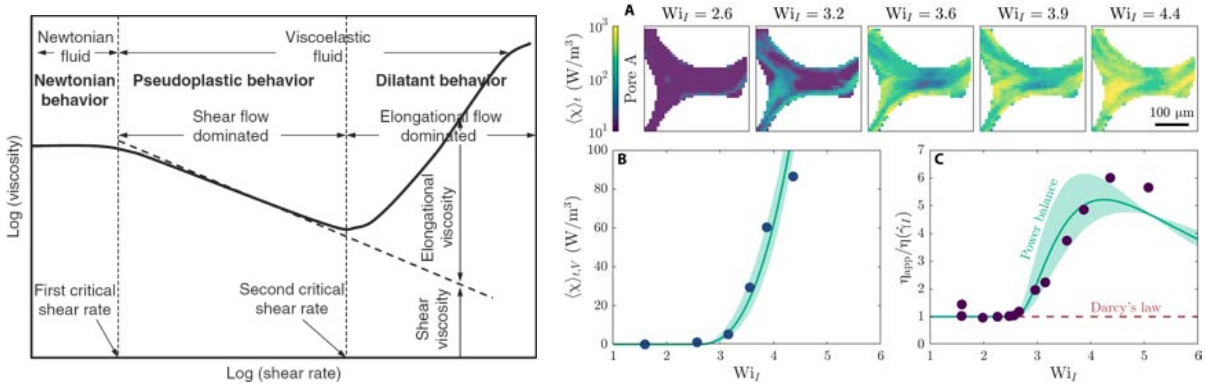

(a) (b)

Fig. 1.9 **Écoulement d'une solution de polymère dans un milieu poreux**. (a) Évolution de la viscosité apparente en fonction du taux de cisaillement [232]. On distingue classiquement trois phases: un plateau newtonien; un comportement rhéofluidifiant; une augmentation brutale de la viscosité. Ici l'augmentation est attribuée à la viscosité élongationnelle. (b) Lien entre l'augmentation de la résistance macroscopique à l'écoulement et les fluctuations [24]. La transition est ici attribuée à une augmentation du taux de dissipation visqueuse, associée à un début de turbulence élastique.

dans les écoulements turbulents [193, 219] et trouve de nombreuses applications notamment dans les oléoducs, les réseaux d'égouts, de chauffage ou d'irrigation [105, 178]. On considérera ici que le nombre de Reynolds est trop faible dans nos structures poreuses pour que les effets élasto-inertielle soient importants.

1.5.7 Augmentation de la résistance à l'écoulement : un problème non résolu

Lorsqu'on fait s'écouler une solution de polymère dans un milieu poreux, un comportement tout-à-fait improbable se produit. En effet, après une diminution de la viscosité apparente à faible débit, on observe, à partir d'un certain débit, une augmentation brutale de la viscosité apparente. Au premier abord, ce comportement semble en contradiction avec la nature rhéofluidifiante de ces fluides [60, 93, 101, 129]. Outre son caractère surprenant, ce comportement est particulièrement problématique, notamment dans les secteurs de l'énergie et de l'environnement, puisqu'il se traduit par une augmentation critique des pressions nécessaires et une baisse de l'injectivité. Diverses hypothèses ont été formulées pour expliquer ce paradoxe, parmi lesquelles l'effet de la viscosité élongationnelle [34, 59, 106, 185, 232] ou la turbulence élastique [24, 36, 65, 102, 122, 161]. Une compréhension détaillée du problème, reliant clairement la physique à l'échelle du pore avec celle à des échelles plus grandes fait encore défaut.

1.6 Vers un modèle macroscopique?

La dérivation de formulations moyennées à l'échelle de Darcy, n'exigeant pas une description détaillée à l'échelle du pore, est un problème fondamental dans l'étude des milieux poreux. L'idée est d'essayer de capturer les phénomènes à petite échelle à travers des opérations de moyenne sur les variables principales et l'utilisation de paramètres effectifs à plus grande échelle. On notera ici $\langle\cdot\rangle$ l'opérateur de moyenne glissante spatiale et $\langle\cdot\rangle^\beta$ l'opérateur de moyenne intrinsèque. Pour un écoulement Newtonien à travers un milieu poreux dans le régime de Stokes, la conservation

de la quantité de mouvement est décrite par une loi de Darcy [42] de la forme

$$\langle \mathbf{u} \rangle = -\frac{\mathbf{K}_0}{\eta_0} \cdot \left(\nabla \langle p \rangle^\beta - \rho \mathbf{g} \right), \tag{1.47}$$

où $\langle \mathbf{u} \rangle$ désigne la vitesse moyenne superficielle, $\nabla \langle p \rangle^\beta$ le gradient de pression intrinsèque et $\rho \mathbf{g}$ la gravité. A cette équation s'ajoute l'incompressibilité donnée par

$$\nabla \cdot \langle \mathbf{u} \rangle = 0.$$

De tels écoulements sont ainsi simplement décrits par la viscosité η_0, constante, qui est propriété propre au fluide et le tenseur perméabilité intrinsèque $\mathbf{K}_0$ qui permet de caractériser l'effet du milieu poreux. En pratique, cette perméabilité est souvent déterminée à partir d'un volume élémentaire représentatif, par diverses méthodes [97, 120, 136]. Une telle description de l'écoulement est, d'un point de vue pratique, extrêmement intéressante. La question de sa généralisation à d'autres d'écoulements tels que celui des solutions de polymère alors se pose donc naturellement.

1.6.1 Généralisations de la loi de Darcy

Dans les simulateurs de réservoirs [3, 177], par exemple, la loi de Darcy est généralisée à des écoulements non-newtoniens à travers une relation de la forme

$$\langle \mathbf{u} \rangle = -\frac{\mathbf{K}_0}{\eta_{app}} \cdot \left(\nabla \langle p \rangle^\beta - \rho \mathbf{g} \right), \tag{1.48}$$

qui fait ainsi intervenir une viscosité apparente η_{app} dépendant du taux de déformation apparent $\dot{\gamma}_{eq}$ à travers la relation du type

$$\eta_{app} = \eta \left(\dot{\gamma}_{eq} \right) R_k, \tag{1.49}$$

où R_k est un facteur décrivant la réduction de perméabilité due au polymère retenu dans le milieu par adsorption ou rétention mécanique [3]. Ce paramètre peut ainsi à la fois dépendre du polymère, de la roche, ou encore de l'écoulement et est calculé à partir de relations semi-empiriques. Quant à la viscosité de référence $\eta \left(\dot{\gamma}_{eq} \right)$, elle est généralement déterminée à partir de mesures en rhéomètre ce qui pose évidemment question du fait que, comme on a pu le voir, le comportement rhéologique des solutions de polymère est très dépendant de la géométrie considérée. Une autre difficulté, non moindre, réside dans la détermination d'un équivalent macroscopique $\dot{\gamma}_{eq}$ du taux de déformation dont de nombreuses estimations différentes ont été proposées et discutés [234].

Cette première généralisation de la loi de Darcy est purement scalaire et ne prend donc pas en compte le fait que, pour un écoulement non-newtonien, les axes principaux du tenseur de perméabilité apparent peuvent changer [88, 150]. Ainsi, une autre possibilité consiste à modifier plutôt le tenseur de perméabilité, comme proposé par [235] dans le cas de fluides quasi-newtoniens. Cette généralisation de la loi de Darcy s'écrit alors

$$\langle \mathbf{u} \rangle = -\frac{\mathbf{K}_{app}}{\eta_0} \cdot \left(\nabla \langle p \rangle^\beta - \rho \mathbf{g} \right), \tag{1.50}$$

où le tenseur de perméabilité apparente est défini par

$$\mathbf{K}_{app} = k_n \mathbf{P} \cdot \mathbf{K}_0, \tag{1.51}$$

avec k_n est un scalaire représentant la modification de la norme de la perméabilité due aux effets non-newtoniens et $\mathbf{P}$ est un tenseur de rotation capturant les modifications de direction de la perméabilité.

1.6.2 Changement d'échelle

La loi de Darcy (1.47) a été établie, à l'origine, de manière empirique [42, 236]. C'est également le cas des lois de Darcy généralisées au fluides non-newtonien (1.48) ou à des écoulements multiphasiques [145] et des formulations macroscopiques de la dispersion [10, 51, 175]. Or il s'avère que la loi de Darcy peut être dérivée grâce à des méthodes de changement d'échelle, directement à partir des équations de Stokes [218]. De la même manière, il existe une grande variété de techniques pour moyenner les équations de transport dans les systèmes multiéchelles et multiphasiques. Parmi ces techniques, ont distingue essentiellement la prise de moyenne volumique [218] et l'homogénéisation [173], une comparaison des deux étant proposée dans [45]. Ces théories effectives trouvent de nombreuses applications que ce soit dans l'étude les tissus biologiques [225] et des biofilms [46], le transport dans les réseaux vasculaires [119] mais également les réservoirs avec de grandes failles [82].

En général, les variables à l'échelle du pore – l'indicatrice de phase par exemple – ont une variation spatiale rapide par rapport aux échelles du domaine macroscopique. Cela signifie que l'échelle de longueur caractéristique du pore, ℓ_β, est beaucoup plus petite que la longueur caractéristique h d'un volume élémentaire représentatif (VER), elle-même plus petite que la taille L du domaine macroscopique, voir Figure 1.10(a). On dit ainsi que l'on a une séparation des échelles

$$\ell_\beta \ll h \ll L,$$

hypothèse essentielle au développement des théories à grandes échelles [128, 176]. Dans le cas de la prise de moyenne volumique, la méthode consiste alors à résoudre un certain sytème d'équation à la petite échelle sur un VER afin d'en déduire des propriété effectives qui seraient valables sur tout le domaine macroscopique.

Considérons, par exemple, un écoulement de Stokes où les équations de conservation sont données par le système

$$\begin{cases} -\nabla p + \eta_0 \Delta \mathbf{u} = 0, \\ \nabla \cdot \mathbf{u} = 0, \end{cases} \tag{1.52}$$

sans considérer la gravité et des conditions aux limites que l'on ne traitera pas ici. L'idée consiste à décomposer les champs de pression p et de vitesse $\mathbf{u}$ en comme la somme de la moyenne intrinsèque et d'une perturbation [217]

$$p = \langle p \rangle^\beta + \tilde{p}, \tag{1.53}$$
$$\mathbf{u} = \langle \mathbf{u} \rangle^\beta + \tilde{\mathbf{u}}. \tag{1.54}$$

On peut ensuite moyenne le problème de Stokes et le soustraire aux équations initiales pour obtenir un problème linéaire sur les perturbations. Se basant cette linéarité, on peut écrire une solution de la forme

$$\tilde{p} = \eta_0 \mathbf{b} \cdot \langle \mathbf{u} \rangle^\beta, \tag{1.55}$$
$$\tilde{\mathbf{u}} = \mathbf{B} \cdot \langle \mathbf{u} \rangle^\beta, \tag{1.56}$$

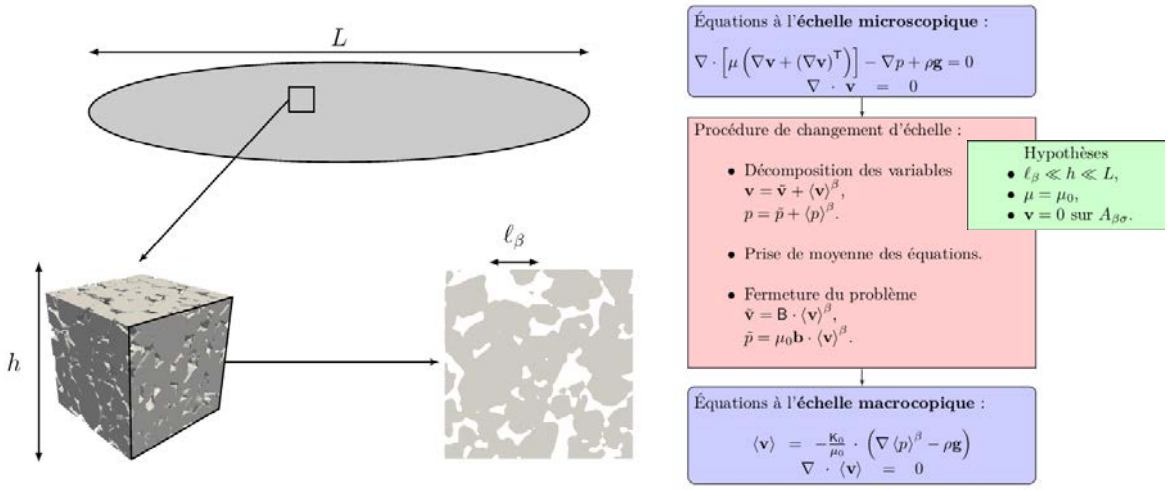

Fig. 1.10 **La méthode du changement d'échelle** [233]. (**a**) Principe de séparation des échelles, la phase solide est ici représentée en gris. (**b**) Exemple de changement d'échelle par prise de moyenne volumique dans le cas de Stokes. La viscosité que l'on note η_0 est ici notée μ_0.

où $\mathbf{b}$ est un vecteur et $\mathbf{B}$ un tenseur de rang 2 qui vérifient le problème de fermeture

$$\begin{cases} -\nabla \mathbf{b} + \Delta \mathbf{B} - \langle -\nabla \mathbf{b} + \Delta \mathbf{B} \rangle^\beta = 0, \\ \nabla \cdot \mathbf{B} = 0, \end{cases} \tag{1.57}$$

avec $\langle \mathbf{b} \rangle^\beta = \langle \mathbf{B} \rangle^\beta = 0$. Ce problème est alors utilisé pour déterminer les propriétés effectives du problème macroscopique. Ainsi, en introduisant le tenseur de perméabilité

$$\mathbf{K}_0 = -\phi^{-1} \langle -\nabla \mathbf{b} + \Delta \mathbf{B} \rangle^\beta, \tag{1.58}$$

on retrouve la loi de Darcy

$$\langle \mathbf{u} \rangle = -\frac{\mathbf{K}_0}{\eta_0} \cdot \nabla \langle p \rangle^\beta. \tag{1.59}$$

L'ensemble de la procédure est récapitulée Figure 1.10(b). Un point important de cette approche est la linéarité du problème à l'échelle microscopique. Ainsi, dans le cas d'un fluide non-newtonien où le système d'équations à l'échelle microscopique n'est plus linéaire, l'écriture d'un problème de fermeture pose question et l'obtention d'une forme macroscopique est généralement plus difficile [233].

1.6.3 Transport de matière

Aux équations de conservation de la masse et de la quantité de mouvement s'ajoute généralement celle de la masse de polymère. Aux grandes échelles, cette équation peut par exemple prendre la forme suivante [159, 227]

$$\partial_t \left(\phi_{eff} c\right) + \nabla \cdot \left(\langle \mathbf{u} \rangle c\right) = \nabla \cdot \left(\phi \mathbf{D}_{eff} \nabla c\right),$$

où c est une concentration en polymères, ϕ_{eff} et $\mathbf{D}_{eff}$ correspondent respectivement à une porosité et un tenseur de diffusion effectifs. La porosité effective ϕ_{eff} permet de prendre en

compte la présence de pores inaccessibles aux polymères. De ce fait, elle est inférieure à la porosité intrinsèque ϕ du milieu. Elle est généralement considérée comme étant uniforme dans tout le domaine bien que celle-ci puisse dépendre des hétérogénéités mais également de la distribution de tailles des molécules qui, du fait de la dégradation, peut diminuer fortement à l'échelle du réservoir. Enfin, au delà de la diffusion, le tenseur $\mathbf{D}_{eff}$ doit également rendre compte de la dispersion qui, dans un écoulement viscoélastique par exemple, peut-être accentuée par la turbulence élastique et l'augmentation du mélange qui l'accompagne [73].

Dans cette étude, on supposera que la concentration en polymère ne varie pas spatialement ce qui est une hypothèse forte. Cela ne préjuge cependant pas de l'organisation locale des chaînes polymériques qui, comme on le verra, joue un rôle essentiel.

1.6.4 Transport de la contrainte polymérique

Bien que la plupart des modèles d'écoulement viscoélastiques en milieux poreux se basent sur une généralisation très simple de Darcy, cette représentation n'a en fait rien d'évident. Dans le cas des fluides viscoélastiques, en plus du transport de la quantité de mouvement, celui de la contrainte élastique liée au polymère doit être pris en compte. Cela suggère que la modélisation de ces écoulements à travers les milieux poreux ne se résume pas simplement à la détermination d'un tenseur de perméabilité apparent et nécessite donc plutôt le développement de modèles spécifiques capturant le couplage entre le transport de la contrainte due au polymère et de la quantité de mouvement. Il n'existe qu'un nombre assez limité d'études qui tentent de réaliser un changement à l'échelle direct des écoulements viscoélastiques à travers des milieux poreux, qui remettent en cause la forme des équations à grande échelle ou qui proposent un ensemble pertinent de paramètres effectifs. [107] utilise par exemple une asymptotique formelle à plusieurs échelles et propose, dans la limite Weissenberg faible, une loi de Darcy généralisée avec un tenseur de perméabilité dynamique. [50] considère quant à lui un fluide de Maxwell et utilise une prise de moyenne volumique pour également dériver une forme dynamique de la loi de Darcy. Malheureusement, dans ces deux travaux, l'homogénéisation est limitée à une forme linéaire de viscoélasticité où l'équation constitutive n'est pas objective et ne capture pas convenablement le transport de la contrainte polymérique. En particulier, cette approximation néglige les termes de production de la forme $\nabla\mathbf{u}\mathbf{c} + \mathbf{c}\,(\nabla\mathbf{u})^{\mathsf{T}}$ qui génèrent les brins biréfringents. Or comme on le verra, ces brins biréfringents jouent un rôle primordiale dans ces écoulements et une formulation moyennée du problème ce doit de les prendre en compte.

1.7 Objectifs et contributions de cette thèse

Comme on a pu le voir, l'écoulement de solutions de polymère à travers des milieux poreux constitue un problème extrêmement riche, combinant la complexité des écoulements à travers des structures poreuses à celle du fluide, non-newtonien, constitué de longues chaînes de polymères qui sont transportées et déformées par l'écoulement tout en rétroagissant sur celui-ci. Un tel problème fait ainsi intervenir une très large gamme d'échelles, de l'échelle moléculaire voire atomique des chaînes de polymère et des surfaces rugueuses du solide à celle de tout un réservoir aquifère en passant par des échelles correspondant à un ou plusieurs pores. Une modélisation complète et précise de tous les mécanismes intervenant à chacune de ces échelles, ainsi que des liens entre celles-ci est inenvisageable et probablement non-souhaitable dans l'état actuel des connaissances.

Dans ce travail, nous nous focaliserons dans un premier temps sur les mécanismes présents à l'échelle des pores. L'objectif est de démêler certains des phénomènes physiques présents à cette échelle afin de les relier aux propriétés à l'échelle de Darcy. Pour ce faire, nous avons simulé

l'écoulement de fluides viscoélastiques à travers des structures poreuses modèles, telles que des réseaux de cylindres en 2D ou des empilements de sphères en 3D, en utilisant des calculs haute performance des modèles Oldroyd-B, FENE-P et FENE-CR. Dans un second temps temps, ayant constaté le rôle important des zones de forte contrainte polymérique sur l'écoulement à l'échelle des pores, nous proposons la dérivation d'un modèle macroscopique qui prend en compte, à l'échelle de Darcy, cette contrainte polymérique et sa rétroaction sur l'écoulement. Le manuscrit est organisé comme suit.

Dans le Chapitre 2, nous présentons un nouveau schéma de projection à grille décalée pour les écoulements viscoélastiques, ainsi que des cas de validation pour le problème de la cavité entraînée et l'écoulement autour d'un cylindre confiné dans un canal. Nous montrons que ce schéma possède une semi-discrétisation spatiale cohérente avec une estimation de l'énergie libre, maintient la positivité du tenseur de conformation, est bien adapté au calcul haute performance (HPC), montre une bonne précision et peut être facilement utilisé pour une variété de lois constitutives viscoélastiques telles que les modèles de type Oldroyd ou FENE. Il est également implémenté pour le calcul haute performance et disponible via la plateforme open-source CALIF^{3}S développée à l'Institut de Radioprotection et de Sûreté Nucléaire (IRSN). Les calculs haute performance de ce travail ont été effectués sur le supercalculateur Pangea de TotalEnergies. Bien que notre approche traite des termes inertiels dans l'équation de transport de la quantité de mouvement, nous nous concentrons sur les effets élastiques et nous limitons donc tous nos travaux aux petits nombres de Reynolds.

Au Chapitre 3, nous utilisons cette approche numérique pour montrer que des zones localisées de grande contrainte polymérique, appelées brins biréfringents, pilotent l'écoulement d'un fluide Oldroyd-B à travers des réseaux de cylindres en 2D. Nous avons découvert que ces brins génèrent une réorganisation complète de l'écoulement avec une augmentation des zones de stagnation, un renforcement des chemins préférentiels et une division des canaux d'écoulement. De plus, nous avons montré que cette réorganisation est la source d'une augmentation de la dissipation visqueuse du solvant et que l'étirement des molécules de polymère dans les brins est associée à une production d'entropie. Ces deux phénomènes conduisent à une augmentation globale de la dissipation qui peut être directement reliée à l'augmentation de la résistance à l'écoulement. Nos résultats démontrent que ce sont les brins biréfringents, et non la viscosité élongationnelle, qui déterminent l'écoulement des fluides viscoélastiques dans les milieux poreux et que l'augmentation de la résistance à l'écoulement peut se produire même en régime permanent, bien avant la transition vers la turbulence élastique.

Nous étudions ensuite, au Chapitre 4, l'écoulement des fluides Oldroyd-B, FENE-P et FENE-CR à travers un réseau hexagonal 2D de cylindres sur une large gamme de nombres de Weissenberg et différentes orientations du terme de forçage générant l'écoulement. Nous montrons que les brins biréfringents contrôlent la direction de l'écoulement moyen. Par le mécanisme de rétroaction, ces brins ont également tendance à adhérer aux cylindres voisins, ce qui conduit à des directions d'écoulement préférentielles et à une succession de bifurcations lorsque l'on fait varier l'angle du terme de forçage. L'effet le plus frappant est la tristabilité et l'hystérésis dans la configuration décalée. Nous démontrons en outre que l'apparition d'un écoulement instationnaire est liée à une instabilité de battement des brins qui oscillent entre des états précédemment tristables et caractérisons l'évolution de l'instabilité en fonction de différents paramètres. Ceci fournit une nouvelle perspective sur les écoulements viscoélastiques instationnaires à travers des milieux poreux et peut aider à comprendre la transition vers le chaos dans des expériences récentes d'écoulements de polymères dans des expériences microfluidiques.

Dans la cinquième partie, nous dérivons une forme moyenne du modèle Oldroyd-B à l'échelle de Darcy. Pour ce faire, nous utilisons une forme de linéarisation du problème, en considérant une limite très diluée, et nous décomposons le problème initial en une séquence de problèmes

à différents ordres. Par exemple, le transport du tenseur de conformation à l'ordre principal peut être calculé sur la base de la vitesse de Stokes. Cette limite est très différente de la limite du faible nombre de Weissenberg car elle peut capturer la formation de brins biréfringents. Nous procédons à la moyenne de chaque problème dans l'espace et dérivons le modèle moyen correspondant pour obtenir une forme modifiée de la loi de Darcy.

Les écoulements viscoélastiques 2D dans des réseaux de cylindres ont suscité beaucoup d'intérêt, en particulier dans une série de travaux expérimentaux récents, et ils nous ont aidé à comprendre les aspects fondamentaux de ces écoulements. Cependant, les écoulements à travers des structures 2D et 3D sont fondamentalement différents. Dans la dernière partie de ce travail, nous présentons donc des résultats préliminaires pour les écoulements viscoélastiques à travers des empilements 3D de sphères. De telles structures conduisent à des régions localisées de contrainte qui peuvent être considérées comme des brins 1D et des hyperplans 2D. Cela soulève des questions importantes sur la façon dont les flux viscoélastiques sont affectés par la dimensionnalité. Par exemple, la différence de topologie conduit-elle à un effet plus faible des brins sur l'écoulement et donc à une augmentation plus faible de la résistance à l'écoulement à l'échelle de Darcy ?

Références

[1] Abraham, F., Behr, M., and Heinkenschloss, M. (2005). Shape optimization in unsteady blood flow: A numerical study of non-newtonian effects. *Computer Methods in Biomechanics and Biomedical Engineering*, 8(3):201–212.

[2] Al-Shakry, B., Skauge, T., Shaker Shiran, B., and Skauge, A. (2018). Impact of mechanical degradation on polymer injectivity in porous media. *Polymers*, 10(7):742.

[3] Anderson, G. A. (2006). *Simulation of chemical flood enhanced oil recovery processes including the effects of reservoir wettability*. PhD thesis.

[4] Aramideh, S., Vlachos, P. P., and Ardekani, A. M. (2019). Unstable displacement of non-aqueous phase liquids with surfactant and polymer. *Transport in Porous Media*, 126(2):455–474.

[5] Ash, S. G., Everett, D. H., and Radke, C. (1973). Thermodynamics of the effects of adsorption on interparticle forces. *Journal of the Chemical Society, Faraday Transactions 2: Molecular and Chemical Physics*, 69:1256–1277.

[6] Astarita, G. (1979). Objective and generally applicable criteria for flow classification. *Journal of Non-Newtonian Fluid Mechanics*, 6(1):69–76.

[7] Astarita, G. (1991). Quasi-newtonian constitutive equations exhibiting flow-type sensitivity. *Journal of Rheology*, 35(4):687–689.

[8] Barnes, H. A. (1995). A review of the slip (wall depletion) of polymer solutions, emulsions and particle suspensions in viscometers: its cause, character, and cure. *Journal of Non-Newtonian Fluid Mechanics*, 56(3):221–251.

[9] Barrett, J. W. and Süli, E. (2018). Existence of large-data global-in-time finite-energy weak solutions to a compressible FENE-P model. *Mathematical Models and Methods in Applied Sciences*, 28(10):1929–2000.

[10] Bear, J. (1961). On the tensor form of dispersion in porous media. *Journal of Geophysical Research*, 66(4):1185–1197.

[11] Bear, J. and Bachmat, Y. (2012). *Introduction to modeling of transport phenomena in porous media*, volume 4. Springer Science & Business Media.

[12] Bernsdorf, J. and Wang, D. (2009). Non-newtonian blood flow simulation in cerebral aneurysms. *Computers & Mathematics with Applications*, 58(5):1024–1029.

[13] Bingham, E. C. (1917). *An investigation of the laws of plastic flow*. Number 278. US Government Printing Office.

[14] Bird, R. B., Curtiss, C. F., Armstrong, R. C., and Hassager, O. (1987). *Dynamics of polymeric liquids, volume 2: Kinetic theory*. Wiley.

[15] Bird, R. B. and Wiest, J. M. (1995). Constitutive equations for polymeric liquids. *Annual Review of Fluid Mechanics*, 27:169–193.

[16] Blunt, M. J., Bijeljic, B., Dong, H., Gharbi, O., Iglauer, S., Mostaghimi, P., Paluszny, A., and Pentland, C. (2013). Pore-scale imaging and modelling. *Advances in Water Resources*, 51:197–216.

[17] Bodiguel, H., Beaumont, J., Machado, A., Martinie, L., Kellay, H., and Colin, A. (2015). Flow enhancement due to elastic turbulence in channel flows of shear thinning fluids. *Physical Review Letters*, 114(2):028302.

[18] Boger, D. V. (1987). Viscoelastic flows through contractions. *Annual Review of Fluid Mechanics*, 19(1):157–182.

[19] Boger, D. V., Hur, D. U., and Binnington, R. J. (1986). Further observations of elastic effects in tubular entry flows. *Journal of Non-Newtonian Fluid Mechanics*, 20:31–49.

[20] Boger, D. V. and Walters, K. (1993). *Rheological phenomena in focus*. Elsevier.

[21] Bonvin, J. and Picasso, M. (1999). Variance reduction methods for connffessit-like simulations. *Journal of Non-Newtonian Fluid Mechanics*, 84(2-3):191–215.

[22] Boyd, J., Buick, J. M., and Green, S. (2007). Analysis of the casson and carreau-yasuda non-newtonian blood models in steady and oscillatory flows using the lattice boltzmann method. *Physics of Fluids*, 19(9):093103.

[23] Braun, D. D. and Rosen, M. R. (2013). *Rheology modifiers handbook: practical use and application*. Elsevier.

[24] Browne, C. A. and Datta, S. S. (2021). Elastic turbulence generates anomalous flow resistance in porous media. *Science Advances*, 7(45):eabj2619.

[25] Browne, C. A., Shih, A., and Datta, S. S. (2020). Pore-scale flow characterization of polymer solutions in microfluidic porous media. *Small*, 16(9):1903944.

[26] Burshtein, N., Zografos, K., Shen, A. Q., Poole, R. J., and Haward, S. J. (2017). Inertioelastic flow instability at a stagnation point. *Physical Review X*, 7(4):041039.

[27] Carreau, P. J., MacDonald, I. F., and Bird, R. B. (1968). A nonlinear viscoelastic model for polymer solutions and melts-ii. *Chemical Engineering Science*, 23(8):901–911.

[28] Carrel, M., Morales, V. L., Beltran, M. A., Derlon, N., Kaufmann, R., Morgenroth, E., and Holzner, M. (2018). Biofilms in 3d porous media: Delineating the influence of the pore network geometry, flow and mass transfer on biofilm development. *Water research*, 134:280–291.

[29] Cartalos, U. and Piau, J. M. (1992). Creeping flow regimes of low concentration polymer solutions in thick solvents through an orifice die. *Journal of non-newtonian fluid mechanics*, 45(2):231–285.

[30] Casanellas, L., Alves, M. A., Poole, R. J., Lerouge, S., and Lindner, A. (2016). The stabilizing effect of shear thinning on the onset of purely elastic instabilities in serpentine microflows. *Soft Matter*, 12(29):6167–6175.

[31] Chauveteau, G. and Kohler, N. (1984). Influence of microgels in polysaccharide solutions on their flow behavior through porous media. *Society of Petroleum Engineers Journal*, 24(03):361–368.

[32] Chauveteau, G., Moan, M., and Magueur, A. (1984). Thickening behaviour of dilute polymer solutions in non-inertial elongational flows. *Journal of Non-Newtonian Fluid Mechanics*, 16(3):315–327.

[33] Chilcott, M. D. and Rallison, J. M. (1988). Creeping flow of dilute polymer solutions past cylinders and spheres. *Journal of Non-Newtonian Fluid Mechanics*, 29:381–432.

[34] Chmielewski, C. and Jayaraman, K. (1992). The effect of polymer extensibility on crossflow of polymer solutions through cylinder arrays. *Journal of Rheology*, 36(6):1105–1126.

[35] Clarke, A., Howe, A. M., Mitchell, J., Staniland, J., Hawkes, L., and Leeper, K. (2015). Mechanism of anomalously increased oil displacement with aqueous viscoelastic polymer solutions. *Soft Matter*, 11(18):3536–3541.

[36] Clarke, A., Howe, A. M., Mitchell, J., Staniland, J., and Hawkes, L. A. (2016). How viscoelastic-polymer flooding enhances displacement efficiency. *SPE Journal*, 21(03):0675–0687.

[37] Cogswell, F. N. (1978). Converging flow and stretching flow: a compilation. *Journal of Non-Newtonian Fluid Mechanics*, 4(1-2):23–38.

[38] Cressely, R. and Decruppe, J. P. (1992). Flow birefringence visualization of transitions in circular couette flow. *Experiments in Fluids*, 13(1):43–48.

[39] Cross, M. M. (1965). Rheology of non-newtonian fluids: a new flow equation for pseudoplastic systems. *Journal of Colloid Science*, 20(5):417–437.

[40] Crowley, D. G., Frank, F. C., Mackley, M. R., and Stephenson, R. G. (1976). Localized flow birefringence of polyethylene oxide solutions in a four roll mill. *Journal of Polymer Science: Polymer Physics Edition*, 14(6):1111–1119.

[41] Cussler, E. L. (2009). *Diffusion: mass transfer in fluid systems*. Cambridge university press.

[42] Darcy, H. (1856). *Les fontaines publiques de la ville de Dijon: exposition et application...* Victor Dalmont.

[43] Das, M. K., Mukherjee, P. P., and Muralidhar, K. (2018). *Modeling transport phenomena in porous media with applications*, volume 123. Springer.

[44] Datta, S. S., Ardekani, A. M., Arratia, P. E., Beris, A. N., Bischofberger, I., Eggers, J. G., López-Aguilar, J. E., Fielding, S. M., Frishman, A., Graham, M. D., et al. (2021). Perspectives on viscoelastic flow instabilities and elastic turbulence. *arXiv preprint arXiv:2108.09841*.

[45] Davit, Y., Bell, C. G., Byrne, H. M., Chapman, L. A. C., Kimpton, L. S., Lang, G. E., Leonard, K. H. L., Oliver, J. M., Pearson, N. C., Shipley, R. J., et al. (2013a). Homogenization via formal multiscale asymptotics and volume averaging: How do the two techniques compare? *Advances in Water Resources*, 62:178–206.

[46] Davit, Y., Byrne, H., Osborne, J., Pitt-Francis, J., Gavaghan, D., and Quintard, M. (2013b). Hydrodynamic dispersion within porous biofilms. *Physical Review E*, 87(1):012718.

[47] De, S., Kuipers, J. A. M., Peters, E. A. J. F., and Padding, J. T. (2017). Viscoelastic flow simulations in random porous media. *Journal of Non-Newtonian Fluid Mechanics*, 248:50–61.

[48] De Gennes, P. G. (1974). Coil-stretch transition of dilute flexible polymers under ultrahigh velocity gradients. *The Journal of Chemical Physics*, 60(12):5030–5042.

[49] De Gennes, P. G. (1979). *Scaling concepts in polymer physics*. Cornell university press.

[50] De Haro, M. L., Del Río, J. A. P., and Whitaker, S. (1996). Flow of maxwell fluids in porous media. *Transport in Porous Media*, 25(2):167–192.

[51] De Josselin de Jong, G. (1958). Longitudinal and transverse diffusion in granular deposits. *Eos, Transactions American Geophysical Union*, 39(1):67–74.

[52] Delamaide, E., Zaitoun, A., Renard, G., and Tabary, R. (2014). Pelican lake field: first successful application of polymer flooding in a heavy-oil reservoir. *SPE Reservoir Evaluation & Engineering*, 17(03):340–354.

[53] Denn, M. M. (1980). Continuous drawing of liquids to form fibers. *Annual Review of Fluid Mechanics*, 12(1):365–387.

[54] DiMarzio, E. A. and McCrackin, F. L. (1965). One-dimensional model of polymer adsorption. *The Journal of Chemical Physics*, 43(2):539–547.

[55] Djabourov, M., Nishinari, K., and Ross-Murphy, S. B. (2013). *Physical gels from biological and synthetic polymers*. Cambridge University Press.

[56] Doi, M. and Edwards, S. F. (1988). *The theory of polymer dynamics*, volume 73. Oxford University Press.

[57] Du, Q., Liu, C., and Yu, P. (2005). Fene dumbbell model and its several linear and nonlinear closure approximations. *Multiscale Modeling & Simulation*, 4(3):709–731.

[58] Duda, J. L., Klaus, E. E., and Fan, S. K. (1981). Influence of polymer-molecule/wall interactions on mobility control. *Society of Petroleum Engineers Journal*, 21(05):613–622.

[59] Durst, F., Haas, R., and Interthal, W. (1987). The nature of flows through porous media. *Journal of Non-Newtonian Fluid Mechanics*, 22(2):169–189.

[60] Durst, F., Haas, R., and Kaczmar, B. U. (1981). Flows of dilute hydrolyzed polyacrylamide solutions in porous media under various solvent conditions. *Journal of Applied Polymer Science*, 26(9):3125–3149.

[61] Farinato, R. S. and Yen, W. S. (1987). Polymer degradation in porous media flow. *Journal of Applied Polymer Science*, 33(7):2353–2368.

[62] Feigl, K., Laso, M., and Oettinger, H. C. (1995). Connffessit approach for solving a two-dimensional viscoelastic fluid problem. *Macromolecules*, 28(9):3261–3274.

[63] François, N., Lasne, D., Amarouchene, Y., Lounis, B., and Kellay, H. (2008). Drag enhancement with polymers. *Physical Review Letters*, 100(1):018302.

[64] Fuller, G. G. and Leal, L. G. (1981). Flow birefringence of concentrated polymer solutions in two-dimensional flows. *Journal of Polymer Science: Polymer Physics Edition*, 19(4):557–587.

[65] Galindo-Rosales, F. J., Campo-Deano, L., Pinho, F. T., Van Bokhorst, E., Hamersma, P. J., Oliveira, M. S. N., and Alves, M. A. (2012). Microfluidic systems for the analysis of viscoelastic fluid flow phenomena in porous media. *Microfluidics and Nanofluidics*, 12(1-4):485–498.

[66] Gampert, B. and Wilkes, C. (2002). Rheo-optical measurements of the elongational flow of aqueous polymer solutions. *Rheologica acta*, 41(4):326–331.

[67] Garrepally, S. (2020). *Scission of polymers in extensional flows, bridging the gap between single contraction and porous mediaux*. PhD thesis, Université Paris sciences et lettres.

[68] Garvey, M. J., Tadros, T. F., and Vincent, B. (1976). A comparison of the adsorbed layer thickness obtained by several techniques of various molecular weight fractions of poly (vinyl alcohol) on aqueous polystyrene latex particles. *Journal of Colloid and Interface Science*, 55(2):440–453.

[69] Giesekus, H. (1982). A simple constitutive equation for polymer fluids based on the concept of deformation-dependent tensorial mobility. *Journal of Non-Newtonian Fluid Mechanics*, 11(1-2):69–109.

[70] Gordon, R. J. and Schowalter, W. R. (1972). Anisotropic fluid theory: a different approach to the dumbbell theory of dilute polymer solutions. *Transactions of the Society of Rheology*, 16(1):79–97.

[71] Green, D. W., Willhite, G. P., et al. (1998). *Enhanced oil recovery*, volume 6. Henry L. Doherty Memorial Fund of AIME, Society of Petroleum Engineers.

[72] Groisman, A. and Steinberg, V. (2000). Elastic turbulence in a polymer solution flow. *Nature*, 405(6782):53–55.

[73] Groisman, A. and Steinberg, V. (2001). Efficient mixing at low reynolds numbers using polymer additives. *Nature*, 410(6831):905–908.

[74] Gurtin, M. E. (1982). *An introduction to continuum mechanics*. Academic press.

[75] Haller, G. (2015). Lagrangian coherent structures. *Annual Review of Fluid Mechanics*, 47:137–162.

[76] Harlen, O. G. (1990). High-deborah-number flow of a dilute polymer solution past a sphere falling along the axis of a cylindrical tube. *Journal of Non-Newtonian Fluid Mechanics*, 37(2-3):157–173.

[77] Harlen, O. G., Hinch, E. J., and Rallison, J. M. (1992). Birefringent pipes: the steady flow of a dilute polymer solution near a stagnation point. *Journal of Non-Newtonian Fluid Mechanics*, 44:229–265.

[78] Haward, S. J., Hopkins, C. C., and Shen, A. Q. (2021). Stagnation points control chaotic fluctuations in viscoelastic porous media flow. *Proceedings of the National Academy of Sciences*, 118(38).

[79] Haward, S. J., McKinley, G. H., and Shen, A. Q. (2016). Elastic instabilities in planar elongational flow of monodisperse polymer solutions. *Scientific Reports*, 6(1):1–18.

[80] Haward, S. J. and Odell, J. A. (2004). Molecular orientation in non-Newtonian flow of dilute polymer solutions around spheres. *Rheologica Acta*, 43(4):350–363.

[81] Hemingway, E. J., Clarke, A., Pearson, J. R. A., and Fielding, S. M. (2018). Thickening of viscoelastic flow in a model porous medium. *Journal of Non-Newtonian Fluid Mechanics*, 251:56–68.

[82] Henn, N., Quintard, M., Bourbiaux, B., and Sakthikumar, S. (2004). Modelling of conductive faults with a multiscale approach. *Oil & Gas Science and Technology*, 59(2):197–214.

[83] Herrchen, M. and Öttinger, H. C. (1997). A detailed comparison of various fene dumbbell models. *Journal of non-newtonian fluid mechanics*, 68(1):17–42.

[84] Hinch, J. and Harlen, O. (2021). Oldroyd B, and not A? *Journal of Non-Newtonian Fluid Mechanics*, 298:104668.

[85] Hopkins, C. C., Haward, S. J., and Shen, A. Q. (2020). Purely elastic fluid–structure interactions in microfluidics: implications for mucociliary flows. *Small*, 16(9):1903872.

[86] Hsieh, C.-C. and Larson, R. G. (2005). Prediction of coil-stretch hysteresis for dilute polystyrene molecules in extensional flow. *Journal of Rheology*, 49(5):1081–1089.

[87] Huilgol, R. R. (1975). On a characterization of simple extensional flows. *Rheologica Acta*, 14(1):48–50.

[88] Idris, Z., Orgéas, L., Geindreau, C., Bloch, J.-F., and Auriault, J.-L. (2004). Microstructural effects on the flow law of power-law fluids through fibrous media. *Modelling and Simulation in Materials Science and Engineering*, 12(5):995.

[89] James, D. and Saringer, J. H. (1982). Flow of dilute polymer solutions through converging channels. *Journal of Non-Newtonian Fluid Mechanics*, 11(3-4):317–339.

[90] James, D. F. (2009). Boger fluids. *Annual Review of Fluid Mechanics*, 41:129–142.

[91] James, D. F. (2016). N1 stresses in extensional flows. *Journal of Non-Newtonian Fluid Mechanics*, 232:33–42.

[92] James, D. F., Chandler, G. M., and Armour, S. J. (1990). A converging channel rheometer for the measurement of extensional viscosity. *Journal of Non-Newtonian Fluid Mechanics*, 35(2-3):421–443.

[93] James, D. F. and McLaren, D. R. (1975). The laminar flow of dilute polymer solutions through porous media. *Journal of Fluid Mechanics*, 70(4):733–752.

[94] James, D. F. and Walters, K. (1993). A critical appraisal of available methods for the measurement of extensional properties of mobile systems. In *Techniques in Rheological Measurement*, pages 33–53. Springer.

[95] Jang, H. Y., Zhang, K., Chon, B. H., and Choi, H. J. (2015). Enhanced oil recovery performance and viscosity characteristics of polysaccharide xanthan gum solution. *Journal of Industrial and Engineering Chemistry*, 21:741–745.

[96] Joanny, J. F., Leibler, L., and De Gennes, P. G. (1979). Effects of polymer solutions on colloid stability. *Journal of Polymer Science: Polymer Physics Edition*, 17(6):1073–1084.

[97] Johnson, E. F., Bossler, D. P., and Bossler, V. O. (1959). Calculation of relative permeability from displacement experiments. *Transactions of the AIME*, 216(01):370–372.

[98] Jones, R. C. and Gainer, J. L. (1976). Diffusion in mixed polymer solutions. *Industrial & Engineering Chemistry Fundamentals*, 15(1):83–85.

[99] Jones, W. M., Hudson, N. E., and Ferguson, J. (1990). The extensional properties of m1 obtained from the stretching of a filament by a falling pendant drop. *Journal of Non-Newtonian Fluid Mechanics*, 35(2-3):263–276.

[100] Joshi, Y. M., Lele, A. K., and Mashelkar, R. A. (2000). Slipping fluids: a unified transient network model. *Journal of non-newtonian fluid mechanics*, 89(3):303–335.

[101] Kauser, N., Dos Santos, L., Delgado, M., Müller, A. J., and Sáez, A. E. (1999). Flow of mixtures of poly (ethylene oxide) and hydrolyzed polyacrylamide solutions through porous media. *Journal of Applied Polymer Science*, 72(6):783–795.

[102] Kawale, D., Marques, E., Zitha, P. L. J., Kreutzer, M. T., Rossen, W. R., and Boukany, P. E. (2017). Elastic instabilities during the flow of hydrolyzed polyacrylamide solution in porous media: effect of pore-shape and salt. *Soft Matter*, 13(4):765–775.

[103] Keller, A. and Odell, J. A. (1985). The extensibility of macromolecules in solution; a new focus for macromolecular science. *Colloid and Polymer Science*, 263(3):181–201.

[104] Khaitan, S., Kalainesan, S., Erickson, L. E., Kulakow, P., Martin, S., Karthikeyan, R., Hutchinson, S. L. L., Davis, L. C., Illangasekare, T. H., and Ng'oma, C. (2006). Remediation of sites contaminated by oil refinery operations. *Environmental Progress*, 25(1):20–31.

[105] Khalil, M. F., Kassab, S. Z., Elmiligui, A. A., and Naoum, F. A. (2002). Applications of drag-reducing polymers in sprinkler irrigation systems: Sprinkler head performance. *Journal of irrigation and drainage engineering*, 128(3):147–152.

[106] Khomami, B. and Moreno, L. D. (1997). Stability of viscoelastic flow around periodic arrays of cylinders. *Rheologica Acta*, 36(4):367–383.

[107] Khuzhayorov, B., Auriault, J.-L., and Royer, P. (2000). Derivation of macroscopic filtration law for transient linear viscoelastic fluid flow in porous media. *International Journal of Engineering Science*, 38(5):487–504.

[108] Kim, C. A., Kim, J. T., Lee, K., Choi, H. J., and Jhon, M. S. (2000). Mechanical degradation of dilute polymer solutions under turbulent flow. *Polymer*, 41(21):7611–7615.

[109] Kumar, M. and Ardekani, A. M. (2021). Elastic instabilities between two cylinders confined in a channel. *Physics of Fluids*, 33(7):074107.

[110] Kumar, M., Guasto, J. S., and Ardekani, A. M. (2022). Transport of complex and active fluids in porous media. *Journal of Rheology*, 66(2):375–397.

[111] Kundu, P. K. (1973). Normal stresses and weissenberg effect. *Transactions of the Society of Rheology*, 17(2):343–349.

[112] Lake, L. W. (1989). Enhanced oil recovery.

[113] Le Bris, C. and Lelievre, T. (2012). Micro-macro models for viscoelastic fluids: modelling, mathematics and numerics. *Science China Mathematics*, 55(2):353–384.

[114] Lee, I. C. Y., Kapur, N., Gaskell, P. H., Savage, M. D., and Homsy, G. M. (2002). Birefringent strands in polymer flows in a co-rotating two-roll mill. *Journal of Non-Newtonian Fluid Mechanics*, 104(1):33–51.

[115] Li, G., Lauga, E., and Ardekani, A. M. (2021). Microswimming in viscoelastic fluids. *Journal of Non-Newtonian Fluid Mechanics*, 297:104655.

[116] Li, S. U. and Gainer, J. L. (1968). Diffusion in polymer solutions. *Industrial & Engineering Chemistry Fundamentals*, 7(3):433–440.

[117] Liao, T. Y., Hu, H. H., and Joseph, D. D. (1994). White-metzner models for rod climbing in a1. *Journal of Non-Newtonian Fluid Mechanics*, 51(2):111–124.

[118] Lions, P.-L. and Masmoudi, N. (2000). Global solutions for some Oldroyd models of non-newtonian flows. *Chinese Annals of Mathematics*, 21(02):131–146.

[119] Lorthois, S. and Cassot, F. (2010). Fractal analysis of vascular networks: insights from morphogenesis. *Journal of Theoretical Biology*, 262(4):614–633.

[120] Loudon, A. G. (1952). The computation of permeability from simple soil tests. *Geotechnique*, 3(4):165–183.

[121] Lund, T., Bjørnestad, E., Stavland, A., Gjøvikli, N. B., Fletcher, A. J. P., Flew, S. G., and Lamb, S. P. (1992). Polymer retention and inaccessible pore volume in north sea reservoir material. *Journal of Petroleum Science and Engineering*, 7(1-2):25–32.

[122] Machado, A., Bodiguel, H., Beaumont, J., Clisson, G., and Colin, A. (2016). Extra dissipation and flow uniformization due to elastic instabilities of shear-thinning polymer solutions in model porous media. *Biomicrofluidics*, 10(4):043507.

[123] Mackley, M. R. (1978). Flow singularities, polymer chain extension and hydrodynamic instabilities. *Journal of Non-Newtonian Fluid Mechanics*, 4(1-2):111–136.

[124] Maerker, J. M. (1975). Shear degradation of partially hydrolyzed polyacrylamide solutions. *Society of Petroleum Engineers Journal*, 15(04):311–322.

[125] Málaga, C. and Rallison, J. M. (2007). A rising bubble in a polymer solution. *Journal of Non-Newtonian Fluid Mechanics*, 141(1):59–78.

[126] Malvern, L. E. (1969). *Introduction to the Mechanics of a Continuous Medium*. Number Monograph.

[127] Mantzaris, N. V., Kelley, A. S., Daoutidis, P., and Srienc, F. (2002). A population balance model describing the dynamics of molecular weight distributions and the structure of pha copolymer chains. *Chemical Engineering Science*, 57(21):4643–4663.

[128] Markov, K. Z. (2000). Elementary micromechanics of heterogeneous media. In *Heterogeneous Media*, pages 1–162. Springer.

[129] Marshall, R. J. and Metzner, A. B. (1967). Flow of viscoelastic fluids through porous media. *Industrial & Engineering Chemistry Fundamentals*, 6(3):393–400.

[130] Martín-Alfonso, J. E., Cuadri, A. A., Berta, M., and Stading, M. (2018). Relation between concentration and shear-extensional rheology properties of xanthan and guar gum solutions. *Carbohydrate Polymers*, 181:63–70.

[131] Maxwell, J. C. (1867). Iv. on the dynamical theory of gases. *Philosophical Transactions of the Royal Society of London*, (157):49–88.

[132] McKinley, G. H. (2005). Visco-elasto-capillary thinning and break-up of complex fluids. *Rheology Reviews*, (3).

[133] McKinley, G. H., Pakdel, P., and Öztekin, A. (1996). Rheological and geometric scaling of purely elastic flow instabilities. *Journal of Non-Newtonian Fluid Mechanics*, 67:19–47.

[134] McKinley, G. H. and Sridhar, T. (2002). Filament-stretching rheometry of complex fluids. *Annual Review of Fluid Mechanics*, 34(1):375–415.

[135] Miles, M. J. and Keller, A. (1980). Conformational relaxation time in polymer solutions by elongational flow experiments: 2. Preliminaries of further developments: chain retraction; identification of molecular weight fractions in a mixture. *Polymer*, 21(11):1295–1298.

[136] Millington, R. J. and Quirk, J. P. (1959). Permeability of porous media. *Nature*, 183(4658):387–388.

[137] Mitchell, J., Lyons, K., Howe, A. M., and Clarke, A. (2016). Viscoelastic polymer flows and elastic turbulence in three-dimensional porous structures. *Soft Matter*, 12(2):460–468.

[138] Moan, M. and Magueur, A. (1988). Transient extensional viscosity of dilute flexible polymer solutions. *Journal of Non-Newtonian Fluid Mechanics*, 30(2-3):343–354.

[139] Morozov, A. and Van Saarloos, W. (2019). Subcritical instabilities in plane poiseuille flow of an Oldroyd-B fluid. *Journal of Statistical Physics*, 175(3):554–577.

[140] Morris, C. and Jackson, K. (1978). Mechanical degradation of polyacrylamide solutions in porous media. In *SPE symposium on improved methods of oil recovery*. OnePetro.

[141] Morris, E. R. (1995). Polysaccharide rheology and in-mouth perception. *Food Polysaccharides and their Applications*, pages 517–546.

[142] Mrokowska, M. M. and Krztoń-Maziopa, A. (2019). Viscoelastic and shear-thinning effects of aqueous exopolymer solution on disk and sphere settling. *Scientific Reports*, 9(1):1–13.

[143] Muggeridge, A., Cockin, A., Webb, K., Frampton, H., Collins, I., Moulds, T., and Salino, P. (2014). Recovery rates, enhanced oil recovery and technological limits. *Philosophical Transactions of the Royal Society A: Mathematical, Physical and Engineering Sciences*, 372(2006):20120320.

[144] Müller, A. J., Odell, J. A., and Keller, A. (1988). Elongational flow and rheology of monodisperse polymers in solution. *Journal of Non-Newtonian Fluid Mechanics*, 30(2-3):99–118.

[145] Muskat, M. (1981). Physical principles of oil production.

[146] Nash, W., Pinder, D. N., Hemar, Y., and Singh, H. (2002). Dynamic light scattering investigation of sodium caseinate and xanthan mixtures. *International Journal of Biological Macromolecules*, 30(5):269–271.

[147] Niavarani, A. and Priezjev, N. V. (2008). Rheological study of polymer flow past rough surfaces with slip boundary conditions. *The Journal of chemical physics*, 129(14):144902.

[148] Oldroyd, J. G. (1950). On the formulation of rheological equations of state. *Proceedings of the Royal Society of London. Series A. Mathematical and Physical Sciences*, 200(1063):523–541.

[149] Oliveira, P. D., Michel, R. C., McBride, A. J. A., Moreira, A. S., Lomba, R. F. T., and Vendruscolo, C. T. (2013). Concentration regimes of biopolymers xanthan, tara, and clairana, comparing dynamic light scattering and distribution of relaxation time. *PLos One*, 8(5):e62713.

[150] Orgéas, L., Idris, Z., Geindreau, C., Bloch, J.-F., and Auriault, J.-L. (2006). Modelling the flow of power-law fluids through anisotropic porous media at low-pore reynolds number. *Chemical engineering science*, 61(14):4490–4502.

[151] Öttinger, H. C. (1995). *Stochastic processes in polymeric fluids*. Springer.

[152] Pakdel, P. and McKinley, G. H. (1996). Elastic instability and curved streamlines. *Physical Review Letters*, 77(12):2459.

[153] Pao, Y.-H. (1957). Hydrodynamic theory for the flow of a viscoelastic fluid. *Journal of Applied Physics*, 28(5):591–598.

[154] Pathak, J. A., Ross, D., and Migler, K. B. (2004). Elastic flow instability, curved streamlines, and mixing in microfluidic flows. *Physics of Fluids*, 16(11):4028–4034.

[155] Perge, C. (2014). *Imagerie ultrasonore dans les matériaux mous*. PhD thesis, Ecole normale supérieure de lyon-ENS LYON.

[156] Perkins, T. T., Smith, D. E., and Chu, S. (1997). Single polymer dynamics in an elongational flow. *Science*, 276(5321):2016–2021.

[157] Perpete, E. and Laso, M. (2006). *Multiscale modelling of polymer properties*. Elsevier.

[158] Peterlin, A. (1966). Hydrodynamics of linear macromolecules. *Pure and Applied Chemistry*, 12(1-4):563–586.

[159] Pettersen, O. (2006). Basics of reservoir simulation with the eclipse reservoir simulator. *Lecture Notes. University of Bergen, Norway*, page 114.

[160] Purnode, B. and Crochet, M. J. (1998). Polymer solution characterization with the fene-p model. *Journal of non-newtonian fluid mechanics*, 77(1-2):1–20.

[161] Qin, B., Salipante, P. F., Hudson, S. D., and Arratia, P. E. (2019). Flow resistance and structures in viscoelastic channel flows at low Re. *Physical Review Letters*, 123(19):194501.

[162] Quintard, M. (2012). Report on flow models involving polymer slugs. *Total external report*.

[163] Rallison, J. M. and Hinch, E. J. (1988). Do we understand the physics in the constitutive equation? *Journal of Non-Newtonian Fluid Mechanics*, 29:37–55.

[164] Renardy, M. (1997). High Weissenberg number boundary layers for the upper convected Maxwell fluid. *Journal of Non-Newtonian Fluid Mechanics*, 68(1):125–132.

[165] Renardy, M. (2000a). Asymptotic structure of the stress field in flow past a cylinder at high Weissenberg number. *Journal of Non-Newtonian Fluid Mechanics*, 90(1):13–23.

[166] Renardy, M. (2000b). *Mathematical analysis of viscoelastic flows*. SIAM.

[167] Risken, H. (1996). Fokker-planck equation. In *The Fokker-Planck Equation*, pages 63–95. Springer.

[168] Rodd, A. B., Dunstan, D. E., and Boger, D. V. (2000). Characterisation of xanthan gum solutions using dynamic light scattering and rheology. *Carbohydrate polymers*, 42(2):159–174.

[169] Rouse Jr, P. E. (1953). A theory of the linear viscoelastic properties of dilute solutions of coiling polymers. *The Journal of Chemical Physics*, 21(7):1272–1280.

[170] Rousseau, D., Henaut, I., Dupas, A., Poulain, P., Tabary, R., Argillier, J. F., and Aubry, T. (2013). Impact of polymer mechanical degradation on shear and extensional viscosities. In *IOR 2013-17th European Symposium on Improved Oil Recovery*, pages cp–342. European Association of Geoscientists & Engineers.

[171] Ryder, J. F. and Yeomans, J. M. (2006). Shear thinning in dilute polymer solutions. *The Journal of Chemical Physics*, 125(19):194906.

[172] Samanta, D., Dubief, Y., Holzner, M., Schäfer, C., Morozov, A. N., Wagner, C., and Hof, B. (2013). Elasto-inertial turbulence. *Proceedings of the National Academy of Sciences*, 110(26):10557–10562.

[173] Sánchez-Palencia, E. (1980). Non-homogeneous media and vibration theory. *Lecture Notes in Physics*, 127.

[174] Saramito, P. (2016). *Complex fluids*. Springer.

[175] Scheidegger, A. E. (1961). General theory of dispersion in porous media. *Journal of Geophysical Research*, 66(10):3273–3278.

[176] Scheidegger, A. E. (2020). The physics of flow through porous media. In *The Physics of Flow Through Porous Media (3rd Edition)*. University of Toronto press.

[177] Schlumberger (2014). Eclipse industry-reference reservoir simulator.

[178] Sellin, R. H. J. and Ollis, M. (1980). Polymer drag reduction in large pipes and sewers: Results of recent field trials. *Journal of Rheology*, 24(5):667–684.

[179] Sentmanat, M., Wang, B. N., and McKinley, G. H. (2005). Measuring the transient extensional rheology of polyethylene melts using the ser universal testing platform. *Journal of rheology*, 49(3):585–606.

[180] Seright, R. S., Fan, T., Wavrik, K., and de Carvalho Balaban, R. (2011a). New insights into polymer rheology in porous media. *SPE Journal*, 16(01):35–42.

[181] Seright, R. S., Fan, T., Wavrik, K., Wan, H., Gaillard, N., and Favéro, C. (2011b). Rheology of a new sulfonic associative polymer in porous media. *SPE Reservoir Evaluation & Engineering*, 14(06):726–734.

[182] Shaqfeh, E. S. G. and Khomami, B. (2021). The Oldroyd-B fluid in elastic instabilities, turbulence and particle suspensions. *Journal of Non-Newtonian Fluid Mechanics*, 298:104672.

[183] Sheng, J. J. (2013). A comprehensive review of alkaline-surfactant-polymer (asp) flooding. In *SPE western regional & AAPG pacific section meeting 2013 joint technical conference*. OnePetro.

[184] Siddique, R. (2019). *Self-compacting concrete: materials, properties and applications*. Woodhead Publishing.

[185] Skauge, A., Zamani, N., Gausdal Jacobsen, J., Shaker Shiran, B., Al-Shakry, B., and Skauge, T. (2018). Polymer flow in porous media: Relevance to enhanced oil recovery. *Colloids and Interfaces*, 2(3):27.

[186] Smith, D. E., Babcock, H. P., and Chu, S. (1999). Single-polymer dynamics in steady shear flow. *Science*, 283(5408):1724–1727.

[187] Smith, M. M., Silva, J. A. K., Munakata-Marr, J., and McCray, J. E. (2008). Compatibility of polymers and chemical oxidants for enhanced groundwater remediation. *Environmental Science & Technology*, 42(24):9296–9301.

[188] Snoeijer, J. H., Pandey, A.and Herrada, M. A., and Eggers, J. (2020). The relationship between viscoelasticity and elasticity. *Proceedings of the Royal Society A*, 476(2243):20200419.

[189] Soares, E. J. (2020). Review of mechanical degradation and de-aggregation of drag reducing polymers in turbulent flows. *Journal of Non-Newtonian Fluid Mechanics*, 276:104225.

[190] Sochi, T. (2010). Non-newtonian flow in porous media. *Polymer*, 51(22):5007–5023.

[191] Sochi, T. (2011). Slip at fluid-solid interface. *Polymer Reviews*, 51(4):309–340.

[192] Sorbie, K. S. (2013). *Polymer-improved oil recovery*. Springer Science & Business Media.

[193] Sreenivasan, K. R. and White, C. M. (2000). The onset of drag reduction by dilute polymer additives, and the maximum drag reduction asymptote. *Journal of Fluid Mechanics*, 409:149–164.

[194] Staggs, J. E. J. (2004). Modelling end-chain scission and recombination of linear polymers. *Polymer Degradation and Stability*, 85(2):759–767.

[195] Staggs, J. E. J. (2006). Discrete bond-weighted random scission of linear polymers. *Polymer*, 47(3):897–906.

[196] Steinberg, V. (2021). Elastic turbulence: An experimental view on inertialess random flow. *Annual Review of Fluid Mechanics*, 53:27–58.

[197] Sun, C.-l. and Huang, H.-Y. (2016). Measurements of flow-induced birefringence in microfluidics. *Biomicrofluidics*, 10(1):011903.

[198] Tagaya, A. (2015). Birefringence of polymer. *Encyclopedia of Polymeric Nanomaterials. Springer, Berlin, Heidelberg*.

[199] Tamano, S., Hamanaka, S., Nakano, Y., Morinishi, Y., and Yamada, T. (2020). Rheological modeling of both shear-thickening and thinning behaviors through constitutive equations. *Journal of Non-Newtonian Fluid Mechanics*, 283:104339.

[200] Tanner, R. I. (2007). Revisitation of PTT model. *Journal of Central South University of Technology*, 14(1):26–29.

[201] te Nijenhuis, K. (1997). *Thermoreversible networks: viscoelastic properties and structure of gels*, volume 130. Springer.

[202] Thien, N. P. and Tanner, R. I. (1977). A new constitutive equation derived from network theory. *Journal of Non-Newtonian Fluid Mechanics*, 2(4):353–365.

[203] Thompson, R. L. and Mendes, P. R. S. (2005). Persistence of straining and flow classification. *International Journal of Engineering Science*, 43(1-2):79–105.

[204] Tirtaatmadja, V. and Sridhar, T. (1993). A filament stretching device for measurement of extensional viscosity. *Journal of Rheology*, 37(6):1081–1102.

[205] Torres, M. D., Hallmark, B., Wilson, D. I., and Hilliou, L. (2014). Natural giesekus fluids: Shear and extensional behavior of food gum solutions in the semidilute regime. *AIChE Journal*, 60(11):3902–3915.

[206] Trouton, F. T. (1906). On the coefficient of viscous traction and its relation to that of viscosity. *Proceedings of the Royal Society of London. Series A, Containing Papers of a Mathematical and Physical Character*, 77(519):426–440.

[207] Van Heel, A. P. G., Hulsen, M. A., and Van den Brule, B. H. A. A. (1998). On the selection of parameters in the FENE-P model. *Journal of non-newtonian fluid mechanics*, 75(2-3):253–271.

[208] Varshney, A. and Steinberg, V. (2017). Elastic wake instabilities in a creeping flow between two obstacles. *Physical Review Fluids*, 2(5):051301.

[209] Veljkovic, V. B., Lazić, M. L., and Skala, D. U. (1988). Studies on dextran fermentation broth rheology. *Enzyme and Microbial Technology*, 10(11):686–688.

[210] Vincent, B. (1974). The effect of adsorbed polymers on dispersion stability. *Advances in Colloid and Interface Science*, 4(2-3):193–277.

[211] Vrentas, J. S. and Duda, J. L. (1979). Molecular diffusion in polymer solutions. *AIChE Journal*, 25(1):1–24.

[212] Wagner, C., Amarouchene, Y., Doyle, P., and Bonn, D. (2003). Turbulent-drag reduction of polyelectrolyte solutions: Relation with the elongational viscosity. *EPL (Europhysics Letters)*, 64(6):823.

[213] Walkama, D. M., Waisbord, N., and Guasto, J. S. (2020). Disorder suppresses chaos in viscoelastic flows. *Physical Review Letters*, 124(16):164501.

[214] Walters, K., Tamaddon-Jahromi, H. R., Webster, M. F., Tomé, M. F., and McKee, S. (2009). The competing roles of extensional viscosity and normal stress differences in complex flows of elastic liquids. *Korea-Australia Rheology Journal*, 21(4):225–233.

[215] Wang, M., Smith, J. M., and McCoy, B. J. (1995). Continuous kinetics for thermal degradation of polymer in solution. *AIChE Journal*, 41(6):1521–1533.

[216] Weissberg, S. G., Simha, R., and Rothman, S. (1951). Viscosity of dilute and moderately concentrated polymer solutions. *Journal of Research of the National Bureau of Standards*, 47(4):298–314.

[217] Whitaker, S. (1973). The transport equations for multi-phase systems. *Chemical Engineering Science*, 28(1):139–147.

[218] Whitaker, S. (1986). Flow in porous media I: A theoretical derivation of Darcy's law. *Transport in porous media*, 1(1):3–25.

[219] White, C. M. and Mungal, M. G. (2008). Mechanics and prediction of turbulent drag reduction with polymer additives. *Annu. Rev. Fluid Mech.*, 40:235–256.

[220] White, J. L. and Metzner, A. B. (1963). Development of constitutive equations for polymeric melts and solutions. *Journal of Applied Polymer Science*, 7(5):1867–1889.

[221] White, S. A., Gotsis, A. D., and Baird, D. G. (1987). Review of the entry flow problem: experimental and numerical. *Journal of Non-Newtonian Fluid Mechanics*, 24(2):121–160.

[222] Wilkes, G. L. (1981). An overview of the basic rheological behavior of polymer fluids with an emphasis on polymer melts. *Journal of Chemical Education*, 58(11):880.

[223] Winter, H. H. and Mours, M. (1997). Rheology of polymers near liquid-solid transitions. *Neutron spin echo spectroscopy viscoelasticity rheology*, pages 165–234.

[224] Wood, B. D., Quintard, M., and Whitaker, S. (2004). Estimation of adsorption rate coefficients based on the smoluchowski equation. *Chemical engineering science*, 59(10):1905–1921.

[225] Wood, B. D. and Whitaker, S. (2000). Multi-species diffusion and reaction in biofilms and cellular media. *Chemical Engineering Science*, 55(17):3397–3418.

[226] Wunderlich, A. M. and James, D. F. (1987). Extensional flow resistance of dilute polyacrylamide and surfactant solutions. *Rheologica acta*, 26(6):522–531.

[227] Yanai, T., Nakano, H., Nakajima, T., Tsuneda, T., Hirata, S., Kawashima, Y., Nakao, Y., Kamiya, M., Sekino, H., and Hirao, K. (2003). Utchem-a program for ab initio quantum chemistry. In *International Conference on Computational Science*, pages 84–95. Springer.

[228] Yasuda, K. Y., Armstrong, R. C., and Cohen, R. E. (1981). Shear flow properties of concentrated solutions of linear and star branched polystyrenes. *Rheologica Acta*, 20(2):163–178.

[229] Yin, H., Wang, D., and Zhong, H. (2006). Study on flow behavoirs of viscoelastic polymer solution in micropore with dead end. In *SPE Annual Technical Conference and Exhibition*. OnePetro.

[230] Ying, Q. and Chu, B. (1987). Overlap concentration of macromolecules in solution. *Macromolecules*, 20(2):362–366.

[231] Youcefi, A., Anne-Archard, D., Boisson, H. C., and Sengelin, M. (1997). On the influence of liquid elasticity on mixing in a vessel agitated by a two-bladed impeller.

[232] Zamani, N., Bondino, I., Kaufmann, R., and Skauge, A. (2015). Effect of porous media properties on the onset of polymer extensional viscosity. *Journal of Petroleum Science and Engineering*, 133:483–495.

[233] Zami-Pierre, F. (2017). *Ecoulements de solutions de polymères en milieux poreux: lien entre physique à l'échelle des pores et comportement macroscopique*. PhD thesis.

[234] Zami-Pierre, F., de Loubens, R., Quintard, M., and Davit, Y. (2016). Transition in the flow of power-law fluids through isotropic porous media. *Physical Review Retters*, 117(7):074502.

[235] Zami-Pierre, F., de Loubens, R., Quintard, M., and Davit, Y. (2018). Effect of disorder in the pore-scale structure on the flow of shear-thinning fluids through porous media. *Journal of Non-Newtonian Fluid Mechanics*, 261:99–110.

[236] Zerner, M. (2011). Aux origines de la loi de Darcy (1856). *Documents pour l'histoire des techniques. Nouvelle série*, (20):29–40.

[237] Zhao, X., Liu, L., Wang, Y., Dai, H., Wang, D., and Cai, H. (2008). Influences of partially hydrolyzed polyacrylamide (HPAM) residue on the flocculation behavior of oily wastewater produced from polymer flooding. *Separation and Purification Technology*, 62(1):199–204.

[238] Zografos, K., Hartt, W., H., M., Oliveira, M. S. N., Alves, M. A., and Poole, R. J. (2020). Viscoelastic fluid flow simulations in the e-VROC geometry. *Journal of Non-Newtonian Fluid Mechanics*, 278:104222.

Chapter 2

Méthodes numériques

Nous présentons dans ce Chapitre un nouveau schéma de projection à grille décalée pour les écoulements viscoélastiques.

La résolution des systèmes d'équation modélisant les écoulements viscoélastiques est réputée difficile et est sujette à des problèmes numériques connus sous le nom de "High Weissenberg number problems" (HWNP) qui limitent généralement les calculs à $Wi \simeq \mathcal{O}(1)$ [37]. Longtemps restée mystérieuse [38], l'origine de ces difficultés numériques semble être liée à la présence des termes de production $\nabla \mathbf{u}\,\mathbf{c} + \mathbf{c}\,(\nabla \mathbf{u})^{\mathsf{T}}$ dans l'équation constitutive qui font intervenir un gradient de vitesse localement élevé et amenant à un profil de conformation difficile à capturer [34]. Ce n'est que récemment, avec l'introduction du logarithme de tenseur de conformation [24], que cette limite a pu être repoussée [19, 21, 45, 46, 50, 51]. L'idée, avec cette transformation, est de passer d'un profil exponentiel de la conformation à un profil linéaire, plus facile à approcher par des approximations polynomiales. Bien qu'issue d'un raisonnement empirique, cette méthode rejoint l'idée de méthodes de type "well-balanced" [28, 35, 11].

Parmi les nombreux schémas numériques proposés dans la littérature [2], on distingue en particulier ceux basés sur le principe de dissipation d'énergie libre [14] où la stabilité est assurée par la conservation, au niveau discret, d'une inégalité l'énergie vérifiée au niveau continu par le système d'équations [33]. Plusieurs schémas numériques basés sur ce critère ont ainsi été proposés [6, 14, 13, 44] mais font généralement intervenir des éléments finis d'ordres élevés et semblent difficile à implémenter dans le cadre de calculs haute performance.

Dans ce cadre, les méthodes de type volumes finis d'ordre faible semblent mieux adaptées. C'est ainsi qu'un code basé sur l'algorithme SIMPLE [52] et implémenté dans OpenFOAM® [17] a récemment été proposé [25] avec l'inconvénient d'utiliser des variables colocalisées ce qui nécessite l'ajout de termes de stabilisation [47].

Nous avons donc cherché à implémenter notre propre outil de calcul qui, basé sur une discrétisation d'ordre faible à grille décalée, soit cohérent avec l'estimation de l'énergie libre, maintienne la positivité du tenseur de conformation tout en montrant une bonne précision, soit bien adapté au calcul haute performance (HPC) et puisse être facilement utilisé pour différentes lois constitutives.

Article 1: A staggered projection scheme for viscoelastic flows

O. Mokhtari[1,3], Y. Davit[1], J.-C. Latché[2] and M. Quintard[1]

[1]Institut de Mécanique des Fluides de Toulouse (IMFT), CNRS & Université de Toulouse, France
[2]Institut de Radioprotection et de Sûreté Nucléaire (IRSN), Cadarache, France
[3]TotalEnergies E&P, CSTJF, Pau, France

Article soumis à ***Mathematical Modelling and Numerical Analysis***

Abstract

We develop a numerical scheme for the flow of viscoelastic fluids, including the Oldroyd-B and FENE-CR constitutive models. The space discretization is staggered, using either the Marker-And-Cell (MAC) scheme for structured nonuniform grids, or the Rannacher and Turek (RT) nonconforming low-order finite element approximation for general quandrangular or hexahedral meshes. The time discretization uses a fractional-step algorithm where the solution of the Navier-Stokes equations is first obtained by a projection method and then the transport-reaction equation for the conformation tensor is solved by a finite volume scheme. In order to obtain consistency, the space discretization of the divergence of the elastic part of the stress tensor in the momentum balance equation is derived using a weak form of the MAC scheme. For stability and accuracy purposes, the solution of the transport-reaction equation for the conformation tensor is split into pure convection steps, with a change of variable to the log-conformation tensor, and a reaction step, which consists in solving one ODE per cell via an Euler scheme with local sub-cycling. Numerical computations for the flow in the lid-driven cavity at Weissenberg numbers above one and the flow around a confined cylinder confirm the efficiency of the scheme.

Keywords: Viscoelastic flows, Finite volume, Staggered discretization, Projection scheme

2.1 Introduction

This paper is dedicated to presenting a new pressure-correction approach, based on a staggered arrangement of the unknowns, for viscoelastic incompressible flows of polymeric liquids. Such flows are usually modelled by solving for $(p, \boldsymbol{u}, \boldsymbol{c})$ in the following coupled system of equations

$$\rho(\partial_t \boldsymbol{u} + \xi \boldsymbol{u}\cdot\boldsymbol{\nabla}\boldsymbol{u}) = -\boldsymbol{\nabla} p + \operatorname{div}\boldsymbol{\tau}_s + \operatorname{div}\boldsymbol{\tau}_p, \qquad \text{in } (0,T)\times\Omega, \quad (2.1a)$$

$$\text{with} \quad \boldsymbol{\tau}_s = \eta_s(\boldsymbol{\nabla}\boldsymbol{u} + (\boldsymbol{\nabla}\boldsymbol{u})^t) \quad \text{and} \quad \boldsymbol{\tau}_p = \frac{\eta_p}{\lambda}\boldsymbol{f}(\boldsymbol{c})(\boldsymbol{c}-\boldsymbol{I}_d),$$

$$\operatorname{div}\boldsymbol{u} = 0, \qquad \text{in } (0,T)\times\Omega, \quad (2.1b)$$

$$\partial_t \boldsymbol{c} + \boldsymbol{u}\cdot\boldsymbol{\nabla}\boldsymbol{c} = (\boldsymbol{\nabla}\boldsymbol{u})\,\boldsymbol{c} + \boldsymbol{c}\,(\boldsymbol{\nabla}\boldsymbol{u})^t - \frac{1}{\lambda}\boldsymbol{g}(\boldsymbol{c})(\boldsymbol{c}-\boldsymbol{I}_d), \qquad \text{in } (0,T)\times\Omega, \quad (2.1c)$$

where Ω is an open bounded connected subset of $\mathbb{R}^d$ with $d \in \{2,3\}$, $(0,T)$ a finite time interval with $T>0$, $\boldsymbol{u}$ the velocity field of the fluid, p the pressure, and $\boldsymbol{c}$ the symmetric positive-definite polymer conformation tensor. The constant coefficients η_s, η_p, ρ, and λ are respectively the solvent viscosity, the polymer viscosity, the fluid density and the polymer retardation time. The coefficient ξ serves to artificially eliminate $\boldsymbol{u}\cdot\boldsymbol{\nabla}\boldsymbol{u}$, so as to obtain the unsteady Stokes equations for $\xi=0$ and the Navier-Stokes equations for $\xi=1$. The tensor $\boldsymbol{\tau}_s$ is the part of the stress accounting for the fluid solvent and $\boldsymbol{\tau}_p$ is the part of the stress accounting for the presence of polymers. The functions $\boldsymbol{f}(\boldsymbol{c})$ and $\boldsymbol{g}(\boldsymbol{c})$ vary depending on the viscoelastic constitutive equations (see [49] and [10] for a review) with, for example, the Oldroyd-B model given by $\boldsymbol{f}(\boldsymbol{c}) = \boldsymbol{g}(\boldsymbol{c}) = \boldsymbol{I}_d$ and the FENE-CR model by $\boldsymbol{f}(\boldsymbol{c}) = \boldsymbol{g}(\boldsymbol{c}) = \frac{b}{b-\operatorname{tr}(\boldsymbol{c})}\boldsymbol{I}_d$, with b a real number greater than the

space dimension d. The dimensionless parameters that characterize the flow are the Reynolds number, $Re = \rho UL/(\eta_s + \eta_p)$, and the Weissenberg number, $Wi = \lambda U/L$, where U and L are a characteristic velocity and lengthscale. This system must be complemented by initial conditions for the velocity and the conformation tensor and by suitable boundary conditions.

A variety of numerical schemes have been proposed for the resolution of this system (see [2] for a recent review). All of these schemes face the long-standing high-Weissenberg number problem (HWNP), which makes numerical simulations extremely difficult as soon as the Weissenberg number gets close to 1. In practice, steep gradients of the stress field rapidly develop, making it difficult to correctly capture the profile of the conformation tensor and to guarantee its positivity. One of the most significant advances in pushing back the limts of the HWNP was the *log-formulation* proposed in [23, 24] and used in many works [19, 21, 45, 46, 50, 51]. It consists in reformulating the problem using a logarithmic transformation of the conformation tensor. The idea described by the authors is that the conformation tensor varies exponentially and it is therefore easier to approach the logarithm of the conformation tensor with polynomial approximations than the tensor itself. Further, this formulation naturally maintains the positive-definiteness of the conformation tensor. It has later given birth to a variety of similar approaches, such as the square-root transformation [4] or the kernel conformation transformation [1]. Despite these advances, the HWNP is also often limited to moderate Weissenberg numbers because of computational costs and much progress is still needed.

One of the most important challenges of the HWNP can be understood by considering the one-dimensional transport of the scalar c posed, say, on $(0, L_1) \times (0, T)$,

$$\partial_t c + \partial_x c = a(x)c, \qquad c(x,0) = c_0(x),\ x \in (0,L_1) \text{ and } c(0,t) = c_i,\ t \in (0,T), \tag{2.2}$$

where $a(x)$ is here to mimick the velocity gradients. This problem is similar to that of [24] but with the difference that we consider here that $a(x)$ can become very large and sharply varies in space. When this is the case, obtaining accurate solutions of this toy problem and, by extension, of the HWNP becomes particularly difficult. This toy problem actually belongs to a class of hyperbolic conservation laws with stiff source terms [18, 41, 42] that are found, for example, in modelling shallow-water flows with non-flat bottoms [3, 22]. A classical method, such as a centered discretization of the source term, yields non-physical solutions [9]. The primary difficulty is to preserve the steady-state solutions in the discrete version of the operators. Schemes that verify this property are usually termed "well-balanced", as introduced in [28, 35, 11]. One of the simplest ways to do this is to incorporate the discrete equilibrium states into the fluxes, which is the principle of the upwinding sources at interfaces ("*U.S.I.*" *schemes)* [9, 11, 36, 12]. These methods are much more accurate than classical approaches but seem next to impossible to generalise to non-scalar 2D or 3D problems. Some viscoelastic flows that admit a steady-state solution (for instance, the so-called lid-driven cavity problem, at least at moderate Wi numbers) may be schematically understood by considering the steady transport problem $\partial_x c = a(x)c$ with a field $a(x)$ generating, by a change of sign, successively opposite variations of c. This may be understood as variations of the tensor $\boldsymbol{c}$ along closed streamlines. In Appendix D, we solve this steady-state problem with large values of $a(x)$ to mimic the HWNP. We show that a logarithmic transformation of the transport equation drastically improves the accuracy of the scheme, even though it does not preserve the steady-state and is therefore not well-balanced.

It has also been suggested in [40, 43] that a numerical scheme for viscoelastic flows should preserve, at the discrete level, a *free-energy* estimate derived at the continuum-level. For the system of equations (2.1), the time derivative of the Helmholtz *free-energy* is equal to the opposite of the dissipation terms plus energy sources from volume forcing terms or boundary conditions. For an initial-value problem with no sources, the Helmholtz *free-energy* must therefore decrease

in time (see [33] and [7, 8]) and its time derivative should be negative. An ideal numerical scheme should preserve this inequality at the discrete level and, in so doing, ensure the long-time stability of solutions. Following this idea, [5, 6, 14] developed numerical schemes that verify the *free-energy* estimate and proved the global-in-time existence of solutions to those discretisations, together with convergence to weak solutions of the continuous problem, under time-step restriction or with an additional dissipative term in the conformation equation. The authors also suggest in [13] (see also [44]) that this approach is not sufficient to guarantee accuracy.

Here, we aim for a numerical scheme that

1. satisfies a discrete equivalent of the the *free-energy* estimate,
2. minimizes CPU costs and is well suited to high-performance computations,
3. shows a good accuracy, in particular to capture steady-state solutions,
4. can be readily used for a variety of viscoelastic constitutive laws.

We present in Sections 2.2 and 2.3 an algorithm that satisfies point (1). We use a piecewise constant space approximation for the conformation tensor, which offers greats advantages from an algorithmic point of view. This discretization makes it possible to treat the right-hand side of the transport-reaction equation for the conformation tensor (2.1c) separately and yields a collection of decoupled cell-by-cell problems. Equation (2.1c) is then solved using a finite-volume scheme. To ensure the so-called *inf-sup* stability while keeping a consistent order of accuracy (and so, of CPU cost), we combine this discretization with a staggered-in-space approximation of the velocity/pressure pair, with either the Marker-And-Cell (MAC) scheme [31, 30], or a nonconforming low-order finite element, namely the Rannacher and Turek (RT) element [48] for quadrilateral or hexahedric cells (extension to simplicial cells with the Crouzeix-Raviart element [20] is straightforward). To keep the algorithm efficent and robust, we introduce a fractional-step algorithm where the solution of the Navier-Stokes equations (2.1a)-(2.1b) is computed by a standard projection method. Satisfying the discrete *free-energy* estimate has however a price: the transport equation for $\boldsymbol{c}$ must remain coupled with the correction step, with the end-of-step conformation tensor and velocity used in both this transport equation and the velocity correction equation. This yields a set of two coupled nonlinear equations for the pressure and $\boldsymbol{c}$, after using the usual trick that consists in combining the velocity correction and the divergence constraint into an elliptic problem for the pressure only. Finally, satisfying the *free-energy* estimate also requires a discrete weak formulation of (2.1a) and, in particular, of the diffusion term and of $\operatorname{div} \boldsymbol{\tau}_p$. This is in fact natural for finite element discretizations, but not so for the MAC scheme for which this discretization is thus derived in Section 2.3.3. We also observe and prove that this weak fromulation enjoys a built-in Lax-Wendroff weak consistency property [26].

Unfortunately, respecting Points (2) and (3) requires that we make a compromise regarding the time discretization, as detailed in Section 2.4. We proceed by decoupling the system of equations for the projection step, using an explicit-in-time approximation of the conformation tensor in the velocity correction equation, which greatly reduces the cost of each iteration but breaks the proof of consistency for the *free-energy* estimate. Consequently, Point (1) is not strictly satisfied anymore: the space semi-discretization of the momentum balance equation is consistent with the *free-energy* estimate, but not the time discretization. For accuracy, we further introduce a log transformation of the (now decoupled) transport equation for the conformation tensor. Unlike the standard approach of [24], however, this transformation is only partial. In the spirit of [46], we proceed by operator splitting in Equation (2.1c), with a change of variable from $\boldsymbol{c}$ to $\log(\boldsymbol{c})$ in pure convection steps and a separate reaction step without any transformation.

This latter step consists in solving one ODE per mesh cell thanks to the piecewise constant discretization of $\boldsymbol{c}$ and, in contrast with [46], these ODEs are solved directly for $\boldsymbol{c}$, and not $\log(\boldsymbol{c})$, so as to avoid any artificial introduction of nonlinearities, together with a cumbersome factorization of the velocity gradient tensor. The viscoelastic constitutive law is only involved in this cell-by-cell procedure, so that it can be easily modified to capture a variety of viscoelastic behaviors (Point (4)). To further gain in efficiency, we use a local time step for the solution of the ODE on each mesh element, thus ensuring stability and preventing a blow-up of the CPU cost. In practice, the velocity gradient is large only in a small number of cells where the ODE becomes stiff and subcycling is needed. This greatly limits the computational cost, although one must be careful in the domain decomposition for parallel computations to keep the computing charge of the processors equilibrated. Summing up, our approach is thus based upon a low-order numerical scheme that is very efficient and reasonably accurate, the most important cause of inaccuracy being tackled by the log transformation in the transport step and a time-step adaptation to cope with the stiffness of the reaction terms. The constitutive laws for the viscoelastic fluids only appear in the resolution of cell-by-cell ODEs and can be easily modified. The resulting solver is available and open-source, as a specific module of the CALIF^{3}S platform developed at the French Institut de Radioprotection et Sûreté Nucléaire (IRSN) [16].

In the last part of the paper, Section 2.5, we study the efficiency and accuracy of the scheme using two benchmark 2D tests, the lid-driven cavity (up to a Weissenberg of 5) and the cylinder confined in a channel. Using massively parallel computations, we obtain solutions for the cylinder problem that are, to our knowledge, more accurate than already published results. In addition, we take benefit of the versatility of our algorithm with respect to the viscoelastic constitutive law to perform a systematic comparison of the results obtained with the Oldroyd-B and the FENE-CR models. This also allows us to discuss the convergence of the FENE-CR model towards the Oldroyd-B model when the parameter b takes large values and the regularizing effects brought by the FENE-CR model.

2.2 Meshes and unknowns

Let $\mathcal{M}$ be a decomposition of the domain Ω, supposed to be regular in the usual sense of the finite element literature. The cells may be:

- convex quadrilaterals ($d=2$) or hexahedra ($d=3$) for a general domain Ω.
- rectangles ($d=2$) or rectangular parallelepipeds ($d=3$) for a domain Ω with boundaries that are hyperplanes normal to a coordinate axis.

$\mathcal{E}$ and $\mathcal{E}(K)$ are, respectively, the set of all $(d-1)$-faces σ of the mesh and of the element $K \in \mathcal{M}$. The set of faces included in the boundary of Ω is $\mathcal{E}_{\text{ext}}$ and the set of internal faces is $\mathcal{E}_{\text{int}} = \mathcal{E} \setminus \mathcal{E}_{\text{ext}}$. A face $\sigma \in \mathcal{E}_{\text{int}}$ separating cells K and L is denoted by $\sigma = K|L$. $\boldsymbol{n}_{K,\sigma}$ is the outward normal vector to a face σ of K . For $1 \leq i \leq d$, we denote by $\mathcal{E}^{(i)}$, $\mathcal{E}^{(i)}_{\text{int}}$ and $\mathcal{E}^{(i)}_{\text{ext}}$ the subset of the faces of $\mathcal{E}$, $\mathcal{E}_{\text{int}}$ and $\mathcal{E}_{\text{ext}}$, respectively, that are perpendicular to the i^{th} unit vector of the canonical basis of $\mathbb{R}^d$. For $K \in \mathcal{M}$ and $\sigma \in \mathcal{E}$, $|K|$ is the measure of K and $|\sigma|$ the $(d-1)$-measure of the face σ.

The space discretization is staggered, using either the Marker-And Cell (MAC) scheme [31, 30] or nonconforming low-order finite element approximations, namely the Rannacher and Turek (RT) element [48] for quadrilateral or hexahedral meshes. The degrees of freedom for the pressure and the conformation (i.e the discrete pressure and conformation unknowns),

$$\{p_K,\ \boldsymbol{c}_K,\ K \in \mathcal{M}\},$$

are associated with the cells of the mesh $\mathcal{M}$. For the velocity, we have the following cases.

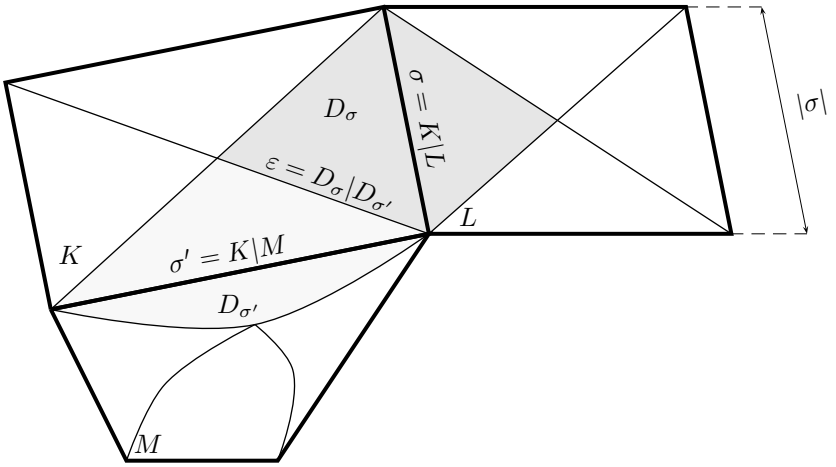

Fig. 2.1 Primal and dual meshes for the Rannacher-Turek elements.

- For the **Rannacher-Turek** discretization, the discrete velocity unknowns are located at the center of the faces of the mesh and we choose the version of the element where they represent the average of the velocity through a face. The Dirichlet boundary conditions are taken into account by setting the velocity unknowns associated with an external face to zero, so the set of discrete velocity unknowns reads

$$\{u_{\sigma,i},\ \sigma \in \mathcal{E}_{\rm int},\ 1 \le i \le d\}.$$

- For the **MAC** discretization, the degrees of freedom for the i^{th} component of the velocity are located at the centre of the faces $\sigma \in \mathcal{E}^{(i)}$, so the whole set of discrete velocity unknowns reads:

$$\{u_{\sigma,i},\ \sigma \in \mathcal{E}^{(i)}_{\rm int},\ 1 \le i \le d\}.$$

Hence, there are d unknowns per face of the primal mesh in the case of the RT scheme, corresponding to the d components of the velocity, and there is only one unknown per face of the primal mesh in the case of the MAC scheme, corresponding to the normal component of the velocity.

We now introduce a dual mesh for the finite volume approximation of the time derivative and convection terms in the momentum balance equation.

- For the **Rannacher-Turek** discretization, the dual mesh is the same for all the velocity components. When $K \in \mathcal{M}$ is a simplex, a rectangle or a cuboid, we define $D_{K,\sigma}$ for $\sigma \in \mathcal{E}(K)$ as the cone with basis σ and with vertex the mass center of K (see Figure 3.4). We thus obtain a partition of K in m sub-volumes, where m is the number of faces of the cell, each sub-volume having the same measure $|D_{K,\sigma}| = |K|/m$. We extend this definition to general quadrangles and hexahedra by supposing that we have built a partition still of equal-volume sub-cells and with the same connectivities. The volume $D_{K,\sigma}$ is referred to as the half-diamond cell associated with K and σ. For $\sigma \in \mathcal{E}_{\rm int}$, $\sigma = K|L$, we now define the diamond cell D_σ associated with σ by $D_\sigma = D_{K,\sigma} \cup D_{L,\sigma}$.

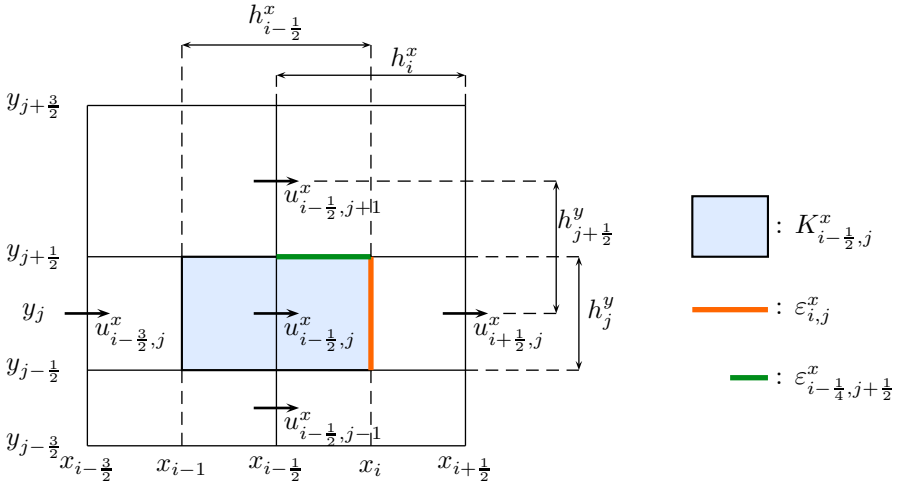

Fig. 2.2 Unknown and dual cell for the x-component of the velocity, notations for staggered discretizations.

- For the **MAC** discretization, the dual mesh depends on the component of the velocity. For each component, the MAC dual mesh only differs from the RT dual mesh by the choice of the half-diamond cell, which, for $K \in \mathcal{M}$ and $\sigma \in \mathcal{E}(K)$, is now the rectangle or rectangular parallelepiped of basis σ and of measure $|D_{K,\sigma}| = |K|/2$ (see Figure 2.2).

We denote by $|D_\sigma|$ the measure (area of volume) of the dual cell D_σ and by $\varepsilon = D_\sigma | D_{\sigma'}$ the face separating two diamond cells D_σ and $D_{\sigma'}$. The set of the (dual) faces of D_σ is denoted by $\overline{\mathcal{E}}(D_\sigma)$.

Finally, in order to be able to write a unique expression of the discrete equations for both MAC and RT scheme, we introduce the set of faces $\mathcal{E}^{(i)}_{\mathcal{S}}$ associated with the degrees of freedom of the i^{th} component of the velocity ($\mathcal{S}$ stands for "scheme"):

$$\mathcal{E}^{(i)}_{\mathcal{S}} = \left| \begin{array}{l} \mathcal{E}^{(i)}_{\rm int} \text{ for the MAC scheme,} \\ \mathcal{E}_{\rm int} \text{ for the RT scheme.} \end{array} \right.$$

2.3 A free-energy preserving pressure correction scheme

Let us first recall the formal derivation of the energy estimate given in [33] for a class of viscoelastic models including the Oldroyd-B model. The starting point is System (2.1) where we set $\boldsymbol{f}(\boldsymbol{c}) = \boldsymbol{g}(\boldsymbol{c}) = \boldsymbol{I}_d$ which is the definition of the Oldroyd-B model. For the sake of simplicity and without loss of generality, we assume here that $\xi = 1$. We consider that all the fields are given initially and that boundary conditions are all no-slip conditions. The idea is that there is no source of energy in the system, either through volume forces or boundary conditions, so that, physically, we expect a constant decrease of the *free-energy* due to dissipation processes. The first step to showing this consists in taking the inner product of the momentum balance Equation (2.1a) with $\boldsymbol{u}$,

$$\partial_t E_c + \boldsymbol{u} \cdot \boldsymbol{\nabla} E_c = \Big(-\boldsymbol{\nabla} p + \operatorname{div} \boldsymbol{\tau}_s(\boldsymbol{u}) + \operatorname{div}\big(\frac{\eta_p}{\lambda}\boldsymbol{c}\big)\Big) \cdot \boldsymbol{u}, \tag{2.3}$$

where E_c is the kinetic energy defined as

$$E_c = \frac{1}{2}\rho|\boldsymbol{u}|^2.$$

Let us also consider the trace of Equation (2.1c) multiplied by $\eta_p/(2\lambda)$. In doing so, we suppose that any tensor $\boldsymbol{c}$ solution of Equation (2.1c) is symmetric definite positive. We have the relationships $\mathrm{tr}(\boldsymbol{\nabla u}\,\boldsymbol{c}) = \boldsymbol{\nabla u} : \boldsymbol{c}$ and $\mathrm{tr}(\boldsymbol{c}(\boldsymbol{\nabla u})^t) = \boldsymbol{\nabla u} : \boldsymbol{c}$, thanks to the fact that $\mathrm{tr}(\boldsymbol{c}) = \mathrm{tr}(\boldsymbol{c}^t)$ and $\mathrm{tr}(\boldsymbol{c}\,\boldsymbol{d}) = \boldsymbol{c} : \boldsymbol{d}^t$ for any symmetric matrix $\boldsymbol{c}$ of $\mathbb{R}^{d\times d}$ and any matrix $\boldsymbol{d}$ of $\mathbb{R}^{d\times d}$. We obtain

$$\frac{\eta_p}{2\lambda}\left(\partial_t \mathrm{tr}(\boldsymbol{c}) + \boldsymbol{u}\cdot\boldsymbol{\nabla}\mathrm{tr}(\boldsymbol{c})\right) = \frac{\eta_p}{\lambda}\boldsymbol{c} : \boldsymbol{\nabla u} - \frac{\eta_p}{2\lambda^2}\mathrm{tr}(\boldsymbol{c} - \boldsymbol{I}_d). \tag{2.4}$$

Since $\boldsymbol{c}$ is supposed to be invertible, we may also multiply Equation (2.1c) by $\boldsymbol{c}^{-1}$ to get

$$\boldsymbol{c}^{-1}\partial_t\boldsymbol{c} + \boldsymbol{c}^{-1}\boldsymbol{u}\cdot\boldsymbol{\nabla c} = \boldsymbol{c}^{-1}(\boldsymbol{\nabla u})\,\boldsymbol{c} + (\boldsymbol{\nabla u})^t - \frac{1}{\lambda}(\boldsymbol{I}_d - \boldsymbol{c}^{-1}). \tag{2.5}$$

We are now going to consider the trace of this equation. For the first term on the left-hand side, we know (see [14, Lemma 1.2]) that $\mathrm{tr}(\boldsymbol{c}^{-1}\partial_t\boldsymbol{c}) = \partial_t\mathrm{tr}(\ln(\boldsymbol{c}))$. For the second term on the left-hand side, consider that

$$\boldsymbol{u}\cdot\boldsymbol{\nabla c} = \sum_{k=1}^{d} u_k\partial_k\boldsymbol{c},$$

with $\partial_k\boldsymbol{c}$ the tensor obtained by deriving each entry of $\boldsymbol{c}$ with respect to the k^{th} space coordinate. By the same identity as for the first term, we therefore have $\mathrm{tr}(\boldsymbol{c}^{-1}\boldsymbol{u}\cdot\boldsymbol{\nabla c}) = \boldsymbol{u}\cdot\boldsymbol{\nabla}\mathrm{tr}(\ln(\boldsymbol{c}))$. For the first term on the right-hand side, we remark that $\mathrm{tr}(\boldsymbol{c}^{-1}\,\boldsymbol{\nabla u}\,\boldsymbol{c}) = \mathrm{tr}(\boldsymbol{c}\,\boldsymbol{c}^{-1}\boldsymbol{\nabla u}) = \mathrm{tr}(\boldsymbol{\nabla u}) = \mathrm{div}(\boldsymbol{u}) = 0$ since $\mathrm{tr}(\boldsymbol{c}\,\boldsymbol{d}) = \mathrm{tr}(\boldsymbol{d}\,\boldsymbol{c})$ for any matrix $\boldsymbol{c}$ and $\boldsymbol{d}$ of $\mathbb{R}^{d\times d}$. For the second term on the right-hand side, we also have $\mathrm{tr}((\boldsymbol{\nabla u})^t) = 0$. Therefore, taking the trace of Equation (2.5) and multiplying by $\dfrac{\eta_p}{2\lambda}$, we get

$$\frac{\eta_p}{2\lambda}\left(\partial_t\mathrm{tr}(\ln(\boldsymbol{c})) + \boldsymbol{u}\cdot\boldsymbol{\nabla}\mathrm{tr}(\ln(\boldsymbol{c}))\right) = -\frac{\eta_p}{2\lambda^2}\,\mathrm{tr}(\boldsymbol{I}_d - \boldsymbol{c}^{-1}), \tag{2.6}$$

which can also be written as

$$\frac{\eta_p}{2\lambda}\left(\partial_t\mathrm{tr}(\ln(\boldsymbol{c}) + \boldsymbol{I}_d) + \boldsymbol{u}\cdot\boldsymbol{\nabla}\mathrm{tr}(\ln(\boldsymbol{c}) + \boldsymbol{I}_d)\right) = -\frac{\eta_p}{2\lambda^2}\,\mathrm{tr}(\boldsymbol{I}_d - \boldsymbol{c}^{-1}), \tag{2.7}$$

considering that

$$\frac{\eta_p}{2\lambda}\left(\partial_t\mathrm{tr}(\boldsymbol{I}_d) + \boldsymbol{u}\cdot\boldsymbol{\nabla}\mathrm{tr}(\boldsymbol{I}_d)\right) = 0. \tag{2.8}$$

We can now build a transport equation for the *free-energy* by adding Equation (2.3) to Equation (2.4) and subtracting Equation (2.7) to obtain

$$\partial_t E + \boldsymbol{u}\cdot\boldsymbol{\nabla}E = \left(-\boldsymbol{\nabla}p + \mathrm{div}\,\boldsymbol{\tau}_s(\boldsymbol{u}) + \mathrm{div}\left(\frac{\eta_p}{\lambda}\boldsymbol{c}\right)\right)\cdot\boldsymbol{u} + \frac{\eta_p}{\lambda}\boldsymbol{c} : \boldsymbol{\nabla u} - \frac{\eta_p}{2\lambda^2}\mathrm{tr}(\boldsymbol{c} + \boldsymbol{c}^{-1} - 2\boldsymbol{I}_d),$$

where E is the *free-energy* defined by

$$E = \frac{1}{2}\rho|\boldsymbol{u}|^2 + \frac{\eta_p}{\lambda}\mathrm{tr}(\boldsymbol{c} - \ln(\boldsymbol{c}) - \boldsymbol{I}_d).$$

Finally, integrating over Ω yields

$$\frac{d}{dt}\int_\Omega E\,\mathrm{d}\boldsymbol{x}+\int_\Omega \boldsymbol{\tau}_s(\boldsymbol{u}):\boldsymbol{\nabla}\boldsymbol{u}\,\mathrm{d}\boldsymbol{x}+\frac{\eta_p}{2\,\lambda^2}\int_\Omega \mathrm{tr}(\boldsymbol{c}+\boldsymbol{c}^{-1}-2\boldsymbol{I}_d)\,\mathrm{d}\boldsymbol{x}=0, \tag{2.9}$$

by integration by parts and using the no-slip boundary condition. For any symmetric positive definite tensor $\boldsymbol{c}$, both $\boldsymbol{c}-\ln(\boldsymbol{c})-\boldsymbol{I}_d$ and $\boldsymbol{c}+\boldsymbol{c}^{-1}-2\boldsymbol{I}_d$ are symmetric positive definite [14, Lemma 1.1]. Thus, $\mathrm{tr}(\boldsymbol{c}+\boldsymbol{c}^{-1}-2\boldsymbol{I}_d)>0$, $\mathrm{tr}(\boldsymbol{c}-\ln(\boldsymbol{c})-\boldsymbol{I}_d)>0$ and the previous relation shows that the *free-energy* E decreases with time, since the viscous dissipation $\boldsymbol{\tau}_s(\boldsymbol{u}):\boldsymbol{\nabla}\boldsymbol{u}$ is non-negative. Equation (2.9) thus provides a stability estimate for the solutions of (2.1).

2.3.1 Time semi-discrete scheme

Our aim is now to derive a time semi-discretization of System (2.1) satisfying a semi-discrete analogue of Equation (2.9). Let a uniform partition $0=t_0<t_1<\ldots<t_N=T$ of $(0,T)$ be given, with a constant time step δt. We consider the following semi-discretization in time of System (2.1), which belongs to the class of pressure correction schemes,

Prediction step – Solve for $\tilde{\boldsymbol{u}}^{n+1}$:

$$\frac{\rho}{\delta t}\,(\tilde{\boldsymbol{u}}^{n+1}-\boldsymbol{u}^n)+\xi\,\rho\,\boldsymbol{u}^n\cdot\boldsymbol{\nabla}\tilde{\boldsymbol{u}}^{n+1}-\eta_s\boldsymbol{\Delta}\tilde{\boldsymbol{u}}^{n+1}+\boldsymbol{\nabla}p^n-\frac{\eta_p}{\lambda}\,\mathrm{div}\,\boldsymbol{c}^n=0. \tag{2.10a}$$

Correction step – Solve for p^{n+1} and $\boldsymbol{u}^{n+1}$:

$$\frac{\rho}{\delta t}\,(\boldsymbol{u}^{n+1}-\tilde{\boldsymbol{u}}^{n+1})+\boldsymbol{\nabla}(p^{n+1}-p^n)-\frac{\eta_p}{\lambda}\mathrm{div}\,(\boldsymbol{c}^{n+1}-\boldsymbol{c}^n)=0, \tag{2.10b}$$

$$\mathrm{div}\,\boldsymbol{u}^{n+1}=0, \tag{2.10c}$$

$$\frac{1}{\delta t}\,\Big(\boldsymbol{c}^{n+1}-\boldsymbol{c}^n\Big)+\boldsymbol{u}^n\cdot\boldsymbol{\nabla}\boldsymbol{c}^{n+1}=\boldsymbol{\nabla}\boldsymbol{u}^{n+1}\,\boldsymbol{c}^{n+1}+\boldsymbol{c}^{n+1}\,(\boldsymbol{\nabla}\boldsymbol{u}^{n+1})^t-\frac{1}{\lambda}(\boldsymbol{c}^{n+1}-\boldsymbol{I}_d). \tag{2.10d}$$

This time semi-discretization satisfies the stability estimate, as stated in the following result.

Proposition 1. *Let $(\boldsymbol{u}^n,p^n,\boldsymbol{c}^n)_{0\le n\le N}$ be the solution of System (2.10). For $0\le n\le N$, let us suppose that $\boldsymbol{c}^n$ is positive definite and let the discrete free-energy of the solution be defined by*

$$E^n(\boldsymbol{u}^n,p^n,\boldsymbol{c}^n,\delta t)=\frac{\rho}{2}\,|\boldsymbol{u}^n|^2+\frac{\eta_p}{2\lambda}\,\mathrm{tr}(\boldsymbol{c}^n-\ln(\boldsymbol{c}^n)-\boldsymbol{I}_d)+\frac{\delta t^2}{2\rho}\,|\boldsymbol{\nabla}p^n-\frac{\eta_p}{\lambda}\mathrm{div}\,\boldsymbol{c}^n|^2. \tag{2.11}$$

Then, for $0\le n\le N-1$, we have the following stability estimate

$$\int_\Omega E^{n+1}\,\mathrm{d}\boldsymbol{x}+\frac{\rho}{2}\int_\Omega|\tilde{\boldsymbol{u}}-\boldsymbol{u}^n|^2\,\mathrm{d}\boldsymbol{x}+\delta t\int_\Omega\eta_s|\boldsymbol{\nabla}\tilde{\boldsymbol{u}}^{n+1}|^2\,\mathrm{d}\boldsymbol{x}$$
$$+\frac{\eta_p}{2\lambda^2}\int_\Omega\mathrm{tr}(\boldsymbol{c}^{n+1}-(\boldsymbol{c}^{n+1})^{-1}-2\,\boldsymbol{I}_d)\,\mathrm{d}\boldsymbol{x}\le\int_\Omega E^n\,\mathrm{d}\boldsymbol{x}. \tag{2.12}$$

Consequently, the integral over the domain of the discrete free-energy is non-increasing.

Proof. Using the identity $2\,a\,(a-b)=a^2+(a-b)^2-b^2$ valid for any pair of real numbers a and b, we have

$$\tilde{\boldsymbol{u}}^{n+1}\cdot\Big(\frac{\rho}{\delta t}\,(\tilde{\boldsymbol{u}}^{n+1}-\boldsymbol{u}^n)+\xi\,\rho\,\boldsymbol{u}^n\cdot\boldsymbol{\nabla}\tilde{\boldsymbol{u}}^{n+1}\Big)\ge\frac{\rho}{2\,\delta t}\,(|\tilde{\boldsymbol{u}}^{n+1}|^2-|\boldsymbol{u}^n|^2)+\frac{\rho}{2}\,\boldsymbol{u}^n\cdot\boldsymbol{\nabla}|\tilde{\boldsymbol{u}}^{n+1}|^2.$$

Hence, using the fact that $\boldsymbol{u}^n$ is divergence-free to recast the transport term as a convection term, thanks to the no-slip boundary condition,

$$\int_\Omega \tilde{\boldsymbol{u}}^{n+1} \cdot \Big(\frac{\rho}{\delta t} \, (\tilde{\boldsymbol{u}}^{n+1} - \boldsymbol{u}^n) + \xi \, \rho \, \boldsymbol{u}^n \cdot \boldsymbol{\nabla} \tilde{\boldsymbol{u}}^{n+1} \Big) \, \mathrm{d}\boldsymbol{x} \geq \int_\Omega \frac{\rho}{2 \, \delta t} \, \left(|\tilde{\boldsymbol{u}}^{n+1}|^2 - |\boldsymbol{u}^n|^2 \right) \mathrm{d}\boldsymbol{x}. \tag{2.13}$$

Thanks once again to the boundary conditions, we have

$$- \int_\Omega \tilde{\boldsymbol{u}}^{n+1} \cdot \eta_s \, \boldsymbol{\Delta} \tilde{\boldsymbol{u}}^{n+1} \, \mathrm{d}\boldsymbol{x} = \int_\Omega \eta_s \, |\boldsymbol{\nabla} \tilde{\boldsymbol{u}}^{n+1}|^2 \, \mathrm{d}\boldsymbol{x}. \tag{2.14}$$

Therefore, taking the inner product of Equation (2.10a) with $\tilde{\boldsymbol{u}}^{n+1}$ and integrating over the computational domain yields

$$\frac{\rho}{2 \, \delta t} \int_\Omega \left(|\tilde{\boldsymbol{u}}^{n+1}|^2 - |\boldsymbol{u}^n|^2 \right) \mathrm{d}\boldsymbol{x} + \int_\Omega \eta_s \, |\boldsymbol{\nabla} \tilde{\boldsymbol{u}}^{n+1}|^2 \, \mathrm{d}\boldsymbol{x} + \int_\Omega \tilde{\boldsymbol{u}}^{n+1} \cdot \Big(\boldsymbol{\nabla} p^n - \frac{\eta_p}{\lambda} \operatorname{div} \boldsymbol{c}^n \Big) \, \mathrm{d}\boldsymbol{x} \leq 0. \tag{2.15}$$

Let us now rewrite Equation (2.10b) as

$$\frac{\rho}{\delta t} \, \boldsymbol{u}^{n+1} + \boldsymbol{\nabla} p^{n+1} - \frac{\eta_p}{\lambda} \operatorname{div} \boldsymbol{c}^{n+1} = \frac{\rho}{\delta t} \, \tilde{\boldsymbol{u}}^{n+1} + \boldsymbol{\nabla} p^n - \frac{\eta_p}{\lambda} \operatorname{div} \boldsymbol{c}^n.$$

Taking the square of the L^2-norm of both sides and multiplying by $\delta t / (2 \, \rho)$ yields

$$\begin{aligned} &\frac{\rho}{2 \, \delta t} \int_\Omega |\boldsymbol{u}^{n+1}|^2 \, \mathrm{d}\boldsymbol{x} - \int_\Omega \frac{\eta_p}{\lambda} \, \boldsymbol{u}^{n+1} \cdot \operatorname{div} \boldsymbol{c}^{n+1} \, \mathrm{d}\boldsymbol{x} + \frac{\delta t}{2 \, \rho} \int_\Omega |\boldsymbol{\nabla} p^{n+1} - \frac{\eta_p}{\lambda} \operatorname{div} \boldsymbol{c}^{n+1}|^2 \, \mathrm{d}\boldsymbol{x} \\ &\quad = \frac{\rho}{2 \, \delta t} \int_\Omega |\tilde{\boldsymbol{u}}^{n+1}|^2 \, \mathrm{d}\boldsymbol{x} + \int_\Omega \tilde{\boldsymbol{u}}^{n+1} \cdot (\boldsymbol{\nabla} p^n - \frac{\eta_p}{\lambda} \operatorname{div} \boldsymbol{c}^n) \, \mathrm{d}\boldsymbol{x} + \frac{\delta t}{2 \, \rho} \int_\Omega |\boldsymbol{\nabla} p^n - \frac{\eta_p}{\lambda} \operatorname{div} \boldsymbol{c}^n|^2 \, \mathrm{d}\boldsymbol{x}. \end{aligned}$$

Note that, to obtain this relation, we have used the following velocity divergence-pressure gradient duality (which holds thanks to the no-slip boundary conditions)

$$\int_\Omega \boldsymbol{\nabla} p^{n+1} \cdot \boldsymbol{u}^{n+1} = - \int_\Omega p^{n+1} \, \operatorname{div}(\boldsymbol{u}^{n+1}) = 0. \tag{2.16}$$

Adding with (2.15), we obtain the following discrete kinetic energy inequality

$$\frac{\rho}{2 \, \delta t} \int_\Omega \left(|\boldsymbol{u}^{n+1}|^2 - |\boldsymbol{u}^n|^2 \right) \mathrm{d}\boldsymbol{x} + \int_\Omega \eta_s \, |\boldsymbol{\nabla} \tilde{\boldsymbol{u}}^{n+1}|^2 \, \mathrm{d}\boldsymbol{x} - \int_\Omega \frac{\eta_p}{\lambda} \, \boldsymbol{u}^{n+1} \cdot \operatorname{div} \boldsymbol{c}^{n+1} \, \mathrm{d}\boldsymbol{x} + T^{n+1} - T^n \leq 0, \tag{2.17}$$

with, for $k = n$ and $k = n+1$,

$$T^k = \frac{\delta t}{2 \, \rho} \int_\Omega |\boldsymbol{\nabla} p^k - \frac{\eta_p}{\lambda} \operatorname{div} \boldsymbol{c}^k|^2 \, \mathrm{d}\boldsymbol{x}.$$

Let us now multiply (2.10d) by $(\boldsymbol{c}^{n+1})^{-1}$ to obtain

$$\frac{1}{\delta t} \, (\boldsymbol{c}^{n+1})^{-1} \Big(\boldsymbol{c}^{n+1} - \boldsymbol{c}^n \Big) + (\boldsymbol{c}^{n+1})^{-1} \boldsymbol{u}^n \cdot \boldsymbol{\nabla} \boldsymbol{c}^{n+1} = (\boldsymbol{c}^{n+1})^{-1} \boldsymbol{\nabla} \boldsymbol{u}^{n+1} \, \boldsymbol{c}^{n+1} + (\boldsymbol{\nabla} \boldsymbol{u}^{n+1})^t - \frac{1}{\lambda} (\boldsymbol{I}_d - (\boldsymbol{c}^{n+1})^{-1}). \tag{2.18}$$

For any symmetric definite positive matrices $\boldsymbol{c}$ and $\boldsymbol{d}$, we have $\operatorname{tr}(\boldsymbol{c}^{-1} \, (\boldsymbol{c} - \boldsymbol{d})) \leq \operatorname{tr} \ln(\boldsymbol{c}) - \operatorname{tr} \ln(\boldsymbol{d})$ (see [14, Lemma 2.1]), which yields

$$\frac{1}{\delta t} \left(\operatorname{tr} \ln(\boldsymbol{c}^{n+1}) - \operatorname{tr} \ln(\boldsymbol{c}^n) \right) + \boldsymbol{u}^n \cdot \boldsymbol{\nabla} \operatorname{tr} \ln(\boldsymbol{c}^{n+1}) \geq \operatorname{tr} \Big(\frac{1}{\delta t} \, (\boldsymbol{c}^{n+1})^{-1} \Big(\boldsymbol{c}^{n+1} - \boldsymbol{c}^n \Big) + (\boldsymbol{c}^{n+1})^{-1} \boldsymbol{u}^n \cdot \boldsymbol{\nabla} \boldsymbol{c}^{n+1} \Big). \tag{2.19}$$

Taking the trace of Relation (2.18) and integrating over Ω, by arguments already used in the continuous setting, we thus get

$$\int_\Omega \operatorname{tr}\ln(\boldsymbol{c}^{n+1}) - \operatorname{tr}\ln(\boldsymbol{c}^n)\,\mathrm{d}\boldsymbol{x} \geq -\int_\Omega \frac{1}{\lambda}\,\operatorname{tr}(\boldsymbol{I}_d - (\boldsymbol{c}^{n+1})^{-1})\,\mathrm{d}\boldsymbol{x}.$$

Taking the trace of Equation (2.10d), adding the discrete kinetic energy balance (2.17) and subtracting this relation as in the continuous setting yields the desired estimate, thanks to the duality relation

$$\int_\Omega \operatorname{tr}(\boldsymbol{\nabla}\boldsymbol{u}^{n+1}\boldsymbol{c}^{n+1})\,\mathrm{d}\boldsymbol{x} = \int_\Omega \boldsymbol{\nabla}\boldsymbol{u}^{n+1} : \boldsymbol{c}^{n+1}\,\mathrm{d}\boldsymbol{x} = -\int_\Omega \boldsymbol{u}^{n+1}\cdot\operatorname{div}\boldsymbol{c}^{n+1}\,\mathrm{d}\boldsymbol{x}. \tag{2.20}$$

□

2.3.2 Towards a fully discrete scheme

A discretization of the scheme (2.10) is obtained by combining a finite volume and a finite element approach for the approximation of the momentum balance equation and using a finite volume technique for the transport of the conformation tensor. The general form of the scheme reads

Prediction step – Solve for $\tilde{\boldsymbol{u}}^{n+1}$:

For $1 \leq i \leq d$, $\forall \sigma \in \mathcal{E}_{\mathrm{S}}^{(i)}$,

$$\frac{\rho}{\delta t}\left(\tilde{u}_{\sigma,i}^{n+1} - u_{\sigma,i}^n\right) + \xi\,\rho\,\mathrm{div}_\sigma(\tilde{u}_i^{n+1}\boldsymbol{u}^n) - \mathrm{div}_{\sigma,i}\,\boldsymbol{\tau}_s(\tilde{\boldsymbol{u}}^{n+1}) + \boldsymbol{\nabla}_{\sigma,i}\,p^n - \mathrm{div}_{\sigma,i}\,\boldsymbol{\tau}_p^n = 0. \tag{2.21a}$$

Correction step – Solve for p^{n+1}, $\boldsymbol{u}^{n+1}$ and $\boldsymbol{c}^{n+1}$:

For $1 \leq i \leq d$, $\forall \sigma \in \mathcal{E}_{\mathrm{S}}^{(i)}$,

$$\frac{\rho}{\delta t}\,(u_{\sigma,i}^{n+1} - \tilde{u}_{\sigma,i}^{n+1}) + \boldsymbol{\nabla}_{\sigma,i}(p^{n+1} - p^n) - \mathrm{div}_{\sigma,i}\,\boldsymbol{\tau}_p^{n+1} + \mathrm{div}_{\sigma,i}\,\boldsymbol{\tau}_p^n = 0, \tag{2.21b}$$

$$\forall K \in \mathcal{M}, \quad \mathrm{div}_K(\boldsymbol{u}^{n+1}) = 0, \tag{2.21c}$$

$\forall K \in \mathcal{M}$,

$$\frac{1}{\delta t}\,(\boldsymbol{c}_K^{n+1} - \boldsymbol{c}_K^n) + \mathrm{div}_K(\boldsymbol{u}^n\,\boldsymbol{c}^{n+1}) = \boldsymbol{\nabla}_K\boldsymbol{u}^{n+1}\,\boldsymbol{c}_K^{n+1} + (\boldsymbol{c}_K^{n+1})^t\,(\boldsymbol{\nabla}_K\boldsymbol{u}^{n+1})^t - \frac{1}{\lambda}(\boldsymbol{c}_K^{n+1} - \boldsymbol{I}_d). \tag{2.21d}$$

In the prediction step and in the velocity correction step, for $k = n$ and $k = n+1$, the tensor $\boldsymbol{\tau}_p^k$ is discretized on the primal cells and is computed as a function of the conformation tensor as

$$(\boldsymbol{\tau}_p^k)_K = \frac{\eta_p}{\lambda}\,(\boldsymbol{c}_K^k - \boldsymbol{I}_d), \quad \text{for } K \in \mathcal{M}.$$

The divergence operator applied to this tensor is defined in Section 2.3.3.

To build a fully discrete scheme that satisfies the same stability estimate as its time-discrete counterpart, we need to consider all the properties that have been used in the proof of Proposition 1 and satisfy them at the discrete level by a suitable definition of the operators in the scheme. First, we require that the transport equation for the tensor $\boldsymbol{c}$ preserves its symmetry and its positive-definiteness. The former property is easy to satisfy by solving a "symmetrized version" of

the right-hand side (i.e a discretization of $\boldsymbol{\nabla u}\,\boldsymbol{c}+\boldsymbol{c}^t\,(\boldsymbol{\nabla u})^t$ instead of $\boldsymbol{\nabla u}\,\boldsymbol{c}+\boldsymbol{c}(\boldsymbol{\nabla u})^t$), as is done in Equation (2.21d). Once the equation is symmetrized, if $\boldsymbol{c}^n$ is symmetric, for $1\leq i,j\leq d$, the discrete equation for $\boldsymbol{c}_{i,j}^{n+1}$ is strictly the same as the equation for $\boldsymbol{c}_{j,i}^{n+1}$. Conversely, a symmetric tensor solution to (2.21d) is also a solution of the original equation and thus switching to (2.21d) preserves the consistency of the scheme. Moreover, it is proved in Appendix A that a first-order backward upwind scheme for (2.21d) preserves the positive definiteness of $\boldsymbol{c}$, under a condition for the time-step depending on the L^∞-norm of $\boldsymbol{\nabla u}^{n+1}$. Finally, for this equation and this convection scheme, we need a discrete analogue of (2.19) which is proved in Appendix C.

Let us now turn to the momentum balance equation. A finite-volume discretization of the convection term for the RT discretization may be found, in the more general context of variable density flows, in [39, Section 4.2]. The discrete kinetic energy balance (i.e the discrete equivalent of (2.13)) is established in [39, Lemma 7.2]. For the MAC scheme, a discretization of the convection term is proposed in [26, Section 2, Equation (29)] and its L^2-stability (i.e, as before, the discrete equivalent of (2.13)) is shown in [26, Lemma 3.6]. The convection operator takes the following general form

$$\text{For } 1\leq i\leq d,\ \forall\sigma\in\mathcal{E}_{\rm S}^{(i)},\quad \rho\,\mathrm{div}_\sigma(\tilde{u}_i^{n+1}\boldsymbol{u}^n)=\frac{1}{|D_\sigma|}\sum_{\varepsilon\in\bar{\mathcal{E}}(D_\sigma)}F_{\sigma,\varepsilon}\ (\tilde{u}_i^{n+1})_\varepsilon,$$

where $F_{\sigma,\varepsilon}$ is an approximation of the mass flux through ε computed from the fluxes through the primal faces (i.e, for $K\in\mathcal{M}$ and $\sigma\in\mathcal{E}(K)$, the quantities $F_{K,\sigma}=\rho\ |\sigma|\ u_{K,\sigma}$ with $u_{K,\sigma}$ given by (2.25a) and (2.30) for the RT and MAC schemes respectively) in such a way that a divergence-free constraint is also satisfied on the dual cells D_σ (i.e $\sum_{\varepsilon\in\bar{\mathcal{E}}(D_\sigma)}F_{\sigma,\varepsilon}=0$). The approximation of the i^{th} component of the velocity at the dual face, $(\tilde{u}_i^{n+1})_\varepsilon$, may be chosen centered.

Finally, we need to ensure the duality of the velocity divergence and pressure gradient, together with the duality relations (2.14), (2.16) and (2.20). All these properties are obtained "by construction" when the associated terms in the momentum balance equation are derived from a variational formulation of this latter equation, as is done with the RT discretization (see Section 2.3.3 below). For the MAC scheme, the pressure gradient-velocity divergence duality is standard. The definition of these operators may be found, for instance, in [26, Section 2] and a proof of their duality is given by [26, Lemma 2.4]. For the viscous diffusion term, we propose in [27] a construction that ensures the positivity of the dissipation, i.e a discrete analogue of Relation (2.14). It consists in obtaining the usual finite-volume discretization of this term by a variational technique, thanks to a discrete H^1-inner product defined for "finite-volume test functions". For the sake of completeness, we recall these developments in Section 2.3.3 below, and give the definition of the velocity divergence, velocity diffusion, and pressure gradient operators. Then, in the same section, we extend this technique to cope with the term $\mathrm{div}_{\sigma,i}\boldsymbol{\tau}_p$, which also yields a definition of the velocity gradient used at the right-hand side of the transport Equation (2.21d) of the conformation tensor.

2.3.3 The discrete total stress divergence term

The aim of this section is to define the divergence term $\mathrm{div}_{\sigma,i}(\boldsymbol{T})$ of the total stress tensor $\boldsymbol{T}=-p\boldsymbol{I}_d+\boldsymbol{\tau}_s+\boldsymbol{\tau}_p$. We want this quantity to satisfy a duality relation of the form

$$-\sum_{i=1}^{d}\sum_{\sigma\in\mathcal{E}_{\rm S}^{(i)}}|D_\sigma|\ \mathrm{div}_{\sigma,i}\boldsymbol{T}\ u_{\sigma,i}=\sum_{K\in\mathcal{M}}|K|\ (\boldsymbol{T}:\boldsymbol{\nabla u})_K\,,\tag{2.22}$$

which is the discrete analogue of the identity

$$-\int_\Omega \mathrm{div}\,\boldsymbol{T}\cdot\boldsymbol{u}\,\mathrm{d}\boldsymbol{x}=\int_\Omega \boldsymbol{T}:\boldsymbol{\nabla}\boldsymbol{u}\,\mathrm{d}\boldsymbol{x}, \tag{2.23}$$

or, in other words, of the duality relations (2.14), (2.16) and (2.20) that, as shown in the previous sections, are crucial for the preservation of the *free-energy* estimate by the scheme. The discretization of this divergence term is different for the RT discretization and for the MAC scheme, and we deal with these two cases separately in the two following sub-sections.

Unstructured discretization For the RT discretization, we use the usual finite element discretization of the stress tensor divergence term

$$-\,\mathrm{div}_{\sigma,i}\boldsymbol{T}=\frac{1}{|D_\sigma|}\sum_{K\in\mathcal{M}}\int_K \boldsymbol{T}:\boldsymbol{\nabla}\boldsymbol{\varphi}_\sigma^{(i)}\,\mathrm{d}\boldsymbol{x}, \tag{2.24}$$

where $\boldsymbol{\varphi}_\sigma^{(i)}$ stands for the vector-valued finite element shape function associated with the i^{th} component of the velocity and the face σ. By definition of the RT finite elements, this shape function is $\varphi_\sigma\boldsymbol{e}^{(i)}$, where φ_σ is the real-valued function of the approximation space whose mean value is 1 over σ and 0 over the other faces of the mesh. We recall that, for the so-called parametric variant of the RT element, the discrete functional space is obtained through the usual Q_1-mapping from the space spanned by the set of functions $\{1,\ x_1,\ x_2,\ x_1^2-x_2^2\}$ on the reference $(0,1)^2$ square ($d=2$) and $\{1,\ x_1,\ x_2,\ x_3,\ x_1^2-x_2^2,\ x_2^2-x_3^2\}$ on the reference $(0,1)^3$ cube ($d=3$).

By a simple reordering of the sums, (2.22) reads

$$\begin{aligned}-\sum_{i=1}^d\sum_{\sigma\in\mathcal{E}_{\rm int}}|D_\sigma|\ \mathrm{div}_{\sigma,i}\boldsymbol{T}\ u_{\sigma,i}&=\sum_{i=1}^d\sum_{\sigma\in\mathcal{E}_{\rm int}}u_{\sigma,i}\sum_{K\in\mathcal{M}}\int_K\boldsymbol{T}:\boldsymbol{\nabla}\boldsymbol{\varphi}_\sigma^{(i)}\,\mathrm{d}\boldsymbol{x}\\&=\sum_{K\in\mathcal{M}}\int_K\boldsymbol{T}:\boldsymbol{\nabla}\Big(\sum_{i=1}^d\sum_{\sigma\in\mathcal{E}_{\rm int}}u_{\sigma,i}\boldsymbol{\varphi}_\sigma^{(i)}\Big)\,\mathrm{d}\boldsymbol{x}=\sum_{K\in\mathcal{M}}\int_K\boldsymbol{T}:\boldsymbol{\nabla}\boldsymbol{u}\,\mathrm{d}\boldsymbol{x}=\sum_{K\in\mathcal{M}}|K|\ (\boldsymbol{T}:\boldsymbol{\nabla}\boldsymbol{u})_K\,.\end{aligned}$$

Considering separately the pressure gradient, the diffusion and the elastic extra-stress terms in $\boldsymbol{T}$, we obtain the following expression for the discrete operators featured in the scheme (2.21), dropping the time index for short

$$\forall K\in\mathcal{M},\qquad \mathrm{div}_K\boldsymbol{u}=\frac{1}{|K|}\int_K\mathrm{div}(\boldsymbol{u})\,\mathrm{d}\boldsymbol{x}=\frac{1}{|K|}\sum_{\sigma\in\mathcal{E}(K)}|\sigma|\ u_{K,\sigma},\quad \text{with } u_{K,\sigma}=\boldsymbol{u}_\sigma\cdot\boldsymbol{n}_{K,\sigma}, \tag{2.25a}$$

$$\forall\sigma\in\mathcal{E}_{\rm int},\ \sigma=K|L,\qquad \boldsymbol{\nabla}_\sigma p=\frac{1}{|D_\sigma|}\sum_{i=1}^d\sum_{M\in\mathcal{M}}p_M\int_M\boldsymbol{\nabla}\boldsymbol{\varphi}_\sigma^{(i)}\,\mathrm{d}\boldsymbol{x}=\frac{|\sigma|}{|D_\sigma|}(p_L-p_K)\boldsymbol{n}_{K,\sigma}, \tag{2.25b}$$

$$\text{For } 1\le i\le d,\ \forall\sigma\in\mathcal{E}_{\rm S}^{(i)},\qquad \mathrm{div}_{\sigma,i}\boldsymbol{\tau}_s(\tilde{\boldsymbol{u}})=\frac{1}{|D_\sigma|}\int_\Omega\boldsymbol{\tau}_s(\tilde{\boldsymbol{u}}):\boldsymbol{\nabla}\boldsymbol{\varphi}_\sigma^{(i)}\,\mathrm{d}\boldsymbol{x}, \tag{2.25c}$$

$$\text{For } 1\le i\le d,\ \forall\sigma\in\mathcal{E}_{\rm S}^{(i)},\qquad \mathrm{div}_{\sigma,i}\boldsymbol{\tau}_p=\frac{1}{|D_\sigma|}\sum_{K\in\mathcal{M}}(\boldsymbol{\tau}_p)_K:\int_K\boldsymbol{\nabla}\boldsymbol{\varphi}_\sigma^{(i)}\,\mathrm{d}\boldsymbol{x}, \tag{2.25d}$$

$$\forall K\in\mathcal{M},\qquad \boldsymbol{\nabla}_K\boldsymbol{u}=\frac{1}{|K|}\int_K\boldsymbol{\nabla}\boldsymbol{u}\,\mathrm{d}\boldsymbol{x}. \tag{2.25e}$$

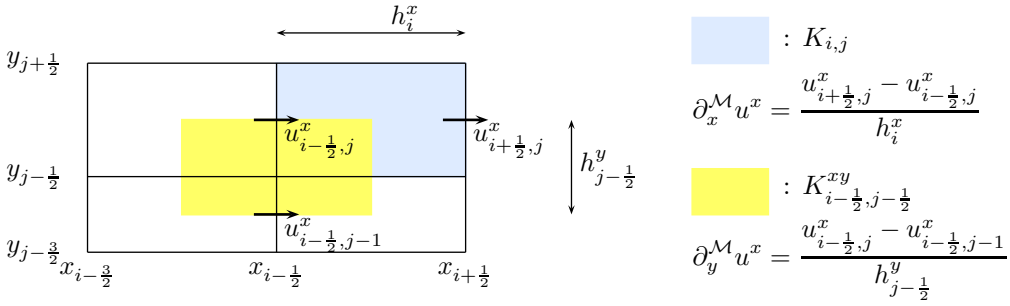

Fig. 2.3 Discrete partial derivatives of the x-component of the velocity.

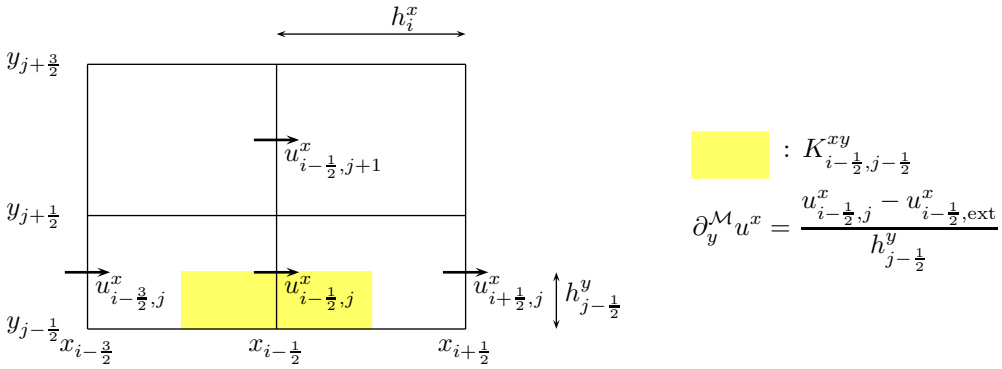

Fig. 2.4 Boundary conditions, x-component of the velocity.

MAC scheme For the MAC scheme, the strategy implemented here is to mimick the RT case, i.e to recast the momentum balance equation under a weak form. We define a discrete gradient operator acting on the velocity discrete functions (i.e piecewise-constant functions over the dual cells). Each component of this discrete gradient is itself a piecewise-constant function, based on a new partition of the computational domain. In two-dimensions, the discrete analogues of $\partial_x u_x$ and $\partial_y u_y$ are defined over the primal cells, while the other components of the velocity gradients are defined over volumes associated with the mesh vertices. With this gradient operator defined, the machinery of standard Galerkin techniques applies for the discretization of the momentum balance. The discrete velocity function space is shown to be spanned by a set of shape functions, and each discrete equation is derived by using these shape functions as test functions. Thanks to this construction, the scheme discrete operators natively satisfy the duality Relation (2.22) (they are indeed obtained from this relation itself), and have formally the same expression than in the finite element case, i.e obey formula similar to System (2.25) above.

This approach was followed in [27] for Newtonian fluids. We briefly recall here these results and use the same technique to cope with the divergence of the elastic extra-stress tensor. For

short, we only address here the two-dimensional case and we refer to [27] for the (natural) extension to the three-dimensional case.

The discrete velocity gradient – The developments of this section rely on the geometric properties of structured meshes and we need to momentarily switch to the notations that are specific to this context. We thus suppose that the primal mesh reads $\mathcal{M} = \{K_{i,j},\ (i,j) \in \mathcal{I}\}$, with $\mathcal{I} \subset \mathbb{N}^2$ with notations for geometrical quantities that are given in Figure 2.3. We detail here the discretization of the terms associated with the first component of the velocity, the adaptation to the second component being straightforward. In the interior of the computational domain, the discrete partial derivatives of this velocity component are defined as follows.

– For $(i,j) \in \mathcal{I}$, let the primal cells be $K_{i,j} = (x_{i-\frac{1}{2}}, x_{i+\frac{1}{2}}) \times (y_{j-\frac{1}{2}}, y_{j+\frac{1}{2}})$. The discrete derivative involved in the divergence (so, for the velocity x-component, only $\partial_x^{\mathcal{M}} u^x$) is defined over the primal cell by, $\forall (i,j) \in \mathcal{I}$ and $\forall \boldsymbol{x} \in K_{i,j}$,

$$\partial_x^{\mathcal{M}} u^x(\boldsymbol{x}) = \frac{u^x_{i+\frac{1}{2},j} - u^x_{i-\frac{1}{2},j}}{h^x_i}. \tag{2.26}$$

– For the other derivatives (so, for the velocity x-component, only $\partial_y^{\mathcal{M}} u^x$), we introduce a fourth mesh which is vertex-centred, and we denote by K^{xy} the generic cell of this new mesh, with $K^{xy}_{i-\frac{1}{2},j-\frac{1}{2}} = (x_{i-1}, x_i) \times (y_{j-1}, y_j)$. We define $\mathcal{I}^{xy}$ the set of pairs (i,j) such that $\boldsymbol{x}_{i-\frac{1}{2},j-\frac{1}{2}}$ is an internal vertex of the mesh (i.e a vertex which does not lie on the boundary). Then, for $(i,j) \in \mathcal{I}^{xy}$ and $\forall \boldsymbol{x} \in K^{xy}_{i-\frac{1}{2},j-\frac{1}{2}}$:

$$\partial_y^{\mathcal{M}} u^x(\boldsymbol{x}) = \frac{u^x_{i-\frac{1}{2},j} - u^x_{i-\frac{1}{2},j-1}}{h^y_{j-\frac{1}{2}}}. \tag{2.27}$$

The only necessary extension of this definition to cope with boundaries concerns the definition of $\partial_y^{\mathcal{M}} u^x$ over a half vertex-centered cell associated with a vertex lying on a horizontal boundary (see Figure 2.4). In this case, we use the usual "fictitious cell trick" in order to apply Relation (2.27): an external cell, of zero y-dimension, is added to the mesh and the horizontal velocity in this cell is set to the prescribed Dirichlet value, or to zero for the test functions defined below. Extending these definitions to the y-component of the velocity, the discrete diffusion tensor can be defined as

$$\boldsymbol{\nabla}^{\mathcal{M}} \boldsymbol{u} = \begin{bmatrix} \partial_x^{\mathcal{M}} u^x & \partial_y^{\mathcal{M}} u^x \\ \partial_x^{\mathcal{M}} u^y & \partial_y^{\mathcal{M}} u^y \end{bmatrix}, \quad \boldsymbol{\tau}_s^{\mathcal{M}}(\boldsymbol{u}) = \eta_s \left(\boldsymbol{\nabla}^{\mathcal{M}} \boldsymbol{u} + (\boldsymbol{\nabla}^{\mathcal{M}} \boldsymbol{u})^t \right). \tag{2.28}$$

Finite-volume test functions – Let us denote by $\mathcal{I}^x \subset \mathbb{N}^2$ (resp. $\mathcal{I}^y \subset \mathbb{N}^2$) the set of pairs (i,j) such that $\boldsymbol{x}_{i-\frac{1}{2},j}$ (resp. $\boldsymbol{x}_{i,j-\frac{1}{2}}$) is the mass center of a vertical (resp. horizontal) internal face of the mesh. For $(i,j) \in \mathcal{I}^x$, we denote by $\boldsymbol{\phi}^{x,(i-\frac{1}{2},j)}$ the test function associated with the degree of freedom of the x-component of the velocity located at $\boldsymbol{x}_{i-\frac{1}{2},j}$. This discrete function is defined as

$$(\boldsymbol{\phi}^{x,(i-\frac{1}{2},j)})^x_{k-\frac{1}{2},\ell} = \delta^i_k\ \delta^j_\ell,\ \forall (k,\ell) \in \mathcal{I}^x \text{ and } (\boldsymbol{\phi}^{x,(i-\frac{1}{2},j)})^y_{k,\ell-\frac{1}{2}} = 0,\ \forall (k,\ell) \in \mathcal{I}^y.$$

Its non-zero partial derivatives are $\partial_x^{\mathcal{M}}\boldsymbol{\phi}^{x,(i-\frac{1}{2},j)}$ and $\partial_y^{\mathcal{M}}\boldsymbol{\phi}^{x,(i-\frac{1}{2},j)}$ with

$$\partial_x^{\mathcal{M}}\boldsymbol{\phi}^{x,(i-\frac{1}{2},j)} = \left| \begin{array}{l} \dfrac{1}{h_{i-1}^x} \text{ over } K_{i-1,j}, \\ \dfrac{-1}{h_i^x} \text{ over } K_{i,j}, \\ 0 \text{ elsewhere,} \end{array} \right. \qquad \partial_y^{\mathcal{M}}\boldsymbol{\phi}^{x,(i-\frac{1}{2},j)} = \left| \begin{array}{l} \dfrac{1}{h_{j-\frac{1}{2}}^y} \text{ over } K^{xy}_{i-\frac{1}{2},j-\frac{1}{2}}, \\ \dfrac{-1}{h_{j+\frac{1}{2}}^y} \text{ over } K^{xy}_{i-\frac{1}{2},j+\frac{1}{2}}, \\ 0 \text{ elsewhere.} \end{array} \right.$$

Since the velocity is prescribed on the boundary, no equation is written on the half-dual cells associated with external faces, so no definition is required for the corresponding test functions.

Discrete pressure gradient, velocity divergence and viscous diffusion – Let us begin with the pressure gradient. Identifying p with its associated piecewise constant function, we have

$$\forall (i,j) \in \mathcal{I}^x, \quad (\boldsymbol{\nabla} p)^x_{i-\frac{1}{2},j} = \frac{-1}{|K^x_{i-\frac{1}{2},j}|} \int_\Omega p \; \partial_x^{\mathcal{M}}\boldsymbol{\phi}^{x,(i-\frac{1}{2},j)} \, \mathrm{d}\boldsymbol{x}. \tag{2.29}$$

Using the expression of the discrete derivatives of the test functions, we get

$$(\boldsymbol{\nabla} p)^x_{i-\frac{1}{2},j} = \frac{-1}{|K^x_{i-\frac{1}{2},j}|} \Big((h^x_{i-1} \; h^y_j) \; p_{i-1,j} \; \frac{1}{h^x_{i-1}} + (h^x_i \; h^y_j) \; p_{i,j} \; \frac{-1}{h^x_i} \Big) = \frac{p_{i,j} - p_{i-1,j}}{h^x_{i-\frac{1}{2}}},$$

and we recover the usual differential quotient for the pressure gradient of the MAC scheme. Note that, returning to the general notations used in this paper, this expression may also be recast as

$$\text{for } 1 \le i \le d, \; \forall \sigma \in \mathcal{E}_{\mathrm{S}}^{(i)}, \; \sigma = K|L, \quad \boldsymbol{\nabla}_{\sigma,i} \, p = \frac{|\sigma|}{|D_\sigma|} \; (p_L - p_K) \; (\boldsymbol{n}_{K,\sigma})_i,$$

which is a definition similar to the RT discretization, Equation (2.25b). The velocity divergence operator immediately follows from the definition of the velocity discrete partial derivatives

$$\forall K \in \mathcal{M}, \quad \mathrm{div}_K(\boldsymbol{u}) = \frac{1}{|K|} \int_K \mathrm{div}(\boldsymbol{u}) \, \mathrm{d}\boldsymbol{x},$$

so, since the partial derivatives of the velocity involved in the divergence are constant over each primal cell,

$$\forall (i,j) \in \mathcal{I}, \quad \mathrm{div}_{K_{i,j}}(\boldsymbol{u}) = \frac{u^x_{i+\frac{1}{2},j} - u^x_{i-\frac{1}{2},j}}{h^x_i} + \frac{u^y_{i,j+\frac{1}{2}} - u^y_{i,j-\frac{1}{2}}}{h^y_j},$$

which is, once again, the standard definition for the MAC scheme. Note that, to get similar expressions for the RT and MAC discretizations, we may also recast this equation as

$$\forall K \in \mathcal{M}, \quad \mathrm{div}_K(\boldsymbol{u}) = \frac{1}{|K|} \sum_{\sigma \in \mathcal{E}(K)} |\sigma| \; u_{K,\sigma}, \quad \text{with, for } \sigma \in \mathcal{E}^{(i)}, \; u_{K,\sigma} = u_\sigma \, \boldsymbol{n}_{K,\sigma} \cdot \boldsymbol{e}^{(i)}. \tag{2.30}$$

Finally, the discrete divergence of the viscous stress tensor is defined by the following weak formulation

$$\forall (i,j) \in \mathcal{I}^x, \quad -(\mathrm{div}\boldsymbol{\tau}_s(\tilde{\boldsymbol{u}}))^x_{i-\frac{1}{2},j} = \frac{1}{|K^x_{i-\frac{1}{2},j}|} \int_\Omega \boldsymbol{\tau}_s^{\mathcal{M}}(\tilde{\boldsymbol{u}}) : \boldsymbol{\nabla}^{\mathcal{M}} \boldsymbol{\phi}^{x,(i-\frac{1}{2},j)} \, \mathrm{d}\boldsymbol{x}, \tag{2.31}$$

By a standard reordering of the sums, we get

$$\sum_{i=1}^{d} \sum_{\mathcal{E}\in\mathcal{E}_S^{(i)}} |D_\sigma|\ \tilde{u}_{\sigma,i}\ \mathrm{div}_{\sigma,i}\boldsymbol{\tau}_s(\tilde{\boldsymbol{u}}) = \int_\Omega \boldsymbol{\tau}_s^{\mathcal{M}}(\tilde{\boldsymbol{u}}) : \boldsymbol{\nabla}^{\mathcal{M}}\tilde{\boldsymbol{u}}\,\mathrm{d}\boldsymbol{x}, \tag{2.32}$$

An important consequence of this relation, with the definition of $\boldsymbol{\tau}_s^{\mathcal{M}}(\tilde{\boldsymbol{u}}) = \eta_s\left(\boldsymbol{\nabla}^{\mathcal{M}}\tilde{\boldsymbol{u}} + (\boldsymbol{\nabla}^{\mathcal{M}}\tilde{\boldsymbol{u}})^t\right)$, is that, thanks to an elementary property of the tensors contraction, we may replace the second tensor $\boldsymbol{\nabla}^{\mathcal{M}}\tilde{\boldsymbol{u}}$ in (2.32) by its symmetrization $\left(\boldsymbol{\nabla}^{\mathcal{M}}\tilde{\boldsymbol{u}} + (\boldsymbol{\nabla}^{\mathcal{M}}\tilde{\boldsymbol{u}})^t\right)/2$. We thus obtain that the dissipation (i.e the integral in (2.32)) is non-negative, which is a discrete counterpart of (2.14). In addition, the duality Relation (2.20) requires that the discretization of $\boldsymbol{\nabla}_K\boldsymbol{u}$ in the right-hand side of the transport equation for the conformation tensor (2.21d) to be

$$\boldsymbol{\nabla}_K\boldsymbol{u} = \frac{1}{|K|}\int_K \boldsymbol{\nabla}^{\mathcal{M}}\boldsymbol{u}\,\mathrm{d}\boldsymbol{x}.$$

This weak formulation of the diffusion term (2.32) is shown in [27] to lead to the usual diffusion operator when the viscosity does not depend on space. The same is true (i.e the weak formulation yields the usual conservative finite-volume scheme) for a space-dependent viscosity only when this quantity is considered as a piecewise-constant function over the same control volumes as the discrete velocity gradient components. For instance, for two-dimensional spaces, in the compression terms $(\boldsymbol{\tau}_s^{\mathcal{M}})_{x,x}$ and $(\boldsymbol{\tau}_s^{\mathcal{M}})_{y,y}$, the viscosity must be associated with the primal cells, while, for the shear components $(\boldsymbol{\tau}_s^{\mathcal{M}})_{x,y}$ and $(\boldsymbol{\tau}_s^{\mathcal{M}})_{y,x}$, it must be associated with the vertices (which, when constructing the scheme by the usual finite volume approach, is in fact rather natural).

Polymeric stress tensor divergence – Let us now derive the discretization of the divergence of the polymeric stress tensor. To this end, we first associate the discrete polymeric stress $\boldsymbol{\tau}_p$ to a piecewise function over the primary cells by

$$\forall (i,j)\in\mathcal{I},\ \forall \boldsymbol{x}\in K_{i,j},\quad \boldsymbol{\tau}_p(\boldsymbol{x}) = \frac{\eta_p}{\lambda}\boldsymbol{f}(\boldsymbol{c}_{i,j})(\boldsymbol{c}_{i,j}-\boldsymbol{I}_d).$$

Then we set

$$\forall (i,j)\in\mathcal{I}^x,\quad -(\mathrm{div}\boldsymbol{\tau}_p)^x_{i-\frac12,j} = \frac{1}{|K^x_{i-\frac12,j}|}\int_\Omega \boldsymbol{\tau}_p : \boldsymbol{\nabla}^{\mathcal{M}}\boldsymbol{\phi}^{x,(i-\frac12,j)}.$$

An easy calculation shows that this relation may be recast as a finite volume formulation, in the sense that the right-hand side may be seen as a sum over the faces of $K^x_{i-\frac12,j}$ of a discretization of the flux associated with $\mathrm{div}\boldsymbol{\tau}_p$, i.e the integral of the first component of $\boldsymbol{\tau}_p\boldsymbol{n}_{K,\sigma}$ (see Figure 2.2).

- On the vertical face $\varepsilon = \varepsilon^x_{i,j}$, the flux is given by

$$\int_\varepsilon (\boldsymbol{\tau}_p\boldsymbol{n}_\varepsilon)^x = \frac{1}{h^y_j}(\boldsymbol{\tau}_p)^{xx}_{i,j} = |\varepsilon^x_{i,j}|(\boldsymbol{\tau}_p)^{xx}_{i,j}.$$

- On the horizontal (half) face $\varepsilon = \varepsilon^x_{i-\frac14,j+\frac12}$, the flux is given by

$$\int_\varepsilon (\boldsymbol{\tau}_p\boldsymbol{n}_\varepsilon)^x = \frac{1}{h^y_{j+\frac12}}\left(\frac{|K_{i,j}|}{4}(\boldsymbol{\tau}_p)^{xy}_{i,j} + \frac{|K_{i,j+1}|}{4}(\boldsymbol{\tau}_p)^{xy}_{i,j+1}\right) = |\varepsilon^x_{i-\frac14,j+\frac12}|\left(\alpha\,(\boldsymbol{\tau}_p)^{xy}_{i,j} + (1-\alpha)(\boldsymbol{\tau}_p)^{xy}_{i,j+1}\right),$$

with

$$\alpha = \frac{h^y_j}{2h^y_{j+\frac{1}{2}}}, \qquad \text{and} \quad 1-\alpha = \frac{h^y_{j+1}}{2h^y_{j+\frac{1}{2}}}.$$

Hence, as usual when such a duality technique is used, the approximation of the tensor at the horizontal faces may seem strange. It is a convex combination of the unknowns in the two neighbouring cells, but with coefficients that are not those which would be given by a linear interpolation. Indeed, on $\varepsilon = \varepsilon^x_{i-\frac{1}{4},j+\frac{1}{2}}$, we have

$$(\boldsymbol{\tau}_p)^{xy}_{\varepsilon} = \alpha\,(\boldsymbol{\tau}_p)^{xy}_{i,j} + (1-\alpha)(\boldsymbol{\tau}_p)^{xy}_{i,j+1},$$

whereas, with a linear interpolation, we would have

$$(\boldsymbol{\tau}_p)^{xy}_{\varepsilon} = (1-\alpha)\,(\boldsymbol{\tau}_p)^{xy}_{i,j} + \alpha\,(\boldsymbol{\tau}_p)^{xy}_{i,j+1},$$

so that the formulae differ on a non-uniform mesh.

Up to now, we have only invoked stability arguments to justify the derivation of the discrete divergence of the elastic extra-stress tensor through a weak formulation. However, thanks to the consistency properties of the discrete gradient $\boldsymbol{\nabla}^{\mathcal{M}}$, this technique also ensures by construction the weak consistency of this discretization in the Lax-Wendroff sense, as stated in the following result for the Oldroyd-B model. For short, it is written for functions depending only on space but trivially extends to time-dependent functions. This result would extend also to non-linear laws, under stronger convergence and boundedness assumptions (and/or regularization of the function $\boldsymbol{g}$) for the sequence of conformation tensors (*in fine*, what is needed is the weak convergence in $L^1(\Omega)^{d\times d}$ of $\boldsymbol{g}(\boldsymbol{c}^{(m)})\,(\boldsymbol{c}^{(m)} - \boldsymbol{I}_d)$).

Lemma 1. *Let $(\mathcal{M}^{(m)})_{m\in\mathbb{N}}$ be sequence of structured discretizations of Ω, with a space step tending to zero. Let $(\boldsymbol{c}^{(m)})_{m\in\mathbb{N}}$ be a sequence of discrete conformation tensors, with $\boldsymbol{c}^{(m)}$ associated with $\mathcal{M}^{(m)}$. We suppose that $(\boldsymbol{c}^{(m)})_{m\in\mathbb{N}}$ weakly converges in $L^1(\Omega)^{d\times d}$ to $\boldsymbol{c}$. Let $\boldsymbol{\varphi} \in C^\infty_c(\Omega)^d$, and let us denote by $\boldsymbol{\varphi}^{(m)}$ the interpolate of $\boldsymbol{\varphi}$ in the space of velocity discrete functions defined by $\boldsymbol{\varphi}^{(m)}_{\sigma,i} = \boldsymbol{\varphi}_i(\boldsymbol{x}_\sigma)$ for $\sigma \in \mathcal{E}^{(i)}$, with $\boldsymbol{x}_\sigma$ the mass center of σ. Then*

$$\lim_{m\to+\infty} \sum_{i=1}^{d} \int_\Omega \mathrm{div}_{\sigma,i}\Big(\frac{\eta_p}{\lambda}\,(\boldsymbol{c}^{(m)} - \boldsymbol{I}_d)\Big)\ \boldsymbol{\varphi}^{(m)}_i \,\mathrm{d}\boldsymbol{x} = -\int_\Omega \frac{\eta_p}{\lambda}\,(\boldsymbol{c} - \boldsymbol{I}_d) : \boldsymbol{\nabla}\boldsymbol{\varphi}\,\mathrm{d}\boldsymbol{x}.$$

Proof. By construction, we have

$$\sum_{i=1}^{d} \int_\Omega \mathrm{div}_{\sigma,i}\Big(\frac{\eta_p}{\lambda}\,(\boldsymbol{c}^{(m)} - \boldsymbol{I}_d)\Big)\ \boldsymbol{\varphi}^{(m)}_i \,\mathrm{d}\boldsymbol{x} = \int_\Omega \Big(\frac{\eta_p}{\lambda}\,(\boldsymbol{c}^{(m)} - \boldsymbol{I}_d)\Big) : \boldsymbol{\nabla}^{\mathcal{M}}\boldsymbol{\varphi}^{(m)}\,\mathrm{d}\boldsymbol{x},$$

and the results follows thanks to the convergence of $\boldsymbol{\nabla}^{\mathcal{M}}\boldsymbol{\varphi}^{(m)}(\boldsymbol{x})$ to $\boldsymbol{\nabla}\boldsymbol{\varphi}(\boldsymbol{x})$ for almost every $\boldsymbol{x} \in \Omega$. □

2.4 A more efficient and accurate pressure correction scheme

Unfortunately, computations show that the scheme (2.21) is not as accurate and efficient as expected. The reasons of this behaviour may be traced back and cured as follows.

- First, the update of the conformation tensor in the projection step (i.e the term $\mathrm{div}_{\sigma,i}\,\boldsymbol{\tau}_p^{n+1} - \mathrm{div}_{\sigma,i}\,\boldsymbol{\tau}_p^{n}$) tightly couples the equations of this step and thus makes its resolution time-consuming. In addition, it does not seem to bring any significant gain in accuracy. This

term is thus suppressed, so as to decouple the transport equation of the conformation tensor (2.21d) from Equations (2.21b)-(2.21c) (which, as usual, are recast under the form of an elliptic problem for the pressure).

- Second, especially at high Weissenberg numbers, the production terms in Equation (2.21d) (i.e the terms $\boldsymbol{\nabla u}_K^{n+1}\boldsymbol{c}_K^{n+1} + (\boldsymbol{c}_K^{n+1})^t(\boldsymbol{\nabla u}_K^{n+1})^t$) are likely to become very stiff, so that stability and accuracy of usual schemes may require prohibitively small space and time steps. The analysis of a toy scalar problem (see Section D) shows that the scheme accuracy is dramatically enhanced by making a change of variable from $\boldsymbol{c}$ to $\log(\boldsymbol{c})$. However, for general equations of state (in particular, as in the FENE-CR model, when the function $g(\boldsymbol{c})$ does not boil down to identity), this change of variable brings additional non-linearities. A solution for this problem is given by the observation that, still on the toy problem, the scheme accuracy is essentially preserved by a 3-steps Strang-type decoupling, that consists in performing one half-step of homogeneous transport of $\log(\boldsymbol{c})$, then dealing with the reaction terms with the original variable $\boldsymbol{c}$ and finishing by the second half-step of transport of $\log(\boldsymbol{c})$. Up to the choice of the variable in the middle step, a similar strategy was already adopted in [46], with a different space discretization. With the specific space discretization considered here, i.e with piecewise-constant discrete conformation tensors, the middle step consists in a family of Ordinary Differential Equations, one per primal cell, for all the tensor components. Since the stiffness of this step is directly correlated to the magnitude of the velocity gradient in the cell, this allows us to adopt a local time-stepping strategy with a time step per cell, which dramatically enhances the accuracy and robustness of the scheme. Moreover, in most applications, we observe that large velocity gradients are localized in very specific zones of the flow so that small local time steps are used only in a few cells and the scheme efficiency is only slightly affected.

Finally, we obtain a two-steps scheme, where we successively deal first with hydrodynamics and then with the conformation tensor transport. The hydrodynamics step reads

Prediction step – Solve for $\tilde{\boldsymbol{u}}^{n+1}$:

$$\text{For } 1 \le i \le d,\ \forall \sigma \in \mathcal{E}_{\mathrm{S}}^{(i)},$$
$$\frac{\rho}{\delta t}\left(\tilde{u}_{\sigma,i}^{n+1} - u_{\sigma,i}^{n}\right) + \xi\ \rho \mathrm{div}_\sigma(\tilde{u}_i^{n+1}\boldsymbol{u}^n) - \mathrm{div}_{\sigma,i}\boldsymbol{\tau}_s(\tilde{\boldsymbol{u}}^{n+1}) + \boldsymbol{\nabla}_{\sigma,i}p^n - \mathrm{div}_{\sigma,i}\boldsymbol{\tau}_p^n = 0. \tag{2.33a}$$

Correction step – Solve for p^{n+1} and $\boldsymbol{u}^{n+1}$:

$$\text{For } 1 \le i \le d,\ \forall \sigma \in \mathcal{E}_{\mathrm{S}}^{(i)},\quad \frac{\rho}{\delta t}(u_{\sigma,i}^{n+1} - \tilde{u}_{\sigma,i}^{n+1}) + \boldsymbol{\nabla}_{\sigma,i}(p^{n+1} - p^n) = 0, \tag{2.33b}$$
$$\forall K \in \mathcal{M},\quad \mathrm{div}_K(\boldsymbol{u}^{n+1}) = 0. \tag{2.33c}$$

Up to the (explicit) term $\mathrm{div}_{\sigma,i}\boldsymbol{\tau}_p^n$ in the prediction step, this system is the usual so-called incremental pressure-correction scheme for incompressible flows. All the discrete operators featured in these equations have already been described in Section 2.3.

The discretization of the constitutive equation (2.1c) is then performed with the following "Strang-log" scheme

Advection I – Solve for $\boldsymbol{c}^{n+\frac{1}{3}}$:

$$\forall K \in \mathcal{M},\quad \frac{1}{\delta t/2}\left(\log \boldsymbol{c}_K^{n+\frac{1}{3}} - \log \boldsymbol{c}_K^{n}\right) + \mathrm{div}_K(\boldsymbol{u}^{n+1}\log \boldsymbol{c}^{n+\frac{1}{3}}) = 0. \tag{2.34a}$$

ODE – Set $\boldsymbol{c}_K(t_n) = \boldsymbol{c}_K^{n+\frac{1}{3}}$ and solve for $\boldsymbol{c}^{n+\frac{2}{3}} = \boldsymbol{c}_K(t_n + \delta t)$:

$$\forall K \in \mathcal{M}, \quad \partial_t \boldsymbol{c}_K - (\boldsymbol{\nabla}_K \boldsymbol{u}^{n+1})\,\boldsymbol{c}_K - \boldsymbol{c}_K^t \left(\boldsymbol{\nabla}_K \boldsymbol{u}^{n+1}\right)^t + \frac{\boldsymbol{g}(\boldsymbol{c}_K)}{\lambda}\,(\boldsymbol{c}_K - \boldsymbol{I}_d) = 0. \tag{2.34b}$$

Advection II – Solve for $\boldsymbol{c}^{n+1}$:

$$\forall K \in \mathcal{M}, \quad \frac{1}{\delta t/2}\left(\log \boldsymbol{c}_K^{n+1} - \log \boldsymbol{c}_K^{n+\frac{2}{3}}\right) + \mathrm{div}_K(\boldsymbol{u}^{n+1} \log \boldsymbol{c}^{n+1}) = 0. \tag{2.34c}$$

Transport steps are discretized by a standard backward first-order upwind scheme. From the form of these equations, these steps preserve the symetry of the conformation tensor: if $\boldsymbol{c}^n$ is symmetric, the same equation is solved for $c_{i,j}^{n+1}$ and $c_{j,i}^{n+1}$, $1 \le i, j \le d$. In addition, since we search for $\log(\boldsymbol{c})$ and then compute $\boldsymbol{c}$ by taking the exponential of the result, these transport steps necessarily yields positive definite conformation tensors. The local ODE (2.34b) is solved using a first-order semi-implicit Euler scheme, with a local sub-time step that reads

$$\frac{1}{\delta t_K}\,(\boldsymbol{c}_K^{n+1} - \boldsymbol{c}_K^n) = \boldsymbol{\nabla}\boldsymbol{u}\;\boldsymbol{c}_K^{n+1} + (\boldsymbol{c}_K^{n+1})^t (\boldsymbol{\nabla}\boldsymbol{u})^t - \frac{\boldsymbol{g}(\boldsymbol{c}_K^n)}{\lambda}\,(\boldsymbol{c}^{n+1} - \boldsymbol{I}_d). \tag{2.35}$$

We prove in Section A that this relation yields a symmetric positive definite tensor under the constraint (2.41) for the choice of the sub-time step δt_K. In addition, for the FENE-CR model, we prove in Section B that, under additional constraints on the sub-time step (see Lemma 6), the solution of (2.35) satisfies $\mathrm{tr}(\boldsymbol{c}^{n+1}) < b$.

2.5 Numerical results

Here we consider the dimensionless version of the system of equations (2.1) in the vanishing inertia limit ($\xi = 0$),

$$\partial_t \boldsymbol{u} = -\boldsymbol{\nabla} p + \beta\,\mathrm{div}\,(\boldsymbol{\nabla}\boldsymbol{u} + (\boldsymbol{\nabla}\boldsymbol{u})^t) + \frac{1-\beta}{Wi}\,\mathrm{div}\,(\boldsymbol{f}(\boldsymbol{c})\,(\boldsymbol{c} - \boldsymbol{I}_d)), \tag{2.36a}$$

$$\mathrm{div}\,\boldsymbol{u} = 0, \tag{2.36b}$$

$$\partial_t \boldsymbol{c} + \boldsymbol{u}\cdot\boldsymbol{\nabla}\boldsymbol{c} - (\boldsymbol{\nabla}\boldsymbol{u})\,\boldsymbol{c} - \boldsymbol{c}\,(\boldsymbol{\nabla}\boldsymbol{u})^t + \frac{1}{Wi}\,\boldsymbol{g}(\boldsymbol{c})\,(\boldsymbol{c} - \boldsymbol{I}_d) = 0, \tag{2.36c}$$

where $\beta = \eta_s/(\eta_s + \eta_p)$ is the viscosity ratio, $Wi = \lambda U/L$, space is non-dimentionalized with the lengthscale L and time with L/U.

We address two benchmark cases from the literature. The first one is the lid-driven cavity, which we solve with the MAC scheme and with the RT discretization, both on Cartesian (uniform and non-uniform) grids. The second one is the flow around a cylinder confined in a channel, which we solve on an unstructured body-fitting mesh using the RT discretization. Even though classic [19, 23, 24, 29, 46, 53, 21, 34], each of these cases is challenging to solve numerically even at moderate Wi numbers. In the case of the lid-driven cavity, it is only with the recent introduction of the log-conformation formulation that results at $Wi \ge 1$ have been obtained [23, 24]. For the flow around the cylinder, a singularity in the wake of the cylinder appears at $Wi \simeq 0.7$ that is very difficult to capture accurately [21, 34].

Our goals are here to validate the proposed scheme by comparison with results from the literature, and to study its accuracy and numerical convergence properties. We present results for both the Oldroyd-B and the FENE-CR models, these results being new in the latter case, and compare the obtained solutions. In the lid-driven cavity case, we quantitatively assess the convergence of the solutions of the FENE-CR model to the solutions of the Oldroyd-B model

when the parameter b limiting the trace of the conformation tensor tends to $+\infty$. To perform these computations, the proposed scheme was implemented in the open-source CALIF^{3}S software developed by the Institut de Radioprotection et de Sûreté Nucléaire IRSN [CALIF^{3}S]. The whole domain is decomposed into several sub-domains with the METIS (4.0.3) graph partitioner and the communication between the sub-domains is done through the OpenMPI (3.1.5) interface. The linear systems are solved using a Block-Jacobi preconditioner. Parallel computations were then carried out on TotalEnergies' group supercomputer Pangea II.

2.5.1 Lid-driven cavity

In this test, the computational domain is the unit-square $\Omega = (0,1)^2$. At the initial time, the fluid is at rest (i.e $\boldsymbol{u}(\boldsymbol{x},0) = 0$ a.e. in Ω) and the conformation tensor is uniformly equal to the identity ($\boldsymbol{c}(\boldsymbol{x},0) = \boldsymbol{I}_d$ a.e. in Ω). Dirichlet boundary conditions are imposed to the velocity components at each side of the square, with $\boldsymbol{u}^t = (8\,x^2\,(1-x)^2\,(1+\tanh(8t-4)),\ 0)$ (see [23]) on the lid and $\boldsymbol{u} = 0$ on the three other sides and at any time. The viscosity ratio is $\beta = 0.5$.

We solve this problem for a sequence of successively refined Cartesian meshes. The three coarsest meshes are uniform 64×64, 128×128 and 256×256 grids. The other ones, denoted by Mn, $n = 1, \ldots, 4$, use a non-uniform step in the two directions. These are built from lists for the x-coordinates and y-coordinates of the edges, which are defined as follows.

- The set of x-coordinates is $\mathcal{G}((0,\ 0.001/n),(0.5,\ 0.004/n)) \cup \mathcal{G}((0.5,\ 0.004/n),(1,\ 0.001/n))$,
- The set of y-coordinates is $\mathcal{G}((0,\ 0.001/n),(1,\ 0.004/n))$,

where $\mathcal{G}((a,\delta x_i),(b,\delta x_f))$ is the set of real numbers beginning at a, ending at b, with a step following a geometrical progression from δx_i at a to δx_f at b. With this procedure, the number of cells for the M4 mesh is close to 5.2 millions.

In these computations, even if, as we will see, a steady state solution is obtained, the time step must be monitored carefully to ensure time convergence. If the time step is too large, the solution shows a spurious unstationary behaviour. Hence, unless explicitly mentioned, the time step is $\delta t = 10^{-5}$ at the initial time and then increases, but is limited to keep the relative difference between the beginning and end-of step values of the velocity and the conformation tensor components lower than 0.001 in the maximum norm. The time step is also not allowed to be greater than $\delta t = 10^{-3}$, which is the time step when the solution becomes stationary. The sub-time-step for the solution of the ODE is set to $\delta t/n_e$ with n_e the smallest integer number such that $\delta t/n_e \leq 1/(2\,m\,||\boldsymbol{\nabla}_K \boldsymbol{u}^{n+1}||_\infty)$ for the Oldroyd-B model and $\delta t/n_e \leq (b-2)/(4\,\lambda\, b\, m\,||\boldsymbol{\nabla}_K \boldsymbol{u}^{n+1}||_\infty^2)$ for the FENE-CR model, with $m = 100$. These bounds are here to preserve the positive definiteness of the conformation tensor when solving the ODE by a backward Euler scheme, see Sections A and B. The CPU-time used in this step remains almost negligible (less than 3% of the total time), so a more sophisticated algorithm would not significantly increase the efficiency.

Oldroyd-B model at $Wi = 1$ and $Wi = 3$ For these two test cases, we observe the same convergence behaviour for the MAC and RT discretizations. For the finest meshes, results cannot be visually distinguished, except for the specific case of the conformation tensor at the cavity lid (see the discussion below). We present here the results obtained with the MAC scheme.

We start by plotting in Figure 2.5 the 2D representations of the velocity magnitude and the trace of the conformation tensor for $Wi = 1$ and $Wi = 3$. The velocity field exhibits some of the classical features that have been observed in the literature. Each corner at the bottom of the cavity contains a vortex at very low velocity that effectively behaves as a stagnant zone. As we increase the Wi, we transition from a left-right symmetry ($Wi = 0$) to an asymmetric

profile with a shift of the primary central vortex and of the region of maximum velocity close to the lid towards the left-hand side. The most interesting features are observed for the trace of the conformations tensor. We see a dramatic increase of the maximum value of the trace from $Wi = 1$ to $Wi = 3$, going from approximately 5×10^3 to more than 10^5. This maximum is reached at the lid with zones of large stresses both in the middle of the lid and in the top right corner. This suggests that mesh convergence in these regions may be particularly difficult to obtain. We also observe that regions of high stresses have extended further inside the cavity at $Wi = 3$ compared to $Wi = 1$, which may impact convergence even away from the lid.

We then study mesh convergence and compare quantitatively our scheme to results from the literature, starting with the Weissenberg number equal to 1 and comparing to results in [24]. The computation is performed up to a time $t = 10$, with a steady state reached for $t \approx 8$. The first component of the velocity, u_x, along the line $x = 0.5$, is presented in Figure (2.6a). The steady state is almost independent from the mesh and is in close agreement with results in [24]. The second component of the velocity, u_y, along the line $y = 0.75$ is plotted in Figure (2.6b). Convergence is slower and seems to be roughly obtained for the 256×256 grid, which is also in close agreement with [24].

The most difficult aspect of these computations is to accurately estimate the conformation tensor near the lid. We investigate this issue here using the Mn meshes that are specifically designed for this purpose, with finer meshes in the region close to the lid. Figure (2.6c) shows $tr(\boldsymbol{c})$ along the line $x = 0.5$ for M1, M2, M3 and M4. On this plot, convergence seems to be achieved for any of the grids. However, we can see in Figure (2.6d) that the profile of $tr(\boldsymbol{c})$ becomes very steep at the top. Figures (2.6e) and (2.6f) show $tr(\boldsymbol{c})$ along the lines $y = 0.975$ and $y = 1$ respectively, for the different meshes. At $y = 0.975$, convergence seems almost achieved. The picture is completely different at $y = 1$ where the maximum value of $tr(\boldsymbol{c})$, obtained close to $x = 0.5$, increases dramatically when refining the mesh. Convergence is very slow as, even for the finest mesh, we see a multiplication of the value of the maximum by a factor of about 1.5 each time the mesh step is divided by $(n+1)/n$ for $n = 1, \ldots, 3$.

We now focus on the case $Wi = 3$ and compare with results in [19, 24]. When the mesh is coarse, an unsteady behavior is observed that disappears when refining the mesh. The temporal evolution of the kinetic energy,

$$E_k = \frac{1}{2} \int_\Omega |\boldsymbol{u}(\boldsymbol{x}, t)|^2 \, \mathrm{d}\boldsymbol{x},$$

is presented in Figure 2.7. For the uniform grid 64×64, we observe periodic oscillations of the kinetic energy that are related to the appearance of vortices in the upper-right corner of the cavity. However, this phenomenon seems to be purely numerical, since, with finer meshes, oscillations disappear and a stationary solution is obtained after $t \approx 40$. Such numerical instabilities had also been observed in [24], although they did not obtain a stable solution by refining the mesh. In [19], solutions for this case may also be slightly unsteady. We compare our stationary solution to the solutions obtained in these two papers at a given time $t = 40$. Figures (2.8a) and (2.8b) depict profiles of the velocity field for the Mn meshes, showing that convergence is slower than for $Wi = 1$. We find that our results for the first velocity component (Figure (2.8a)) are in very good agreement with those of the literature [19, 24]. For the second component, we observe differences with both [19] and [24] in the region where $x \gtrsim 0.5$. However, both results in [19] and in [24] are also significantly different from one another and our solution lies roughly in between the results of these two papers. The zone where this discrepancy is observed is also the area which is likely to be impacted by unstationarities generated near the upper right corner (this was observed in our computations with coarse meshes). For the conformation tensor, difficulties in converging are no longer confined to the very top of the cavity but rather propagate further

inwards (see Figures (2.8c)–(2.8e)). As for $Wi = 1$, we still obtain an acceptable convergence everywhere except in the region closest to the lid (Figure (2.8f)).

Since momentum and conformation transport are strongly coupled, the absence of convergence for the conformation tensor locally in the lid region, which we believe is a common feature of all numerical results so far, raises concern for the convergence of the velocity field. The first clue that we may have convergence for the velocity field is of course the observed mesh convergence for the velocity components, together with the perfect consistency between the MAC and RT results (not shown here). We will also see in the next section that studying a limit of the FENE-CR model provides another clue that the velocity profiles are actually correct.

Oldroyd-B model at $Wi = 5$ Finally, we consider the case $Wi = 5$. This case has been studied in [24] and [21], where the authors obtained an unsteady regime. In [24], where they use a uniform grid MAC discretization, they obtained oscillations of the kinetic energy with a frequency that decreases with the mesh size. We obtain a similar result in Figure 2.9 (top) with our MAC scheme on coarse meshes and a stabilization for the M1 mesh. These oscillations arise from the fact that the zones where $tr(\boldsymbol{c})$ is high form a very thin filament for $Wi = 5$ that is very difficult to capture numerically. When the mesh is not sufficiently refined, the filament can rupture, generating energy transfer and kinetic energy oscillations. Refining the mesh delays this rupture and decreases the frequency of the kinetic energy oscillations. By switching to the RT discretization, oscillations disappear and we visually obtain a plateau of kinetic energy at $t \approx 50$, Figure 2.9 (bottom). However, it seems that oscillations of very small amplitude either subsist in the numerical solution or may redevelop if the time step is relaxed. Whatever the reason for this, this prevents increasing the time step at the end of the computation. For the M4 mesh, the minimum time step is set at 10^{-6} and the time step remains close to 10^{-5} at the end of the computing time. However, in this case also, we believe that the mechanism leading to temporal oscillations is once again numerical.

The results obtained at $Wi = 5$ at steady state are shown on Figure 2.11 for the RT discretization. For mesh M4, the time step δt in the final plateau is reduced to avoid a possible numerical destabilization. As in the previous cases, convergence is obtained on the velocity and the conformation tensor profiles, except close to the lid, for the conformation tensor.

FENE-CR model We now study the solutions of the FENE-CR model. As we will see, convergence is more easily reached than with the Oldroyd-B model, so the MAC and RT discretizations yield equivalent results. The solutions plotted here are obtained with the MAC scheme.

The 2D plots of the trace of the conformation tensor (log-scale) for $Wi = 1$ and $Wi = 3$ are compared in Figure 2.12 for different values of b. Zones of large polymeric stresses are similar to that of the Oldroyd-B model, with large elongations in the lid region. However, when normalized by b, the regions of large stresses are much more diffuse and their size tends to reduce as b increases. To understand this, recall that the primary difference between the Oldroyd-B and FENE-CR models is that the elongation of the polymer is bounded by b in the case of the FENE-CR model, while it can become arbitrarily large in the Oldroyd-B model. In all results below, this means that the maximum value of $\mathrm{tr}(\boldsymbol{c})$ is lower than b (so the plotted ratio $\mathrm{tr}(\boldsymbol{c})/b$ always remains lower than 1). Small values of b can considerably limit polymer elongation, the polymeric stress and the impact of polymers on flow. This is also clear when considering the limits of the FENE-CR model, with $b \to d$ leading to Stokes flow and $b \to \infty$ to the Oldroyd-B model.

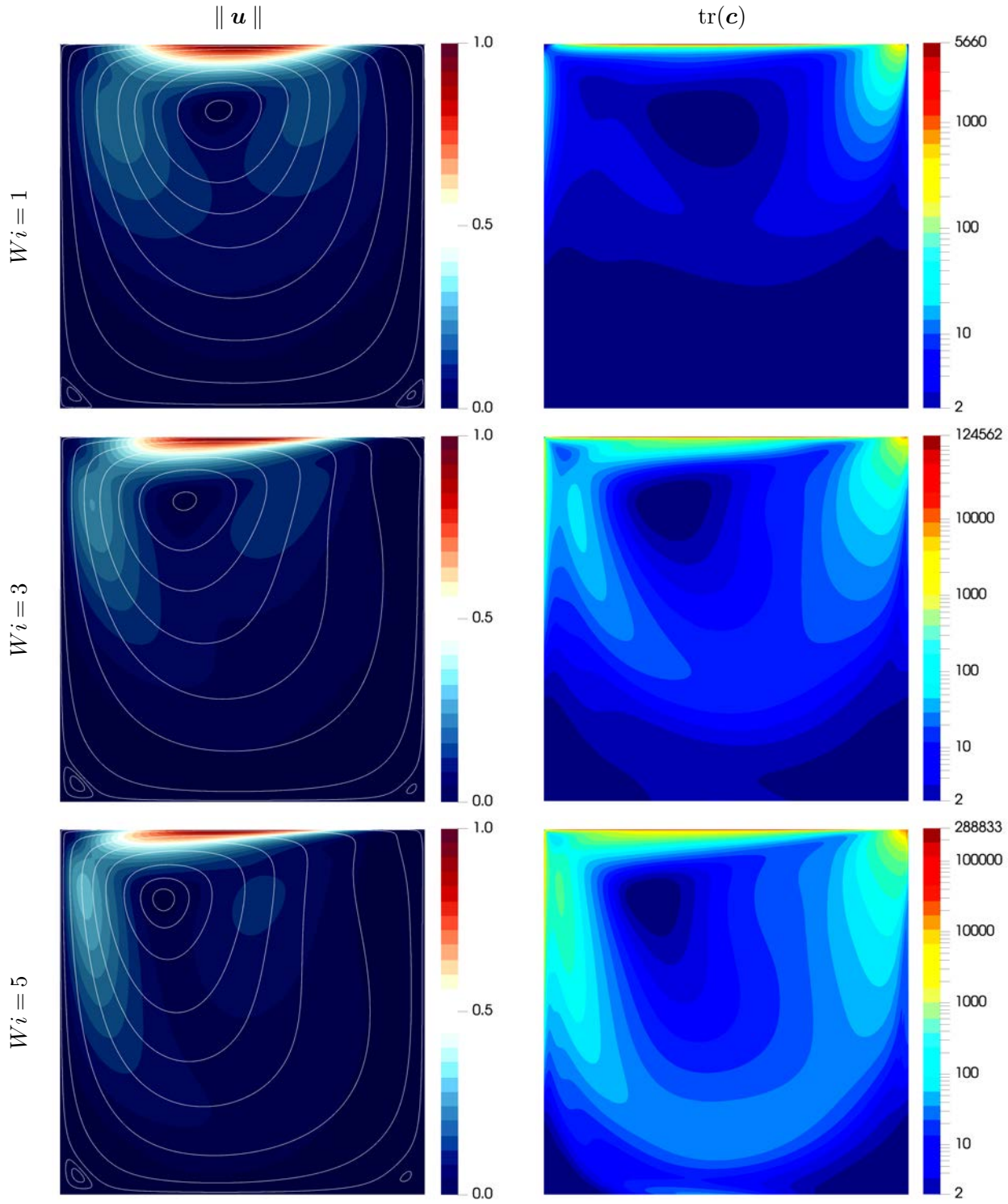

Fig. 2.5 Evolution of velocity and tr($\boldsymbol{c}$) fields with the Weissenberg number. Lid-driven cavity, Oldroyd-B model. From top to bottom: $Wi = 1$, $Wi = 3$ and $Wi = 5$ (with RT discretisation). Left: velocity magnitude and streamlines. Right: trace of the conformation tensor (in log-scale). Results obtained with mesh M4.

Figures 2.13 and 2.14 show the mesh convergence for $b = 1000$ at $Wi = 1$ and $Wi = 3$, respectively. For the components of the velocity, convergence is similar to that of the Oldroyd-B

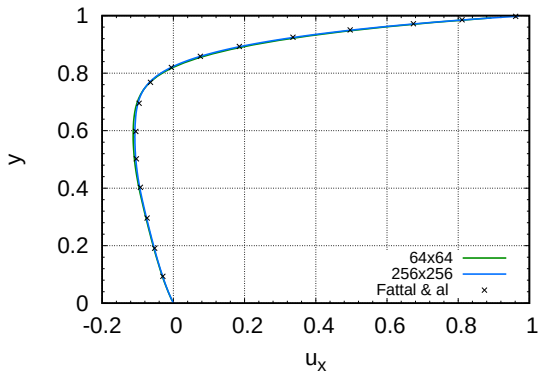

(a) First velocity component along $x = 0.5$

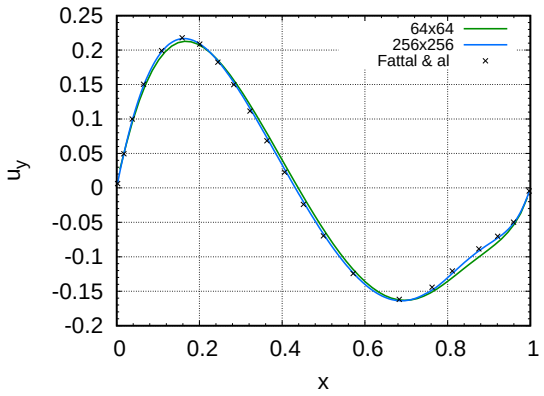

(b) Second velocity component along $y = 0.75$

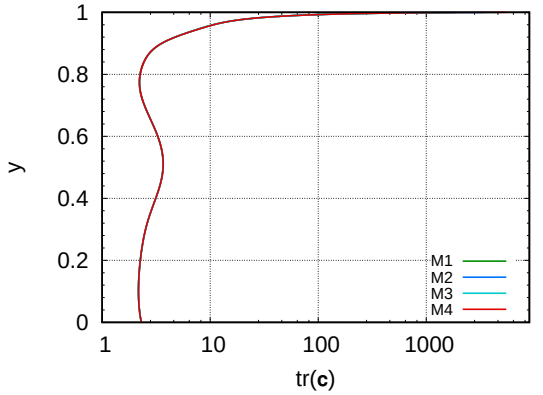

(c) Profile of $\mathrm{tr}(\boldsymbol{c})$ along along $x = 0.5$

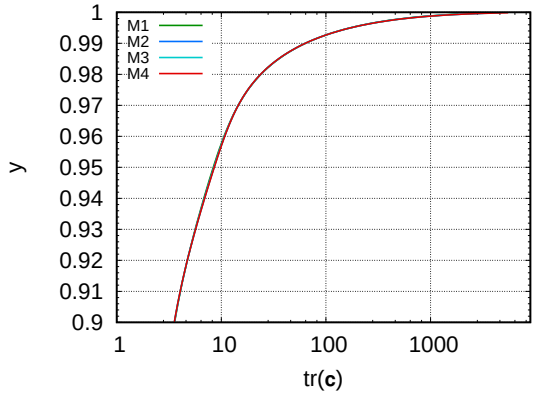

(d) Profile of $\mathrm{tr}(\boldsymbol{c})$ along $x = 0.5$ near the top

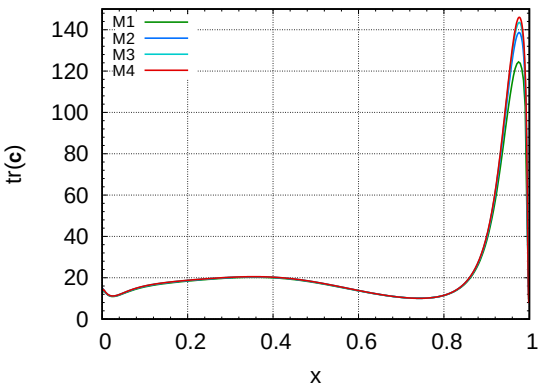

(e) Profile of $\mathrm{tr}(\boldsymbol{c})$ along $y = 0.975$

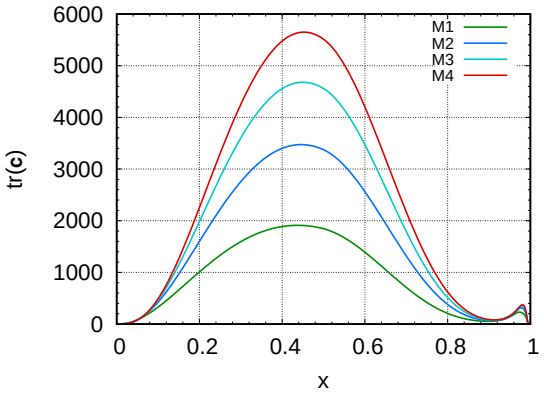

(f) Profile of $\mathrm{tr}(\boldsymbol{c})$ along $y = 1$

Fig. 2.6 Profiles of u_x, u_y and $\mathrm{tr}(\boldsymbol{c})$ along different lines for different meshes. Lid-driven cavity, Oldroyd-B model, $Wi = 1$.

model. For the conformation tensor, the behavior is radically different, especially close to the lid. Convergence is much faster in the case of the FENE-CR model, as expected from the effects of the limitation of the polymer elongation. Figure 2.15 and 2.16 show results of the FENE-CR model for different values of b at $Wi = 1$ and $Wi = 3$, respectively. These are further compared with the Stokes and Oldroyd-B models. As expected, results for the FENE-CR model get closer to the Newtonian solution when b decreases and to the Oldroyd-B solution in the limit $b \to +\infty$.

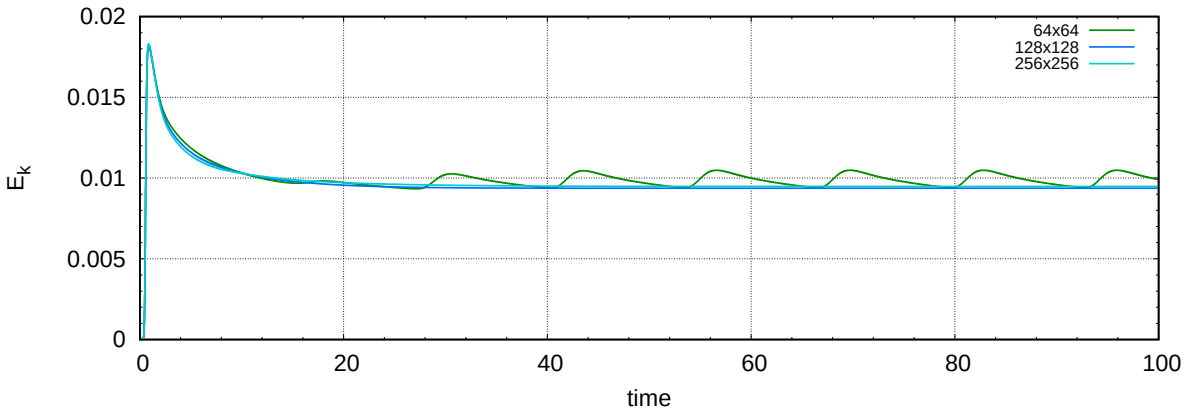

(a) Uniform grids

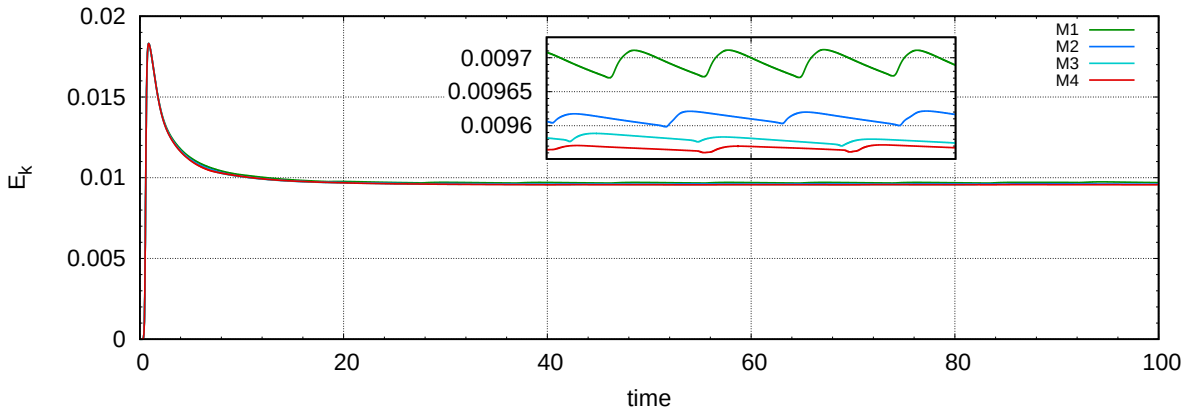

(b) Mn meshes (insert: zoom between $t = 40$ and $t = 80$)

Fig. 2.7 Time evolution of the kinetic energy E_k for different meshes. Lid-driven cavity, Oldroyd-B model, $Wi = 3$.

Figure 2.17 shows the evolution, as a function of b, of the difference (in L2-norm) between the velocity fields:

$$\| \boldsymbol{u}_b - \boldsymbol{u}_O \|_{L^2} = \left(\int_\Omega \| \boldsymbol{u}_b(\boldsymbol{x}) - \boldsymbol{u}_O(\boldsymbol{x}) \|^2 \, \mathrm{d}\boldsymbol{x} \right)^{1/2},$$

with $\boldsymbol{u}_O$ the velocity field obtained with the Oldroyd-B model and $\boldsymbol{u}_b$ that obtained with the FENE-CR model (for this norm computation, each velocity component is supposed to be piecewise constant over its associated dual mesh). By increasing b, we converge towards the Oldroyd-B model, with a faster convergence at $Wi = 1$. Since results for the FENE-CR model are converged for both the velocity and conformation fields, this convergence supports the claim that the velocity profiles for the Oldroyd-B fluid are correct.

2.5.2 Flow past a confined cylinder

We now consider the case of a two-dimensional flow around a confined cylinder. Schematics of the geometry are presented in Figure 2.18. It consists of a cylinder of radius $R = 1$ confined in a channel of width $W = 4$ and length $L = 30$. No-slip and no-penetration boundary conditions, $u_x = u_y = 0$, are imposed on the top/bottom boundary and on the cylinder. Periodic boundary conditions are used for the left/right boundaries. This yields a top/bottom symmetry, which

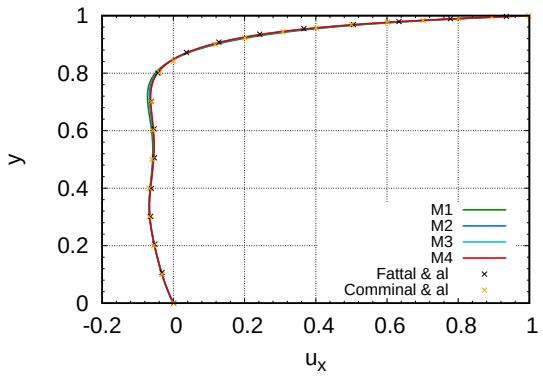

(a) First velocity component along $x = 0.5$

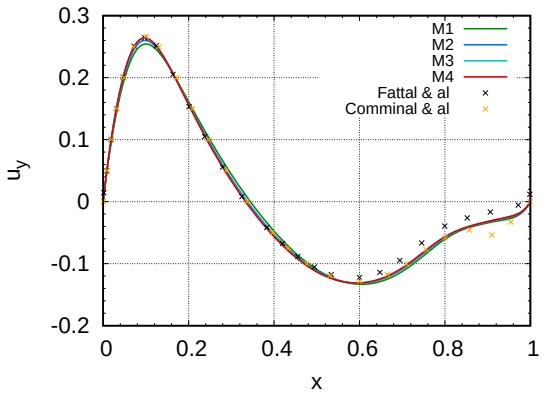

(b) Second velocity component along $y = 0.75$

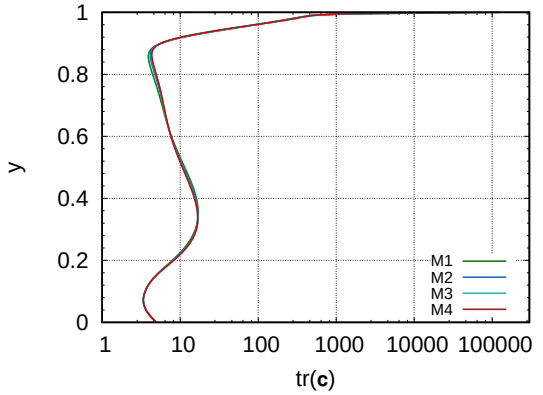

(c) Profile of $\mathrm{tr}(\boldsymbol{c})$ along $x = 0.5$

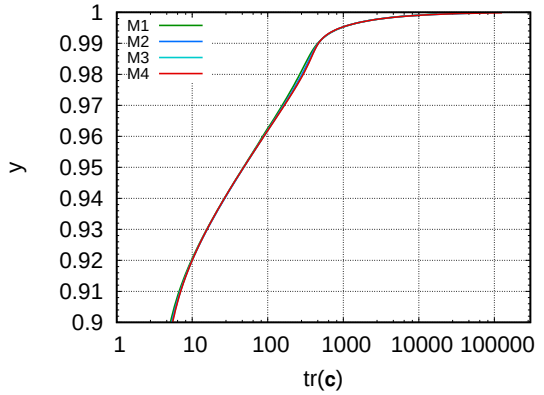

(d) Profile of $\mathrm{tr}(\boldsymbol{c})$ along $x = 0.5$ near the top

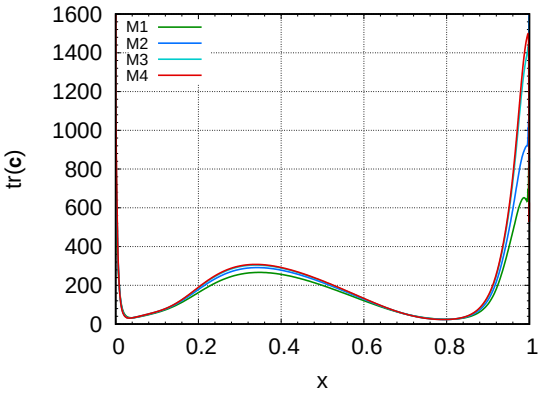

(e) Profile of $\mathrm{tr}(\boldsymbol{c})$ along $y = 0.975$

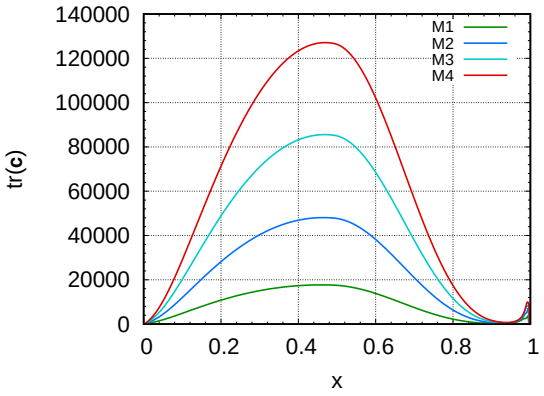

(f) Profile of $\mathrm{tr}(\boldsymbol{c})$ along $y = 1$

Fig. 2.8 Profiles of u_x, u_y and $\mathrm{tr}(\boldsymbol{c})$ along different lines for different meshes. Lid-driven cavity, Oldroyd-B model, $Wi = 3$.

allows us to simulate the flow only in the upper half of the channel. The flow results from a uniform body force $\mathbf{F} = F\,\boldsymbol{e}_x$ (where $\boldsymbol{e}_x$ stands for the first vector of the canonical basis of $\mathbb{R}^2$), with F adjusted so that the flow rate is constant and set to $Q = 2$. We further fix $\beta = 0.59$ and obtain the target Weissenberg number, $Wi = \lambda Q / WR$, by changing the relaxation time λ.

The presence of a stagnation point in the wake of the cylinder generates a thin zone of very large polymer elongation, a “filament”, located on the symmetry axis and starting from the

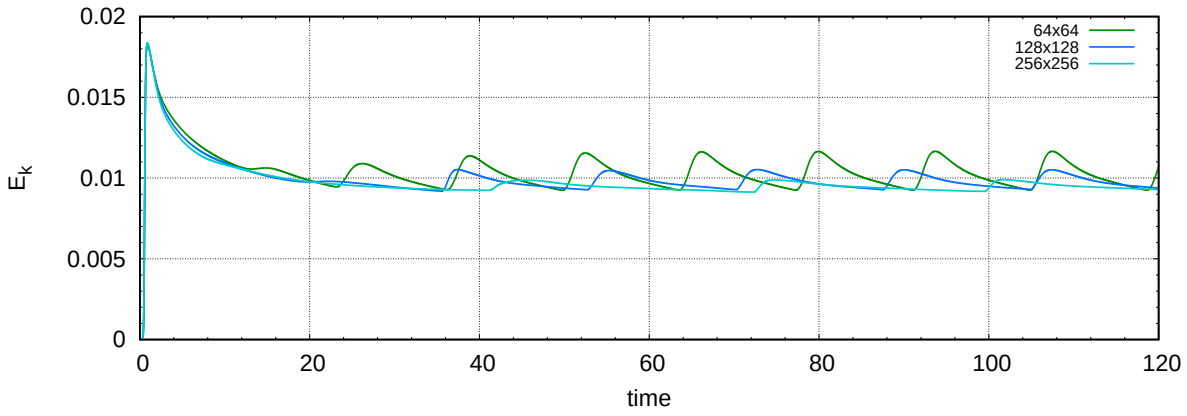

(a) Uniform grids

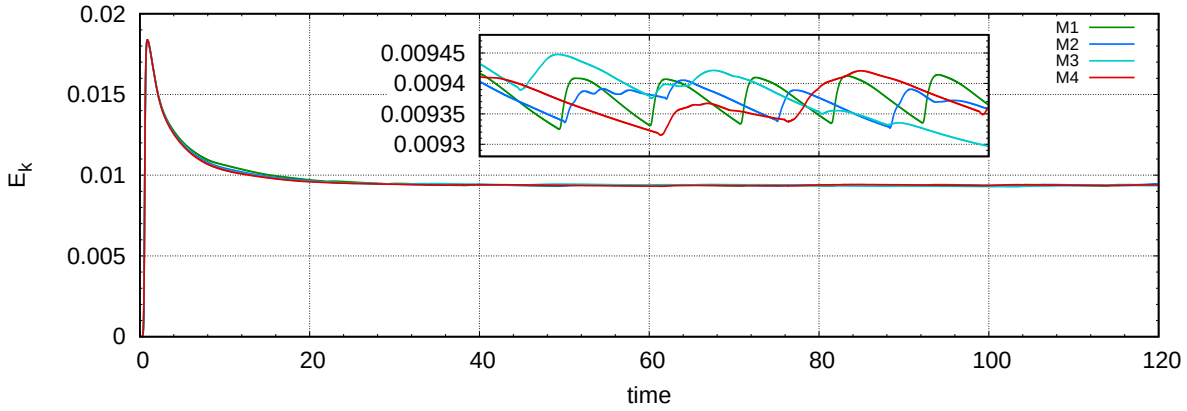

(b) Mn meshes (insert: zoom between $t = 40$ and $t = 100$)

Fig. 2.9 Time evolution of the kinetic energy E_k for different meshes with MAC discretization. Lid-driven cavity, Oldroyd-B model, $Wi = 5$.

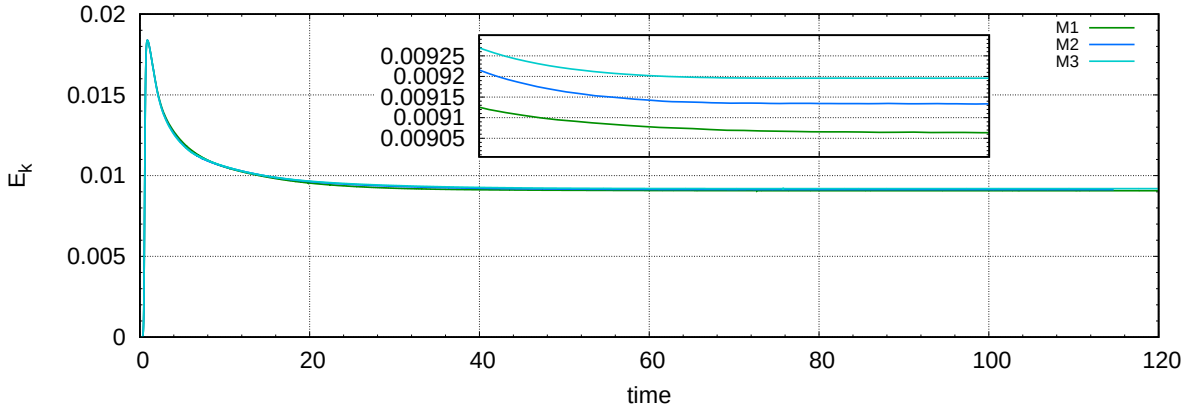

Fig. 2.10 Time evolution of the kinetic energy E_k for the Mn meshes with RT discretization. Lid-driven cavity, Oldroyd-B model, $Wi = 5$.

intersection of the latter with the boundary of the cylinder. This filament is often referred to as a birefringent strand in the literature, in reference to an experimental method to visualize it.

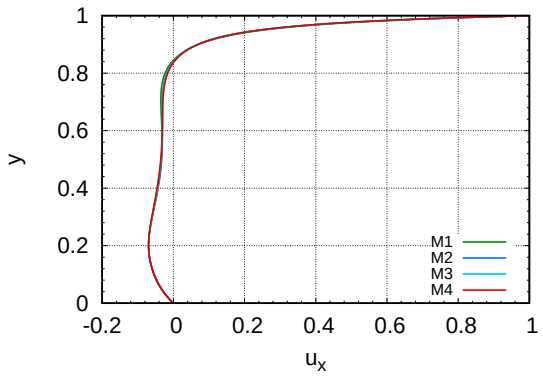

(a) First velocity component along $x = 0.5$

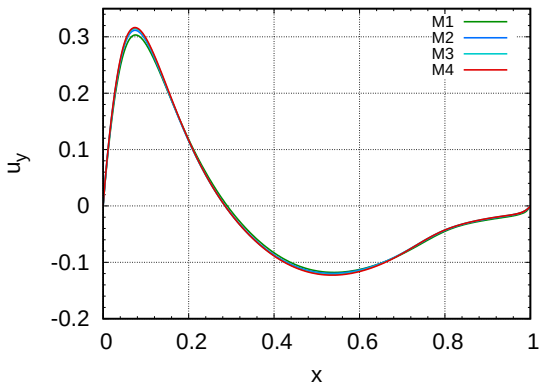

(b) Second velocity component along $y = 0.75$

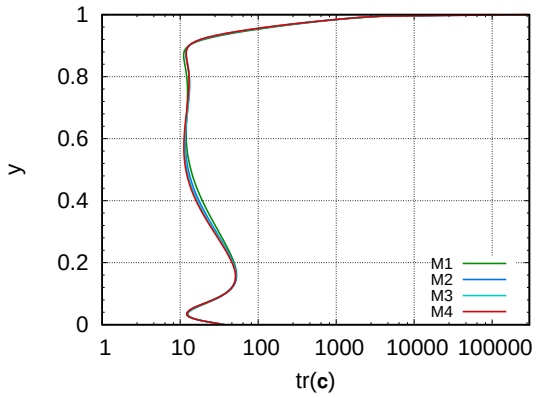

(c) Profile of $\mathrm{tr}(\boldsymbol{c})$ along $x = 0.5$

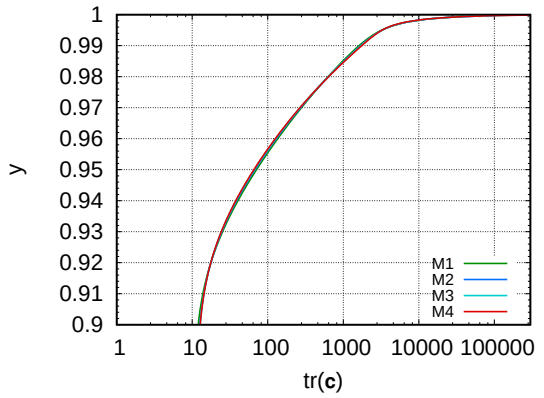

(d) Profile of $\mathrm{tr}(\boldsymbol{c})$ along $x = 0.5$ near the top

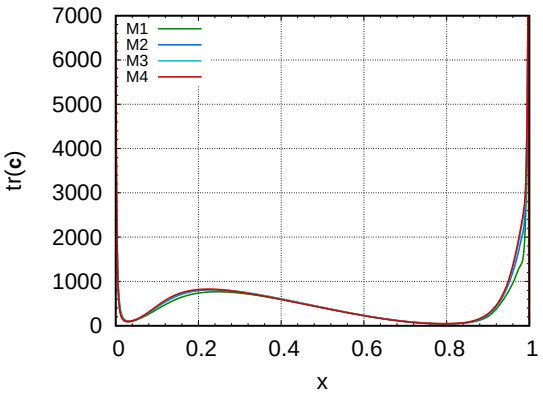

(e) Profile of $\mathrm{tr}(\boldsymbol{c})$ along $y = 0.975$

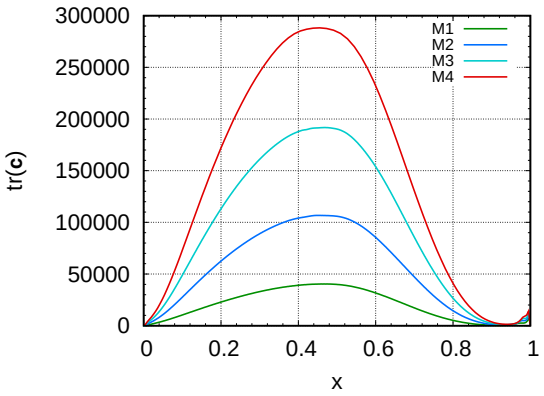

(f) Profile of $\mathrm{tr}(\boldsymbol{c})$ along $y = 1$

Fig. 2.11 Profiles of u_x, u_y and $\mathrm{tr}(\boldsymbol{c})$ along different lines for different meshes. Lid-driven cavity, Oldroyd-B model, $Wi = 5$.

It is notoriously difficult to capture in flow simulations because of both the large values of the conformation tensor and the strong gradients. Mesh convergence for the conformation tensor $\boldsymbol{c}$ and, equivalently, for the polymer stress tensor

$$\boldsymbol{\tau}_p = \frac{\eta_p}{\lambda}\ \boldsymbol{f}(\boldsymbol{c})\ (\boldsymbol{c} - \boldsymbol{I}_d)$$

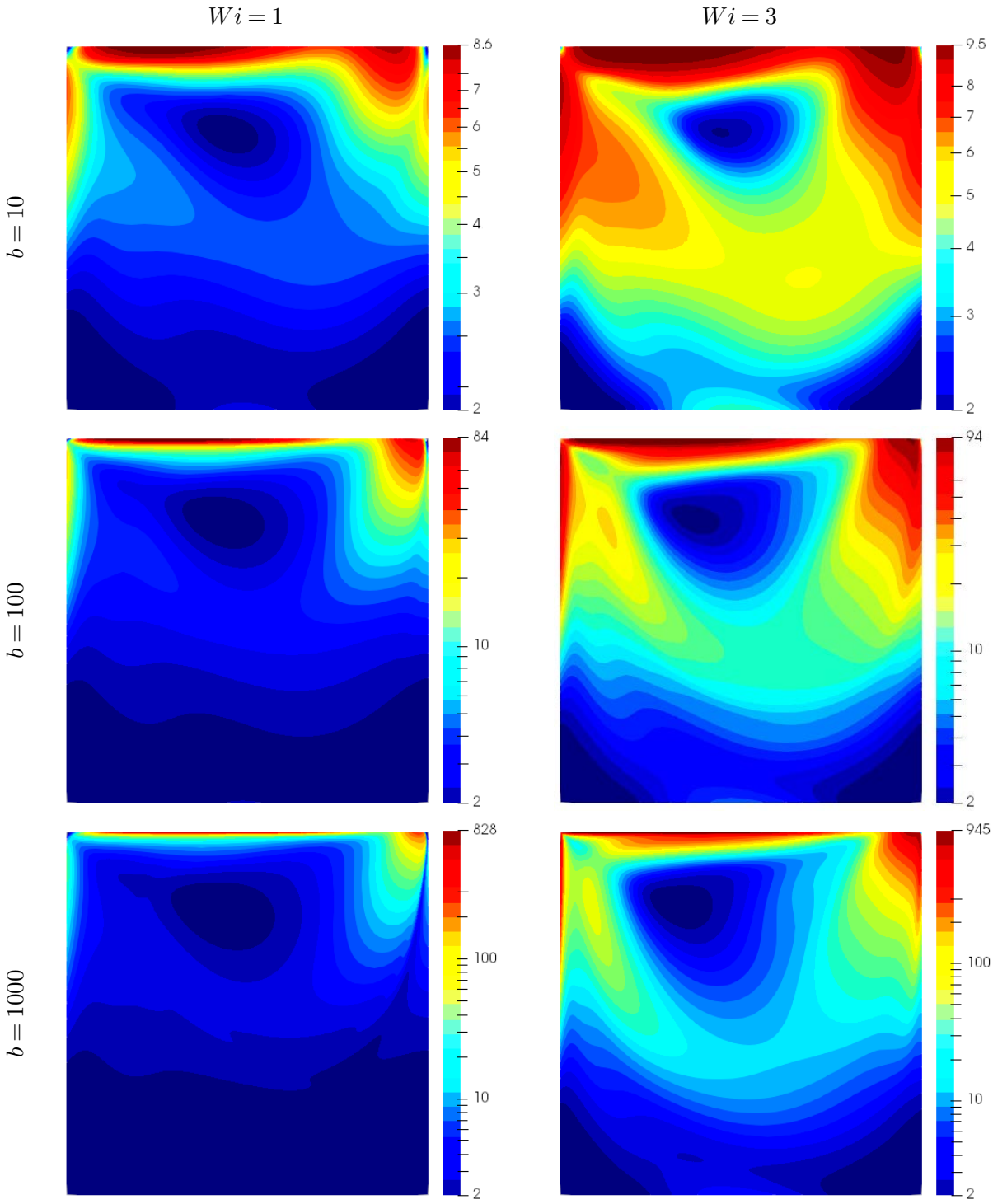

Fig. 2.12 Trace of the conformation tensor scaled by the elongation parameter b for $Wi = 1$ (left) and $Wi = 3$ at $t = 40$ (right), in log-scale. Lid-driven cavity, FENE-CR model. From top to bottom : $b = 10$, $b = 100$ and $b = 1000$.

requires a very refined discretization in this area. To solve this issue, we use a set of non-structured meshes (Figure 2.18) with the RT space approximation. These meshes are built with the GMSH mesher (version 4.4) as follows:

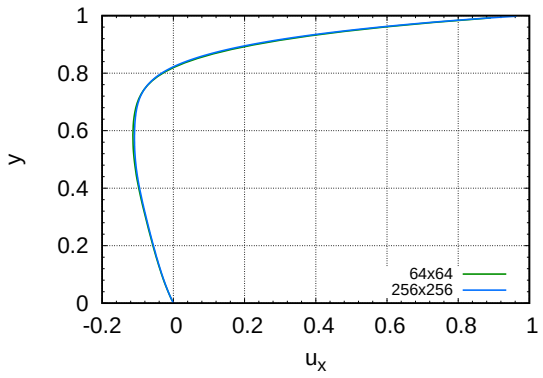

(a) First velocity component along $x = 0.5$

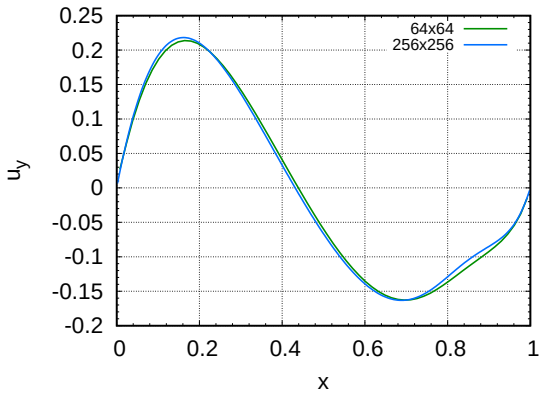

(b) Second velocity component along $y = 0.75$

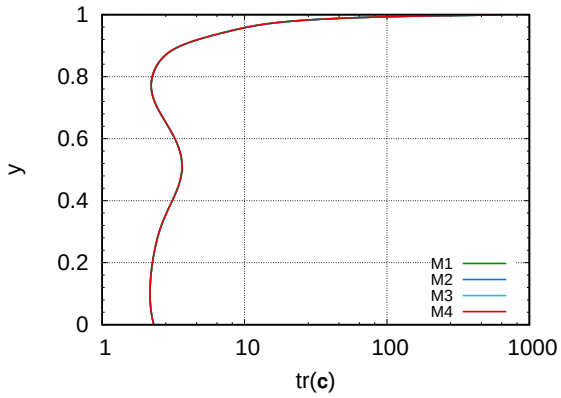

(c) Profile of $\mathrm{tr}(\boldsymbol{c})/b$ along $x = 0.5$

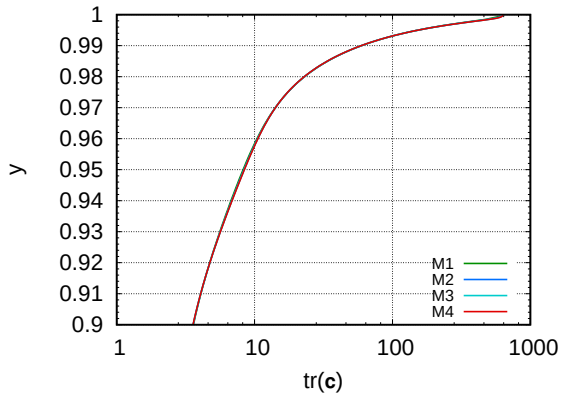

(d) Profile of $\mathrm{tr}(\boldsymbol{c})/b$ along $x = 0.5$ near to the top

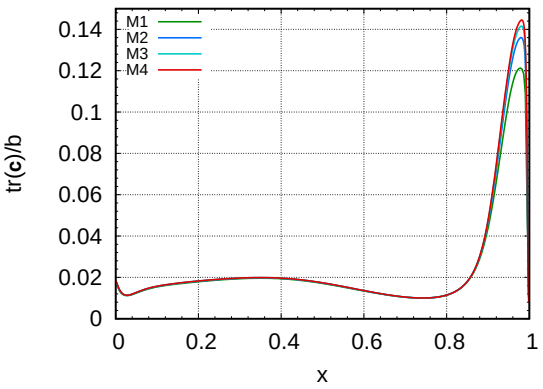

(e) Profile of $\mathrm{tr}(\boldsymbol{c})$ along $y = 0.975$

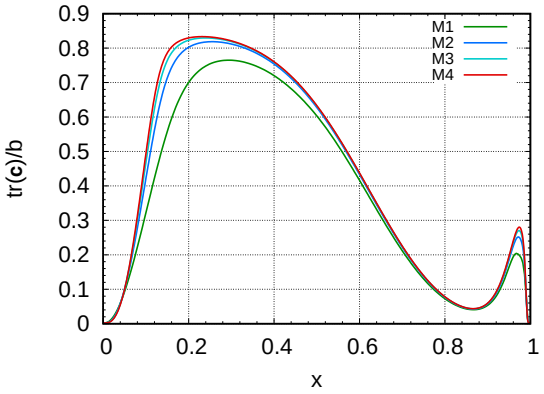

(f) Profile of $\mathrm{tr}(\boldsymbol{c})$ along $y = 1$

Fig. 2.13 Profiles of u_x, u_y and $\mathrm{tr}(\boldsymbol{c})$ along different lines for different meshes. Lid-driven cavity, FENE-CR model with $b = 1000$, $Wi = 1$.

- outside of the blue zone in Figure 2.18 (delimited by the vertices $(12.5, 0)$, $(12.5, 0.5)$, $(14, 2)$, $(16, 2)$, $(17.5, 0.5)$ and $(17.5, 0)$, if the bottom left corner of the channel is associated with the origin), the length of the cell edges is roughly kept constant at value δ_{max} and cells have two horizontal edges. Mesh elements are almost square, except near the symmetry axis where they take the form of (rather flat) rectangles, since the refinement described in the following item propagates up to the left and right boundaries.

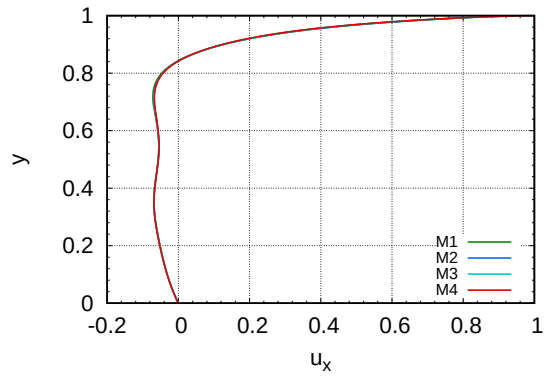

(a) First velocity component along $x = 0.5$

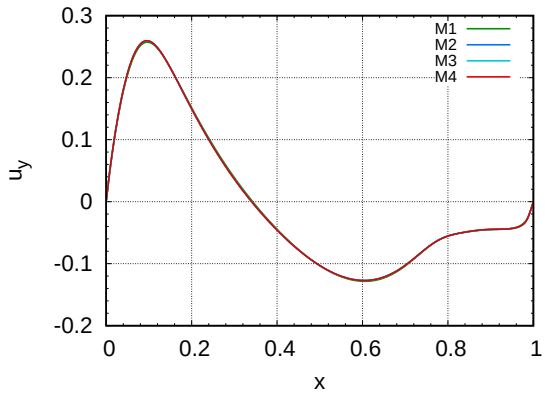

(b) Second velocity component along $y = 0.75$

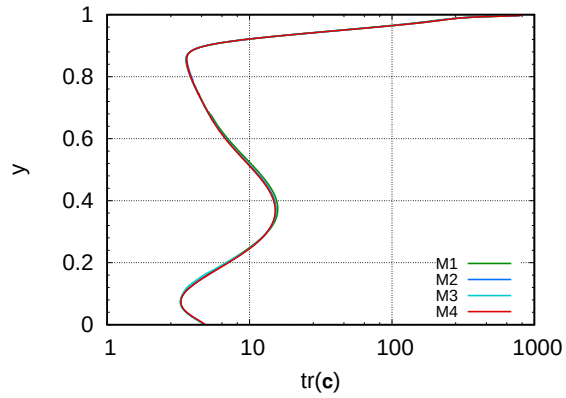

(c) Profile of $\mathrm{tr}(\boldsymbol{c})/b$ along $x = 0.5$

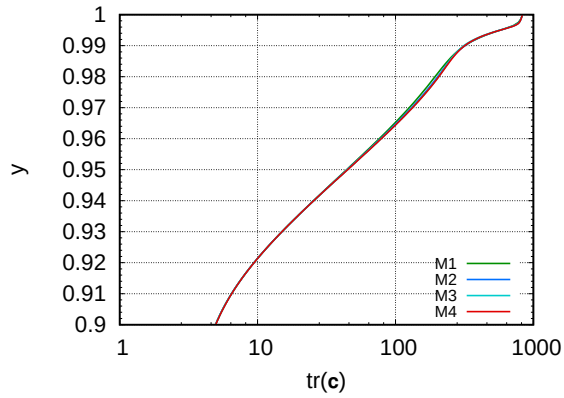

(d) Profile of $\mathrm{tr}(\boldsymbol{c})/b$ along $x = 0.5$ near to the top

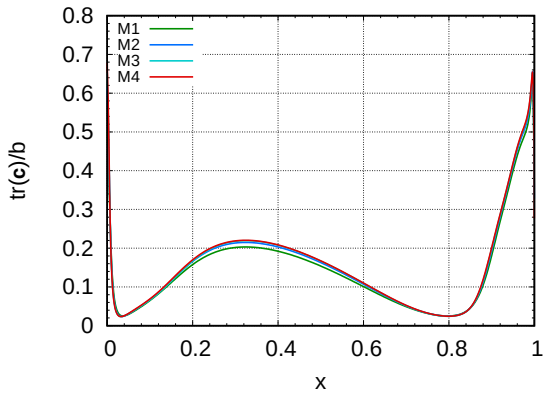

(e) Profile of $\mathrm{tr}(\boldsymbol{c})$ along $y = 0.975$

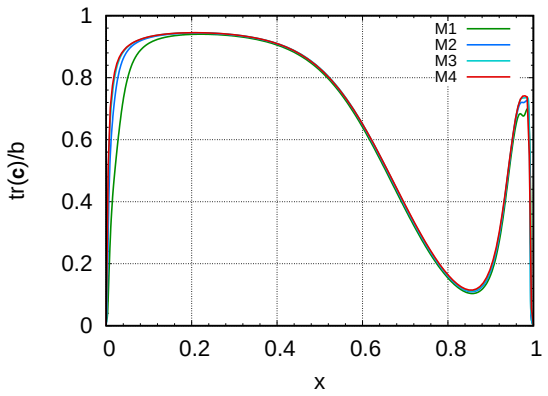

(f) Profile of $\mathrm{tr}(\boldsymbol{c})$ along $y = 1$

Fig. 2.14 Profiles of u_x, u_y and $\mathrm{tr}(\boldsymbol{c})$ along different lines for different meshes. Lid-driven cavity, FENE-CR model with $b = 1000$, $Wi = 3$.

- inside the blue zone, the mesh is refined. Cells always have two edges aligned with the radial direction of the cylinder. Along this direction, the size of the cells progressively increases from δy_{min} at the boundary to a value close to δ_{max} at the blue line that delimits the refined zone. Along the cylinder boundary, the size of the cell edges progressively increases and then decreases, the smallest cells being located at the intersections between the cylinder boundary and the symmetry axis, and being almost square.

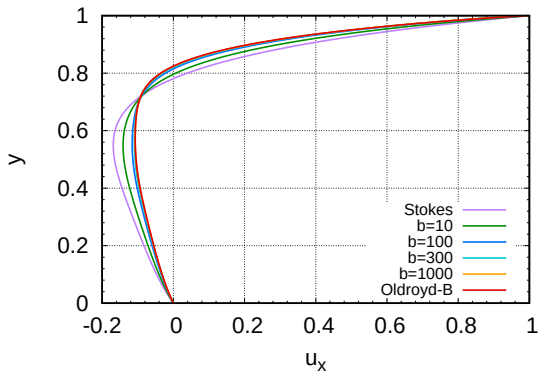

(a) First velocity component along $x = 0.5$

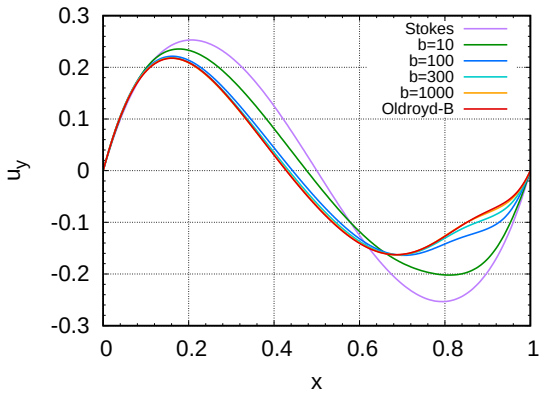

(b) Second velocity component along $y = 0.75$

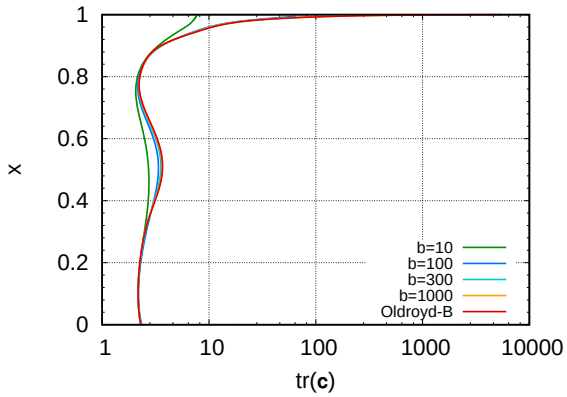

(c) Profile of $\mathrm{tr}(\boldsymbol{c})$ along $x = 0.5$

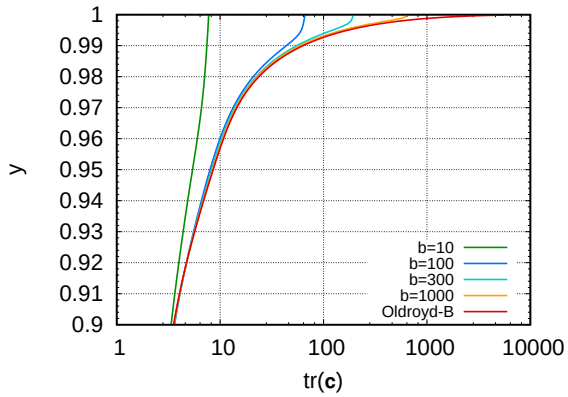

(d) Profile of $\mathrm{tr}(\boldsymbol{c})$ along $x = 0.5$ near the top

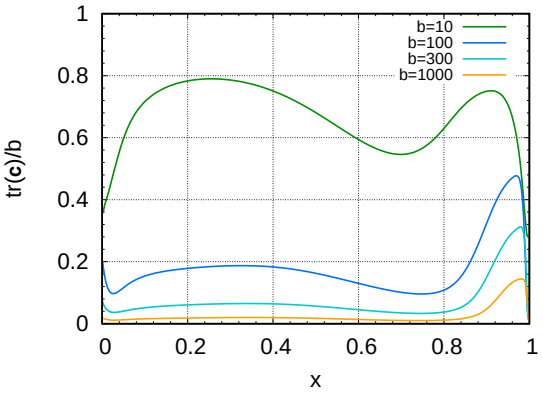

(e) Profile of $\mathrm{tr}(\boldsymbol{c})$ along $y = 0.975$

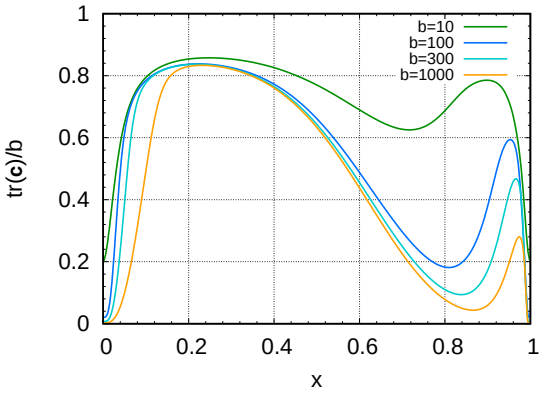

(f) Profile of $\mathrm{tr}(\boldsymbol{c})$ along $y = 1$

Fig. 2.15 Comparaison with Oldroyd-B model for different values of the elongation parameter b. Lid-driven cavity, FENE-CR model, $Wi = 1$. Results obtained with mesh M4.

Two families of meshes are built in this way. For the first one, meshes are denoted by MC1,..., MC5, $\delta_{max} = 1/100$ and the total number of cells is close to 400,000. For the second one, meshes are denoted by MR1,..., MR7, $\delta_{max} = 1/300$ and the total number of cells is close to 4 millions. For each of these meshes, the smallest cell width, δy_{min} is given in Table 2.1a (MC family of meshes) and Table 2.1b (MR family of meshes). The time step is chosen between 10^{-3} (for the coarsest meshes) and 3×10^{-5} (for the most refined ones) and, as in the case of the lid-driven cavity, the sub-time-step for the solution of the ODE is set to $\delta t / n_e$ with n_e the

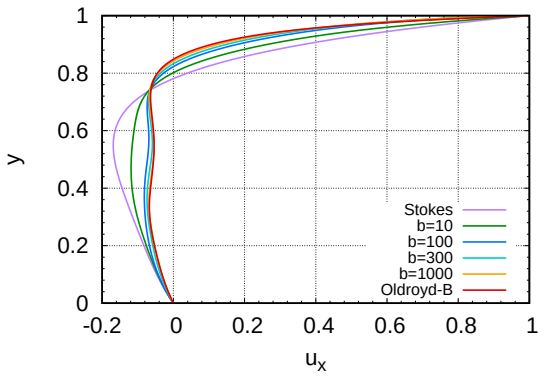

(a) First velocity component along $x = 0.5$

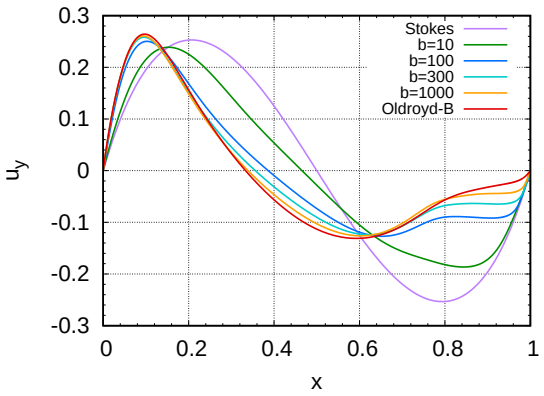

(b) Second velocity component along $y = 0.75$

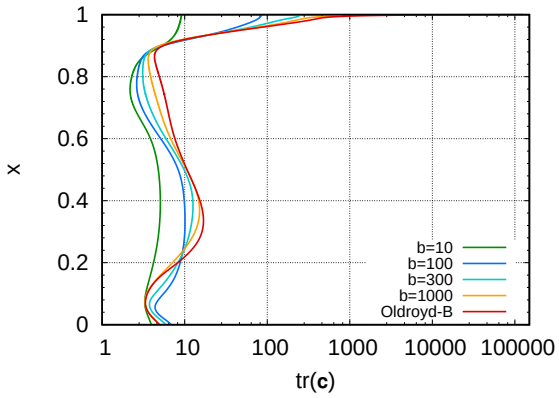

(c) Profile of $\mathrm{tr}(\boldsymbol{c})$ along $x = 0.5$

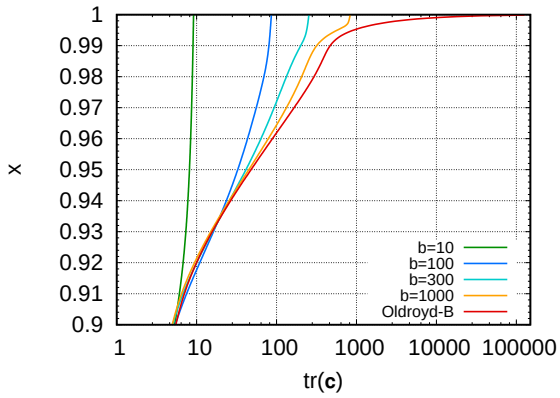

(d) Profile of $\mathrm{tr}(\boldsymbol{c})$ along $x = 0.5$ near the top

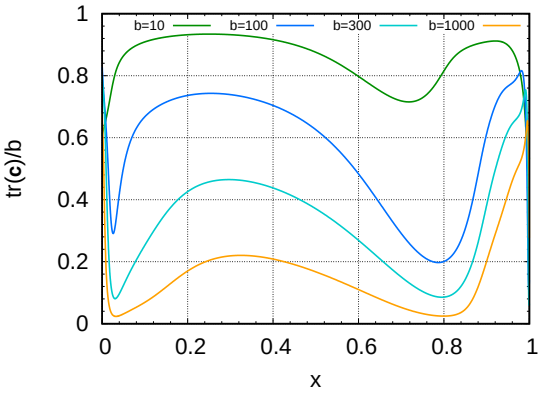

(e) Profile of $\mathrm{tr}(\boldsymbol{c})$ along $y = 0.975$

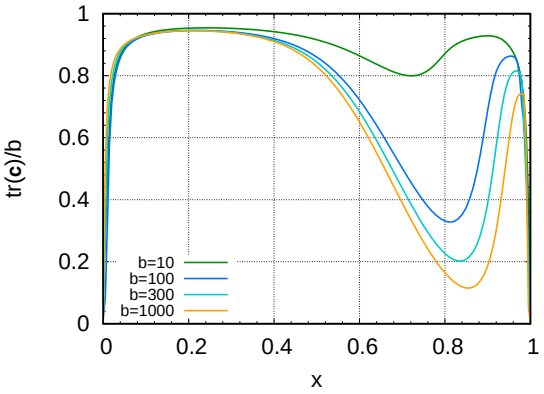

(f) Profile of $\mathrm{tr}(\boldsymbol{c})$ along $y = 1$

Fig. 2.16 Comparaison with Oldroyd-B model for different values of the elongation parameter b. Lid-driven cavity, FENE-CR model, $Wi = 3$. Results obtained with the mesh M4.

smallest integer number such that $\delta t/n_e \leq 1/(2m\ ||\boldsymbol{\nabla}_K \boldsymbol{u}^{n+1}||_\infty)$ for the Oldroyd-B model and $\delta t/n_e \leq (b-2)/(4\lambda b m\ ||\boldsymbol{\nabla}_K \boldsymbol{u}^{n+1}||_\infty^2)$ for the FENE-CR model, with $m = 100$.

Oldroyd-B model We present the results for two Weissenberg numbers, $Wi = 0.6$ and $Wi = 0.7$. In both cases, the overall characteristics of the flow are the same. So we only plot in Figure 2.19 the two-dimensional fields (velocity, pressure and trace of the conformation tensor)

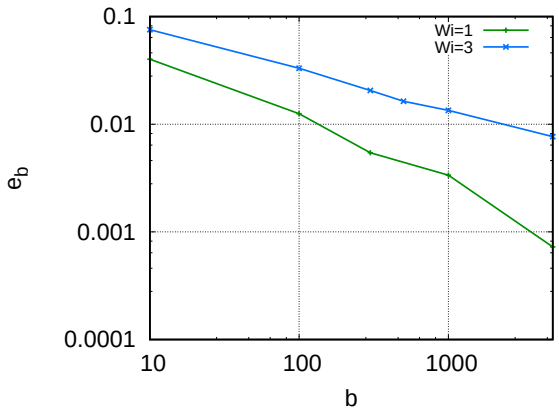

Fig. 2.17 Difference from the Oldroyd-B velocity field for different values of the elongation parameter b. Lid-driven cavity, FENE-CR model, $Wi = 1$ and $Wi = 3$. Results obtained with the mesh M4.

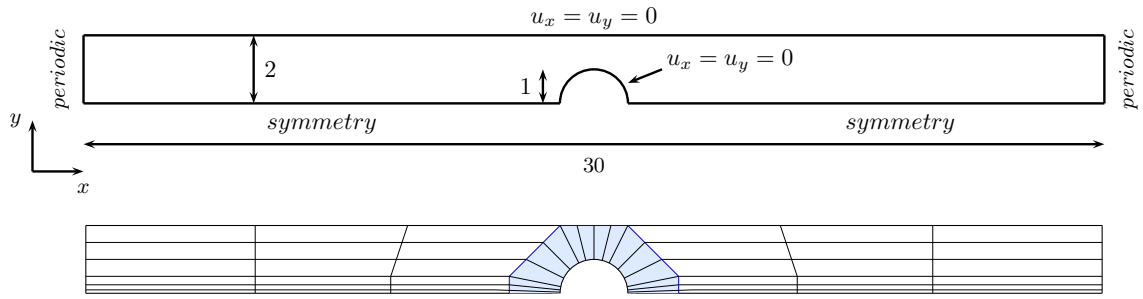

Fig. 2.18 Flow past a confined cylinder – Geometry outline and coarse version of the mesh.

Minimum cell size of meshes of type MC					
Mesh	MC1	MC2	MC3	MC4	MC5
δy_{min}	8.0×10^{-04}	4.0×10^{-04}	2.0×10^{-04}	1.0×10^{-04}	5.0×10^{-05}

(a) MC-type meshes

Minimum cell size of meshes of type MR							
Mesh	MR1	MR2	MR3	MR4	MR5	MR6	MR7
δy_{min}	6.0×10^{-04}	3.0×10^{-04}	1.5×10^{-04}	8.0×10^{-05}	4.0×10^{-05}	2.0×10^{-05}	1.0×10^{-05}

(b) MR-type meshes

Table 2.1 Minimum width δy_{min} of the cells located in the wake of the cylinder.

on the MC4 mesh for the highest Weissenberg number, once the flow has reached stationary state. For $Wi = 0.7$, this occurs at time $t \approx 3$. We observe three regions of large polymer stresses. As discussed previously, a filament is present in the wake of the cylinder. Two large elongation zones also appear between the upper part of the cylinder and the opposite solid surface, at the neighborhood of the boundary, on both sides.

To go further, we compare our results with those proposed in [21, 34]. For $Wi = 0.6$, the stationary regime is obtained at time $t \approx 2$. Figure 2.20 shows the xx-component of the polymer

stress,

$$\tau_{xx} = \frac{\eta_p}{\lambda}(c_{xx} - 1),$$

as a function of the curvilinear coordinate s along the line composed of the cylinder boundary and the part of the symmetry axis located in the wake of the cylinder. The two stagnations points at the cylinder boundary correspond to $s = 0$ for the front one and $s = \pi$ for the rear one. As expected from the two-dimensional plot, we observe two peaks for τ_{xx}. The first one, more pronounced, is approximately centered at the throat between the cylinder and the solid surface, $s \approx \pi/2$, and the second one is located in the wake close to the cylinder. These results are in very good agreement with both [21] and [34].

We now turn to the case $Wi = 0.7$, for which a lack of convergence on τ_{xx} in the wake of the cylinder is generally reported in the literature (see [21, 34]). This is observed in Figure 2.21 (left) with the MC-type meshes. We find a profile close to the one proposed in [34] with the MC1 mesh and close to the one proposed in [21] with the MC3 one. Beyond MC3, we need finer meshes that make it possible to capture thinner filaments with larger values of the conformation tensor. To explore this, we consider the second family of refined meshes, MR1, ..., MR7. The stress profiles are shown in Figure 2.21 (right), making it obvious that mesh convergence is very difficult to obtain and that the peak value increases as the mesh is refined. However, convergence seems close with the MR7 mesh.

FENE-CR model Finally, we consider the FENE-CR fluid at $Wi = 0.7$ for different values of the elongation parameter b. Figure 2.22 shows the trace of the conformation tensor in log-scale normalized by b. As for the lid-driven cavity, when the value of b increases, the zones of high elongation become thinner and profiles look qualitatively similar to those obtained with the Oldroyd-B model.

Results obtained for the xx-component of the polymer stress,

$$\tau_{xx} = \frac{\eta_p}{\lambda}\frac{b}{b - \mathrm{tr}(\boldsymbol{c})}(c_{xx} - 1),$$

in the wake of the cylinder are shown in Figure 2.23, for $b = 100$ and $b = 1000$. For $b = 100$, mesh convergence is reached relatively easily, whereas convergence becomes slower for $b = 1000$. In this last case, difficulties are similar to those encountered with the Oldroyd-B model, with in fact similar values of the maximum value of the trace (about 187 for the Oldroyd-B model and 135 for the FENE-CR model). This is explained by the fact that the limit $b = 1000$ is far beyond the maximum value taken by $\mathrm{tr}(\boldsymbol{c})$ with the Oldroyd-B model, so the prefactor $b/(b - \mathrm{tr}(\boldsymbol{c}))$ in the FENE-CR constitutive law remains close to one everywhere in the flow (contrary to what happens in the lid-driven cavity case).

2.6 Appendix

A Positivity of a (discretely) transported tensor

The aim of this section is to prove that, with a first-order backward upwind scheme for the transport term, the solution of the transport equation for the conformation tensor (2.21d) remains definite positive, under a constraint for the time-step. We proceed in two steps. We first deal with the homegeneous transport (i.e the sub-problem obtained by setting the reaction terms to zero), then with the pure reaction equation (i.e the sub-problem obtained by setting the convection velocity to zero), and finally merge the arguments to obtain the positivity result for the original equation.

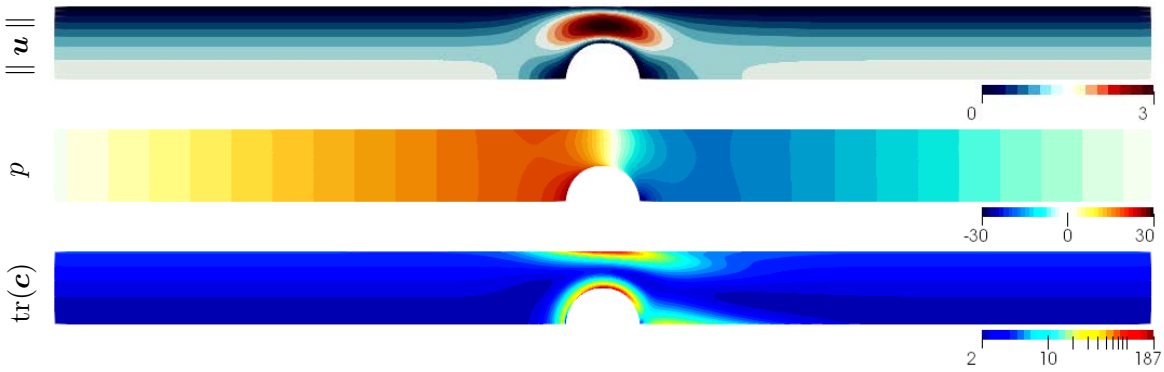

Fig. 2.19 Velocity magnitude, pressure and tr($\boldsymbol{c}$) (in log-scale) fields. Flow past a confined cylinder, Oldroyd-B model, $Wi = 0.7$. Top to Bottom: velocity magnitude, pressure and trace of the conformation tensor (in log-scale).

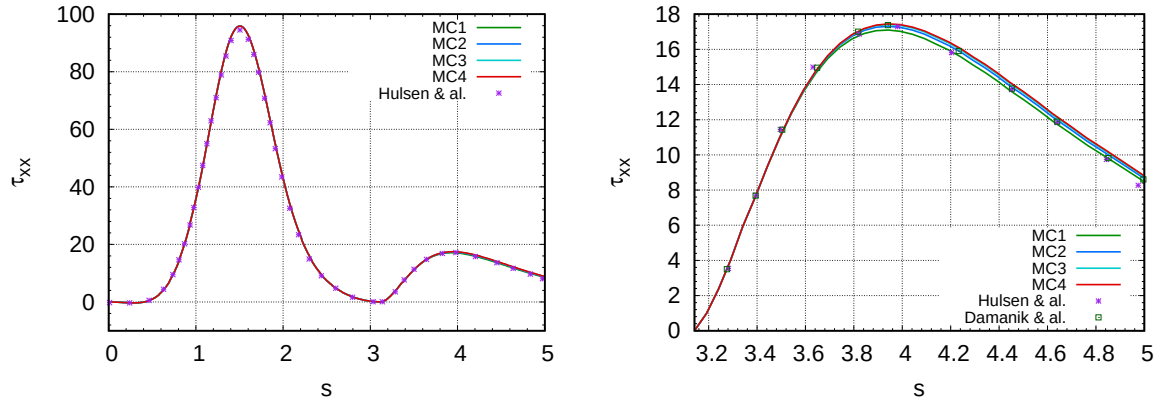

(a) Profile along the curve coordinate (b) Profile zoomed in the wake of the cylinder

Fig. 2.20 Profile of first normal polymer stress τ_{xx} along the curve coordinate s. Flow past a confined cylinder, Oldroyd-B model, $Wi = 0.6$. Left: profile along the cylinder surface and in the wake of the cylinder. Right: the same profile zoomed in the wake of the cylinder.

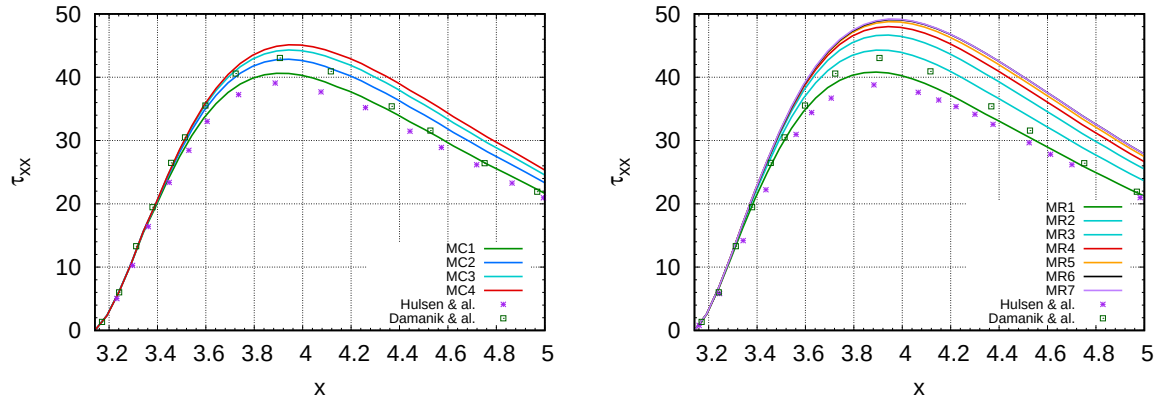

(a) MC-type meshes (b) MR-type meshes

Fig. 2.21 First normal polymer stress τ_{xx} profile zoomed in the wake of the cylinder. Flow past a confined cylinder, Oldroyd-B model, $Wi = 0.7$. Initial meshes (left) and refined meshes (right).

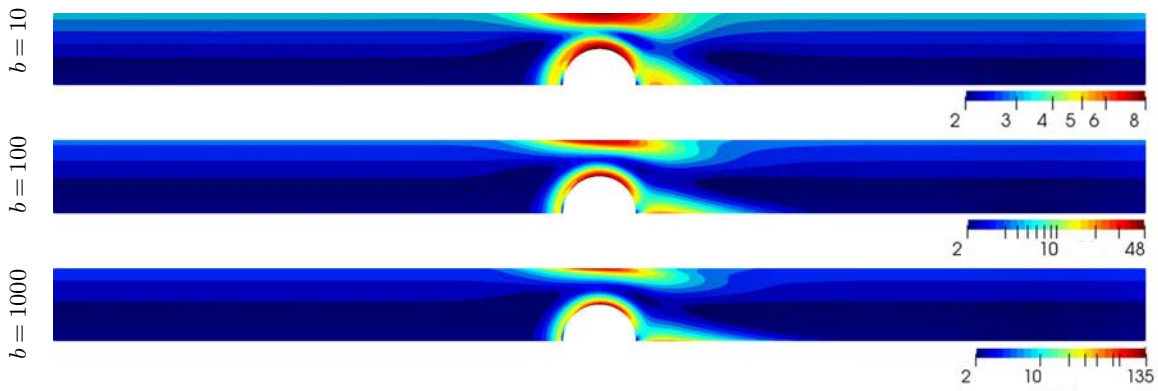

Fig. 2.22 Trace of the conformation tensor normalised by the elongation parameter b (in log-scale). Flow past a confined cylinder, FENE-CR model, $Wi = 0.7$. Top to Bottom: $b = 10$, $b = 100$ and $b = 1000$.

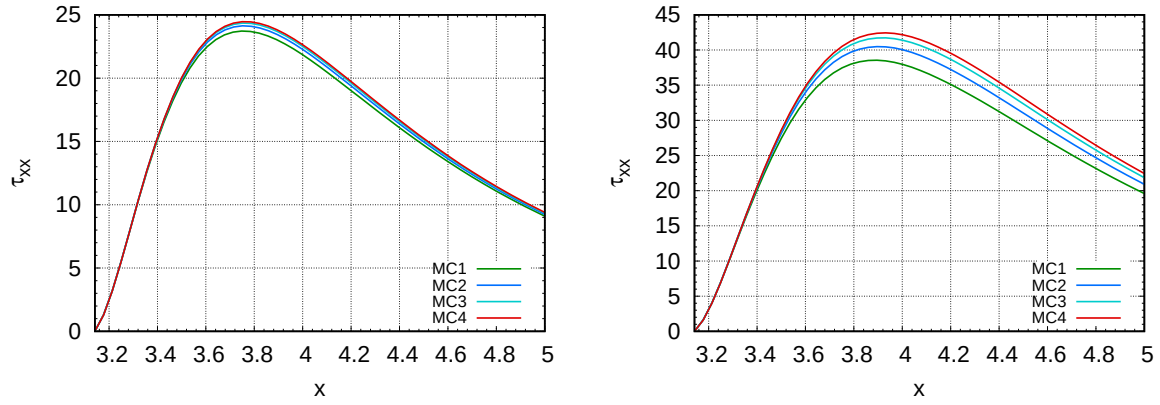

(a) $b = 100$ (b) $b = 1000$

Fig. 2.23 First normal polymer stress τ_{xx} profile zoomed in near wake of the cylinder. Flow past a confined cylinder, FENE-CR model, $Wi = 0.7$. Left: $b = 100$. Right: $b = 1000$. Results obtained with the MC-type meshes.

We suppose that the fraction $\boldsymbol{g}(\boldsymbol{c})/\lambda$ is equal to a constant, which we denote by $1/\lambda$ for short. However, the following arguments only need that $\boldsymbol{g}(\boldsymbol{c})/\lambda$ be a known and non-negative value in each cell of the mesh. Hence, they also hold for the FENE-CR model if the time-discretization is such that the coefficient $\boldsymbol{g}(\boldsymbol{c})/\lambda$ is computed with the beginning-of-step value of $\boldsymbol{c}$, $\boldsymbol{c}^n$, provided that $\mathrm{tr}(\boldsymbol{c}^n)$ is lower than b in any cell of the mesh. This is indeed the case with the scheme used in this paper, at the price of constraints for the time step (see Section B), which will need to be satisfied as the same time as those appearing in this section.

Pure transport We first recall the arguments showing the positivity of the conformation tensor in the continuous setting, before mimicking the proof in the discrete setting.

Let $\boldsymbol{c}(x,t) \in \mathbb{R}^{d\times d}$ be a tensor satisfying

$$\partial_t \boldsymbol{c} + \boldsymbol{u}\cdot\boldsymbol{\nabla}\boldsymbol{c} = 0 \quad \text{i.e } \partial_t c_{i,j} + \boldsymbol{u}\cdot\boldsymbol{\nabla} c_{i,j} = 0 \text{ for } 1 \le i,j \le d, \tag{2.37}$$

with $\boldsymbol{c}(\boldsymbol{x},0)$ positive and definite. The problem is supposed to be posed over a finite domain $\Omega \subset \mathbb{R}^d$ and, for the sake of simplicity, we suppose that $\boldsymbol{u}\cdot\boldsymbol{n}_{\partial\Omega} = 0$ over the whole domain

boundary and that the velocity field $\boldsymbol{u}$ is divergence-free. Let $\boldsymbol{X} \in \mathbb{R}^d$ be a (fixed) vector. Then, for $1 \le i,j \le d$, we have

$$X_i\,X_j\Big[\partial_t c_{i,j} + \boldsymbol{u}\cdot\boldsymbol{\nabla} c_{i,j}\Big] = \partial_t(c_{i,j}\,X_i\,X_j) + \boldsymbol{u}\cdot\boldsymbol{\nabla}(c_{i,j}\,X_i\,X_j) = 0.$$

Summing over the indices i and j yields

$$\partial_t((\boldsymbol{c}\boldsymbol{X},\boldsymbol{X})) + \boldsymbol{u}\cdot\boldsymbol{\nabla}((\boldsymbol{c}\boldsymbol{X},\boldsymbol{X})) = 0.$$

Since the transport equation satifies a maximum principle and that $(\boldsymbol{c}(\boldsymbol{x},0)\boldsymbol{X},\boldsymbol{X}) > 0$ over Ω by assumption on the initial data, we get that $(\boldsymbol{c}(\boldsymbol{x},t)\boldsymbol{X},\boldsymbol{X}) > 0$ over $\Omega\times\mathbb{R}$, i.e that the tensor $\boldsymbol{c}$ remains positive definite at all locations and times. The following lemma states a discrete counterpart to this property.

Lemma 2. *The discretization of (2.37) by the first-order backward-Euler upwind scheme preserves the positivity of the tensor $\boldsymbol{c}$.*

Proof. The discretization of (2.37) by the first-order backward-Euler upwind scheme reads

$$\text{for } 1 \le i,j \le d,\ \forall K \in \mathcal{M},\quad \frac{|K|}{\delta t}\Big((c_{i,j})_K^{n+1} - (c_{i,j})_K^n\Big) + \sum_{\sigma=K|L} |\sigma|\ (c_{i,j})_\sigma^{n+1}\ u_{K,\sigma} = 0,$$

where $u_{K,\sigma}$ is an approximation of $\boldsymbol{u}\cdot\boldsymbol{n}_{K,\sigma}$ such that the following divergence-free constraint is satisfied (remember that $\boldsymbol{u}$ is supposed to be divergence-free):

$$\sum_{\sigma=K|L} |\sigma|\ u_{K,\sigma} = 0. \tag{2.38}$$

and

$$(c_{i,j})_\sigma^{n+1} = (c_{i,j})_K^{n+1} \text{ if } u_{K,\sigma} \ge 0,\ (c_{i,j})_\sigma^{n+1} = (c_{i,j})_L^{n+1} \text{ otherwise.} \tag{2.39}$$

Note that, to simplify notations, we do not associate a time-index to the velocity, but the fact that the velocity depends on time is indifferent in the present proof. Let $\boldsymbol{X} \in \mathbb{R}^d$ be a (fixed) vector. Then, for $K \in \mathcal{M}$ and $1 \le i,j \le d$, we have

$$\frac{|K|}{\delta t}\Big(X_i\,X_j\,(c_{i,j})_K^{n+1} - X_i\,X_j\,(c_{i,j})_K^n\Big) + \sum_{\sigma=K|L} |\sigma|\ X_i\,X_j\,(c_{i,j})_\sigma^{n+1}\ u_{K,\sigma} = 0.$$

Let us define $S_K^n = (\boldsymbol{c}_K^n\boldsymbol{X},\boldsymbol{X})$. Then, summing the previous relation over i and j yields

$$\frac{|K|}{\delta t}(S_K^{n+1} - S_K^n) + \sum_{\sigma=K|L} |\sigma|\ S_\sigma^{n+1}\ u_{K,\sigma} = 0,$$

with, thanks to Definition (2.39), $S_\sigma^{n+1} = S_K^{n+1}$ if $u_{K,\sigma} \ge 0$ and $S_\sigma^{n+1} = S_L^{n+1}$ otherwise. We may see S as an unknown obeying a first-order backward-Euler upwind scheme, which is known to preserve the positivity. For any reasonable initialization, we have $S_K^0 > 0$ for $K \in \mathcal{M}$, so $S_K^n > 0$ for $n > 0$, which means that the discrete tensor $\boldsymbol{c}$ is positive in each cell and at any time. □

Remark 1 (Explicit scheme)**.** *The same result is obtained with a similar proof for the forward Euler scheme, still with a first-order upwind scheme in space.*

Remark 2 (On higher order schemes)**.** *Note that the previous proof relies on the very specific approximation (2.39) of $\boldsymbol{c}$ at the faces, and in particular on the fact that (2.39) deals in the*

same way with every component of the tensor $\boldsymbol{c}$*. This may not be the case for a higher order scheme, and we now give an example showing how things may go wrong with a MUSCL scheme. We suppose that the problem boils down to a one-dimensional problem, and consider a stripe of uniform cells numbered from* -2 *to* 1 *with:*

$$\boldsymbol{c}_{-2}^n = \begin{bmatrix} 1/2 & 1-\varepsilon \\ 1-\varepsilon & 3 \end{bmatrix}, \quad \boldsymbol{c}_{-1}^n = \begin{bmatrix} 1/2 & 1-\varepsilon \\ 1-\varepsilon & 2 \end{bmatrix},$$
$$\boldsymbol{c}_{0}^n = \begin{bmatrix} 1 & 1-\varepsilon \\ 1-\varepsilon & 1 \end{bmatrix}, \quad \boldsymbol{c}_{1}^n = \begin{bmatrix} 2 & 1-\varepsilon \\ 1-\varepsilon & 1/2 \end{bmatrix},$$

with $0 < \varepsilon < 1$*, so* $\boldsymbol{c}$ *is positive in all cells (both its trace, i.e the sum of the eigenvalues, and its determinent, i.e the product of its eigenvalues, are positive). Let us suppose that the (first component of the) velocity is positive. Using a ultra-bee limiter, we get:*

$$\boldsymbol{c}_{-1/2}^n = \begin{bmatrix} 1/2 & 1-\varepsilon \\ 1-\varepsilon & 3/2 \end{bmatrix}, \quad \boldsymbol{c}_{1/2}^n = \begin{bmatrix} 3/2 & 1-\varepsilon \\ 1-\varepsilon & 3/4 \end{bmatrix},$$

where $\boldsymbol{c}_{-1/2}^n$ *and* $\boldsymbol{c}_{1/2}^n$ *stand for the approximation of* $\boldsymbol{c}$ *at the face separating the cells* -1 *and* 0 *and the cells* 0 *and* 1 *respectively. Note that these values all correspond to centered choices except* $(c_{1,1})_{-1/2}^n$ *which is taken at its upwind value since* $c_{1,1}$ *presents an extremum in cell* -1*. Then, with a forward ultra-bee scheme, we get:*

$$(c_{1,1})_0^{n+1} = 1-\nu, \quad (c_{2,2})_0^{n+1} = 1+\frac{3}{4}\nu,$$

with ν *the cfl number; the other components of* $\boldsymbol{c}$ *remain constant. Hence, for any cfl number in* $(0,1)$*, taking a sufficiently small* ε *yields a negative determinent for* $\boldsymbol{c}_0^{n+1}$*.*

Remark 3. *In the case with the change of variable to the log-conformation tensor, taking the exponential after the advection step allows to automatically ensure the positivity of* $\boldsymbol{c}$*.*

The pure reaction problem With the implicit variant, the ODE step for the conformation tensor can be written in each cell, dropping for short the cell index,

$$\frac{1}{\delta t}\,(\boldsymbol{c}^{n+1} - \boldsymbol{c}^n) = \boldsymbol{\nabla u}\;\boldsymbol{c}^{n+1} + (\boldsymbol{c}^{n+1})^t(\boldsymbol{\nabla u})^t - \frac{1}{\lambda}(\boldsymbol{c}^{n+1} - \boldsymbol{I}_d). \tag{2.40}$$

Note that, in the second term on the right-hand side, we have replaced $\boldsymbol{c}^{n+1}$ by $(\boldsymbol{c}^{n+1})^t$. This is justified by the fact that, provided that $\boldsymbol{c}^n$ is symmetrical, any solution of (2.40) is also symmetrical and thus satisfies the initial equation. Equation (2.40) is a linear system for the components of $\boldsymbol{c}^{n+1}$ which is regular for δt small enough. For instance, the condition

$$\frac{1}{\delta t} + \frac{1}{\lambda} > 2\,\max_{1\le i\le d}\sum_{j=1}^{d}|(\boldsymbol{\nabla} u)_{i,j})| \tag{2.41}$$

ensures that the diagonal of the matrix of this system is strictly dominant. The following lemma states that the scheme (2.40) preserves the definite positivity of the unknown.

Lemma 3. *Let us suppose that the time step is such that Condition* (2.41) *is satisfied, and that* $\boldsymbol{c}^n$ *is a symmetric positive definite tensor. Then so is* $\boldsymbol{c}^{n+1}$*.*

Proof. Let $\alpha \mapsto \boldsymbol{c}(\alpha)$, $[0,1] \to \mathbb{R}^{d\times d}$ be the function defined by taking $\boldsymbol{c}(\alpha)$ as the solution to Equation (2.40) with $\alpha\,\delta t$ instead of δt:

$$\frac{1}{\delta t}\,(\boldsymbol{c}(\alpha)-\boldsymbol{c}^n) = \alpha\Big[\boldsymbol{\nabla u}\;\boldsymbol{c}(\alpha)+\boldsymbol{c}(\alpha)^t(\boldsymbol{\nabla u})^t-\frac{1}{\lambda}(\boldsymbol{c}(\alpha)-\boldsymbol{I}_d)\Big]. \tag{2.42}$$

Since, thanks to Condition (2.41), $\boldsymbol{c}(\alpha)$ is the solution to a regular linear system, the function $\boldsymbol{c}(\alpha)$ is regular. In addition, $\boldsymbol{c}(0)=\boldsymbol{c}^n$ is a symmetric positive definite tensor. Let us suppose that $\boldsymbol{c}(\alpha)$ is not definite positive for some $\alpha\in[0,1]$, which means that one at least of its eigenvalues is non-positive. Then, by continuity of $\alpha\mapsto \min(\text{eigenvalues of } \boldsymbol{c}(\alpha))$, there exists $\alpha_0\in(0,1]$ such that $\boldsymbol{c}(\alpha_0)$ has a zero eigenvalue. Let $\boldsymbol{X}\in\mathbb{R}^d$ be a unit eigenvector associated with this zero eigenvalue. We have, by Equation (2.42),

$$\begin{aligned}-\frac{1}{\delta t}\,(\boldsymbol{c}^n\boldsymbol{X},\boldsymbol{X}) &= \alpha_0\Big[(\boldsymbol{\nabla u}\;\boldsymbol{c}(\alpha_0)\boldsymbol{X},\boldsymbol{X})+(\boldsymbol{c}(\alpha_0)^t(\boldsymbol{\nabla u})^t\boldsymbol{X},\boldsymbol{X})+\frac{1}{\lambda}\Big]\\ &= \alpha_0(2\;(\boldsymbol{\nabla u}\;\boldsymbol{c}(\alpha_0)\boldsymbol{X},\boldsymbol{X})+\frac{1}{\lambda}) = \frac{\alpha_0}{\lambda},\end{aligned}$$

which raises a contradiction since, by assumption, $(\boldsymbol{c}^n\boldsymbol{X},\boldsymbol{X})>0$. □

The complete transport-reaction equation Let us now consider the complete transport equation for the conformation tensor:

$$\forall K\in\mathcal{M},\quad \frac{1}{\delta t}\Big(\boldsymbol{c}_K^{n+1}-\boldsymbol{c}_K^n\Big)+\frac{1}{|K|}\sum_{\sigma=K|L}|\sigma|\;\boldsymbol{c}_\sigma^{n+1}\;u_{K,\sigma}=\boldsymbol{\nabla u}_K\;\boldsymbol{c}_K^{n+1}+(\boldsymbol{c}_K^{n+1})^t(\boldsymbol{\nabla u}_K)^t-\frac{1}{\lambda}(\boldsymbol{c}_K^{n+1}-\boldsymbol{I}_d), \tag{2.43}$$

where the velocity field is supposed to be discretely divergence-free (i.e satisfies Equations (2.38)) and the conformation tensor value at the face σ, $\boldsymbol{c}_\sigma^{n+1}$, is given by the first-order backward upwind choice (2.39). We introduce the following set of constraints for the time step:

$$\forall K\in\mathcal{M},\qquad \frac{1}{\delta t}+\frac{1}{\lambda}>2\;\max_{1\le i\le d}\sum_{j=1}^{d}|(\boldsymbol{\nabla u}_K)_{i,j})|. \tag{2.44}$$

We are now in position to state the following result.

Lemma 4. *Let the time step be such that Equations (2.44) are verified, and let us assume that, for $K\in\mathcal{M}$, $\boldsymbol{c}_K^n$ is a symmetric positive definite tensor. Then the linear System (2.43) is uniquely solvable and, for $K\in\mathcal{M}$, the tensor $\boldsymbol{c}_K^{n+1}$ solution of (2.43) is symmetric positive definite.*

Proof. The proof of this result is obtained by combining the arguments of the two previous sections. First, for each cell K, the upwind choice (2.39) implies that the convection operator produces, in the system for the tensor components associated with K, an additional non-negative term on the diagonal and non-positive off-diagonal additional entries. Moreover, thanks to Relation (2.38), the diagonal additional term is equal to the sum of the off-diagonal ones. Inequality (2.44) thus still implies that the diagonal of the matrix of this system is dominent.

Then, as in Section A, let us multiply the right-hand side of (2.43) by $\alpha\in[0,1]$; we easily check that the obtained system is still uniquely solvable, and denote by $(\boldsymbol{c}_K^\alpha)_{K\in\mathcal{M}}$ its solution. By Section A, we know that, for $\alpha=0$, $\boldsymbol{c}_K^\alpha$ is symmetric definite positive, for any $K\in\mathcal{M}$. If, for $\alpha=1$, $\boldsymbol{c}_K^\alpha$ is not definite positive in at least one cell, by continuity, there exists $\alpha_0\in(0,1]$ and $K_0\in\mathcal{M}$ such that $\boldsymbol{c}_L^{\alpha_0}$ is non-negative in all cells $L\in\mathcal{M}$ and $\boldsymbol{c}_{K_0}^{\alpha_0}$ has a zero eigenvalue.

Let $\boldsymbol{X} \in \mathbb{R}^d$ be a unit eigenvector associated with this zero eigenvalue. We have, by the same computations as in Sections A and A,

$$-\frac{1}{\delta t}\ (\boldsymbol{c}_{K_0}^n \boldsymbol{X}, \boldsymbol{X}) + \frac{1}{|K|} \sum_{\sigma \in \mathcal{E}(K_0)} |\sigma|\ (\boldsymbol{c}_\sigma^{\alpha_0} \boldsymbol{X}, \boldsymbol{X})\ u_{K,\sigma} = \frac{\alpha_0}{\lambda},$$

and, since $\boldsymbol{c}_{K_0}^n$ is definite positive, $(\boldsymbol{c}_{K_0}^{\alpha_0} \boldsymbol{X}, \boldsymbol{X}) = 0$ and $(\boldsymbol{c}_L^{\alpha_0} \boldsymbol{X}, \boldsymbol{X}) \geq 0$ for $L \in \mathcal{M}$, we easily check that the upwind choice for $\boldsymbol{c}_\sigma^{\alpha_0}$ implies that the left-hand side is negative, which raises a contradiction. □

B Stability of the ODE step for the FENE-CR model

We study in this section the stability of the following semi-implicit scheme for the ODE step, for the FENE-CR model:

$$\frac{1}{\delta t}\ (\boldsymbol{c}^{n+1} - \boldsymbol{c}^n) = \boldsymbol{\nabla u}\ \boldsymbol{c}^{n+1} + (\boldsymbol{c}^{n+1})^t (\boldsymbol{\nabla u})^t - \frac{b}{\lambda\,(b - \mathrm{tr}(\boldsymbol{c}^n))}\,(\boldsymbol{c}^{n+1} - \boldsymbol{I}_d), \tag{2.45}$$

where b is a real number strictly greater than the space dimension d. From Section A, we easily deduce that, provided that $\boldsymbol{c}^n$ is a symmetric definite positive tensor such that $\mathrm{tr}(\boldsymbol{c}^n) < b$, then $\boldsymbol{c}^{n+1}$ is also symmetric definite positive, under the stability constraint for the time step:

$$\frac{1}{\delta t} > 2\ \max_{1 \leq i \leq d} \sum_{j=1}^{d} |(\boldsymbol{\nabla} u)_{i,j})|. \tag{2.46}$$

We search for an upper bound for δt that ensures that $\mathrm{tr}(\boldsymbol{c}^{n+1}) < b$. To this purpose, we will use the following lemma.

Lemma 5. *Let $\boldsymbol{A}$ be a symmetric positive $d \times d$ matrix of entries $(A_{i,j})_{1 \leq i,j \leq d}$. Then:*

$$||\boldsymbol{A}||_{L^1} = \sum_{i,j=1}^{d} |A_{i,j}| \leq d\ \mathrm{tr}(\boldsymbol{A}).$$

Proof. Let $\mathrm{sgn}(\boldsymbol{A})$ be the matrix of entries $(\mathrm{sgn}(A_{i,j}))_{1 \leq i,j \leq d}$. Then $||\boldsymbol{A}||_{L^1} = \boldsymbol{A} : \mathrm{sgn}(\boldsymbol{A})$. In addition, $\mathrm{sgn}(\boldsymbol{A})$ is a symmetric diagonalizable matrix and its eigenvalues α_i, $1 \leq i \leq d$, satisfy

$$|\alpha_i| \leq \max_{\boldsymbol{X} \in \mathbb{R}^d} \frac{\mathrm{sgn}(\boldsymbol{A})\boldsymbol{X} \cdot \boldsymbol{X}}{||\boldsymbol{X}||^2}.$$

We have, since the entries of $\mathrm{sgn}(\boldsymbol{A})$ are either 1 or -1,

$$|\mathrm{sgn}(\boldsymbol{A})\boldsymbol{X} \cdot \boldsymbol{X}| = \Big|\sum_{i=1}^{d} X_i \sum_{j=1}^{d} \mathrm{sgn}(A_{i,j})\ X_j\Big| \leq \sum_{i,j=1}^{d} |X_i\, X_j| \leq \frac{1}{2} \sum_{i,j=1}^{d} (X_i^2 + X_j^2) = d\ ||\boldsymbol{X}||^2.$$

Thus $|\alpha_i| \leq d$, for $1 \leq i \leq d$. Since $\boldsymbol{A}$ is symmetric and positive, all its eigenvalues are non-negative and the results follows from the matrix Ky Fan inequality:

$$\boldsymbol{A} : \mathrm{sgn}(\boldsymbol{A}) \leq \Gamma(\boldsymbol{A}) \cdot \Gamma\big(\mathrm{sgn}(\boldsymbol{A})\big),$$

where, for a symmetric matrix $\boldsymbol{B}$, $\Gamma(\boldsymbol{B})$ stands for the vector obtained from the ordered set of the eigenvalues of $\boldsymbol{B}$. □

Taking the trace of Equation (2.45), we get

$$\frac{1}{\delta t}\,\left(\mathrm{tr}(\boldsymbol{c}^{n+1})-\mathrm{tr}(\boldsymbol{c}^{n})\right)=2\;\boldsymbol{\nabla u}:\boldsymbol{c}^{n+1}-\frac{b}{\lambda\left(b-\mathrm{tr}(\boldsymbol{c}^{n})\right)}\left(\mathrm{tr}(\boldsymbol{c}^{n+1})-d\right).$$

Under the constraint (2.46) for the time-step, the linear System (2.45) for $\boldsymbol{c}^{n+1}$ is regular. Thus, by continuity, since $\mathrm{tr}(\boldsymbol{c}^{n})<b$, $\mathrm{tr}(\boldsymbol{c}^{n+1})<b$ for δt small enough. Let us suppose that there exists some values of the time step satisfying (2.46) and such that $\mathrm{tr}(\boldsymbol{c}^{n+1})\geq b$; still by continuity, we may define δt_0 as the smallest time step such that $\mathrm{tr}(\boldsymbol{c}^{n+1})=b$, which yields:

$$\frac{1}{\delta t_0}\,\left(b-\mathrm{tr}(\boldsymbol{c}^{n})\right)=2\;\boldsymbol{\nabla u}:\boldsymbol{c}^{n+1}-\frac{b}{\lambda\left(b-\mathrm{tr}(\boldsymbol{c}^{n})\right)}\left(b-d\right).$$

We thus have

$$\frac{1}{\delta t_0}\,\left(b-\mathrm{tr}(\boldsymbol{c}^{n})\right)+\frac{b\,(b-d)}{\lambda\left(b-\mathrm{tr}(\boldsymbol{c}^{n})\right)}\leq 2\;||\boldsymbol{\nabla u}||_{L^\infty}\;||\boldsymbol{c}^{n+1}||_{L^1},$$

so, thanks to Lemma 5,

$$\frac{1}{\delta t_0}\,\left(b-\mathrm{tr}(\boldsymbol{c}^{n})\right)+\frac{b\,(b-d)}{\lambda\left(b-\mathrm{tr}(\boldsymbol{c}^{n})\right)}\leq 2\,d\;||\boldsymbol{\nabla u}||_{L^\infty}\;\mathrm{tr}(\boldsymbol{c}^{n+1})=2\,d\,b\;||\boldsymbol{\nabla u}||_{L^\infty}. \tag{2.47}$$

We observe that the two terms at the left-hand side are positive. This inequality is thus impossible, and we have $\mathrm{tr}(\boldsymbol{c}^{n+1})<b$ for any value of the time step, if

$$\frac{b-d}{2\,d\,\lambda\left(b-\mathrm{tr}(\boldsymbol{c}^{n})\right)}>||\boldsymbol{\nabla u}||_{L^\infty}. \tag{2.48}$$

Let us suppose that this condition is not satisfied. Inequality (2.47) also yields:

$$\frac{1}{\delta t_0}\,\left(b-\mathrm{tr}(\boldsymbol{c}^{n})\right)\leq 2\,d\,b\;||\boldsymbol{\nabla u}||_{L^\infty},$$

which, by contradiction, shows that $\mathrm{tr}(\boldsymbol{c}^{n+1})<b$ provided that

$$\delta t<\frac{b-\mathrm{tr}(\boldsymbol{c}^{n})}{2\,d\,b\;||\boldsymbol{\nabla u}||_{L^\infty}}. \tag{2.49}$$

Finally, keeping all the terms of the left-hand side of (2.47), the same argument yields that $\mathrm{tr}(\boldsymbol{c}^{n+1})<b$ if

$$\delta t<\frac{b-\mathrm{tr}(\boldsymbol{c}^{n})}{2\,d\,b\;||\boldsymbol{\nabla u}||_{L^\infty}-\dfrac{b\,(b-d)}{\lambda\left(b-\mathrm{tr}(\boldsymbol{c}^{n})\right)}}.$$

The right-hand side may be seen as a function of the quantity $b-\mathrm{tr}(\boldsymbol{c}^{n})$ defined on the part of $\mathbb{R}$ where the denominator is positive, and which takes a minimum value. This latter thus gives an upper bound for δt which is independent of $\boldsymbol{c}^{n}$ and reads:

$$\delta t<\frac{b-d}{d^2\,b\,\lambda\;||\boldsymbol{\nabla u}||_{L^\infty}^2}. \tag{2.50}$$

Summing up the developments of this section, we get the following result.

Lemma 6. *Let δt satisfy (2.46), and $\boldsymbol{c}^{n}$ be a symmetric definite positive tensor such that $\mathrm{tr}(\boldsymbol{c}^{n})<b$. Then System (2.45) has a unique solution $\boldsymbol{c}^{n+1}$, which is a symmetric definite*

positive tensor. If, in addition, one of the inequalities (2.48), (2.49) *or* (2.50) *is satisfied, then* $\mathrm{tr}(\boldsymbol{c}^{n+1}) < b$.

C A stability property of the upwind convection of tensors

Let $\boldsymbol{c} \in \mathbb{R}^{d\times d}$, $\boldsymbol{u}$ be a divergence-free regular velocity field and let $\mathcal{F}: \mathbb{R}^{d\times d} \to \mathbb{R}$ be a regular function. Then, we have

$$(\mathcal{F}'(\boldsymbol{c}), \partial_t \boldsymbol{c} + \mathrm{div}(\boldsymbol{u}\,\boldsymbol{c})) = \partial_t \mathcal{F}(\boldsymbol{c}) + \mathrm{div}(\boldsymbol{u}\,\mathcal{F}(\boldsymbol{c})).$$

The aim of this section is to state and prove a discrete analogue of this relation with an implicit upwind discretization of the convection operator. This result turns out to be an inequality and holds only when the function $\mathcal{F}$ is convex, as stated in Lemma 7 below. A similar result for a scalar unknown is an easy consequence of [32, Lemma A2]. The specialization of Lemma 7 to the function of interest in the stability analysis of the scheme, namely $\boldsymbol{c} \mapsto -\mathrm{tr}(\ln \boldsymbol{c})$, is used and proved in [14].

Lemma 7. *Let* $\mathcal{C}$ *be an open convex subset of* $\mathbb{R}^{d\times d}$, *and let* $\mathcal{F}$ *a convex differentiable function from* $\mathcal{C}$ *to* $\mathbb{R}$. *Let* $\boldsymbol{c}$ *and* $\boldsymbol{c}^\star$ *be two elements of* $\mathcal{C}$, α *a positive real number and* $(u_\sigma)_{\sigma\in\mathcal{E}}$ *a family of real numbers (*$\mathcal{E}$ *is a finite set of indexes) satisfying*

$$\sum_{\sigma\in\mathcal{E}} u_\sigma = 0. \tag{2.51}$$

For $\sigma \in \mathcal{E}$, *let* $\boldsymbol{c}_\sigma \in \mathcal{C}$ *and let us suppose that* $\boldsymbol{c}_\sigma = \boldsymbol{c}$ *if* $u_\sigma \geq 0$. *Then*

$$(\mathcal{F}'(\boldsymbol{c}),\ \alpha(\boldsymbol{c}-\boldsymbol{c}^\star) + \sum_{\sigma\in\mathcal{E}} u_\sigma \boldsymbol{c}_\sigma) \geq \alpha(\mathcal{F}(\boldsymbol{c}) - \mathcal{F}(\boldsymbol{c}^\star)) + \sum_{\sigma\in\mathcal{E}} u_\sigma \mathcal{F}(\boldsymbol{c}_\sigma).$$

Proof. Let us write $(\mathcal{F}'(\boldsymbol{c}),\ \alpha(\boldsymbol{c}-\boldsymbol{c}^\star) + \sum_{\sigma\in\mathcal{E}} u_\sigma \boldsymbol{c}_\sigma) = T_{\partial/\partial_t} + T_{\mathrm{div}}$ with

$$T_{\partial/\partial_t} = (\mathcal{F}'(\boldsymbol{c}),\ \alpha(\boldsymbol{c}-\boldsymbol{c}^\star)) \quad \text{and} \quad T_{\mathrm{div}} = (\mathcal{F}'(\boldsymbol{c}),\ \sum_{\sigma\in\mathcal{E}} u_\sigma \boldsymbol{c}_\sigma).$$

By convexity of the function $\mathcal{F}$, we have $T_{\partial/\partial_t} \geq \alpha(\mathcal{F}(\boldsymbol{c}) - \mathcal{F}(\boldsymbol{c}^\star))$. In addition, thanks to the equality (2.51), we may recast T_{div} as

$$T_{\mathrm{div}} = \sum_{\sigma\in\mathcal{E}} u_\sigma \mathcal{F}(\boldsymbol{c}_\sigma) + \sum_{\sigma\in\mathcal{E}} u_\sigma\, R_\sigma \quad \text{with } R_\sigma = (\mathcal{F}'(\boldsymbol{c}),\ \boldsymbol{c}_\sigma - \boldsymbol{c}) + \mathcal{F}(\boldsymbol{c}) - \mathcal{F}(\boldsymbol{c}_\sigma).$$

By convexity of $\mathcal{F}$, $R_\sigma \leq 0$. In addition, when $u_\sigma \geq 0$, we have $\boldsymbol{c}_\sigma = \boldsymbol{c}$ (by assumption) and R_σ vanishes. The product $u_\sigma R_\sigma$ is thus non-negative, which concludes the proof. □

Let us now apply this lemma to provide the argument requested in Section 2.3.2 for the stability of the scheme, i.e a discrete analogue of Relation (2.19). First, we recall the following classical results for functions of tensors [15].

Lemma 8. *Let* $\mathcal{F}$ *be the function* $\mathbb{S}^*_+(\mathbb{R}^{d\times d}) \to \mathbb{R}$ *defined by* $\boldsymbol{c} \mapsto -\ln\det(\boldsymbol{c})$. *Then* $\mathcal{F}$ *is convex, regular and its first derivative is*

$$(\mathcal{F}'(\boldsymbol{c}), \boldsymbol{d}) = -\mathrm{tr}(\boldsymbol{c}^{-1}\ \boldsymbol{d}), \qquad \forall \boldsymbol{d} \in \mathbb{S}^*_+(\mathbb{R}^{d\times d}).$$

In addition, for any $\boldsymbol{c} \in \mathbb{S}^*_+(\mathbb{R}^{d\times d})$, $\mathrm{tr}(\ln \boldsymbol{c}) = \ln\det(\boldsymbol{c})$.

Proof. The proof is equivalent to show that, $\forall \boldsymbol{a},\boldsymbol{b} \in \mathbb{S}^*_+(\mathbb{R}^{d\times d})$, the function $g:(0,1)\to\mathbb{R}$ defined by $g(t)=\ln\det(\boldsymbol{a}+t\,\boldsymbol{b})$ is concave. Let us denote by $\boldsymbol{a}^{\frac{1}{2}} \in \mathbb{S}^*_+(\mathbb{R}^{d\times d})$ the square root of $\boldsymbol{a}$, so $\boldsymbol{a}=\boldsymbol{a}^{\frac{1}{2}}\,\boldsymbol{a}^{\frac{1}{2}}$. We introduce $\hat{\boldsymbol{b}}=\boldsymbol{a}^{-\frac{1}{2}}\,\boldsymbol{b}\,\boldsymbol{a}^{-\frac{1}{2}}$. By definition, $\hat{\boldsymbol{b}}\in\mathbb{S}^*_+(\mathbb{R}^{d\times d})$ and may be decomposed as $\hat{\boldsymbol{b}}=\boldsymbol{q}\,\boldsymbol{\lambda}\,\boldsymbol{q}^t$ with $\boldsymbol{q}\,\boldsymbol{q}^t=\boldsymbol{q}^t\,\boldsymbol{q}=\boldsymbol{I}_d$, $\det(\boldsymbol{q})=1$, $\boldsymbol{\lambda}=\mathrm{diag}\{\lambda_i\}_{i=1,\dots,d}$ and $\mathrm{tr}(\boldsymbol{\lambda})=\mathrm{tr}(\hat{\boldsymbol{b}})$. Then we have :

$$
\begin{aligned}
g(t) &= \ln\det\left(\boldsymbol{a}+t\,\boldsymbol{b}\right)=\ln\det\big(\boldsymbol{a}^{\frac{1}{2}}(\boldsymbol{I}_d+t\,\hat{\boldsymbol{b}})\boldsymbol{a}^{\frac{1}{2}}\big)=\ln\det(\boldsymbol{I}_d+t\,\hat{\boldsymbol{b}})+\ln\det(\boldsymbol{a})\\
&=\ln\det\big(\boldsymbol{q}\,(\boldsymbol{I}_d+t\,\boldsymbol{\lambda})\,\boldsymbol{q}^t\big)+\ln\det(\boldsymbol{a})=\ln\det(\boldsymbol{I}_d+t\,\boldsymbol{\lambda})+\ln\det(\boldsymbol{a})=\sum_{i=1}^{d}\ln(1+\lambda_i)+\ln\det(\boldsymbol{a}).
\end{aligned}
$$

Taking the first derivative of this function, we get

$$
\big(\mathcal{F}'(\boldsymbol{a}),\boldsymbol{b}\big)=g'(0)=\mathrm{tr}(\boldsymbol{\lambda})=\mathrm{tr}(\hat{\boldsymbol{b}})=\mathrm{tr}(\boldsymbol{a}^{-\frac{1}{2}}\,\boldsymbol{b}\,\boldsymbol{a}^{-\frac{1}{2}})=\mathrm{tr}(\boldsymbol{a}^{-1}\boldsymbol{b}).
$$

In addition,

$$
g''(t)=-\sum_{i=1}^{d}\frac{\lambda_i^2}{(1+t\lambda_i)^2}<0.
$$

So g is concave and this concludes the proof. □

Returning to the scheme for the transport of $\boldsymbol{c}$, the application of Lemma 7 to the function $\mathcal{F}(\boldsymbol{c})=-\mathrm{tr}(\ln\boldsymbol{c})$ readily yields

$$
\begin{aligned}
\forall K\in\mathcal{M},\qquad \mathrm{tr}\Big((\boldsymbol{c}^{n+1})^{-1}\big(\frac{|K|}{\delta t}\,(\boldsymbol{c}_K^{n+1}-\boldsymbol{c}_K^{n})+\mathrm{div}_K(\boldsymbol{u}^n\boldsymbol{c}^{n+1})\big)\Big)\leq\\
\frac{|K|}{\delta t}\,\big(\mathrm{tr}(\ln\boldsymbol{c}_K^{n+1})-\mathrm{tr}\big(\ln\boldsymbol{c}_K^{n}\big)\big)+\mathrm{div}_K(\boldsymbol{u}^n\mathrm{tr}(\ln\boldsymbol{c}^{n+1})).
\end{aligned}
$$

This is the identity needed to prove the stability of the scheme.

D A scalar model problem

We consider the following model problem on $I\times(0,T)$, with $I=(-1,1)$,

$$
\partial_t c+\partial_x c=a(x)\,c \text{ on } I\times(0,T),\quad c(x,0)=1 \text{ for } x\in I,\quad c(-1,t)=c_L \text{ for } t\in(0,T). \tag{2.52}
$$

Since the inlet condition c_L is constant, the solution of this problem is stationary for $t\geq 2$. The form of the source term $a(x)\,c$ is chosen to mimick the production term $(\boldsymbol{\nabla u})\,\boldsymbol{c}+\boldsymbol{c}(\boldsymbol{\nabla u})^t$ involved in the transport equation of the conformation tensor. In addition, we are interested here in the situation where $a(x)$ takes locally large values, so as to simulate zones of high elongation in a viscoelastic flows. Our understanding of viscoelastic flows is that the stiffness of this right-hand side is actually the origin of the so-called High Weissenberg Problem, i.e the difficulty for numerical schemes to accurately capture (or, worse, not to blow up) for moderate-to-high the Weissenberg numbers. Finally, even if it is probably not essential, we chose $a(x)$ in such a way that $c(1,t)=c_L$ which, to some extent, may be considered to represent what happens along a closed streamline in a viscoelastic flow. The chosen source term $a(x)$ and the corresponding

stationary solution $c_s(x)$ are

$$a(x)=\begin{cases}0 & -1\ \le x<-x_0,\\ -\beta\sin(\dfrac{\pi}{x_0}x) & -x_0\le x\le x_0,\\ 0 & x_0<x\le 1.\end{cases}\qquad c_s(x)=\begin{cases}c_L & -1\ \le x<-x_0,\\ c_L\exp\Big(\beta\dfrac{x_0}{\pi}(1+\cos(\dfrac{\pi}{x_0}x))\Big) & -x_0\le x\le x_0,\\ c_L & x_0<x\le 1.\end{cases}$$

where β and $x_0<1$ are given parameters. The stationary solution is obtained for $t>2$. The problem may be made stiffer when decreasing x_0 and increasing β.

Let us consider a uniform partition $0=t^0<t^1<\cdots<t^N=T$ of the time interval $(0,T)$, and let $\delta t=t^{n+1}-t^n$ for $0\le n\le N-1$ be the constant time step. Let us also consider the uniform partition $-1=x_0<x_1<\cdots<x_K=1$ of the space interval I with $h=x_{k+1}-x_k$ for $0\le k\le K-1$ the constant space step. The solution of (2.52) is approximated by piecewise constant unknowns $c^n_{k+\frac12}$, for $0\le k\le K-1$ and $0\le n\le N$, where $c^n_{k+\frac12}$ is an approximation of the mean value of $c(x,t^n)$ over (x_k,x_{k+1}). The scheme is initialized by

$$c^0_{k+\frac12}=1,\quad \text{for } 0\le k\le K-1.$$

Then the unknowns are updated in time by a second order in time operator-splitting technique, which reads, in a semi-discrete setting

Advection I – Solve for $c^{n+\frac13}$:

$$\partial_t c+\partial_x c=0 \text{ on } I\times(t^n,t^n+\frac{\delta t}{2}),\qquad c(x,t^n)=c^n \text{ for } x\in I. \tag{2.53a}$$

ODE – Set $c_{k+\frac12}(t_n)=c^{n+\frac13}_{k+\frac12}$ and solve for $c^{n+\frac23}_{k+\frac12}=c_{k+\frac12}(t_n+\delta t)$:

$$\partial_t c_{k+\frac12}(t)=a_{k+\frac12}\ c_{k+\frac12}(t),\quad \text{for } 0\le k\le K-1. \tag{2.53b}$$

Advection II – Solve for c^{n+1}:

$$\partial_t c+\partial_x c=0 \text{ on } I\times(t^n+\frac{\delta t}{2},t^{n+1}),\qquad c(x,t^n+\frac{\delta t}{2})=c^{n+\frac23} \text{ for } x\in I. \tag{2.53c}$$

In the *ODE* step, the real number $a_{k+\frac12}$ is defined as the mean value of $a(x)$ over (x_k,x_{k+1}). This step is solved quasi-exactly by

$$c^{n+\frac23}_{k+\frac12}=c^{n+\frac13}_{k+\frac12}\ \exp(a_{k+\frac12}\ \delta t).$$

We test four different ways of solving the advection steps:

(i) The usual implicit first order upwind scheme

$$c^{n+1}_{k+\frac12}=c^n_{k+\frac12}-\frac{\delta t}{h}\ (c^{n+1}_{k+\frac12}-c^{n+1}_k),\qquad \text{for } 0\le k\le K-1,$$

where c^{n+1}_k stands for $c^{n+1}_{k-\frac12}$ for $k\ge 1$ and $c^{n+1}_0=c_L$.

(ii) The same upwind scheme applied to the following logarithmic formulation of the transport equation (easily obtained by multiplication of Equation (2.52) by $1/c$)

$$\log(c^{n+1}_{k+\frac12})=\log(c^n_{k+\frac12})-\frac{\delta t}{h}\ (\log(c^{n+1}_{k+\frac12})-\log(c^{n+1}_k)),\qquad \text{for } 0\le k\le K-1.$$

(iii) An explicit MUSCL-type scheme which reads

$$c_{k+\frac{1}{2}}^{n+1} = c_{k+\frac{1}{2}}^{n} - \frac{\delta t}{h}\ (c_{k+1}^{n} - c_{k}^{n}), \qquad \text{for } 0 \leq k \leq K-1,$$

where c_{k+1}^{n}, the approximation of the unknown at x_{k+1}^{n}, is defined, for $1 \leq k \leq K-2$ by

$$c_{k+1}^{n} - c_{k+\frac{1}{2}}^{n} = \text{minmod}\big((c_{k+\frac{3}{2}}^{n} - c_{k+\frac{1}{2}}^{n})/2,\ c_{k+\frac{1}{2}}^{n} - c_{k-\frac{1}{2}}^{n}\big),$$

with the usual definition of the minmod function, namely, for any pair of real numbers (a,b), $\text{minmod}(a,b) = \text{sgn}(a,b)\ \min(|a|,|b|)$, $\text{sgn}(a,b)$ being equal to the sign of a and b if a and b have the same sign and 0 otherwise. The definition of the face approximations for $k=0$, $k=1$ and $k=K$ is the same as for the upwind scheme (which, in fact, does not matter in the application case below, since the solution is almost constant near the beginning and end of the interval I).

(iv) The same MUSCL-type scheme applied to the logarithmic formulation of choice (ii).

We compare the resolution of Equation (2.52) with these different numerical schemes. The stiffness parameters are fixed to $\beta = 50$ and $x_0 = 0.1$, which indeed yields a rather stiff problem. The time step is fixed to $\delta t = 1/(2\,K)$, so as to satisfy the stability constraints of the (explicit-in-time) MUSCL schemes. Results for $K = 200$ are plotted in Figure 2.24, together with a convergence study with respect to the number of cells. In both cases, we consider the results at $t = 10$, when the solution is stationary both in the continuous and discrete cases. The first conclusion is that, even with the accurate solution of the *ODE* step implemented here, large errors may be obtained. Second, we observe that switching to the logarithmic formulation in the transport steps dramatically improves the scheme accuracy. On the opposite, the MUSCL discretization does not bring a decisive gain in accuracy. These conclusions motivate our choice for the scheme developed in this paper for the transport of the conformation tensor: we use the logarithmic formulation for the transport steps and keep an implicit linear and monotone (so first order upwind) scheme for their solution.

Note that, for one-dimensional problems as considered in this section, more sophisticated methods to cope with stiff source terms are proposed in the literature such as the so-called "well-balanced" schemes, designed to preserve at the discrete level specific "equilibrium" (i.e steady) states [28, 35, 11]. Such schemes are not tested here because their extension to multi-dimensional flow problems is not straightforward.

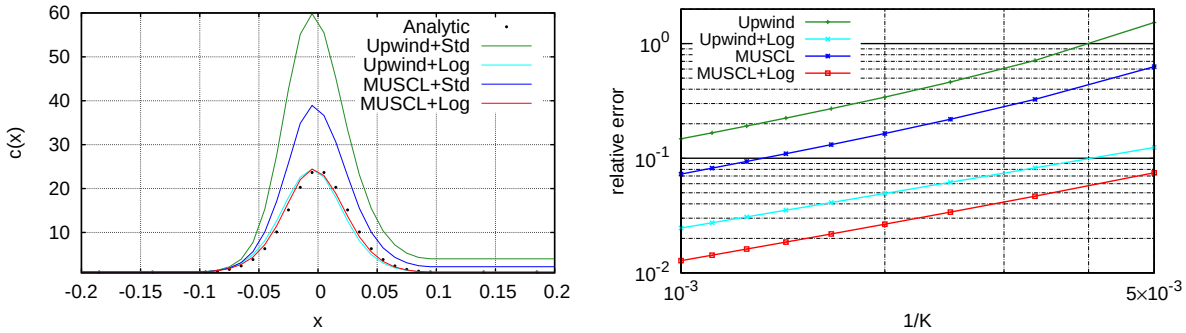

Fig. 2.24 Comparison of the different methods of discretization of the advection step with $\beta = 50$ and $x_0 = 0.1$. Left: Stationary states obtained for $K = 200$. Right: Relative errors (in discrete L^2-norm) with respect to the analytical solution as a function of the number of cells.

Références

[1] Afonso, A. M., Pinho, F. T., and Alves, M. A. (2012). The kernel-conformation constitutive laws. *Journal of Non-Newtonian Fluid Mechanics*, 167:30–37.

[2] Alves, M. A., Oliveira, P. J., and Pinho, F. T. (2021). Numerical methods for viscoelastic fluid flows. *Annual Review of Fluid Mechanics*, 53:509–541.

[3] Audusse, E., Bouchut, F., Bristeau, M.-O., Klein, R., and Perthame, B. (2004). A fast and stable well-balanced scheme with hydrostatic reconstruction for Shallow Water flows. *SIAM Journal on Scientific Computing*, 25:2050–2065.

[4] Balci, N., Thomases, B., Renardy, M., and Doering, C. R. (2011). Symmetric factorization of the conformation tensor in viscoelastic fluid models. *Journal of Non-Newtonian Fluid Mechanics*, 166:546–553.

[5] Barrett, J. W. and Boyaval, S. (2011). Existence and approximation of a (regularized) Oldroyd-B model. *Mathematical Models and Methods in Applied Sciences*, 21:1783–1837.

[6] Barrett, J. W. and Boyaval, S. (2018). Finite element approximation of the FENE-P model. *IMA Journal of Numerical Analysis*, 38:1599–1660.

[7] Barrett, J. W., Schwab, C., and Süli, E. (2005). Existence of global weak solutions for some polymeric flow models. *Mathematical Models and Methods in Applied Sciences*, 15:939–983.

[8] Barrett, J. W. and Süli, E. (2007). Existence of global weak solutions to some regularized kinetic models for dilute polymers. *Multiscale Modeling & Simulation*, 6:506–546.

[9] Bermudez, A. and Vazquez, M. E. (1994). Upwind methods for hyperbolic conservation laws with source terms. *Computers & Fluids*, 23:1049–1071.

[10] Bird, R. B. and Wiest, J. M. (1995). Constitutive equations for polymeric liquids. *Annual Review of Fluid Mechanics*, 27:169–193.

[11] Botchorishvili, R., Perthame, B., and Vasseur, A. (2003). Equilibrium schemes for scalar conservation laws with stiff sources. *Mathematics of Computation*, 72:131–157.

[12] Bouchut, F., Ounaissa, H., and Perthame, B. (2007). Upwinding of the source term at interfaces for Euler equations with high friction. *Computers & Mathematics with Applications*, 53:361–375.

[13] Boyaval, S. (2010). Lid-driven-cavity simulations of Oldroyd-B models using free-energy-dissipative schemes. In *Numerical Mathematics and Advanced Applications 2009*, pages 191–198. Springer.

[14] Boyaval, S., Lelièvre, T., and Mangoubi, C. (2009). Free-energy-dissipative schemes for the Oldroyd-B model. *Mathematical Modelling and Numerical Analysis*, 43:523–561.

[15] Boyd, S. and Vandenberghe, L. (2004). *Convex Optimization*. Cambridge University Press.

[CALIF^{3}S] CALIF^{3}S. A software components library for the computation of fluid flows. https://gforge.irsn.fr/gf/project/califs.

[17] Chen, G., Xiong, Q., Morris, P. J., Paterson, E. G., Sergeev, A., and Wang, Y. (2014). Openfoam for computational fluid dynamics. *Notices of the AMS*, 61(4):354–363.

[18] Chen, G.-Q., Levermore, C. D., and Liu, T.-P. (1994). Hyperbolic conservation laws with stiff relaxation terms and entropy. *Communications on Pure and Applied Mathematics*, 47:787–830.

[19] Comminal, R., Spangenberg, J., and Hattel, J. H. (2015). Robust simulations of viscoelastic flows at high Weissenberg numbers with the streamfunction/log-conformation formulation. *Journal of Non-Newtonian Fluid Mechanics*, 223:37–61.

[20] Crouzeix, M. and Raviart, P. (1973). Conforming and nonconforming finite element methods for solving the stationary Stokes equations. *RAIRO Série Rouge*, 7:33–75.

[21] Damanik, H., Hron, J., Ouazzi, A., and Turek, S. (2010). A monolithic FEM approach for the log-conformation reformulation (LCR) of viscoelastic flow problems. *Journal of Non-Newtonian Fluid Mechanics*, 165:1105–1113.

[22] Duran, A., Marche, F., Turpault, R., and Berthon, C. (2015). Asymptotic preserving scheme for the shallow water equations with source terms on unstructured meshes. *Journal of Computational Physics*, 287:184–206.

[23] Fattal, R. and Kupferman, R. (2004). Constitutive laws for the matrix-logarithm of the conformation tensor. *Journal of Non-Newtonian Fluid Mechanics*, 123:281–285.

[24] Fattal, R. and Kupferman, R. (2005). Time-dependent simulation of viscoelastic flows at high Weissenberg number using the log-conformation representation. *Journal of Non-Newtonian Fluid Mechanics*, 126:23–37.

[25] Favero, J. L., Secchi, A. R., Cardozo, N. S. M., and Jasak, H. (2010). Viscoelastic flow analysis using the software openfoam and differential constitutive equations. *Journal of Non-Newtonian Fluid Mechanics*, 165(23-24):1625–1636.

[26] Gallouët, T., Herbin, R., Latché, J.-C., and Mallem, K. (2018). Convergence of the Marker-And-Cell scheme for the incompressible Navier-Stokes equations on non-uniform grids. *Foundations of Computational Mathematics*, 18:249–289.

[27] Grapsas, D., Herbin, R., Kheriji, W., and Latché, J.-C. (2016). An unconditionally stable staggered pressure correction scheme for the compressible Navier-Stokes equations. *SMAI Journal of Computational Mathematics*, 2:51–97.

[28] Greenberg, J. M. and Leroux, A. Y. (1996). A Well-Balanced Scheme for the Numerical Processing of Source Terms in Hyperbolic Equations. *SIAM Journal on Numerical Analysis*, 33:1–16.

[29] Grillet, A. M., Yang, B., Khomami, B., and Shaqfeh, E. S. (1999). Modeling of viscoelastic lid driven cavity flow using finite element simulations. *Journal of Non-Newtonian Fluid Mechanics*, 88:99–131.

[30] Harlow, F. and Amsden, A. (1971). A numerical fluid dynamics calculation method for all flow speeds. *Journal of Computational Physics*, 8:197–213.

[31] Harlow, F. and Welsh, J. (1965). Numerical calculation of time-dependent viscous incompressible flow of fluid with free surface. *Physics of Fluids*, 8:2182–2189.

[32] Herbin, R., Kheriji, W., and Latché, J.-C. (2014). On some implicit and semi-implicit staggered schemes for the shallow water and euler equations. *Mathematical Modelling and Numerical Analysis*, 48:1807–1857.

[33] Hu, D. and Lelievre, T. (2007). New entropy estimates for the Oldroyd-B model and related models. *Communications in Mathematical Sciences*, 5:909–916.

[34] Hulsen, M. A., Fattal, R., and Kupferman, R. (2005). Flow of viscoelastic fluids past a cylinder at high Weissenberg number: Stabilized simulations using matrix logarithms. *Journal of Non-Newtonian Fluid Mechanics*, 127:27–39.

[35] Jin, S. (1999). Efficient asymptotic-preserving (AP) schemes for some multiscale kinetic equations. *SIAM Journal on Scientific Computing*, 21:441–454.

[36] Katsaounis, T., Perthame, B., and Simeoni, C. (2004). Upwinding sources at interfaces in conservation laws. *Applied Mathematics Letters*, 17:309–316.

[37] Keunings, R. (1986). On the high weissenberg number problem. *Journal of Non-Newtonian Fluid Mechanics*, 20:209–226.

[38] Keunings, R. (2000). A survey of computational rheology. In *Proceedings of the XIIIth International Congress on Rheology*, volume 1, pages 7–14. British Soc. Rheol.

[39] Latché, J.-C. and Saleh, K. (2018). A convergent staggered scheme for the variable density incompressible Navier-Stokes equations. *Mathematics of Computation*, 87:581–632.

[40] Lee, Y.-J. and Xu, J. (2006). New formulations, positivity preserving discretizations and stability analysis for non-Newtonian flow models. *Computer Methods in Applied Mechanics and Engineering*, 195:1180–1206.

[41] LeVeque, R. J. and Jinghua, W. (1993). *A Linear Hyperbolic System with Stiff Source Terms*, pages 401–408. Friedrich Vieweg & Sohn, Wiesbaden.

[42] Lorin, E. and Seignole, V. (2003). Convection systems with stiff source terms. *Mathematical Models and Methods in Applied Sciences*, 13:971–1018.

[43] Lozinski, A. and Owens, R. G. (2003). An energy estimate for the Oldroyd-B model: theory and applications. *Journal of Non-Newtonian Fluid Mechanics*, 112:161–176.

[44] Lukáčová-Medvid'ová, M., Notsu, H., and She, B. (2016). Energy dissipative characteristic schemes for the diffusive Oldroyd-B viscoelastic fluid. *International Journal for Numerical Methods in Fluids*, 81:523–557.

[45] Moreno, L., Codina, R., Baiges, J., and Castillo, E. (2019). Logarithmic conformation reformulation in viscoelastic flow problems approximated by a VMS-type stabilized finite element formulation. *Computer Methods in Applied Mechanics and Engineering*, 354:706–731.

[46] Pan, T.-W., Hao, J., and Glowinski, R. (2009). On the simulation of a time-dependent cavity flow of an Oldroyd-B fluid. *International Journal for Numerical Methods in Fluids*, 60:791–808.

[47] Pimenta, F. and Alves, M. A. (2017). Stabilization of an open-source finite-volume solver for viscoelastic fluid flows. *Journal of Non-Newtonian Fluid Mechanics*, 239:85–104.

[48] Rannacher, R. and Turek, S. (1992). Simple nonconforming quadrilateral Stokes element. *Numerical Methods for Partial Differential Equations*, 8:97–111.

[49] Renardy, M. (2000). *Mathematical analysis of viscoelastic flows*. SIAM.

[50] Saramito, P. (2014). On a modified non-singular log-conformation formulation for Johnson-Segalman viscoelastic fluids. *Journal of Non-Newtonian Fluid Mechanics*, 211:16–30.

[51] Tomé, M. F., Castelo, A., Afonso, A. M., Alves, M. A., and Pinho, F. (2012). Application of the log-conformation tensor to three-dimensional time-dependent free surface flows. *Journal of Non-Newtonian Fluid Mechanics*, 175:44–54.

[52] Van Doormaal, J. P. and Raithby, G. D. (1984). Enhancements of the SIMPLE method for predicting incompressible fluid flows. *Numerical Heat Transfer*, 7(2):147–163.

[53] Yapici, K., Karasozen, B., and Uludag, Y. (2009). Finite volume simulation of viscoelastic laminar flow in a lid-driven cavity. *Journal of Non-Newtonian Fluid Mechanics*, 164:51–65.

Chapter 3

Effet des brins biréfringents sur les écoulements stationnaires à travers des réseaux de cylindres 2D

Nous montrons dans ce Chapitre le rôle clé des brins biréfringents dans l'écoulement des fluides viscoélastiques à travers des réseaux de cylindres en 2D.

Au Chapitre précédent, nous avons développé un outil performant nous permettant d'envisager des calculs sur des domaines suffisamment grands pour être représentatifs d'un milieu poreux et à des nombres de Weissenberg suffisamment élevés pour observer les effets élastiques. Entre autres, nous avons montré la capacité du schéma à capturer les zones de forte contrainte apparaissant dans le sillage d'un cylindre et qui, comme on le verra, jouent un rôle primordial.

La diminution de la perméabilité apparente observée à l'échelle macroscopique nous semble fortement liée à une restructuration du champ de vitesse que l'on peut observer à l'échelle mésoscopique, dans des écoulements à travers des treillis de cylindres [78, 88] ou des empilement de billes [15] et caractérisée par un renforcement des chemins d'écoulement préférentiels et une augmentation des zones de stagnation. Nous nous sommes donc d'abord focalisé sur l'étude des treillis de cylindres en 2D, suffisamment complexes pour révéler les non-linéarités du problème tout en restant accessible à une étude poussée, avec pour objectif de comprendre quels sont les mécanismes, à l'échelle du pore, responsables de cette restructuration de l'écoulement. Après avoir considéré bon nombre d'hypothèses et éliminé plusieurs pistes et malgré une bonne concordance entre nos résultats et les résultats expérimentaux [78, 88], la compréhension de l'écoulement semblait toujours nous échapper : il nous manquait un outil d'interprétation.

C'est alors que nous avons découvert une étude, très récente, qui considère une géométrie constituée de deux cylindres placés côte à côte dans un canal et qui montre, en fonction de l'écart relatif entre les cylindres, l'apparition d'un écoulement préférentiel entre les cylindres ou autour d'eux [40] : nous avions là un problème modèle simple et on ne pouvait comprendre les écoulements dans des géométries complexes sans comprendre celui-ci.

Article 2 : Birefringent strands drive the flow of viscoelastic fluids through porous media

O. Mokhtari[1,3], J.-C. Latché[2], M. Quintard[1] and Y. Davit[1]

[1]Institut de Mécanique des Fluides de Toulouse (IMFT), CNRS & Université de Toulouse, France
[2]Institut de Radioprotection et de Sûreté Nucléaire (IRSN), Cadarache, France
[3]TotalEnergies E&P, CSTJF, Pau, France

Article soumis à ***Journal of Fluid Mechanics***.

Abstract

The flow of polymer solutions past solid obstacles or through porous media gives rise to rich physical phenomena over a wide range of spatial and temporal scales. Viscoelasticity, in particular, can induce a strong nonlinear response with an increase of flow resistance even for a solution whose viscosity decreases in simple shear flow. Various hypotheses have been proposed to explain this phenomenon but a clear picture of the pore-scale mechanisms involved and their impact upon larger scales is still lacking. Here we show that localized zones of large polymeric stress, known as birefringent strands, drive the flow of an Oldroyd-B fluid through 2D arrays of cylinders. Combining a recently developed numerical scheme with high performance computing, we found that these strands generate a complete reorganization of the flow with an increase of stagnation zones, a reinforcement of preferential paths and a splitting of flow channels. Furthermore, we showed that this reorganization is the source of an increase in the viscous dissipation of the solvent and also that the stretching of polymer molecules in the strands is associated with entropy production. Both these phenomena yield a global increase in dissipation that can be directly linked with the increase of flow resistance. Our results demonstrate that the birefringent strands–not the elongational viscosity–drive the flow of viscoelastic fluids through porous media and that the increase of flow resistance can occur even at steady-state, long before the transition to elastic turbulence. *Keywords:* Complex Fluids, Birefringent strands, Asymptotic Analysis, FV Method, HPC

3.1 Introduction

Birefringent strands [28] are localized regions of large strain and stress in viscoelastic flows of polymer solutions. At the molecular level, they correspond to polymers that are highly stretched and tend to align in a thin region that is optically anisotropic. Birefringent strands have been observed in a variety of systems [48, 59], including roll mills [13, 20, 23, 53], opposed jets [66, 69], cross-slot devices [34, 62, 67, 77, 83], flows around cylinders [34, 37, 39, 84] and flows around spheres [36]. Examples of flow-induced birefringence in the case of a cross-slot device and the flow around one and two cylinders are shown in figure 3.1.

Geometries with a cylinder are often used as model systems–in experiments [22, 71, 80, 87], numerical approaches [2, 9, 19, 56, 92] and theoretical analyses [3, 73]–to study the fundamental fluid mechanics of viscoelastic flow past solid obstacles. Flow around a cylinder leads to the formation of a birefringent strand in the wake. The strand develops close to stagnation points, where elongation is strong and the residence time is long compared to the relaxation time of the polymer [28], and is then transported with a competition between advection and relaxation. Continuum representations of the viscoelastic flow, in particular Oldroyd-B and FENE-type models, capture the formation of the strands through a two-way coupling between a polymeric stress tensor, τ_p, in the momentum balance and a separate transport equation for its components.

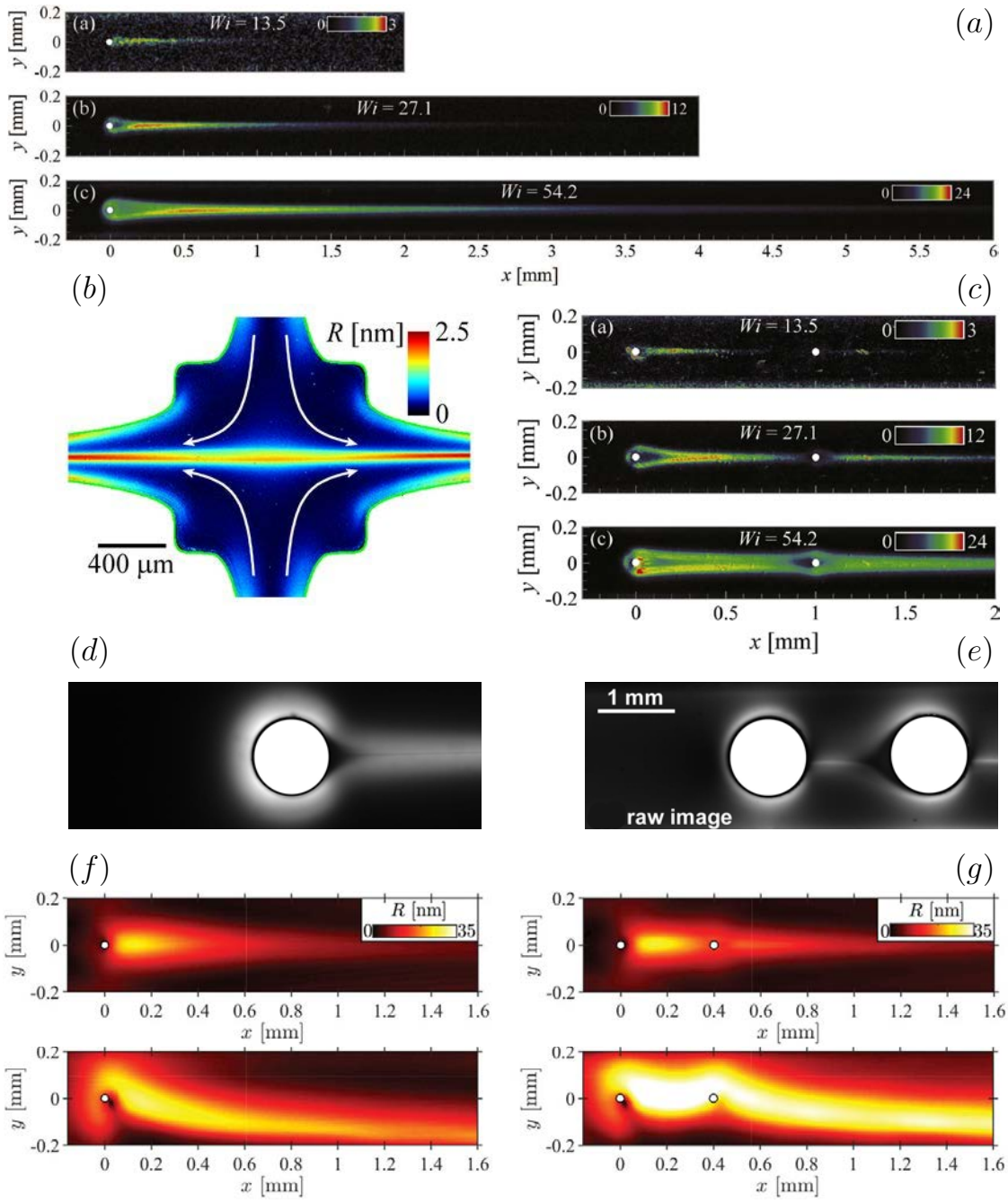

Fig. 3.1 Examples of experimental observations of the formation of birefringent strands in the literature, with (a), (d) and (f) cases with one cylinder; (c), (e) and (g) cases with two cylinders; and (b) a cross slot device. In (f) and (g), the results correspond to two different regimes of flow with (top) steady symmetric and (bottom) steady asymmetric. (a) and (c) are reproduced from [37] with permission. (b) is reproduced from [34] with permission. (d) and (e) are from [84] with permission. (f) and (g) are reproduced from [39] with permission. In all pictures, birefringence is characterized by the retardation, R[nm], between two optical paths, which stems from differences in refractive index due to polymer molecules. This local change in the optical property of the polymer solution is also a proxy to visualizing stress as it can be linked to the local principal stress difference through the stress-optic law which states that there is a linear relationship between R and the difference in principal stresses.

The problem can be simplified by considering a one-way coupling with no feedback of the polymeric stress upon the velocity field, for instance in a limit of extreme dilution. The velocity field is calculated in the Newtonian limit and then used for the transport of the polymeric stress. This approach has made it possible to determine the structure of the stress field and its scalings near a curved boundary [73], around a cylinder and in its wake [74] or near a flat wall [3, 85]. On the other hand, the feedback of the strand upon the flow has been described through approaches such as the birefringent strand technique, which treats the strand of extended polymers as a line distribution of forces surrounded by a Newtonian fluid [72, 28]. This force, exerted by the polymers upon the fluid, leads to a jump in shear-rate across the strand and to a decrease of the velocity in the wake of the cylinder [28]. This method was also used in [26] for the flow past a falling sphere, in [27] to study the case of opposed-jet, in [53] for co-rotating two-roll mill and in [60] for rising bubbles.

Configurations with more than one cylinder have also been recently considered to unravel interaction mechanisms. For instance, Haward et al. [37] studied the case of two cylinders aligned with the flow using microfluidics. They show that the strand formed in the wake of the first cylinder can interact with the second cylinder, encapsulate it completely and even create a stagnation zone between the two cylinders. Hopkins et al. [40] considered the case of two cylinders in a confined microfluidic channel–with the line segment joining the centers of the cylinders being orthogonal to the flow direction–and studied the flow as a function of the gap between the cylinders. For small gaps, the flow is "divergent" with the flow rate between the cylinders being smaller than in the Newtonian case. For large gaps, on the contrary, the flow converges with the flow rate between the cylinders being larger than in the Newtonian case. A rupture of symmetry can occur, which was also observed in the case of a single cylinder (see figure 3.1(f)). This phenomenon is linked to the shear-thinning rheology of the fluid [30, 33, 32, 86] and is hypothesized to stem from a positive feedback mechanisms involving the strand [32]. Khan and Sasmal [49] recovered these results and showed a change of curvature sign in the convergent and divergent cases. This observation, along with the known effect of a strand in slowing down the flow in the wake of a single cylinder, suggests that strands may play a central role in controlling the relative flow through the different parts of the geometry and the transition mechanisms.

In porous media, little is known about the interaction between the strands, the flow and the geometrical structure. De et al. [14] observed numerically the formation of strands in steady flows through random arrays of cylinders and the concomitant appearance of preferential flow paths. To illustrate such effects, we show in figure 3.2 some results of our steady-state simulations for an incompressible Oldroyd-B fluid in a 2D geometry with biperiodic conditions and a body force oriented from left to right (see Section 3.5). The strands exhibit surprisingly rich behaviors that have yet to be understood. In some regions, they completely encapsulate large regions containing some fluid and several cylinders. In other regions, they form channel-like structures that seem to drive the flow paths through the structure. This raises many questions about these strands including how they modify the flow, how they interact with solid obstacles and with each other, or what their effect is on larger scales. For instance, could these strands be involved in the increase of flow resistance through porous structures–a phenomenon reported in numerous studies [17, 43, 46, 61]? Although, a variety of hypotheses have been formulated, such as the effect of extensional viscosity of the fluids [10, 16, 50, 75, 81, 94] or elastic turbulence [6, 12, 24, 47, 58, 70], a detailed picture of the problem that clearly links pore-scale physics with larger scales is still lacking.

In this work, our goal is to study the formation of strands in porous structures and to understand how they modify the flow, how they interact with each other and how they interact with the solid structure. With this fundamental understanding at the pore-scale, we also aim at providing a link with the macro-scale through energetic considerations. Our numerical approach

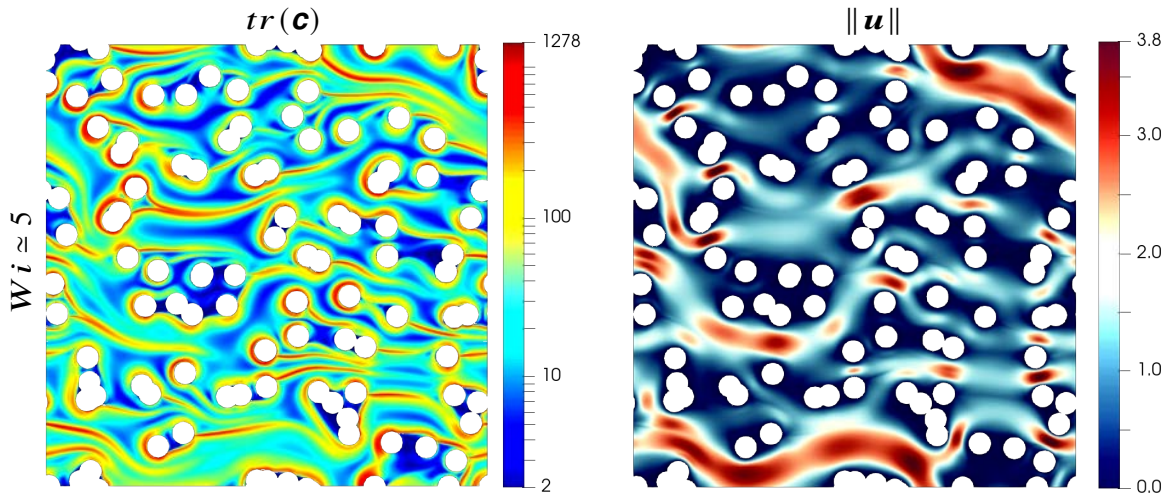

Fig. 3.2 Example simulations of the flow of an Oldroyd-B fluid through an array of cylinders in the case with a Weissenberg number $\simeq 5$ and $\beta = 1$ (see Section 3.2.1 for definitions). Plots of the trace of the conformation tensor $tr(\boldsymbol{c})$ (left), which represents the stretching of the polymer chains, and velocity magnitude $\|\boldsymbol{u}\|$ (right).

is presented in Section 3.2 and is based upon the Oldroyd-B model (Section 3.2.1), which has proven very useful in describing Boger-type viscoelastic fluids with constant viscosity in simple shear flow [42, 79]. Viscoelastic fluids give rise to rich physics even without inertial effects [52] so that we focus here on steady incompressible flow in the creeping limit. We use simulations based on a recently developed HPC code [64] that is summarized in Section 3.2.2. We cannot start directly by porous structures since, as illustrated in figure 3.2, the fields are complex and difficult to interpret. Rather, our strategy consists in progressively increasing the complexity of the problem, starting with a single cylinder (Section 3.3). We detail the fundamental mechanisms that generate the strand, describe its behaviour and quantify important properties, in particular its length and its effect upon the flow. We then study cases with two cylinders (Section 3.4) either aligned or with the line segment joining the centers of the cylinders being orthogonal to the flow direction, outlining strand/cylinder and strand/strand interactions and quantifying their effect upon the flow. Finally, we get back to more complex porous media consisting of arrays of cylinders (Section 3.5) and compute pore-scale and Darcy-scale quantities, in particular the resistance to flow for a range of Weissenberg numbers and ratios of polymer to solvent viscosities.

3.2 Numerical approach

3.2.1 Governing equations

We consider the Oldroyd-B model for an incompressible fluid in the creeping flow limit. Momentum and continuity equations read

$$\begin{aligned} -\boldsymbol{\nabla}\mathfrak{p} + \eta_s \boldsymbol{\nabla}\cdot\left(\boldsymbol{\nabla}\mathfrak{u} + (\boldsymbol{\nabla}\mathfrak{u})^{\mathsf{T}}\right) + \boldsymbol{\nabla}\cdot\tau_p + \mathfrak{F} = 0, \\ \boldsymbol{\nabla}\cdot\mathfrak{u} = 0, \end{aligned} \tag{3.1}$$

where η_s is the solvent viscosity, $\mathfrak{u}$ the fluid velocity, $\mathfrak{p}$ the pressure, $\mathfrak{F}$ is a body force acting on the fluid and τ_p is the polymeric stress. In the Oldroyd-B model, τ_p is proportional to the

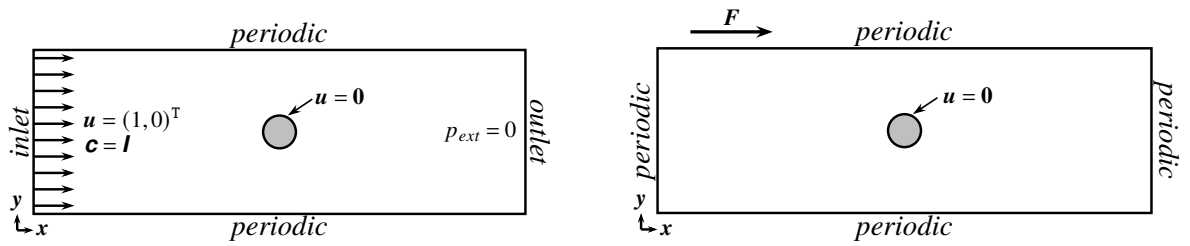

(*a*) Inlet/outlet (*b*) Biperiodic

Fig. 3.3 Typical geometry with boundary conditions. The boundary conditions are top-bottom periodicity and $\boldsymbol{u} = (0,0)^{\mathsf{T}}$ on the cylinder. Two types of boundary conditions are used for left and right sides, either (a) an inlet condition on the left-hand side, $\boldsymbol{u} = (1,0)^{\mathsf{T}}$ and $\boldsymbol{c} = \boldsymbol{I}$, and an outlet condition on the right-hand side, $p_{ext} = 0$ (see (3.7)), or (b) periodic boundary conditions with the flow generated through a body force $\boldsymbol{F}$.

deviation of the conformation tensor from its equilibrium state

$$\tau_p = {}^{\eta_p}/_{\lambda}\,(\boldsymbol{c} - \boldsymbol{I})\,, \tag{3.2}$$

with η_p a viscosity associated with the polymers and λ a relaxation time. The constitutive equation for the evolution of the conformation tensor is given by

$$\partial_t \boldsymbol{c} + (\mathbf{u}\cdot\boldsymbol{\nabla})\,\boldsymbol{c} = \boldsymbol{\nabla}\mathbf{u}\,\boldsymbol{c} + \boldsymbol{c}\,(\boldsymbol{\nabla}\mathbf{u})^{\mathsf{T}} - \frac{1}{\lambda}\,(\boldsymbol{c} - \boldsymbol{I})\,. \tag{3.3}$$

Non-dimensionalizing space by a lengthscale R and time by ${}^{R}/_{U}$, where U is a reference velocity, we obtain the following dimensionless version of the equations

$$-\boldsymbol{\nabla} p + \boldsymbol{\nabla}\cdot\left(\boldsymbol{\nabla}\boldsymbol{u} + (\boldsymbol{\nabla}\boldsymbol{u})^{\mathsf{T}}\right) + \frac{\beta}{Wi}\boldsymbol{\nabla}\cdot\boldsymbol{c} + \boldsymbol{F} = 0, \tag{3.4}$$

$$\boldsymbol{\nabla}\cdot\boldsymbol{u} = 0, \tag{3.5}$$

$$\partial_t \boldsymbol{c} + (\boldsymbol{u}\cdot\boldsymbol{\nabla})\,\boldsymbol{c} = \boldsymbol{\nabla}\boldsymbol{u}\,\boldsymbol{c} + \boldsymbol{c}\,(\boldsymbol{\nabla}\boldsymbol{u})^{\mathsf{T}} - \frac{1}{Wi}\,(\boldsymbol{c} - \boldsymbol{I})\,, \tag{3.6}$$

where $\beta = {}^{\eta_p}/_{\eta_s}$ is a viscosity ratio and $Wi = {}^{\lambda U}/_{R}$ the Weissenberg number. This system of equations must be complemented by suitable boundary and initial conditions for the velocity and the conformation tensor. For initial conditions, we will consider uniform fields in the form $\boldsymbol{u} = \boldsymbol{u}_0$ and $\boldsymbol{c} = \boldsymbol{c}_0$ where $\boldsymbol{c}_0$ is a symmetric positive definite tensor. Unless otherwise stated, we will systematically impose $\boldsymbol{u}_0 = \boldsymbol{0}$ and $\boldsymbol{c}_0 = \boldsymbol{I}$. A schematic 2D geometry is represented in figure 3.3, along with the two types of boundary conditions that we will use in this work. The characteristic lengthscale, R, for the non-dimensionalization will be the radius of the cylinders. Boundary conditions on the surface of the cylinder are no-slip and no-penetration boundary conditions, $\boldsymbol{u} = \boldsymbol{0}$. Periodic boundary conditions are used for the top/bottom boundaries and two types of boundary conditions will be considered for the left/right boundaries, with either

- inlet/outlet boundary conditions. In this case, Dirichlet conditions $\mathbf{u} = \mathbf{u}_{in}$ and $\boldsymbol{c} = \boldsymbol{I}$ are imposed for both the velocity and the conformation tensor at the inlet. The reference velocity will then be the euclidean norm of the inlet velocity, $U = \|\mathbf{u}_{in}\|$. At the outlet, the fluid is supposed to obey a Neumann boundary condition, with an external force normal

to the boundary

$$\left(-p\boldsymbol{I}+\boldsymbol{\nabla u}+(\boldsymbol{\nabla u})^{\mathsf{T}}+\frac{\beta}{Wi}\boldsymbol{c}\right)\mathbf{n}_{ext}=-p_{ext}\mathbf{n}_{ext}, \tag{3.7}$$

where $\mathbf{n}_{ext}=\mathbf{e}_x$ is the normal vector, $\mathbf{e}_x$ being the first vector of the canonical basis of $\mathbb{R}^2$. The external pressure p_{ext} is fixed to zero. When these boundary conditions are used, we systematically have $\boldsymbol{F}=\mathbf{0}$,

- periodic boundary conditions, leading to biperiodic conditions. The flow is then imposed through a uniform body force $\boldsymbol{F}=F\mathbf{e}_x$. In this case, the reference velocity is determined a posteriori and will be the euclidean norm of the average velocity, $U=\|\langle\mathbf{u}\rangle\|$ where the averaging operator is defined by

$$\langle\bullet\rangle=\frac{1}{|\Omega|}\int_{\Omega}\bullet\, dS \tag{3.8}$$

with Ω the fluid part of the domain. Note that, with this definition, the average velocity $\langle\boldsymbol{u}\rangle$ is the intrinsic velocity of the fluid and not the Darcy velocity. For cases with one or two cylinders, the porosity is close to 1 so that the values of intrinsic and Darcy velocities are very similar. For arrays of cylinders, intrinsic and Darcy velocities are significantly different.

3.2.2 Numerical method

To solve this problem, we have developed a novel approach that is detailed and validated against two benchmarks (lid-driven cavity and confined cylinder) in [64]. Here we simply summarize the numerical scheme. The scheme implements a fractional step approach. First, the unstationary Stokes system (i.e. mass and momentum balance equations) is decoupled from the transport equation for the conformation tensor by using a beginning-of-step approximation of the latter in the momentum balance equation. Then, we use a standard projection scheme to once again decouple the momentum balance equation from the divergence constraint, to circumvent the solution of a discrete saddle point problem. Let dt be the time step. The solution of hydrodynamics is thus obtained by the following algorithm:

$$\begin{aligned}
&\textbf{Prediction step}-\text{Solve for } \tilde{\boldsymbol{u}}^{n+1}:\\
&\frac{1}{dt}\left(\tilde{\boldsymbol{u}}^{n+1}-\boldsymbol{u}^{n}\right)+\boldsymbol{\nabla}p^{n}-\boldsymbol{\nabla}\cdot\left(\boldsymbol{\nabla}\tilde{\boldsymbol{u}}^{n+1}+\left(\boldsymbol{\nabla}\tilde{\boldsymbol{u}}^{n+1}\right)^{\mathsf{T}}\right)-\frac{\beta}{Wi}\boldsymbol{\nabla}\cdot\boldsymbol{c}^{n}-\boldsymbol{F}=0.\\
&\textbf{Correction step}-\text{Solve for } p^{n+1} \text{ and } \boldsymbol{u}^{n+1}:\\
&\frac{1}{dt}\left(\boldsymbol{u}^{n+1}-\tilde{\boldsymbol{u}}^{n+1}\right)+\boldsymbol{\nabla}\left(p^{n+1}-p^{n}\right)=0,\\
&\boldsymbol{\nabla}\cdot\boldsymbol{u}^{n+1}=0.
\end{aligned} \tag{3.9}$$

The discretization of the constitutive equation is then performed using a Strang-type decoupling. We first perform one half-step of homogeneous transport of $\boldsymbol{c}$, then treat the reaction terms, and finish by the second half-step of transport of $\boldsymbol{c}$. For accuracy, and as previously proposed in [21, 41], we introduce a log transformation of the conformation tensor that is applied to the decoupled transport equation for the conformation tensor. The scheme reads

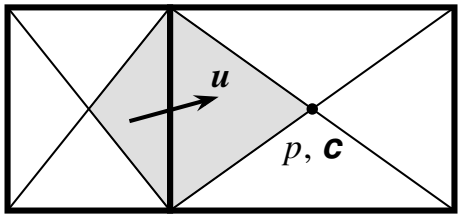

Fig. 3.4 Schematics of mesh and unknowns corresponding to the RT element for quadrilateral cells. The degrees of freedom for the pressure and the conformation tensor are located at the center of the cells. The degrees of freedom for the velocity components are located at the center of the faces of the mesh and associated with the dual cells. For a rectangular mesh and each face of it, the dual cell is the union of the cones with basis the face and vertex the mass center of an adjacent cell. The dual cell corresponding to the face between the two rectangular cells is shown in grey.

$$
\begin{aligned}
&\textbf{Advection I} - \text{Solve for } \boldsymbol{c}^{n+\frac{1}{3}}: \\
&\quad \frac{1}{dt/2}\left(\log \boldsymbol{c}^{n+\frac{1}{3}} - \log \boldsymbol{c}^{n}\right) + \boldsymbol{\nabla}\cdot\left(\boldsymbol{u}^{n+1}\log \boldsymbol{c}^{n+\frac{1}{3}}\right) = 0. \\
&\textbf{ODE} - \text{Set } \boldsymbol{c}(t_n) = \boldsymbol{c}^{n+\frac{1}{3}} \text{ and solve for } \boldsymbol{c}^{n+\frac{2}{3}} = \boldsymbol{c}(t_n + dt): \\
&\quad \dot{\boldsymbol{c}} - \left(\boldsymbol{\nabla}\boldsymbol{u}^{n+1}\right)\boldsymbol{c} - \boldsymbol{c}\left(\boldsymbol{\nabla}\boldsymbol{u}^{n+1}\right)^{\mathsf{T}} + \frac{1}{Wi}\left(\boldsymbol{c} - \boldsymbol{I}\right) = 0. \\
&\textbf{Advection II} - \text{Solve for } \boldsymbol{c}^{n+1}: \\
&\quad \frac{1}{dt/2}\left(\log \boldsymbol{c}^{n+1} - \log \boldsymbol{c}^{n+\frac{2}{3}}\right) + \boldsymbol{\nabla}\cdot\left(\boldsymbol{u}^{n+1}\log \boldsymbol{c}^{n+1}\right) = 0.
\end{aligned}
\tag{3.10}
$$

The local ODE is solved using a first-order semi-implicit Euler scheme

$$
\frac{1}{\delta t}\left(\boldsymbol{c}^{n+1} - \boldsymbol{c}^{n}\right) = \boldsymbol{\nabla}\boldsymbol{u}\ \boldsymbol{c}^{n+1} + \left(\boldsymbol{c}^{n+1}\right)^{\mathsf{T}}(\boldsymbol{\nabla}\boldsymbol{u})^{\mathsf{T}} - \frac{1}{Wi}\left(\boldsymbol{c}^{n+1} - \boldsymbol{I}\right), \tag{3.11}
$$

where δt is a local time-step for the solution of the ODE on each mesh element, small enough to ensure stability. When the velocity gradient is large, the ODE becomes stiff and sub-cycling is needed. In practice, this occurs in a small number of cells so that the computational cost associated with the ODE is limited. Note that the viscoelastic constitutive law is only involved in this ODE, so that it can be easily modified for a variety of viscoelastic constitutive laws.

In all the computations, the steady state is obtained by running a transient computation until the solution stabilizes in time. The time step is monitored to ensure time convergence and obtain steady state solutions. We use $dt = 10^{-4}$ as the initial time step. We then increase dt progressively with the constraint that the relative difference–in the maximum norm–between the beginning and end-of-step values must be lower than 10^{-3} for all component of the velocity and the conformation tensor. The decoupling of the equations may require a limitation of the time step, with an upper limit decreasing with the space step–a choice of a time step too large may make it difficult to reach a steady state solution. Further, to preserve the positive definiteness of the conformation tensor, the local time-step for the solution of the ODE is set to $\delta t = {}^{dt}/_{n_e}$ with n_e the smallest integer number such that $\delta t \leq 1/\left(200\|\boldsymbol{\nabla}u^{n+1}\|_\infty\right)$, see [64]. With this strategy, the CPU-time used in the ODE step remains almost negligible (less than 3% of the total time for each calculation).

geometry	mesh type	min width	max width	min height	max height	max aspect ratio
1 cylinder	non-uniform	$1/32$	$1/32$	$1/1024$	$1/32$	32
2 cylinders	uniform	$1/32$	$1/32$	$1/32$	$1/32$	1
array of cylinders	uniform	$1/50$	$1/50$	$1/50$	$1/50$	1

Table 3.1 Characteristics of the meshes used for the calculations. Lengths are dimensionless with the radius of the cylinder as a reference.

The space discretization relies on a partition of the domain with quadrilateral cells and consists in a staggered approximation of the velocity/pressure pair with nonconforming low-order finite elements, namely the Rannacher and Turek (RT) element. As shown in figure 3.4, the discrete pressure and conformation unknowns are associated with the cells of the mesh and the discrete velocity unknowns are located at the center of the faces of the mesh. The conformation tensor is discretized as piecewise constant and the constitutive equation is then solved using a finite-volume scheme. In the spirit of [**?** **?**], the scheme uses a space discretization such that a discrete free-energy estimate is obtained with more sophisticated (and, unfortunately, costly) time marching algorithms, so that it may be hoped to inherit the resulting stability property, at least at small time steps.

The mesh itself is structured, either uniform or non-uniform depending on the configuration. Cylinders are obtained by making holes into the mesh and are thus approximated as "stair steps". In the case of a single cylinder, the position of the strand is known a priori so that the mesh can easily be refined in the wake of the cylinder. We thus consider a rectilinear non-uniform grid with square meshes far away from the cylinder and an aspect ratio that progressively decreases using a geometric progression towards the central axis. In the case of several cylinders, the position of the strands is not known a priori. The mesh then consists in a Cartesian grid and mesh refinement is obtained by cutting each face into 2 equal parts and each cell into 2×2 parts in 2D. The characteristic sizes of the meshes used in this study are summarized in table 3.1.

To summarize important properties detailed in [64], the scheme

- is a low-order approximation using a staggered space discretization,
- uses a space discretization consistent with a free-energy estimate,
- is well suited to high-performance computations,
- shows good accuracy and captures well steady-state solutions, mostly thanks to the log transformation in the transport step.

3.2.3 Implementation and high performance computing

The solver was implemented as a specific module of the CALIF^{3}S platform developed at the French Institut de Radioprotection et de Sûreté Nucléaire (IRSN). Parallel computations were carried out on TotalEnergies' group supercomputer Pangea II through a domain decomposition approach using the METIS (4.0.3) graph partitioner [45] and the OpenMPI (3.1.5) library [25]. The linear systems coming from the prediction step and the conformation advection are solved using the GMRES method while the projection step is solved using a classical conjugate gradient method. All this linear systems are preconditionned by a Block-Jacobi preconditioner. Finally, the linear systems coming from the local ODE, of size 6×6 (in $2D$), are solved using a direct LU method. For each array of cylinders, we used approximately 10^6 mesh cells and the entire work required about 10^7 cores $\times$ h.

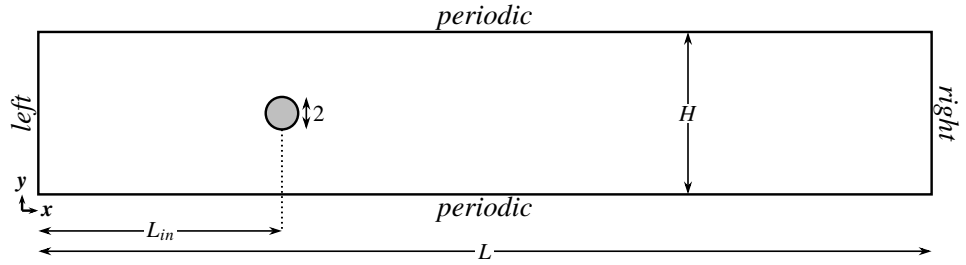

Fig. 3.5 Schematics of the geometry for a single cylinder. The lengthscales of the system are $H = 20$ the height of the domain, $L_{in} = 25$ the distance from the inlet to the center of the cylinder and L the total length of the domain. The length $L = L_{in} + 30Wi$ is chosen sufficiently large so that the conformation tensor relaxes to its equilibrium value $\boldsymbol{c} = \boldsymbol{I}$ before reaching the boundary condition on the right-hand side. The boundary conditions are top-bottom periodicity and $\boldsymbol{u} = \boldsymbol{0}$ on the cylinder. Left/right boundary conditions are either inlet/outlet conditions or periodicity depending on the calculation.

3.3 Steady viscoelastic flow past a single cylinder

In this section, we study the formation of a strand in the wake of a single cylinder. The geometry is presented in figure 3.5. The mesh consists in a structured non uniform grid with a cell size equal to $1/32$ away from the cylinder and refined vertically on the centreline, where the presence of the strand is expected, using a geometric progression towards a size of $1/1024$.

Our goals are to describe how the strand forms, to highlight some of its fundamental properties and to analyze its feedback upon the flow. We start by exemplifying the concept through typical cases of strand formation at different Wi numbers. Next, we detail the mechanisms leading to the formation of the strand and its structure in the limit case $\beta = 0$, which consists in Stokes flow and transport of $\boldsymbol{c}$ with a fixed velocity field. Last, we study the feedback of the strand upon the flow through β asymptotics and fully coupled simulations at $\beta > 0$.

3.3.1 Examples and preliminary observations

The first column in figure 3.6 shows how $tr(\boldsymbol{c})$, a measure of the stretching of the polymer chains, evolves with the Wi number in the case $\beta = 1$. For sufficiently large values of the Wi number, a strand corresponding to large values of $tr(\boldsymbol{c})$ appears in the wake of the cylinder. The length of this strand increases with the Wi number and can become very large compared to the diameter of the cylinder from which it originates. Consistent with experimental results in [37, 86], the strand length appears linear with the Wi number for sufficiently large Wi numbers, with e.g. a doubling of the length observed when the Wi number is doubled. The width of this strand seems to increase with the Wi number–in the logarithmic scale representation–but we will see later that the core region of the strand that features extremely large values of $tr(\boldsymbol{c})$ is actually getting thinner with increasing Wi number. We also see in figure 3.6 that the intensity of $tr(\boldsymbol{c})$ is strongly non-linear, with a maximum value that is $O(1)$ for $Wi = 1$, $O(10^1)$ for $Wi = 2$ and $Wi = 4$, $O(10^2)$ for $Wi = 8$ and $O(10^3)$ for $Wi = 16$. This is a remarkable feature of this strand, which is particularly difficult to capture numerically. Polymer chains are strongly stretched and the component c_{xx} reaches extremely high values in a thin zone that is reminiscent of an hyperplane.

In examining the different mechanisms at play in the formation of the strand and their effect upon the flow, one of the difficulties is the two-way coupling between the transport equations for the conformation tensor and for the momentum. In the Oldroyd-B model, the feedback of $\boldsymbol{c}$

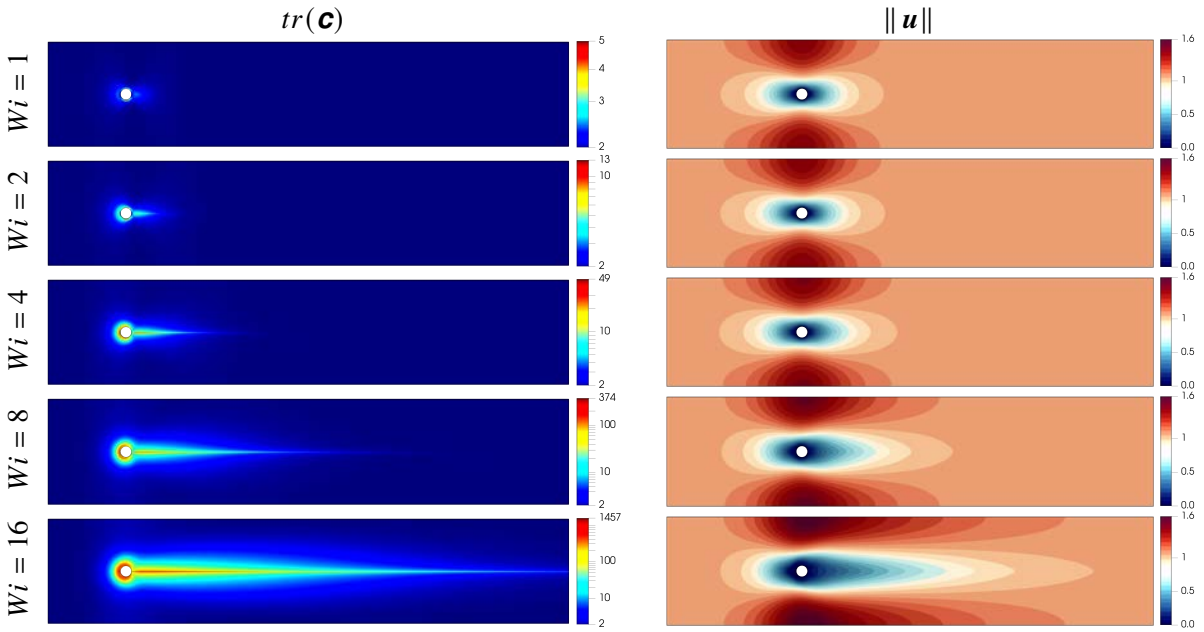

Fig. 3.6 Flow past a single cylinder in the case $\beta = 1$ and inlet/outlet boundary conditions. $tr(\boldsymbol{c})$ (left) and $\|\boldsymbol{u}\|$ (right) for different Wi numbers. Top to bottom, $Wi = 1$, $Wi = 2$, $Wi = 4$, $Wi = 8$ and $Wi = 16$. For ease of visualization, the range of the colourbar for the velocity field has been fixed to the interval $[0, 1.6]$ with 1.6 corresponding to the maximum value in the case $Wi = 16$.

on the velocity field is done through the term $\frac{\beta}{Wi}\boldsymbol{\nabla}\cdot\boldsymbol{c}$ in the momentum transport equation. The second column in figure 3.6 shows example cases of how the magnitude of the velocity field evolves with the Wi number. In the limit of small Wi numbers, the flow tends towards a Stokes solution with a for-aft symmetry. When the Wi number is larger, the velocity in the wake of the cylinder slows down because of the presence of the strand and, consistent with experimental and numerical observations in [37, 86], we observe a symmetry breaking compared to Stokes flow solution. On the other hand, the transport equation on $\boldsymbol{c}$ also depends on $\boldsymbol{u}$ and $\boldsymbol{\nabla u}$, so that the changes in the velocity field generated by the strand also modify the strand itself. To overcome these difficulties, our strategy consists in first studying the case $\beta = 0$ without any feedback, with the velocity field determined by Stokes flow and the transport of the conformation tensor that is based on a fixed velocity field. Then, we analyze the feedback of the strand upon the flow through β asymptotics and finally get back to the general case $\beta > 0$.

3.3.2 Formation and structure of the strand in the case $\beta = 0$

To provide a first intuition of how such strands develop, we go back to the transport equation for the conformation tensor. In the case $\beta = 0$, it reads

$$\partial_t \boldsymbol{c} + \left(\boldsymbol{u}^0 \cdot \boldsymbol{\nabla}\right)\boldsymbol{c} = \boldsymbol{\nabla u}^0 \boldsymbol{c} + \boldsymbol{c}\left(\boldsymbol{\nabla u}^0\right)^{\mathsf{T}} - \frac{1}{Wi}(\boldsymbol{c} - \boldsymbol{I}), \tag{3.12}$$

with $\boldsymbol{u}^0$ the velocity field of Stokes flow. Taking the trace of (3.12), we have

$$\partial_t tr(\boldsymbol{c}) + \underbrace{\left(\boldsymbol{u}^0 \cdot \boldsymbol{\nabla}\right) tr(\boldsymbol{c})}_{\text{Advective transport}} = \underbrace{2\boldsymbol{\nabla u}^0 : tr(\boldsymbol{c})}_{\text{Source}} \underbrace{- \frac{1}{Wi}(tr(\boldsymbol{c}) - 2)}_{\text{Relaxation}}, \tag{3.13}$$

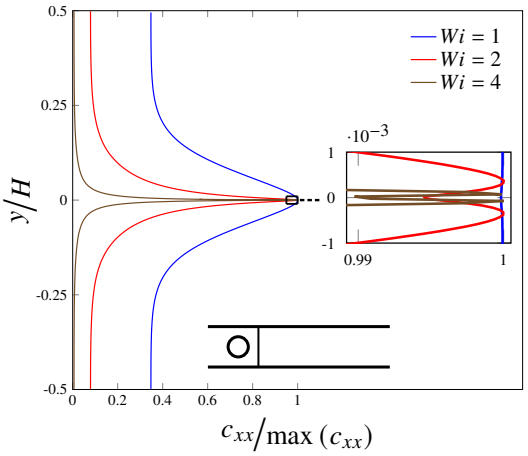

(*a*) c_{xx} (normalized) along $x = 1$

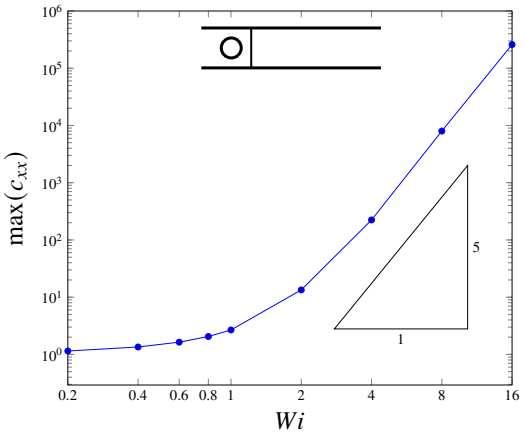

(*b*) Max of c_{xx} along $x = 1$

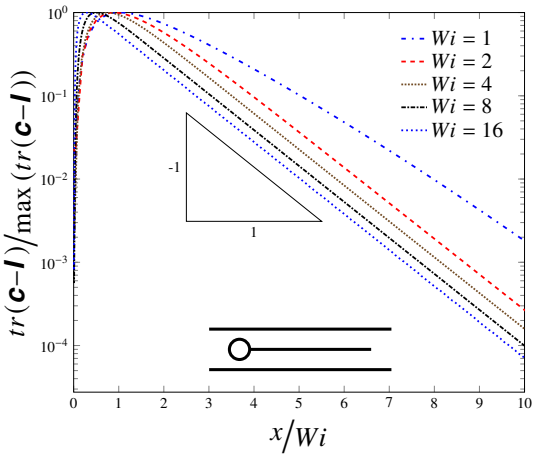

(*c*) $tr(\boldsymbol{c}-\boldsymbol{I})$ (normalized) in the wake

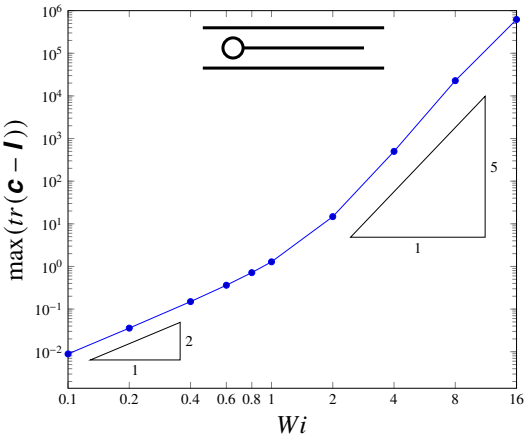

(*d*) Max of $tr(\boldsymbol{c}-\boldsymbol{I})$ in the wake

Fig. 3.7 Flow past a single cylinder in the case $\beta = 0$. (a) c_{xx} along the line $x = 1$ for different values of Wi. (b) Maximum of c_{xx} along the line $x = 1$ as a function of Wi (log-log axis). (c) $tr(\boldsymbol{c}-\boldsymbol{I})$ along the centreline in the wake of the cylinder for different values of Wi (log-linear axis). (d) Maximum of $tr(\boldsymbol{c}-\boldsymbol{I})$ along the centreline in the wake as a function of Wi (log-log axis).

One way to think about this equation is as an advection-reaction transport equation for $tr(\boldsymbol{c})$. The advection is due to $(\boldsymbol{u}^0 \cdot \boldsymbol{\nabla})\, tr(\boldsymbol{c})$, which has the important consequence that strands tend to follow streamlines at steady-state. The reaction is due to both a source and a relaxation term. The growth rate of the conformation tensor is controlled by $\boldsymbol{\nabla u}^0$ and the relaxation rate by $1/Wi$. Roughly speaking, large values of $\|\boldsymbol{\nabla u}^0\|$ are therefore expected to yield large values of $tr(\boldsymbol{c})$. This can be understood through the following 1D model transport equation

$$\begin{cases} \partial_t c + \partial_x c = a(x)\, c - \frac{1}{Wi} c, \\ c(0,t) = 1, \end{cases} \tag{3.14}$$

where $a(x)$ is here to mimic the velocity gradients [64]. At steady-state, the profile of $c(x)$ grows exponentially at a rate $a(x) - 1/Wi$ and the solution is given by

$$c(x) = \exp \int_0^x \left(a(s) - \frac{1}{Wi} \right) ds. \tag{3.15}$$

Of course the tensorial equation gives rise to various complications but this simple conceptual simplification is helpful in understanding the problem and was already used in [74] to study 1D analytical solutions along the streamline corresponding to the rear stagnation point.

To further grasp the physical phenomena that control where the strands form, we need to consider the full tensorial form of the equations. $\|\boldsymbol{\nabla u}\|$ can become large in different types of flow and yet the strands seem to originate from very specific regions in the domain, developing close to stagnation points, where both the elongation is strong and the residence time of the polymer is long compared to its relaxation time [28]. To better understand why these stagnation points are predominant, let us consider pure shear and pure elongational flows in a limit of very large Wi numbers–large enough that the relaxation can be neglected [82]. On a streamline, the equation of evolution of $\boldsymbol{c}$ is given by the ODE $\dot{\boldsymbol{c}} = \boldsymbol{\nabla u c} + \boldsymbol{c}(\boldsymbol{\nabla u})^{\mathsf{T}}$. If we consider the initial condition $\boldsymbol{c}(0) = \boldsymbol{I}$ and a simple shear flow with a velocity gradient given by

$$\boldsymbol{\nabla u} = \begin{pmatrix} 0 & \dot{\gamma} \\ 0 & 0 \end{pmatrix}, \tag{3.16}$$

where $\dot{\gamma}$ is the local rate-of-shear, the solution for $\boldsymbol{c}$ is

$$\boldsymbol{c}(t) = \begin{pmatrix} 1 + (\dot{\gamma} t)^2 & \dot{\gamma} t \\ \dot{\gamma} t & 1 \end{pmatrix}. \tag{3.17}$$

In the case of an elongational flow with a velocity gradient given by

$$\boldsymbol{\nabla u} = \begin{pmatrix} \dot{E} & 0 \\ 0 & -\dot{E} \end{pmatrix}, \tag{3.18}$$

with $\dot{E}$ the local rate-of-extension, the solution is

$$\boldsymbol{c}(t) = \begin{pmatrix} \exp(2\dot{E}t) & 0 \\ 0 & \exp(-2\dot{E}t) \end{pmatrix}. \tag{3.19}$$

This simple example shows that elongational flow is much more efficient in producing $tr(\boldsymbol{c})$ than shear–exponential versus power law. Points in the system that are associated with strong elongation, in particular stagnation points, thus play a key role in the formation of the strands.

We next summarize some of the key results for the flow of an Oldroyd-B fluid around a cylinder. Renardy [74] studied this problem in the limit of large Wi numbers with a fixed velocity field corresponding to a Newtonian flow past a cylinder confined in a channel–which is equivalent to considering the case $\beta = 0$, ignoring the effects of velocity boundary conditions. Along the edge of the cylinder, polymers experience simple shear that produces a thin boundary layer of stretched polymer with a width of order Wi^{-1} and a stress of order Wi. As mentioned above, the two stagnation points at the front and at the rear of the cylinder correspond to strong elongation and thus strong sources in (3.12). At the front stagnation point, polymers experience a bi-axial elongation. Past the point, they remain close to the surface, giving rise to a thin layer following the edge of the cylinder. At the rear stagnation point, polymers experience an uniaxial extension that yields a strand along the symmetry axis downstream of the cylinder. The width of the core region of this strand is of order Wi^{-2} and the stress of order Wi^3. The asymptotic analysis also predicts that the stress grows faster in a region just outside the strand in the wake, where the stress is of order Wi^5. This is because polymers in this region feel the stress from both the front and rear stagnation points. If the front stagnation point is removed, for instance by treating the cylinder wake as a flow near a flat wall as in [3], the scaling obtained is Wi^3 for the stress and Wi^{-2} for the width. This is also interesting because the scalings seem to depend little on the kinematics, as suggested in [92] where the same scalings are obtained numerically for a different type of velocity field.

For large Wi numbers, the fine structure of the strand downstream of the cylinder is thus composed of a thin zone with thickness of order Wi^{-2} and stress of order Wi^3 surrounded by a zone with stress of order Wi^5. The details of this structure are challenging to capture numerically. Figure 3.7(a) shows results of our simulations for the c_{xx} component of the conformation tensor as a function of y on the line $x = 1$–with $x = 0$ corresponding to the rear point–for $\beta = 0$ and different values of the Wi number. For Wi numbers around 2, the structure of the strand is well recovered numerically and consists of two symmetrical zones of high stress surrounding a zone of lower stress. Upon increasing the Wi number, these different zones become thinner and, beyond $Wi = 4$, the central zone is so thin that it is no longer possible to capture it with our mesh. Figure 3.7(b) shows the evolution of $\max(c_{xx})$ along lines at $x = 1$, similarly to that presented in figure 3.7(a). The zone surrounding the core of the strand scales approximately as Wi^5 from $Wi \simeq 2$, when polymers do not have time to fully relax before reaching the rear of the cylinder. These results are consistent with the theoretical analysis in [74] and with previous numerical results in [92] where, using a Lagrangian technique with a given Newtonian-like velocity field ($\beta = 0$), the authors obtained scalings for the stress components that are close to Wi^5. This transition occurs, however, for $Wi \simeq 8$ in [92] and not $Wi \simeq 2$ as in our results. This may stem from the difference between the velocity fields.

We now study the structure of the strand along the x-axis. Figure 3.7(c) shows $tr(\boldsymbol{c} - \boldsymbol{I})$ at $y = 0$ for various Wi numbers. Close to the cylinder, the polymer elongation increases until it reaches a maximum value. The slope in this region tends to increase with the Wi number so that the maximum gets closer to the cylinder. Further away from the cylinder, after the maximum, $tr(\boldsymbol{c})$ simply decays to its equilibrium value. For $Wi > 2$, this decay evolves approximately as $\exp(-x/Wi)$. For sufficiently large Wi numbers, the characteristic lengthscale for the increase of $tr(\boldsymbol{c})$ close to the cylinder becomes negligible compared to that of the relaxation and the length of the strand can thus be defined as the characteristic length in the exponential decay corresponding to the relaxation, which in dimensionless form is simply the Wi number. As we will see, the length of the strand is an important information for understanding the effect on the flow and, in the case of flows in more complex geometries, the interaction between the strand and geometric structures.

Finally, we plot the evolution of $\max(tr(\boldsymbol{c}-\boldsymbol{I}))$ on the line $y=0$ as a function of the Wi number. At low Wi numbers, the evolution is close to quadratic with a transition around $Wi \simeq 1$ leading to a scaling in Wi^5 at large Wi numbers. We hypothesize that this evolution in Wi^5, and not in Wi^3 as theoretically expected, results from the impossibility of the mesh to capture the fine structure of the strand in the y direction for large Wi numbers. The extremely thin zones scaling in Wi^5 and Wi^3 mix in the relatively coarse mesh and the strand appears as made up of an unique zone that evolves as Wi^5.

3.3.3 Feedback of the strand on the flow

We are now interested in understanding how this strand modifies the flow. We start our analysis with asymptotics in β, which yields a detailed picture of the feedback and the mechanisms corresponding to each order. We then move on to presenting results for the general case $\beta > 0$.

β asymptotics Much work on flow of viscoelastic fluids has been done by considering the low Wi number (weakly nonlinear) regime. However, the formation of the strands and the large stress concentration downstream objects cannot be captured through Wi asymptotics. Another approach to simplifying the transport equations and still capture the strands is to consider the limit β small, which may be thought of as the limit of low polymer concentrations. This method was introduced for flow around a sphere by Moore and Shelley [65] and has been used to study stress localization for high Wi at extensional points and around objects by Li et al. [55].

We consider a case where Wi scales as $O(1)$ and β is a small parameter that is $o(1)$. We express a one-way coupling solution of this problem as

$$\begin{aligned} p &\simeq p^0 + \beta p^1, \\ \boldsymbol{u} &\simeq \boldsymbol{u}^0 + \beta \boldsymbol{u}^1, \\ \boldsymbol{c} &\simeq \boldsymbol{c}^0. \end{aligned} \tag{3.20}$$

At order 0, the velocity field is Newtonian

$$\begin{aligned} -\boldsymbol{\nabla} p^0 + \boldsymbol{\nabla} \cdot \left(\boldsymbol{\nabla} \boldsymbol{u}^0 + \left(\boldsymbol{\nabla} \boldsymbol{u}^0 \right)^{\mathsf{T}} \right) + \boldsymbol{F} = 0, \\ \boldsymbol{\nabla} \cdot \boldsymbol{u}^0 = 0, \end{aligned} \tag{3.21}$$

and the transport equation for the conformation tensor reads

$$\partial_t \boldsymbol{c}^0 + \boldsymbol{u}^0 \cdot \boldsymbol{\nabla} \boldsymbol{c}^0 = \boldsymbol{\nabla} \boldsymbol{u}^0 \boldsymbol{c}^0 + \boldsymbol{c}^0 \left(\boldsymbol{\nabla} \boldsymbol{u}^0 \right)^{\mathsf{T}} - \frac{1}{Wi} (\boldsymbol{c}^0 - \boldsymbol{I}). \tag{3.22}$$

The solution for $(p^0, \boldsymbol{u}^0)$ and $\boldsymbol{c}^0$ thus corresponds to the case presented in the previous Section with $\beta = 0$. At order 1, the pressure and velocity correction fields are given by

$$\begin{aligned} -\boldsymbol{\nabla} p^1 + \boldsymbol{\nabla} \cdot \left(\boldsymbol{\nabla} \boldsymbol{u}^1 + \left(\boldsymbol{\nabla} \boldsymbol{u}^1 \right)^{\mathsf{T}} \right) + \frac{1}{Wi} \boldsymbol{\nabla} \cdot \left(\boldsymbol{c}^0 - \boldsymbol{I} \right) = 0, \\ \boldsymbol{\nabla} \cdot \boldsymbol{u}^1 = 0. \end{aligned} \tag{3.23}$$

The field $\boldsymbol{u}^1$ thus represents the feedback induced by the strand upon Stokes flow. The $(p^1, \boldsymbol{u}^1)$ correction is solved numerically using the fractional step approach given by (3.9).

Figure 3.8 shows the structure of the force field, $\boldsymbol{\nabla} \cdot \boldsymbol{c}^0$, generated by the presence of the polymers. We see that the force is oriented in the direction of the flow close to the cylinder and opposite to the flow everywhere else. This corresponds to polymers being first stretched and

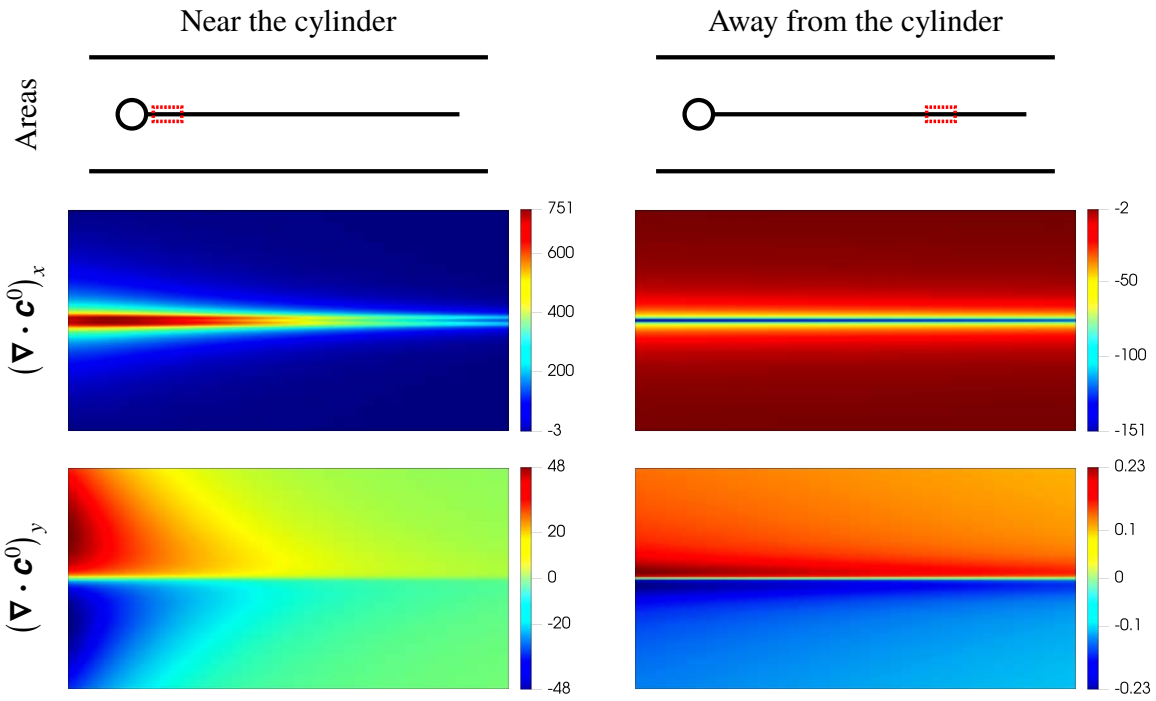

Fig. 3.8 Flow past one cylinder in the case $\beta = 0$ and $Wi \simeq 9$. Magnified areas near (left) and away (right) from the cylinder for the first and second components of $\nabla \cdot \boldsymbol{c}^0$.

then relaxing towards their equilibrium position. Further, the force is primarily tangential to the strand in both regions, with a normal component that is several orders of magnitude smaller. Therefore, the strand essentially acts as a line distribution of forces that are oriented in the direction of the flow in a small elongation zone close to the cylinder and then opposite to the direction of the flow where relaxation dominates.

The idea that the strand acts as a line distribution of tangential forces was already used in [26], whereby the system is simplified as a line distribution of forces within an otherwise Newtonian fluid. The analysis starts by considering that the flow around the strand is mainly horizontal and that the dominant terms in the equation of motion are

$$2\partial_{xx}u_x^1 + \partial_{yy}u_x^1 + \frac{1}{Wi}\left(\partial_x c_{xx}^0\right)_{|y=0}\delta(y) = \partial_x p^1, \tag{3.24}$$

where δ is a Dirac function associated with an "infinitely thin" strand. Integrating through the strand and making its width tend towards 0 then leads to

$$\left[\partial_y u_x^1\right]_{y=0} = -\frac{1}{Wi}\left(\partial_x c_{xx}^0\right)_{|y=0}, \tag{3.25}$$

so that stretched polymers give rise to a jump in shear-stress across the strand. By symmetry, we have

$$\partial_y u_x^1\left(0^+\right) = -\partial_y u_x^1\left(0^-\right) = -\frac{1}{2Wi}\left(\partial_x c_{xx}^0\right)_{|y=0}. \tag{3.26}$$

Therefore, the strand can also be seen as a Neumann boundary condition for u_x^1. Since the Newtonian case corresponds to $\partial_y u_x^1(0) = 0$, the sign of $\left(\partial_x c_{xx}^0\right)_{|y=0}$ determines whether the strand tends to reduce or increase the viscous shear stress on the central line–and therefore whether the strand slows down or accelerates the flow compared to the Newtonian case.

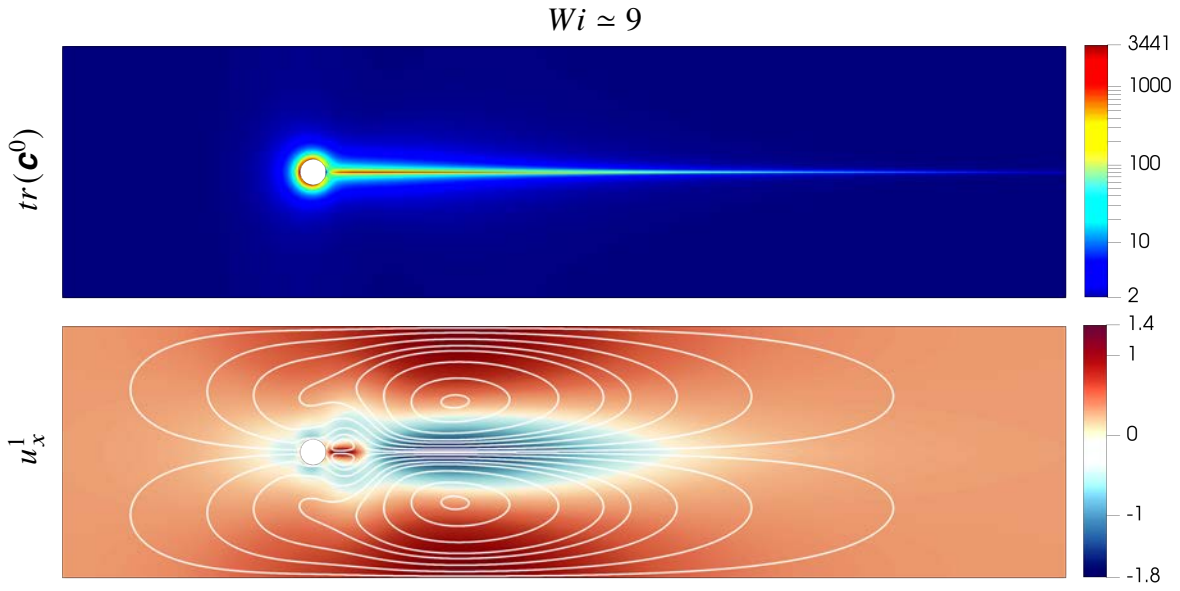

Fig. 3.9 Flow past one cylinder with $Wi \simeq 9$ and biperiodic boundary conditions. Plots of (top) the trace of the zero order conformation $\boldsymbol{c}^0$ and (bottom) the longitudinal component of the first order velocity u_x^1 with streamlines.

Figure 3.9 shows the corresponding component u_x^1 of the velocity in the case $Wi \simeq 3.3$. Close to the cylinder, where the elongation of the polymers increases $(\partial_x c_{xx}^0 > 0)$, the velocity perturbation u_x^1 is positive and $u_x^0 + \beta u_x^1$ is larger than Stokes velocity. In the second zone, which is much longer, the conformation tensor relaxes towards the identity with $\partial_x c_{xx}^0 < 0$, u_x^1 is negative and the strand slows down the flow over most of its length. For a given flow rate, this reduction in velocity close to the strand results, by conservation, in a velocity increase away from it and in a for-aft symmetry breaking compared to Stokes flow solution.

In the Oldroyd-B equations, the coupling is two-ways so that this modification in the velocity field will, in turn, affect the formation of the strand. In the case of a single cylinder, the streamline is unaffected by $\boldsymbol{u}^1$ and the strand will remain on the horizontal line. However, the transport velocity along the streamline is modified and $\boldsymbol{\nabla u}$ also changes with $\boldsymbol{u}^1$ so that the profile of $\boldsymbol{c}$ is modified in both x and y directions. This effect is evident when considering the order-1 correction of the conformation tensor,

$$\boldsymbol{c} \simeq \boldsymbol{c}^0 + \beta \boldsymbol{c}^1. \tag{3.27}$$

The corresponding transport equation for $\boldsymbol{c}^1$ is

$$\partial_t \boldsymbol{c}^1 + \boldsymbol{u}^0 \cdot \boldsymbol{\nabla c}^1 - \boldsymbol{\nabla u}^0 \boldsymbol{c}^1 - \boldsymbol{c}^1 \left(\boldsymbol{\nabla u}^0\right)^{\mathsf{T}} + \frac{1}{Wi} \boldsymbol{c}^1 = -\boldsymbol{u}^1 \cdot \boldsymbol{\nabla c}^0 + \boldsymbol{\nabla u}^1 \boldsymbol{c}^0 + \boldsymbol{c}^0 \left(\boldsymbol{\nabla u}^1\right)^{\mathsf{T}}. \tag{3.28}$$

The left-hand side of this equation is the linear operator for the transport of $\boldsymbol{c}^1$ and terms on the right-hand are the sources. These sources capture the changes in the velocity field, through $\boldsymbol{u}^1$ and $\boldsymbol{\nabla u}^1$, generated by the strand with a fixed velocity.

General case We now turn to the fully coupled case. Figure 3.10(a) shows the trace of the conformation tensor for different values of β. The global structure of the field is similar to that of the order-zero approximation. There is an initial increase due to the elongation of polymers

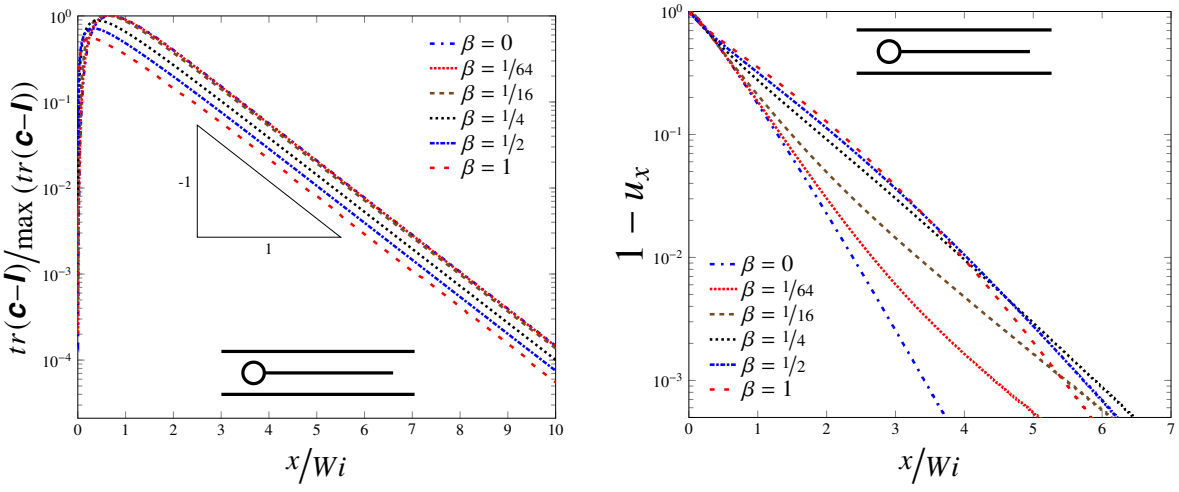

(a) $tr(\boldsymbol{c}-\boldsymbol{I})/\max(tr(\boldsymbol{c}-\boldsymbol{I}))$ (b) $1-u_x$

Fig. 3.10 Flow past a single cylinder in the case $Wi = 4$. (a) $tr(\boldsymbol{c}-\boldsymbol{I})$ normalized by its max and (b) $1-u_x$ along the centerline in the near wake of the cylinder for different values of β.

close to the cylinder and then a relaxation in $\exp(-x/Wi)$. However, the behaviour differs quantitatively. The intensity of the peak $tr(\boldsymbol{c})$ reduces with increasing β. For $\beta > 0$, the strand slows down the flow, therefore reduces the velocity and the velocity gradients in the wake, which results in a decrease in the peak value of $tr(\boldsymbol{c})$, as discussed for the order-1 correction in β.

For the velocity field, previous results remain valid for the jump in shear-stress across the strand [see 26]

$$[\partial_y u]_{y=0} = -\frac{\beta}{Wi}\,(\partial_x c_{xx})_{|y=0}\,. \tag{3.29}$$

The strand accelerates or decelerates the flow depending on the sign of $\partial_x c_{xx}$. The difference here is that the field $\boldsymbol{c}$ is no longer fixed and is corrected by feedback effects. Figure 3.10(b) shows the profile of $1-u_x$ at the centreline in the wake of the cylinder for different values of β and $Wi = 4$. At $\beta = 0$, the velocity evolves as $1-\exp(-x/b)$ where, with our boundary conditions, $b \approx 0.3$. Larger values of β lead to an increase of the velocity in the wake close to the cylinder and to a decrease of the velocity further away from the cylinder. For $\beta \geq 0.5$, we observe a behaviour that is monotonic just after the elongation zone but then becomes non-monotonic sufficiently far away from the cylinder. In this last region, we see that $1-u_x$ goes faster to zero in the case $\beta = 1$ than in the case $\beta = 1/16$. This is actually a signature of a strong feedback, whereby the strand slows down the fluid so much that the length of the strand starts to decrease (see figure 3.10(b) and associated paragraph). Once the strand has disappeared, the velocity profile returns to a Newtonian behaviour and the slope goes back to the one observed in the case $\beta = 0$.

3.3.4 Summary of important properties of the strand

- In 2D, strands are very thin zones of highly stretched polymers (large $tr(\boldsymbol{c})$) that originate from the cylinder stagnation points and follow the streamlines at steady-state.
- The unique strand that appears in the wake of the cylinder is a composition of strands originating from the two stagnation points. Its fine structure in the direction transverse to the flow reflects this origin, with several zones of different width and Wi scalings.

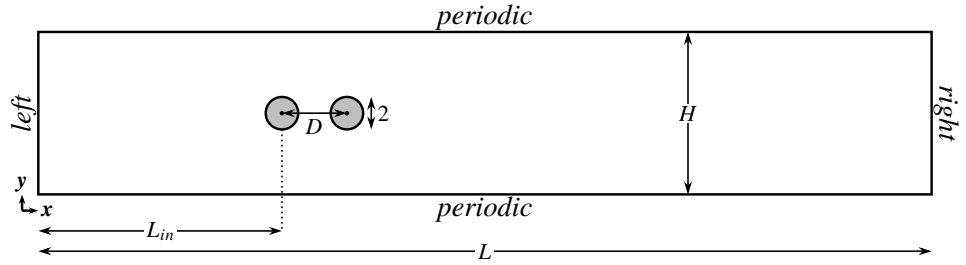

Fig. 3.11 Schematics of the geometry for two cylinders aligned with the flow. The lengthscales of the system are $H = 20$ the height of the domain, D the distance between the cylinders centers, $L_{in} = 25$ the distance from the inlet to the center of the cylinder and L the total length of the domain. The length $L = L_{in} + D + 30Wi$ is chosen sufficiently large so that the conformation tensor relaxes to its equilibrium value $\boldsymbol{c} = \boldsymbol{I}$ before reaching the boundary condition on the right-hand side. The boundary conditions are top-bottom periodicity and $\boldsymbol{u} = \boldsymbol{0}$ on the cylinder. Left/right boundary conditions are either inlet/outlet conditions or periodicity, depending on the calculation. Meshes are uniform structured grids where the cylinders are defined by holes.

- In the direction of the flow, $tr(\boldsymbol{c})$ first increases, reaches a maximum and then decreases as $\exp(-x/Wi)$. For sufficiently large Wi numbers, the length of the strand can be approximated as Wi.
- The strand acts as a line distribution of tangential forces. For sufficiently large Wi numbers, these forces oppose the flow over most of the strand length. The primary effect of the strand is therefore to slow down the flow in its vicinity.

3.4 Steady viscoelastic flow past two cylinders

Here we consider two different cases, each with two cylinders but with orthogonal orientations of the flow. The first case focuses on two cylinders aligned with the direction of the flow, while in the second case the two cylinder centers define a line forming a 90 degree angle with the flow; in the latter situation, we say for short in the following that the cylinders are orthogonal to the flow. The idea is to progressively build up in complexity towards a large array of cylinders, as shown in figure 3.2. Two cylinders represent the minimal system allowing us to study how high-stress strands interact with solid surfaces and with each other.

3.4.1 Cylinders aligned with the flow

We first focus on two cylinders aligned with the flow as presented in figure 3.11. When the distance between the two cylinders, D, is comparable with the diameter of the cylinders, the Newtonian velocity field is different from the case with only one cylinder and presents a stagnation zone between the two cylinders. The left column in figure 3.12 shows a case where D is three times the radius of the cylinders, $D = 3$. The morphology of the high-stress zones is completely modified and the two cylinders behave in a way that is similar to a single elongated object. The rear stagnation point of the second cylinder is the origin of a strand that is very similar to that of the case with one cylinder. The front stagnation point of the first cylinder also generates high-stress zones that are similar to the case with one cylinder, but with the difference that they envelope the two cylinders rather than just a single one. Kumar and Ardekani [51] studied the flow of a FENE-P fluid around 2 aligned cylinders in a channel with a relatively high value of β–$\beta = 19$ with our definitions. A similar envelope was observed around the two closely placed

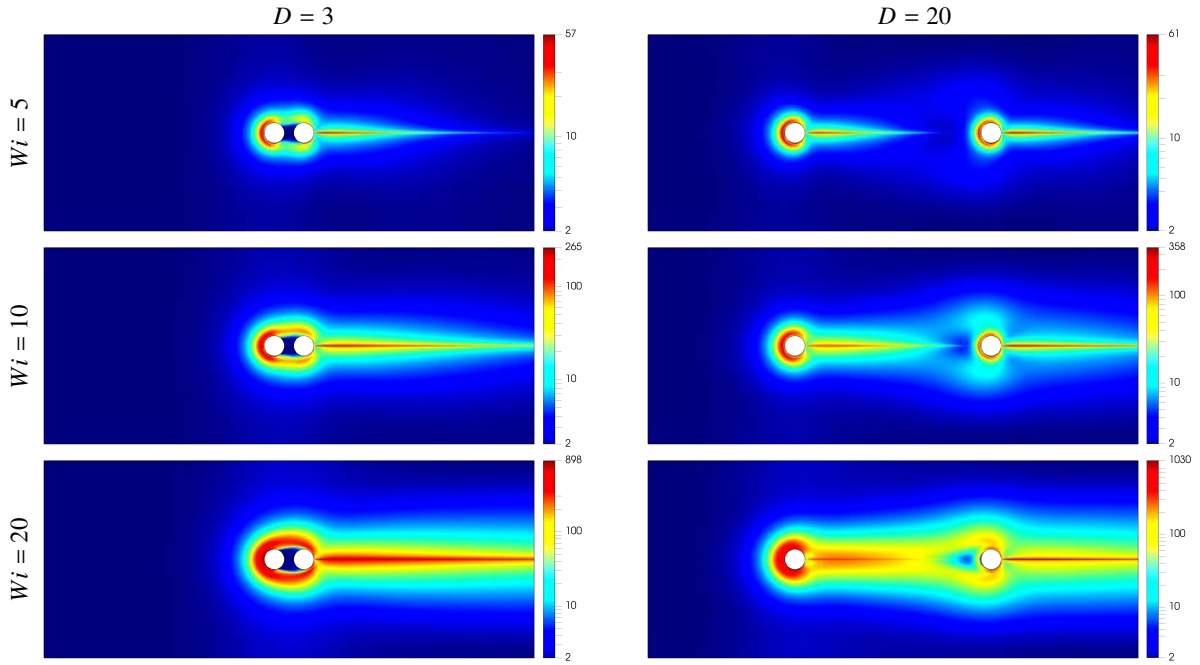

Fig. 3.12 Flow past two cylinders aligned with the flow with $\beta = 1$. $tr(\boldsymbol{c})$ as a function of the Wi number in the case $D = 3$ (left) and $D = 20$ (right). From top to bottom, $Wi = 5$, $Wi = 10$ and $Wi = 20$. Boundary conditions are inlet/outlet conditions.

cylinders, as well as a recirculation zone between the cylinders that forms at relatively small Wi number, $Wi = 1.88$, which can be explained by the high value of β. Increasing further the Wi number, a transition to asymmetric flow is observed, which can be attributed to shear-thinning in the FENE-P model [32].

The right column in figure 3.12 shows the evolution of the strands with the Wi number in the case $D = 20$. When the distance between the two cylinders, D, is significantly larger than their diameter, the Newtonian flow is similar to that of the case with one cylinder. Furthermore, for sufficiently low Wi numbers, the strand generated in the wake of the first cylinder disappears before reaching the second cylinder so that the situation is that of two isolated cylinders without interactions. When the Wi number is increased, the strands become longer until the first strand reaches the second cylinder. When that happens, the first strand starts separating into two parts and forms an envelope encapsulating the second cylinder. As the Wi number is increased further, the envelope gets larger and expands upstream of the second cylinder, encapsulating both the cylinder and a fluid region of relatively low stress. Such an interaction was already observed experimentally in viscoelastic flows using birefringence and micro-particle image velocimetry [37], with the strand encapsulating the second cylinder and creating a stagnation zone upstream of the second cylinder.

One important aspect of the interaction between the strands and solid obstacles is the formation of an envelope around the cylinders. The simplest case is the one where the distance between the cylinders is similar to the diameter of the cylinders, which always leads to the formation of an envelope. When the distance between the cylinders is much larger than the diameter, the envelope starts forming when the first strand reaches the second cylinder. The formation of the envelope is thus controlled by the distance between the cylinders and the relaxation time of the polymer. The length of the strand can be approximed as Wi but the Wi number does not contain any information about the distance between the cylinders, thus

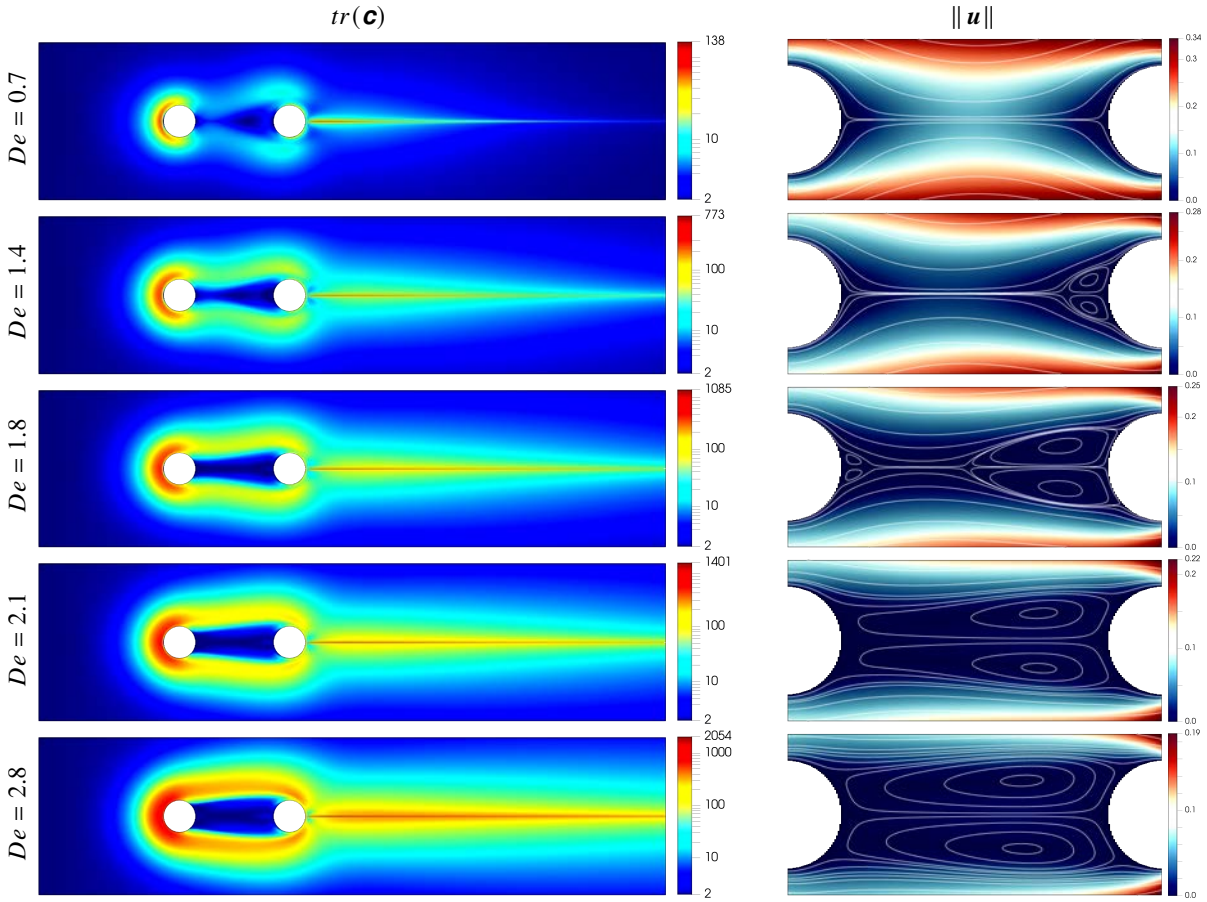

Fig. 3.13 Flow past two cylinders aligned with the flow in the case $\beta = 1$, $D = 7$ and inlet/outlet boundary conditions. (a) $tr(\boldsymbol{c})$ and (b) velocity magnitude with streamlines magnified between the cylinders, as a function of the De number. From top to bottom, $De = 0.7$, $De = 1.4$, $De = 1.8$, $De = 2.1$ and $De = 2.8$.

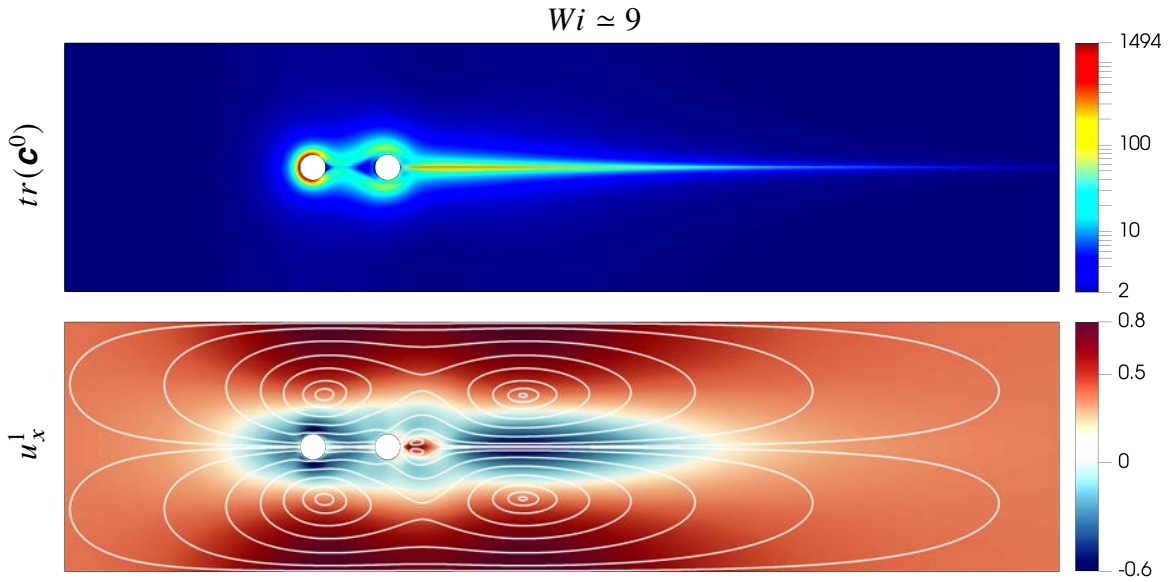

Fig. 3.14 Flow past two aligned cylinders with $Wi \simeq 9$, $De \simeq 1.5$ and biperiodic boundary conditions. Plots of (top) the trace of the zero order conformation $\boldsymbol{c}^0$ and (bottom) the longitudinal component of the first order velocity u_x^1 with streamlines.

cannot capture this transition. To characterize the transition, the length of the strand must be compared to the distance between the cylinders using a Deborah number $De = {}^{Wi}/_{D}$. This De number corresponds to the ratio between the relaxation time of the polymer and the transport time from the first to the second cylinder, $De = {}^{\lambda U}/_{DR}$–recall that D is dimensionless here so that DR is simply the dimensional distance between cylinders. A De number much larger than 1 means that the relaxation time is much larger than the transport time, so that the envelope forms. On the contrary, when the De number is much smaller than 1 the strand disappears before reaching the second cylinder and the envelope does not form.

We now focus on the role of the strands and envelope on the velocity field. We consider an intermediate case with a distance $D = 7$, which allows us to study a wide range of De numbers without reaching very large Wi numbers that cannot be accurately computed. Figure 3.13 shows a detailed analysis of the correspondence between the fields for the trace of the conformation tensor and for the velocity. For moderate De numbers, two symmetrical counter-rotating vortices appear just upstream the second of cylinder. If we increase the De number, the two strands move apart and the vortices expand upstream until they completely fill the area between the two cylinders. For the zone within the envelope, the flow is reminiscent of a symmetric two-sided lid-driven cavity with symmetric counter-rotating vortices. For the flow outside this region, the two cylinders and the envelope essentially act as a large obstacle.

To better understand how this envelope expands upstream the second cylinder, we use asymptotics in β as done previously in the case with one cylinder. Figure 3.14 shows both $tr(\boldsymbol{c}^0)$ and the first order correction to the velocity, u_x^1. Between the two cylinders, the direct effect of the envelope is to produce negative values u_x^1 and therefore to slow down the flow compared to Stokes flow. This creates a positive feedback effect whereby the stagnation zone between the cylinders increases, which has the consequence of reducing the curvature of the streamlines and pushing the two strands away from each other, which in turn makes the stagnation zone larger. This mechanism can also be observed in figure 3.15, which shows the evolution of the envelope

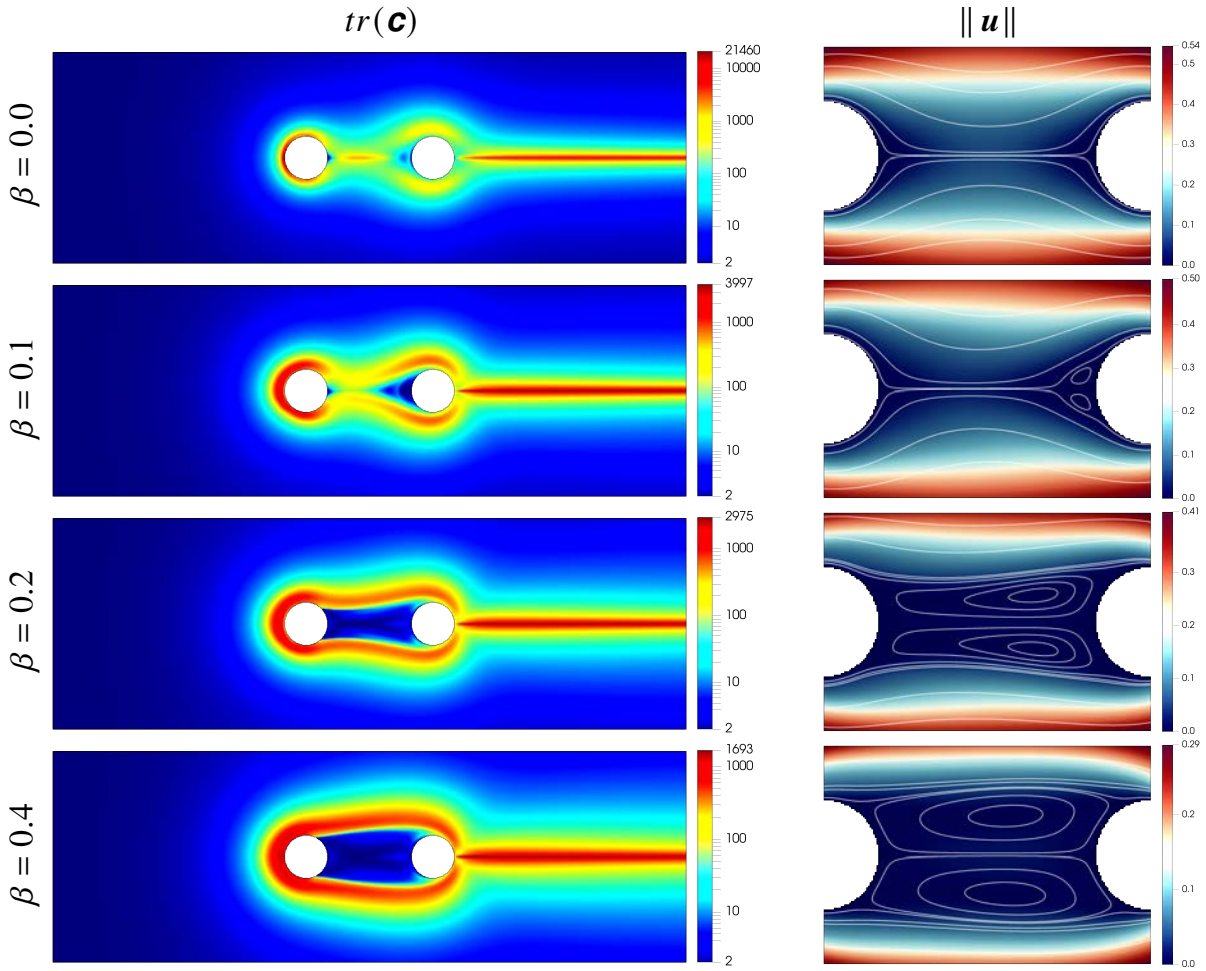

Fig. 3.15 Flow past two cylinders aligned with the flow with $Wi = 20$, $De = 3.33$ and inlet/outlet boundary conditions. $tr(\boldsymbol{c})$ (left) and velocity magnitude with streamlines (right) as a function of β. Top to bottom, $\beta = 0$, $\beta = 0.1$, $\beta = 0.2$ and $\beta = 0.4$.

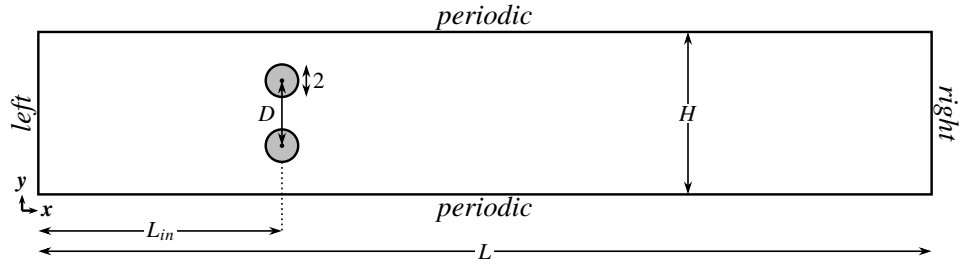

Fig. 3.16 Schematics of the geometry for two cylinders orthogonal to the direction of the flow. The lengthscales of the system are $H = 20$ the height of the domain, D the distance between the cylinders centers, $L_{in} = 25$ the distance from the inlet to the center of the cylinder and L the total length of the domain. The length $L = L_{in} + 30Wi$ is chosen sufficiently large so that the conformation tensor relaxes to its equilibrium value $\boldsymbol{c} = \boldsymbol{I}$ before reaching the boundary condition on the right-hand side. This geometry is characterized by the gap ratio, $G = \frac{D-2}{H-(D+2)}$. The boundary conditions are top-bottom periodicity and $\boldsymbol{u} = \boldsymbol{0}$ on the cylinder. Left/right boundary conditions are either inlet/outlet conditions or periodicity, depending on the calculation. Meshes are uniform structured grids where the cylinders are defined by holes.

as a function of the parameter β controlling the amplitude of the feedback. By increasing β, the two strands progressively separate, forming an envelope which encloses the two cylinders.

3.4.2 Cylinders orthogonal to the direction of the flow

We now consider the case of two cylinders orthogonal to the direction of the flow as presented in figure 3.16. As we will see, this geometry allows us to study the interactions of strands with each other and the effect of these strands on the flow paths. Thanks to the periodic boundary conditions, the computed solution corresponds to an infinite set of cylinders aligned along a vertical line and separated by D (for the cylinders present in the computational domain Ω, see figure 3.16) and $D' = H - D$ (for a cylinder in Ω and the nearest cylinder outside Ω). The fluid thus flows through two gaps of height $D-2$ and $H-D-2$ respectively. We define G as the ratio between these two gaps, $G = \frac{D-2}{H-D-2}$.

We are first interested in the evolution of the strands and of the velocity field as a function of the Wi number. Results are presented in figure 3.17 for $G = 0.6$ (so $D < D'$). Consistent with previous results, we observe the formation of a strand behind each cylinder, which grows in length and intensity with the Wi number. Unlike the case with a single cylinder, however, the strands are curved and progressively get closer to each other with increasing the Wi number. The flow through the center gap is always smaller than above and below, but this difference increases with the Wi number. In the Newtonian limit, the difference in flow rates is simply because of the asymmetry (i.e. the fact that $D < D'$). There is thus an existing preferential flow path above and below the two cylinders. For larger Wi numbers, the strands tend to slow down the fluid in the center gap even more, further amplifying preferential flow. This effect is quantified in figure 3.18 using calculations of the flow rates through the center gap Q, normalized by the Newtonian value Q_N, as a function of the Wi number for different values of G. The flow rate decreases with the Wi number for $G < 1$ and increases for $G > 1$. In the case $G = 1$, the strands are horizontal and Q/Q_N remains constant.

To better understand how the coupling works, we use asymptotics in β. Figure 3.19 shows the dependence of $tr(\boldsymbol{c}^0)$ upon the gap ratio G for $Wi = 10$. Again, by changing G, we modify the Newtonian velocity field and the relative flow rates between the central and peripheral gaps. This changes the curvature of the streamlines and thus of the strands, with strands remaining

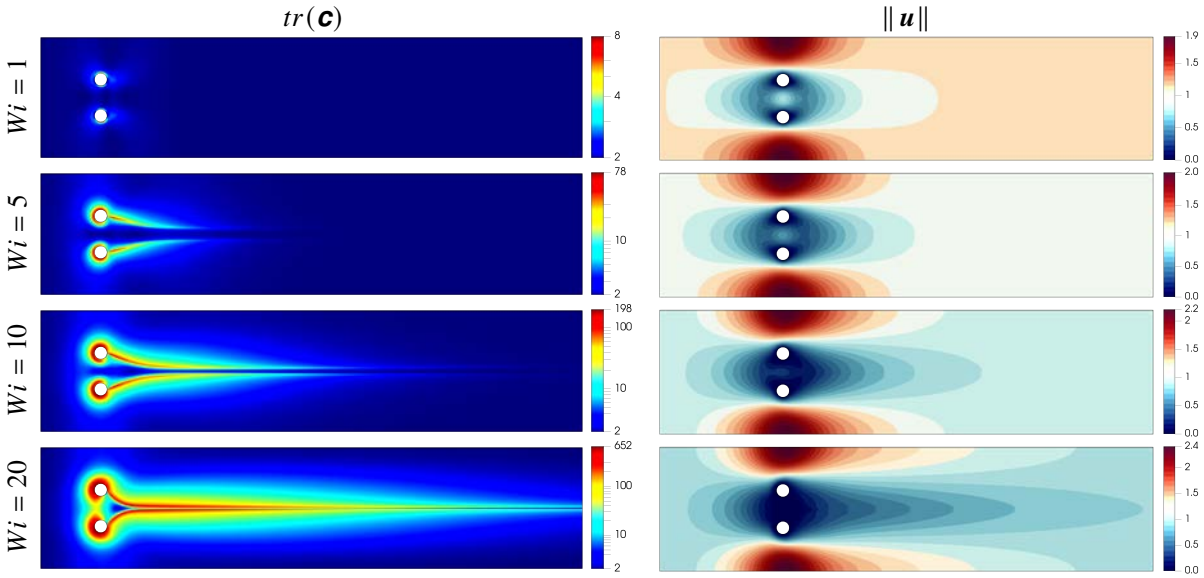

Fig. 3.17 Flow past two cylinders orthogonal to the flow in the case with $\beta = 1$, $G = 0.6$ and inlet/outlet boundary conditions. $tr(\boldsymbol{c})$ (left) and velocity magnitude (right) as a function of Wi. Top to bottom, $Wi = 1$, $Wi = 5$, $Wi = 10$ and $Wi = 20$.

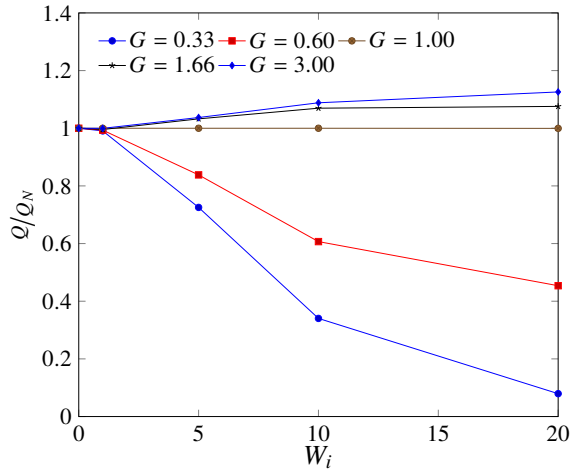

Fig. 3.18 Flow past two cylinders orthogonal to the flow in the case $\beta = 1$. Flow rate between the cylinders, normalized by the Newtonian value, as a function of the Wi number for different values of the gap ratio G.

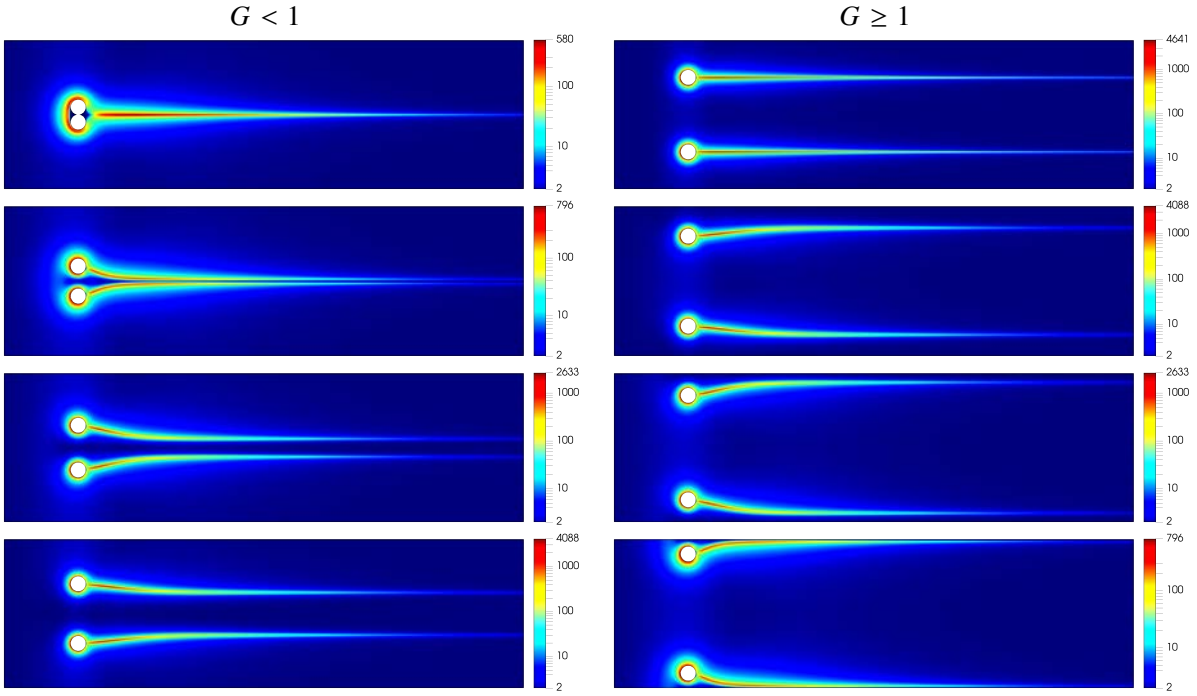

Fig. 3.19 Flow past two cylinders orthogonal to the flow in the case with $\beta = 0$, $Wi = 10$ and inlet/outlet boundary conditions. $tr(\boldsymbol{c}^0)$ as a function of G . Left: $G < 1$, from top to bottom $G = 0$, $G = 0.14$, $G = 0.33$ and $G = 0.6$. Right: $G \geq 1$, from top to bottom $G = 1$, $G = 1.67$, $G = 3$ and $G = 7$.

completely horizontal only for $G = 1$. Let us now look in detail at the case of a small value of the gap ratio, $G = 0.33$, in figure 3.20. We see that the strands tend to slow down the fluid within the central gap for the longitudinal component of u_x^1. In turn, this curves the streamlines even more and therefore tends to get the two strands closer to each other. Figure 3.21 shows that large values of β increase the feedback upon the flow, reduce the flow rate in the central gap and get the strands closer to each other. This is quantified in figure 3.22, which shows how the flow rate between the cylinders depends upon β for different values of G.

This effect of amplification of the preferential flow paths of the Newtonian regime was recovered numerically in [49] using a two-species Vasquez–Cook–McKinley (VCM) constitutive model and observed experimentally in [40]. For small gap ratios and sufficiently large Wi numbers, [40] describes another transition with a symmetry breaking where the fluid selects a single preferential flow path either above or below the pair of cylinders. This second transition is attributed to shear-thinning–thus outside the scope of our work–and was also observed around a single cylinder in [33, 30, 86].

3.4.3 Summary of important properties of strand interactions

- For the case with two cylinders aligned with the flow, the interaction between a strand generated by a cylinder with another cylinder positioned downstream depends on the distance between the cylinders and is characterized by a De number. When the De number is low, the strand of each cylinder behaves as in the case of a single isolated cylinder. When the De number is of order 1 or larger, the strands splits in two, creating a low-velocity stagnation zone upstream of the downstream cylinder. For sufficiently large De numbers, the strands form an envelope encapsulating the two cylinders with a

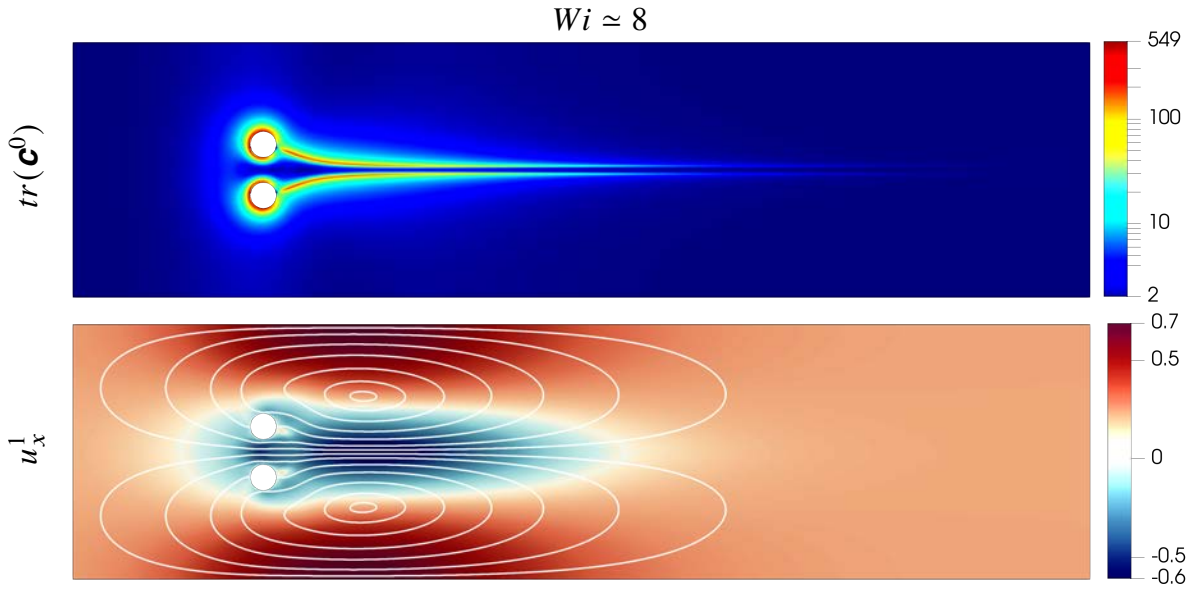

Fig. 3.20 Flow past two cylinders orthogonal to the flow with $Wi \simeq 8$, $G = 0.23$ and biperiodic boundary conditions. Plots of (top) the trace of the zero order conformation $\boldsymbol{c}^0$ and (bottom) the longitudinal component of the first order velocity u_x^1 with streamlines.

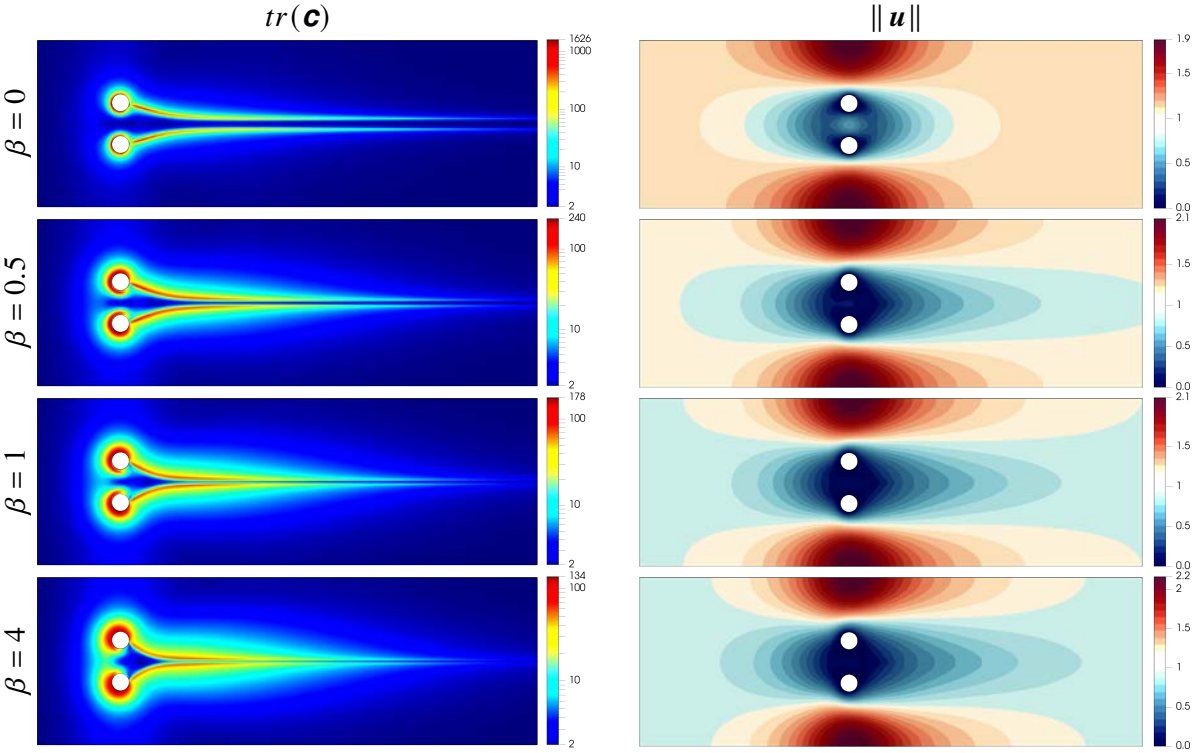

Fig. 3.21 Flow past two cylinders orthogonal to the flow with $Wi = 10$, $G = 0.23$ and inlet/outlet boundary conditions. $tr(\boldsymbol{c})$ (left) and velocity magnitude (right) as a function of β. From top to bottom, $\beta = 0$, $\beta = 0.5$, $\beta = 1$ and $\beta = 4$.

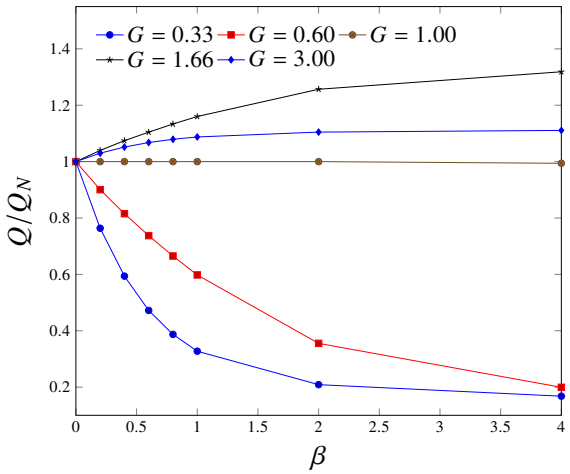

Fig. 3.22 Flow past two cylinders orthogonal to the flow with $Wi = 10$. Flow rate between the cylinders, normalized by the Newtonian value, as a function of β for different values of G.

flow inside inside the envelope that is reminiscent of a two-sided lid-driven cavity with symmetric counter-rotating vortices. This is also the case when the distance between the cylinders is comparable with their diameter, the Newtonian velocity field has a stagnation zone between the two cylinders and the strands generated by the first cylinder envelope the two cylinders.

- For the case with two cylinders orthogonal to the flow, the strands amplify existing preferential flow paths. This is because the strands are curved towards the low flow channel and slow down the flow, thus redirecting it towards channels with already larger flows. This creates a positive feedback effect where the strands are further curved and slow down the flow in the low flow channel even more.

3.5 Steady viscoelastic flow through an array of cylinders

We now turn to the core part of this paper. Until now, we have used simple model cases to highlight the fundamental mechanisms that drive the formation of the strands, the feedback upon the flow, in particular the increase of the stagnation zones and the amplification of the preferential flow paths. Here we describe how these mechanisms operate in more complex porous systems consisting of cylinder arrays. The idea is to start by studying the pore-scale velocity and conformation fields for crystalline and amorphous arrays over a range of Wi numbers. We then analyze the pressure drop through energetic and entropic considerations and pinpoint the mechanisms yielding an apparent increase of resistance to flow at Darcy-scale.

3.5.1 Preferential flow paths

The geometry considered is presented figure 3.23. We start from a 10×10 crystalline structure of cylinders organized on a square lattice with a period (i.e. the distance between the cylinder centers along a line or a row) $P = 4$. We then generate several amorphous porous structures by disordering the structure. To do so, we displace each cylinder independently by sampling each component of the displacement vector from a uniform distribution between 0 and ε and allowing for overlaps between cylinders. Here again, the position of the strands is not pre-established. We will therefore consider uniform structured meshes where the cylinders are holes.

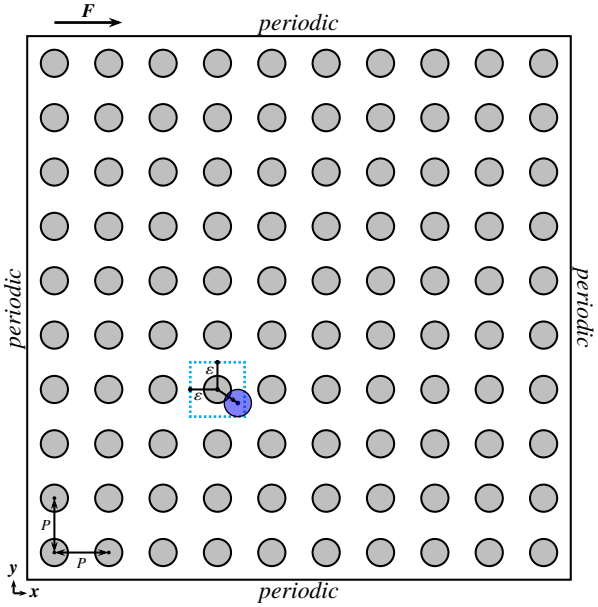

Fig. 3.23 Schematics of the 10×10 crystalline cylinder structure and example of random displacement (blue cylinder) with a maximum displacement ε. Boundary conditions are biperiodic and the flow is imposed through a body force $\boldsymbol{F}$. Meshes are uniform structured grids where the cylinders are defined by holes.

Figure 3.24 shows the dependence of $tr(\boldsymbol{c})$ upon both ε and Wi. In the crystalline case, the pattern of $tr(\boldsymbol{c})$ is similar to the configuration with two cylinders aligned with the flow. An envelope forms around successive cylinders and creates a stagnant zone between cylinders. The difference with the case with two cylinders is, of course, the periodicity of the pattern. This structure of the field of $tr(\boldsymbol{c})$ is very specific to the crystalline structure. In amorphous cases, we observe patterns that are a lot more complex but can be interpreted on the basis of configurations with one or two cylinders. When cylinders are very close to each other, they are surrounded by an envelope of high polymeric stress making the aggregate of cylinders essentially act as a single obstacle, which is similar to what we observed for two cylinders. We also see that strands originate from stagnation points of the cylinders, as we described for a single cylinder. A strand formed in the wake of a cylinder will interact with cylinders downstream, bypassing some cylinders and surrounding others, consistent with the configuration with two cylinders aligned with the flow. It will also interact with the other strands, sometimes coming together with others to form a single strand, as observed for two cylinders orthogonal to the flow.

As we have seen before, strands and envelopes also modify the flow. Figure 3.25 shows both $tr(\boldsymbol{c})$ and the velocity field as a function of the Wi number for a realization corresponding to $\varepsilon = 3$. When increasing the Wi number, we observe primarily three effects of the strands and envelopes:

1. an increase of stagnation zones, which are created in fluid zones trapped between strands or inside envelopes. Figure 3.26(A) shows an example of cylinders being surrounded by an envelope at $Wi \simeq 11.5$ and not at $Wi \simeq 1.5$. At $Wi \simeq 1.5$, the fluid flows between the cylinders and not at $Wi \simeq 11.5$, where we clearly see the creation of a stagnation area. Figure 3.27 shows the corresponding probability density functions (PDFs) for the x-component of the velocity field, u_x. These PDFs allow us to summarize the complex 2D fields presented figure 3.25 on a relatively simple 1D graph. They can be understood as normalized histograms for the velocity fields and are constructed similarly to those in

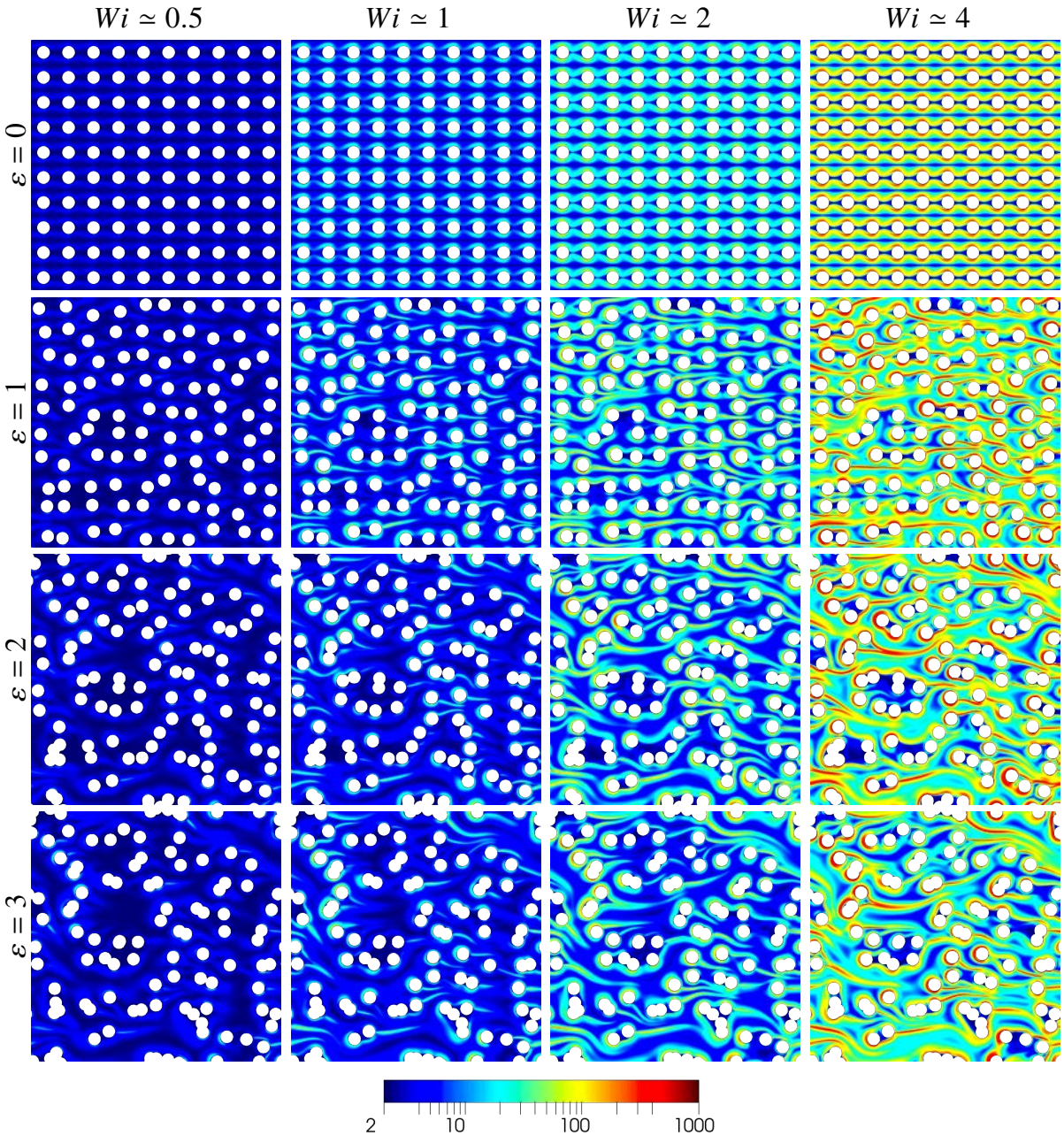

Fig. 3.24 Flow through arrays of cylinders for $\beta = 1$. Table of $tr(\boldsymbol{c})$ fields as a function of the Wi number and of the maximum displacement, ε, of each cylinder.

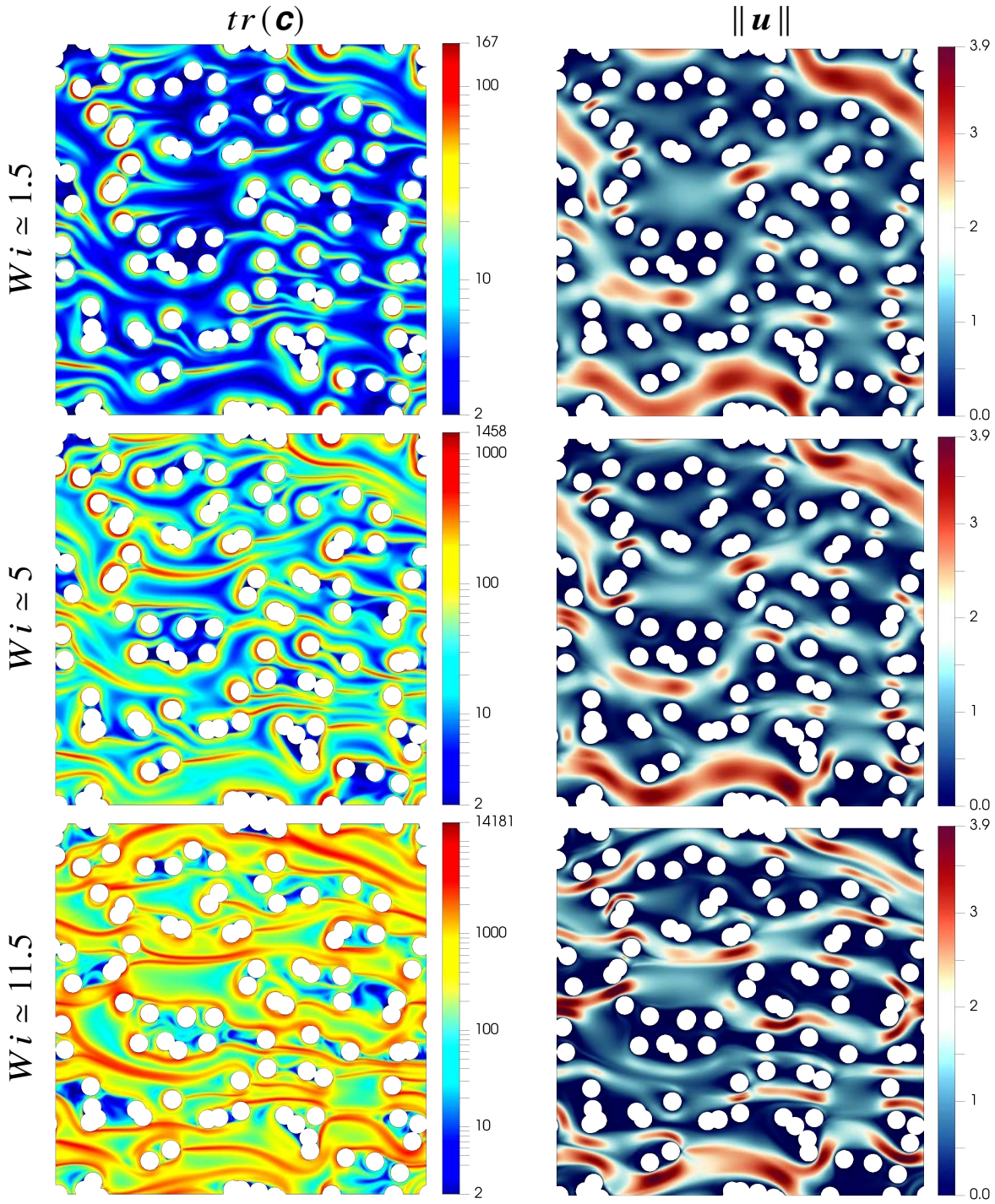

Fig. 3.25 Flow through an array of cylinders in the case $\beta = 1$ and $\varepsilon = 3$. $tr(\boldsymbol{c})$ (left) and velocity magnitude (right) as a function of the Wi number. From top to bottom, $Wi \simeq 1.5$, $Wi \simeq 5$ and $Wi \simeq 11.5$.

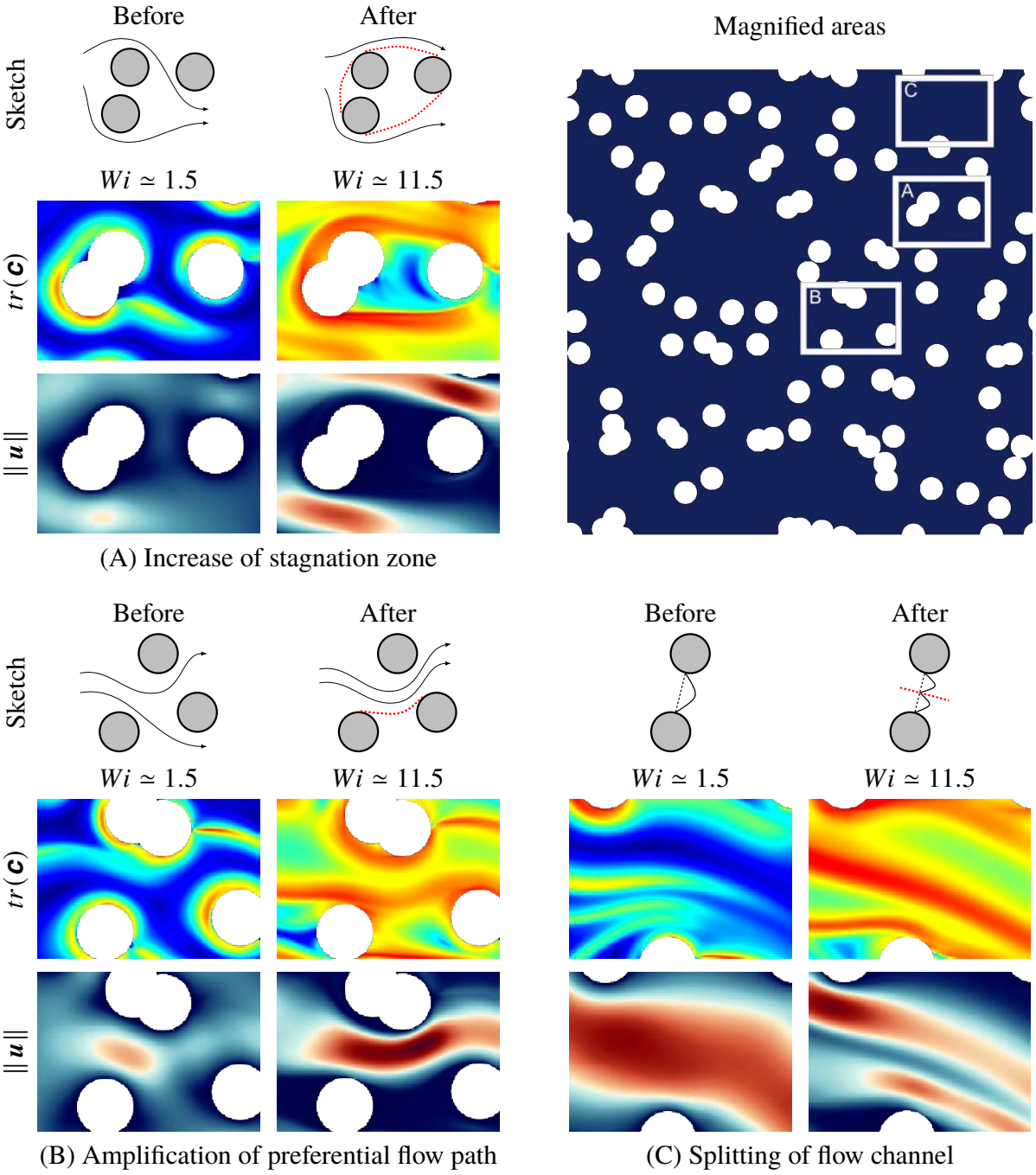

Fig. 3.26 Flow through an array of cylinders in the case $\beta = 1$ and $\varepsilon = 3$. Magnified areas for $tr(\boldsymbol{c})$ and the velocity magnitude presented in figure 3.25. These areas capture the three principal effects of the strands and envelopes on the flow through an array of cylinders with (A) an increase of the zones of stagnation, (B) an amplification of the preferential flow paths and (C) a splitting of flow channels. The top right figure positions each magnified area in the array.

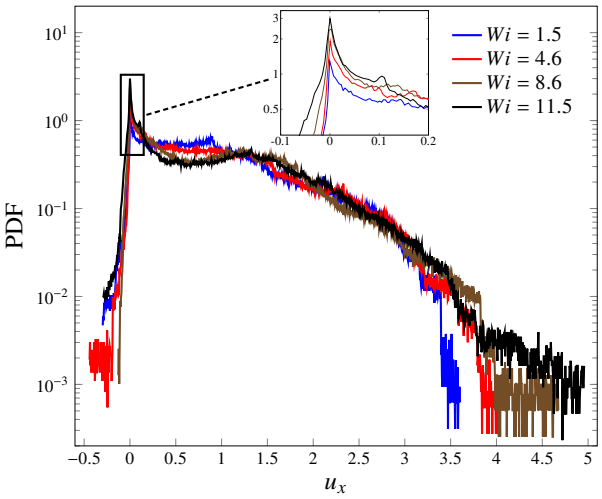

Fig. 3.27 Flow through an array of cylinders in the case $\beta = 1$ and $\varepsilon = 3$. Probability density functions for the longitudinal component of the velocity field, u_x, as a function of the Wi number. The insert is a magnification of the framed area.

[95]. We observe an increase of zones at extremely low velocities, with a peak at 0 that is increased threefold from $Wi \simeq 1.5$ to $Wi \simeq 11.5$.

2. an amplification of preferential flow paths. As described in the case of two cylinders orthogonal to the flow, strands tend to amplify existing preferential flow paths. This is exemplified in figure 3.26(B). At low Wi number, $Wi \simeq 1.5$, we see different flow channels and a bifurcation of the flow around the cylinder on the right-hand side. At $Wi \simeq 11.5$, a strand develops between cylinders and seems to obstruct one of the path with initially lower flow rate. The flow is thus deflected towards the other path, leading to a global reduction of existing flow paths and an amplification of pre-existing preferential flow paths. The PDFs in figure 3.27 show that the maximum velocity increases and is multiplied by $\simeq 1.5$ from $Wi \simeq 1.5$ to $Wi \simeq 11.5$. This is consistent with [15] for FENE-P fluid flows in random 3D porous media, where PDFs also show preferential flows and an increase in the maximum velocity.

3. a splitting of the flow channels. When a strand develops in an existing flow channel, it will slow down the flow in the vicinity of the strand and may appear to split this channel in two. Figure 3.25(C) shows an example of splitting at $Wi = 11.5$ where we observe the formation of two flow paths in the same pore separated by a strand.

3.5.2 Permeability and energies

The starting point of the analysis are entropy estimates derived in [**?**]. Considering an isothermal system, the reduced rate of entropy production for an Oldroyd-B fluid at zero Reynolds number is

$$\int_\Omega \mathcal{E}\, dS = \underbrace{\frac{1}{2}\int_\Omega \left(\boldsymbol{\nabla u} + (\boldsymbol{\nabla u})^\mathsf{T}\right) : \left(\boldsymbol{\nabla u} + (\boldsymbol{\nabla u})^\mathsf{T}\right) dS}_{\text{Solvent viscous dissipation}} + \underbrace{\frac{\beta}{2Wi^2}\int_\Omega tr\left(\boldsymbol{c} + \boldsymbol{c}^{-1} - 2\boldsymbol{I}\right) dS}_{\text{Polymeric contribution}}, \quad (3.30)$$

where Ω is the fluid domain. The first term on the right-hand side corresponds to the standard viscous dissipation associated with the viscosity of the solvent. The second term is the contribution of the polymers and essentially captures the dissipative properties of the Oldroyd-B fluid with

$$\int_\Omega \dot{\psi}\, dS = -\int_\Omega \mathcal{E}\, dS + \int_\Omega \boldsymbol{F}\cdot\boldsymbol{u}\, dS, \tag{3.31}$$

where ψ is the Helmholtz free energy given by [4, 76, 91, 93]

$$\psi = \frac{\beta}{2Wi} tr\left(\boldsymbol{c} - \boldsymbol{I} - \ln(\boldsymbol{c})\right). \tag{3.32}$$

Here, the term in $tr\left(\boldsymbol{c}-\boldsymbol{I}\right)$ corresponds to the internal energy and $tr\left(\ln(\boldsymbol{c})\right)$ is entropic [89]. The more general version of (3.31) involves the sum of the Helmholtz free energy and the kinetic energy, rather than just the Helmholtz free energy–the kinetic energy disappears in the zero Reynolds number limit. At steady-state, we have an equilibrium between energy sources and dissipation, which may be expressed as

$$0 = -\int_\Omega \mathcal{E}\, dS + \int_\Omega \boldsymbol{F}\cdot\boldsymbol{u}\, dS \tag{3.33}$$

From these considerations, we can define a pointwise dissipation functional as

$$\mathcal{E} = \frac{1}{2}\left(\boldsymbol{\nabla u} + (\boldsymbol{\nabla u})^{\mathsf{T}}\right) : \left(\boldsymbol{\nabla u} + (\boldsymbol{\nabla u})^{\mathsf{T}}\right) + \frac{\beta}{2Wi^2} tr\left(\boldsymbol{c} + \boldsymbol{c}^{-1} - 2\boldsymbol{I}\right), \tag{3.34}$$

that is always non-negative ($\boldsymbol{c}$ is symmetric definite positive). We further decompose this functional into two non-negative parts as

$$\mathcal{E} = \mathcal{E}_v + \mathcal{E}_e \tag{3.35}$$

with

$$\mathcal{E}_v = \frac{1}{2}\left(\boldsymbol{\nabla u} + (\boldsymbol{\nabla u})^{\mathsf{T}}\right) : \left(\boldsymbol{\nabla u} + (\boldsymbol{\nabla u})^{\mathsf{T}}\right) \tag{3.36}$$

and

$$\mathcal{E}_e = \frac{\beta}{2Wi^2} tr\left(\boldsymbol{c} + \boldsymbol{c}^{-1} - 2\boldsymbol{I}\right). \tag{3.37}$$

Figures 3.28 and 3.29 show the fields $tr(\boldsymbol{c})$, $\mathcal{E}_v$ and $\mathcal{E}_e$ at different Wi numbers in the case $\beta = 1$ for an array of cylinders with $\varepsilon = 0$ and $\varepsilon = 2$, respectively. We observe two fundamental mechanisms. On the one hand, the strands modify the standard part of the solvent dissipation, $\mathcal{E}_v$. At low Wi number ($Wi \simeq 1$), the strands are not well formed and $\mathcal{E}_v$ is mainly located close to the cylinders where the shear rate is large. For a larger Wi number ($Wi \simeq 5$), the strands develop and lead to a jump in shear-stress across them, see Section 3.3.3. As observed in figure 3.28, this results in a local increase in the viscous dissipation in the vicinity of the strand. For $\varepsilon = 2$, the strands also amplify the preferential flows and therefore generate an increase in viscous dissipation in the preferential flow paths. On the other hand, we also observe an increase in $\mathcal{E}_e$ with the Wi number, which corresponds to polymers stretching within the strands. Thus, the strands contribute to a global increase in dissipation in two ways with

1. an increase in the solvent viscous dissipation, $\mathcal{E}_v$, due to the changes in the velocity field, in particular the creation of preferential flow paths and the local effect of the strand on the shear rate.

2. a strong entropy generation in the strands themselves through $\mathcal{E}_e$.

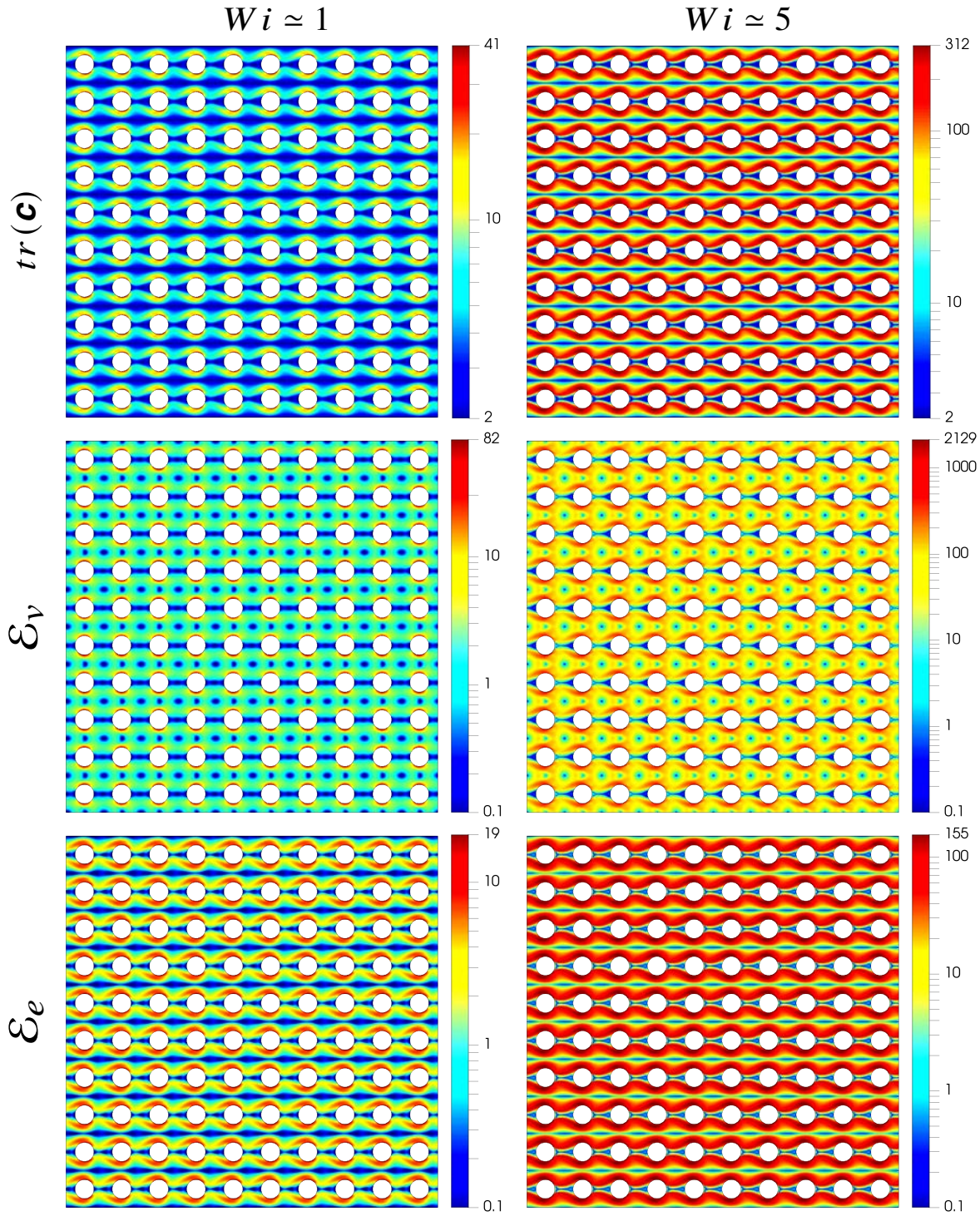

Fig. 3.28 Flow through an array of cylinders in the case $\beta = 1$ and $\varepsilon = 0$. $tr(\boldsymbol{c})$ (top), viscous dissipation $\mathcal{E}_v$ (middle) and polymeric dissipation $\mathcal{E}_p$ (bottom) as a function of the Wi number. For visualization purposes, the colourbars for dissipations starts at 0.1, so all values below 0.1 are represented in dark blue.

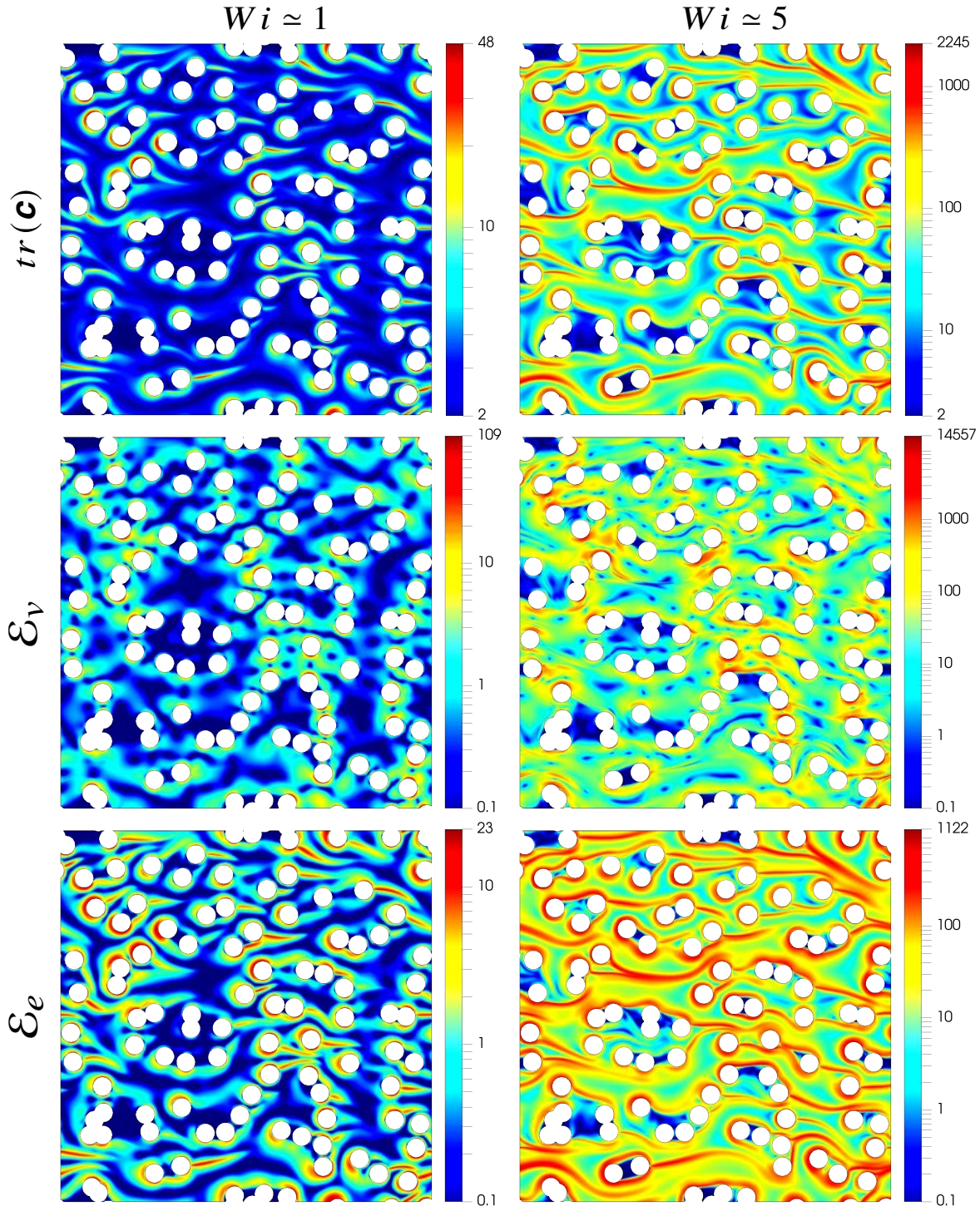

Fig. 3.29 Flow through an array of cylinders in the case $\beta = 1$ and $\varepsilon = 2$. $tr(\boldsymbol{c})$ (top), viscous dissipation $\mathcal{E}_v$ (middle) and polymeric dissipation $\mathcal{E}_p$ (bottom) as a function of the Wi number. For visualization purposes, the colourbars for dissipations starts at 0.1, so all values below 0.1 are represented in dark blue.

We can take these results one step further and use them to better understand the pressure drop of viscoelastic fluids across porous structures. For convenience, we use the averaging operator defined by (3.8). We define a drag coefficient $\mathcal{C}$ through a Darcy-type relation

$$\mathcal{C}\langle \boldsymbol{u}\rangle = \boldsymbol{F}. \tag{3.38}$$

Considering (3.33) at steady-state, we have $\boldsymbol{F}\cdot\langle \boldsymbol{u}\rangle = \langle \mathcal{E}\rangle$ and therefore $\mathcal{C}$ can be expressed as

$$\mathcal{C} = \frac{\langle \mathcal{E}\rangle}{\|\langle \boldsymbol{u}\rangle\|^2}, \tag{3.39}$$

corresponding to the ratio between the dissipated energy, $\langle \mathcal{E}\rangle$, and a macroscopic kinetic energy, $\|\langle \boldsymbol{u}\rangle\|^2$. We can also define, in a same manner, a Darcy-type permeability $\mathcal{K}$ through

$$\langle \boldsymbol{u}\rangle = \frac{\mathcal{K}}{1+\beta}\boldsymbol{F}, \tag{3.40}$$

and we have the following relation

$$\mathcal{C}^{-1} = \frac{\mathcal{K}}{1+\beta}. \tag{3.41}$$

The inverse of $\mathcal{C}$, $\mathcal{C}^{-1}$, may be understood as some sort of efficiency of the porous structure with $\mathcal{C}^{-1} = \|\langle \boldsymbol{u}\rangle\|^2/\langle \mathcal{E}\rangle = \|\langle \boldsymbol{u}\rangle\|^2/(\boldsymbol{F}\cdot\langle \boldsymbol{u}\rangle)$ being a ratio between a macroscopic kinetic energy and dissipation/sources. Using our previous decomposition, we have the decomposition

$$\mathcal{C} = \frac{\langle \mathcal{E}_v\rangle}{\|\langle \boldsymbol{u}\rangle\|^2} + \frac{\langle \mathcal{E}_e\rangle}{\|\langle \boldsymbol{u}\rangle\|^2}. \tag{3.42}$$

Figure 3.30 shows each of these contributions and their sum, $\mathcal{C}$–normalized by the Newtonian value of $\mathcal{C}$ in the limit $Wi \to 0$–as a function of the Wi number for different values of β in the case $\varepsilon = 2$. When $Wi \to 0$, both $\langle \mathcal{E}_v\rangle/\|\langle \boldsymbol{u}\rangle\|^2$ and $\langle \mathcal{E}_e\rangle/\|\langle \boldsymbol{u}\rangle\|^2$ start with a Newtonian plateau with the value of β determining the ratios of values between the two plateaus. This is because $\langle \mathcal{E}_e\rangle = \beta\langle \mathcal{E}_v\rangle + O(Wi)$ in the limit of small Wi numbers. To understand this, we need to calculate $\langle tr(\boldsymbol{c}+\boldsymbol{c}^{-1}-2\boldsymbol{I})\rangle$ in the limit $Wi \to 0$. First, consider the product between $\boldsymbol{c}^{-1}$ and (3.6), which leads to

$$\boldsymbol{u}\cdot\boldsymbol{\nabla}\ln(\boldsymbol{c}) = \boldsymbol{\nabla u} + \boldsymbol{c}(\boldsymbol{\nabla u})^{\mathsf{T}}\boldsymbol{c}^{-1} - \frac{1}{Wi}(\boldsymbol{I}-\boldsymbol{c}^{-1}). \tag{3.43}$$

Taking the trace of this equation and integrating with biperiodic boundary conditions leads to

$$\left\langle tr\left(\boldsymbol{c}^{-1}-\boldsymbol{I}\right)\right\rangle = 0, \tag{3.44}$$

so that

$$\langle \mathcal{E}_e\rangle = {}^{\beta}/_{(2Wi^2)}\left\langle tr\left(\boldsymbol{c}+\boldsymbol{c}^{-1}-2\boldsymbol{I}\right)\right\rangle = {}^{\beta}/_{(2Wi^2)}\langle tr(\boldsymbol{c}-\boldsymbol{I})\rangle. \tag{3.45}$$

Now let us consider Wi asymptotics in the form

$$\boldsymbol{u} = \boldsymbol{u}^{0\star} + Wi\,\boldsymbol{u}^{1\star} + O\left(Wi^2\right), \tag{3.46}$$

$$\boldsymbol{c} = \boldsymbol{c}^{0\star} + Wi\boldsymbol{c}^{1\star} + Wi^2\boldsymbol{c}^{2\star} + O\left(Wi^3\right), \tag{3.47}$$

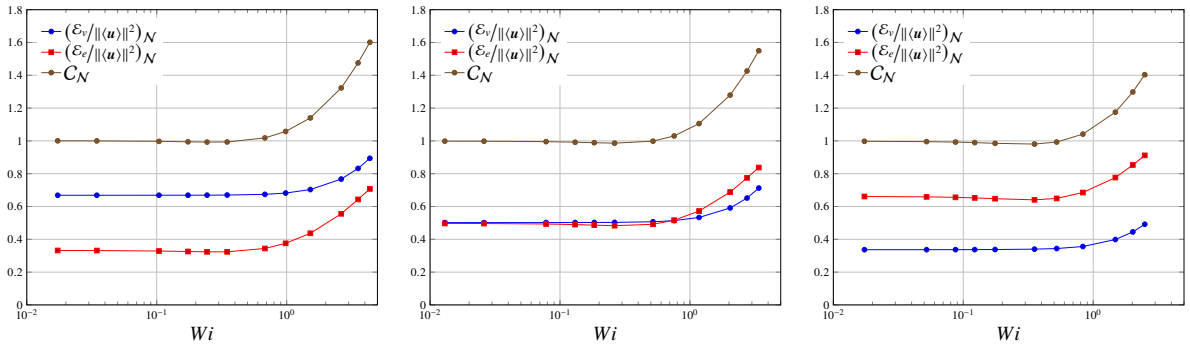

(a) $\beta = 0.5$ (b) $\beta = 1$ (c) $\beta = 2$

Fig. 3.30 Flow through an array of cylinders in the case $\varepsilon = 2$. Evolution of the viscous and polymeric dissipations and their sum corresponding to the drag coefficient $\mathcal{C}$ as a function of the Wi number for different values of β. The subscript $_{\mathcal{N}}$ indicates the normalization by the Newtonian value of $\mathcal{C}$ in the limit $Wi \to 0$.

and use this in (3.6) to obtain

$$\begin{aligned}\boldsymbol{c} = \boldsymbol{I} + Wi\left(\boldsymbol{\nabla u}^{0\star} + \left(\boldsymbol{\nabla u}^{0\star}\right)^{\mathsf{T}}\right) - Wi^2\left(\boldsymbol{u}^{0\star}\cdot\boldsymbol{\nabla}\left(\boldsymbol{\nabla u}^{0\star} + \left(\boldsymbol{\nabla u}^{0\star}\right)^{\mathsf{T}}\right)\right)\\ + Wi^2\left(\boldsymbol{\nabla u}^{0\star}\left(\boldsymbol{\nabla u}^{0\star} + \left(\boldsymbol{\nabla u}^{0\star}\right)^{\mathsf{T}}\right) + \left(\boldsymbol{\nabla u}^{0\star} + \left(\boldsymbol{\nabla u}^{0\star}\right)^{\mathsf{T}}\right)\left(\boldsymbol{\nabla u}^{0\star}\right)^{\mathsf{T}}\right)\\ + Wi^2\left(\boldsymbol{\nabla u}^{1\star} + \left(\boldsymbol{\nabla u}^{1\star}\right)^{\mathsf{T}}\right) + O\left(Wi^3\right). \quad (3.48)\end{aligned}$$

Upon taking the trace of (3.48) and integrating with biperiodic boundary conditions, we thus have

$$\langle tr\left(\boldsymbol{c} - \boldsymbol{I}\right)\rangle = Wi^2\left\langle\left(\boldsymbol{\nabla u}^{0\star} + \left(\boldsymbol{\nabla u}^{0\star}\right)^{\mathsf{T}}\right) : \left(\boldsymbol{\nabla u}^{0\star} + \left(\boldsymbol{\nabla u}^{0\star}\right)^{\mathsf{T}}\right)\right\rangle + O\left(Wi^3\right), \quad (3.49)$$

so that $\langle \mathcal{E}_e\rangle = \beta\langle \mathcal{E}_v\rangle + O(Wi)$. Note that this result can also be obtained by considering directly the limit of the term $^{\beta}/_{Wi}\boldsymbol{\nabla}\cdot\boldsymbol{c}$ through Wi asymptotics at lower order [5].

We also observe that the viscous dissipation contribution $\langle \mathcal{E}_v\rangle$ is monotonically increasing with the Wi number while $\langle \mathcal{E}_e\rangle$ is (slighlty) non-monotonic, leading to the appearance of a minimum in $\mathcal{C}$ with a small decrease in flow resistance that is quickly superseded by a stronger increase. The relative contribution of the two mechanisms depends on β but the contribution of the solvent viscous dissipation is always increasing and never negligible.

Flows of dilute polymer solutions through porous media are known to generate an increase in the resistance to flow [7, 17, 43, 46, 61]–which is often termed an apparent shear-thickening in reference to the viscosity in Darcy's law. Previous works have recovered this effect numerically, including [38] using numerical simulations of Oldroyd-B and FENE-type fluids past a biperiodic array of cylinders. De et al. [14] obtained an apparent thickening by simulating the flow of a FENE-P fluid through bidisperse random arrays of cylinders. Liu et al. [57] also observed this effect in the case of an Oldroyd-B fluid flowing through randomly aligned arrays of cylinders and [1] obtained similar results in the case of a FENE-P fluid. However, the mechanisms underlying the increase of flow resistance are still a matter of debate. Our work clearly shows that, at steady-state, it results from an increase in the solvent viscous dissipation and entropy creation in the strands, both of these mechanisms playing an important role.

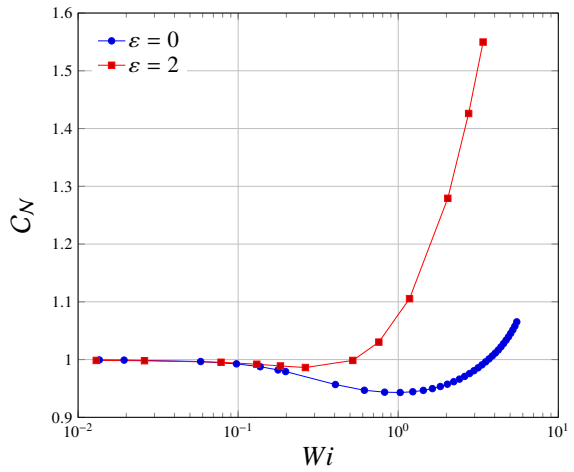

Fig. 3.31 Flow through arrays of cylinders in the case $\beta = 1$. Comparison of the drag coefficient evolution with the Wi number between the cases $\varepsilon = 0$ and $\varepsilon = 2$. The subscript $_N$ indicates the normalization by the Newtonian value of $\mathcal{C}$, corresponding to the limit $Wi \to 0$.

These results are consistent with several previous works. Chauveteau and Moan [8] studied experimentally the flow of dilute polymer solutions through successive contractions and expansions. The authors suggest that the increase in pressure drop results from an increase in viscous dissipation due the elongation of the polymer molecules in the converging parts of the flow. De et al. [15] used correlations between the flow topology and the dissipation function distribution to show that the increase in flow resistance is mainly caused by shear regions. Using a characterization through the flow type parameter, they even observed a decrease in the extension zones in favour of shear. In a second study [14], the same authors compared the normal stress difference to the flow type parameter. They found that the largest values for the normal stress difference are located in the shear dominant flow regions and they concluded that the normal stress is responsible for the increase in flow resistance. Since the strands are precisely zones where normal stress differences are very large, this is fully consistent with our results. The role of the normal stress difference in the increase of flow resistance was also pointed out in [18, 44, 75].

Haward and Odell [35] focused on flow experiments through crystalline structures. By comparing a simple cubic arrangement to a body centered cubic array, they observed a greater apparent shear-thickening in the simple cubic array where the polymer extension is more important. In a second study, Odell and Haward [68] showed that a greater apparent shear-thickening occurs in porous media containing stagnation points than in porous media devoid of stagnation points. Our results show that this effect is not localised close to the stagnation point but a consequence of strand formation. In this sense, our work contradicts those that attribute the pressure drop to the elongational viscosity [10, 16, 50, 75, 81, 94]. Although the extensional flow of polymer solutions produces large stresses locally at stagnation points, this effect is insufficient, as previously discussed in [44]. Stagnation points are fundamental in the formation of strands but, from an energetic point of view, contribute very little to dissipation, as we observed in figures 3.28 and 3.29.

Recent results also show a correlation between the increase of flow resistance and the onset of elastic turbulence [6, 11, 12, 24, 47, 58, 63, 70]. The authors thus suggest that temporal fluctuations may be responsible for the additional energy dissipation, in a manner that is reminiscent of high Reynolds turbulence [90]. Our results show that the increase of flow

resistance can also be observed at steady state, before reaching any sort of unsteady regime. Elastic turbulence most likely also increases flow resistance, but it is not the only mechanism at play. Since experimental results in [6, 11, 24, 47, 58] rely on crystalline or quasi-crystalline structures, we hypothesize that the absence of flow resistance increase before transition to elastic turbulence may be specific to such structures. To substantiate this hypothesis, we present in figure 3.31 the evolution of the drag coefficient $\mathcal{C}$, normalized by its Newtonian value, as a function of the Wi number with $\beta = 1$ in the crystalline cylinder array corresponding to $\varepsilon = 0$. After a Newtonian plateau, we first observe a slight reduction of flow resistance followed by an abrupt increase–also reported by Hemingway et al. [38]. After this increase, the flow rapidly becomes unsteady, which is the first step towards elastic turbulence. By comparison with the case $\varepsilon = 2$, there is a significant delay in the increase of flow resistance with the Wi number and the apparent shear-thickening at steady-state is much less evident. These results are similar to those reported by Liu et al. [57] thus suggesting that the structure of the porous medium plays an essential role in the development of the strands and the apparent shear-thickening. In the cases of crystalline structures, apparent shear-thickening may indeed be linked to unsteady flows. Porosity, topology and dimensionality may also have an impact.

3.6 Conclusion

Our results demonstrate that birefringent strands are key in understanding viscoelastic flows past obstacles and through porous structures. They essentially act as a distribution of tangential forces that reduce the velocity in their vicinity and can induce a complete reorganization of the flow on large scales within porous structures. They also generate an increase in the resistance to flow through a double dissipation mechanism, with an increase of the solvent viscous dissipation and an important entropy creation within the strands.

Arrays of cylinders that can be treated as a 2D flow problem have recently attracted a lot of attention in the field [88, 31] and our work follows the same line. These structures capture many important mechanisms inherent to viscoelastic flows through porous media, while being simple and allowing us to easily tune the properties of the structure. Walkama et al. [88] showed that introducing disorder in a staggered geometry locally reduces polymer stretching and enhances flow stability with a transition to chaos that is delayed. By modifying this geometry to a non-staggered one, Haward et al. [31] demonstrated instead that the stagnation points control this transition, independently from disorder. Haward et al. [31] showed a very different arrangement of the strands in staggered and non-staggered geometries, which raises the question of the role of the strands in the transition to chaos. As suggested by Harris and Rallison [29], there is evidence that these may actually play an important role in a cross-slot geometry. Could it thus be that birefringent strands also control the transition to chaos in porous structures?

Furthermore, even though such 2D structures teach us a lot about viscoelastic flows, 2D and 3D flows are fundamentally different [54]. For polymeric stress localisation, 3D porous structures will see the formation of both 1D strands and 2D hyperplanes, which have been observed experimentally in the case of a flow around two spheres [36]. This raises fascinating questions about how viscoelastic flows are affected by the dimensionality, which we believe would be an interesting area of research in the future.

Acknowledgements The authors thank R. de Loubens, from TotalEnergies, for valuable discussions on this topic and F. Babik, from the CALIF^{3}S development team at IRSN, for his precious support. The authors would also like to thank TotalEnergies for funding and supporting this work, in particular through access to the PANGEA II supercomputer.

3.7 Appendix: Mesh convergence

We consider here the evolution of the averaged drag quantity $\mathcal{C}$ with the size of the mesh. The geometry consists in a 4×4 square with a cylinder of radius 1 centered in the domain (i.e. the center of the cylinder is the mass center of the square), as shown figure 3.32(a). Periodic boundary conditions are applied to the pairs constituted by the left/right and top/bottom sides, so we may consider that we compute the flow in a periodic array of cylinders, aligned along x and y-axis. The Cartesian mesh is obtained by cutting each side of the square into N equal parts with cells taken as holes if they are cut by the cylinder. An example of a mesh is given in figure 3.32(b) in the case $N = 10$. This mesh is refined by splitting each face into r equal parts, which amounts to splitting each cell into $r \times r$ parts. An example of refinement corresponding to the cases $N = 10$ and $r = 2$ is given in figure 3.32(c). Figure 3.33(a) shows the evolution of the quantity $\mathcal{C}$ as a function of the Wi number for different values of N in the case $r = 1$. Note that, in this case, the actual geometry changes with the mesh size because of the way holes are generated in the mesh, resulting in a better approximation of the boundary (so the convergence study with respect to N encompasses the assessment of the convergence with respect to the approximation of the geometry of the computational domain). Nevertheless, we obtain a convergence with N, which validates the approximation of a cylinder by stair steps. Figure 3.33(b) shows the dependence in r in the case $N = 100$. For an integral quantity as the drag coefficient, we observe a good convergence with the mesh refinement, even for $Wi = 5$. In the paper, the mesh size in the case of a uniform grid, given in table 3.1, is equivalent to the case $N = 100$ and $r = 2$ here, which is a compromise between precision and computational cost.

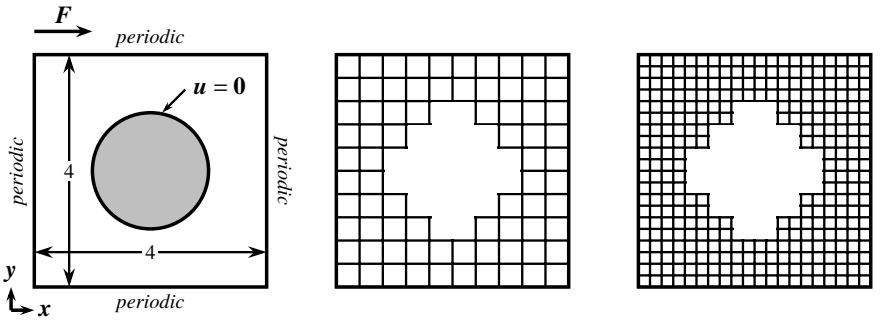

(*a*) Geometrie and boundary conditions

(*b*) Example of mesh ($N = 10$)

(*c*) Example of refinement ($r = 2$)

Fig. 3.32 Biperiodic array of cylinder. (*a*) Schematics of the geometry and boundary conditions. The geometry consists of a single cylinder of radius 1 in a square of size 4. The boundary conditions are top-bottom and left-right periodicity and $\boldsymbol{u} = 0$ on the cylinder. (*b*) Initial mesh in the case $N = 10$. (*c*) Refinement in the case $r = 2$.

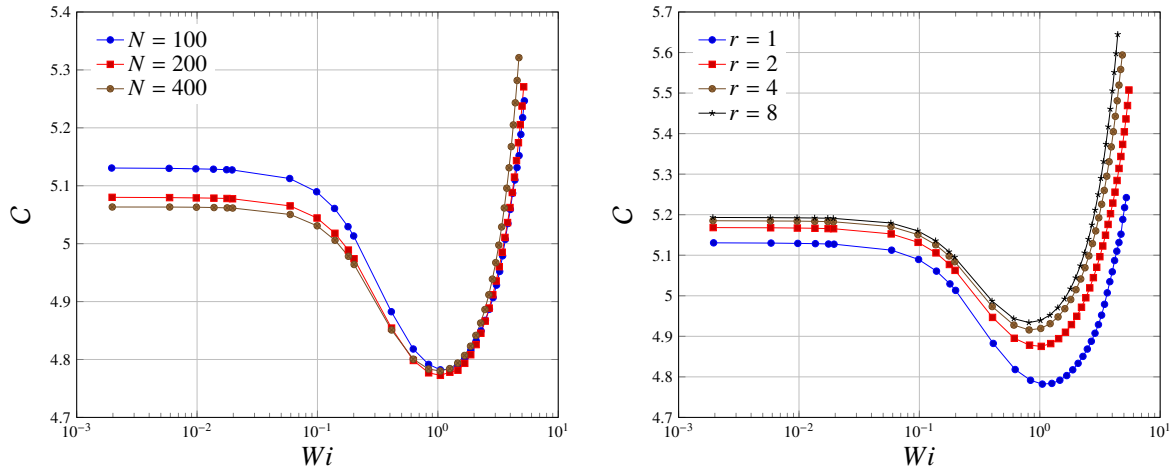

(a) Dependence in N

(b) Dependence in r

Fig. 3.33 Biperiodic array of cylinder. Evolution of the drag coefficient as a function of the Wi number for (a) different values of the mesh size N with a constant refinement $r = 1$ and (b) different values of the refinement r with a constant mesh size $N = 100$.

Références

[1] Aramideh, S., Vlachos, P. P., and Ardekani, A. M. (2019). Nanoparticle dispersion in porous media in viscoelastic polymer solutions. *Journal of Non-Newtonian Fluid Mechanics*, 268:75–80.

[2] Bajaj, M., Pasquali, M., and Prakash, J. R. (2008). Coil-stretch transition and the breakdown of computations for viscoelastic fluid flow around a confined cylinder. *Journal of Rheology*, 52(1):197–223.

[3] Becherer, P., van Saarloos, W., and Morozov, A. N. (2009). Stress singularities and the formation of birefringent strands in stagnation flows of dilute polymer solutions. *Journal of Non-Newtonian Fluid Mechanics*, 157(1-2):126–132.

[4] Booij, H. C. (1984). The energy storage in the rouse model in an arbitrary flow field. *The Journal of Chemical Physics*, 80(9):4571–4572.

[5] Bresch, D. and Prange, C. (2014). Newtonian limit for weakly viscoelastic fluid flows. *SIAM Journal on Mathematical Analysis*, 46(2):1116–1159.

[6] Browne, C. A. and Datta, S. S. (2021). Elastic turbulence generates anomalous flow resistance in porous media. *Science Advances*, 7(45):eabj2619.

[7] Browne, C. A., Shih, A., and Datta, S. S. (2020). Pore-scale flow characterization of polymer solutions in microfluidic porous media. *Small*, 16(9):1903944.

[8] Chauveteau, G. and Moan, M. (1981). The onset of dilatant behaviour in non-inertial flow of dilute polymer solutions through channels with varying cross-sections. *Journal de Physique Lettres*, 42(10):201–204.

[9] Chilcott, M. D. and Rallison, J. M. (1988). Creeping flow of dilute polymer solutions past cylinders and spheres. *Journal of Non-Newtonian Fluid Mechanics*, 29:381–432.

[10] Chmielewski, C. and Jayaraman, K. (1992). The effect of polymer extensibility on crossflow of polymer solutions through cylinder arrays. *Journal of Rheology*, 36(6):1105–1126.

[11] Clarke, A., Howe, A. M., Mitchell, J., Staniland, J., Hawkes, L., and Leeper, K. (2015). Mechanism of anomalously increased oil displacement with aqueous viscoelastic polymer solutions. *Soft Matter*, 11(18):3536–3541.

[12] Clarke, A., Howe, A. M., Mitchell, J., Staniland, J., and Hawkes, L. A. (2016). How viscoelastic-polymer flooding enhances displacement efficiency. *SPE Journal*, 21(03):0675–0687.

[13] Crowley, D. G., Frank, F. C., Mackley, M. R., and Stephenson, R. G. (1976). Localized flow birefringence of polyethylene oxide solutions in a four roll mill. *Journal of Polymer Science: Polymer Physics Edition*, 14(6):1111–1119.

[14] De, S., Kuipers, J. A. M., Peters, E. A. J. F., and Padding, J. T. (2017a). Viscoelastic flow past mono-and bidisperse random arrays of cylinders: flow resistance, topology and normal stress distribution. *Soft Matter*, 13(48):9138–9146.

[15] De, S., Kuipers, J. A. M., Peters, E. A. J. F., and Padding, J. T. (2017b). Viscoelastic flow simulations in random porous media. *Journal of Non-Newtonian Fluid Mechanics*, 248:50–61.

[16] Durst, F., Haas, R., and Interthal, W. (1987). The nature of flows through porous media. *Journal of Non-Newtonian Fluid Mechanics*, 22(2):169–189.

[17] Durst, F., Haas, R., and Kaczmar, B. U. (1981). Flows of dilute hydrolyzed polyacrylamide solutions in porous media under various solvent conditions. *Journal of Applied Polymer Science*, 26(9):3125–3149.

[18] Evans, A. R., Shaqfeh, E. S. G., and Frattini, P. L. (1994). Observations of polymer conformation during flow through a fixed fibre bed. *Journal of Fluid Mechanics*, 281:319–356.

[19] Fan, Y., Yang, H., and Tanner, R. I. (2005). Stress boundary layers in the viscoelastic flow past a cylinder in a channel: limiting solutions. *Acta Mechanica Sinica*, 21(4):311–321.

[20] Farrell, C. J. and Keller, A. (1978). The observation of high polymer chain extension with two counter-rotating rollers. *Colloid and Polymer Science*, 256(10):966–969.

[21] Fattal, R. and Kupferman, R. (2004). Constitutive laws for the matrix-logarithm of the conformation tensor. *Journal of Non-Newtonian Fluid Mechanics*, 123(2-3):281–285.

[22] François, N., Lasne, D., Amarouchene, Y., Lounis, B., and Kellay, H. (2008). Drag enhancement with polymers. *Physical Review Letters*, 100(1):018302.

[23] Fuller, G. G. and Leal, L. G. (1980). Flow birefringence of dilute polymer solutions in two-dimensional flows. *Rheologica Acta*, 19(5):580–600.

[24] Galindo-Rosales, F. J., Campo-Deano, L., Pinho, F. T., Van Bokhorst, E., Hamersma, P. J., Oliveira, M. S. N., and Alves, M. A. (2012). Microfluidic systems for the analysis of viscoelastic fluid flow phenomena in

porous media. *Microfluidics and Nanofluidics*, 12(1-4):485–498.

[25] Graham, R. L., Woodall, T. S., and Squyres, J. M. (2005). Open MPI: A flexible high performance MPI. In *International Conference on Parallel Processing and Applied Mathematics*, pages 228–239. Springer.

[26] Harlen, O. G. (1990). High-deborah-number flow of a dilute polymer solution past a sphere falling along the axis of a cylindrical tube. *Journal of Non-Newtonian Fluid Mechanics*, 37(2-3):157–173.

[27] Harlen, O. G., Hinch, E. J., and Rallison, J. M. (1992). Birefringent pipes: the steady flow of a dilute polymer solution near a stagnation point. *Journal of Non-Newtonian Fluid Mechanics*, 44:229–265.

[28] Harlen, O. G., Rallison, J. M., and Chilcott, M. D. (1990). High-deborah-number flows of dilute polymer solutions. *Journal of Non-Newtonian Fluid Mechanics*, 34(3):319–349.

[29] Harris, O. J. and Rallison, J. M. (1994). Instabilities of a stagnation point flow of a dilute polymer solution. *Journal of Non-Newtonian Fluid Mechanics*, 55(1):59–90.

[30] Haward, S. J., Hopkins, C. C., and Shen, A. Q. (2020). Asymmetric flow of polymer solutions around microfluidic cylinders: Interaction between shear-thinning and viscoelasticity. *Journal of Non-Newtonian Fluid Mechanics*, 278:104250.

[31] Haward, S. J., Hopkins, C. C., and Shen, A. Q. (2021a). Stagnation points control chaotic fluctuations in viscoelastic porous media flow. *Proceedings of the National Academy of Sciences*, 118(38).

[32] Haward, S. J., Hopkins, C. C., Varchanis, S., and Shen, A. Q. (2021b). Bifurcations in flows of complex fluids around microfluidic cylinders. *Lab on a Chip*.

[33] Haward, S. J., Kitajima, N., Toda-Peters, K., Takahashi, T., and Shen, A. Q. (2019). Flow of wormlike micellar solutions around microfluidic cylinders with high aspect ratio and low blockage ratio. *Soft Matter*, 15(9):1927–1941.

[34] Haward, S. J. and McKinley, G. H. (2013). Instabilities in stagnation point flows of polymer solutions. *Physics of Fluids*, 25(8):083104.

[35] Haward, S. J. and Odell, J. A. (2003). Viscosity enhancement in non-Newtonian flow of dilute polymer solutions through crystallographic porous media. *Rheologica Acta*, 42(6):516–526.

[36] Haward, S. J. and Odell, J. A. (2004). Molecular orientation in non-Newtonian flow of dilute polymer solutions around spheres. *Rheologica Acta*, 43(4):350–363.

[37] Haward, S. J., Toda-Peters, K., and Shen, A. Q. (2018). Steady viscoelastic flow around high-aspect-ratio, low-blockage-ratio microfluidic cylinders. *Journal of Non-Newtonian Fluid Mechanics*, 254:23–35.

[38] Hemingway, E. J., Clarke, A., Pearson, J. R. A., and Fielding, S. M. (2018). Thickening of viscoelastic flow in a model porous medium. *Journal of Non-Newtonian Fluid Mechanics*, 251:56–68.

[39] Hopkins, C. C., Haward, S. J., and Shen, A. Q. (2020). Purely elastic fluid–structure interactions in microfluidics: implications for mucociliary flows. *Small*, 16(9):1903872.

[40] Hopkins, C. C., Haward, S. J., and Shen, A. Q. (2021). Tristability in viscoelastic flow past side-by-side microcylinders. *Physical Review Letters*, 126(5):054501.

[41] Hulsen, M. A., Fattal, R., and Kupferman, R. (2005). Flow of viscoelastic fluids past a cylinder at high Weissenberg number: stabilized simulations using matrix logarithms. *Journal of Non-Newtonian Fluid Mechanics*, 127(1):27–39.

[42] James, D. F. (2009). Boger fluids. *Annual Review of Fluid Mechanics*, 41:129–142.

[43] James, D. F. and McLaren, D. R. (1975). The laminar flow of dilute polymer solutions through porous media. *Journal of Fluid Mechanics*, 70(4):733–752.

[44] James, D. F., Yip, R., and Currie, I. G. (2012). Slow flow of Boger fluids through model fibrous porous media. *Journal of Rheology*, 56(5):1249.

[45] Karypis, G. and Kumar, V. (1998). A fast and high quality multilevel scheme for partitioning irregular graphs. *SIAM Journal on Scientific Computing*, 20(1):359–392.

[46] Kauser, N., Dos Santos, L., Delgado, M., Müller, A. J., and Sáez, A. E. (1999). Flow of mixtures of poly (ethylene oxide) and hydrolyzed polyacrylamide solutions through porous media. *Journal of Applied Polymer Science*, 72(6):783–795.

[47] Kawale, D., Marques, E., Zitha, P. L. J., Kreutzer, M. T., Rossen, W. R., and Boukany, P. E. (2017). Elastic instabilities during the flow of hydrolyzed polyacrylamide solution in porous media: effect of pore-shape and salt. *Soft Matter*, 13(4):765–775.

[48] Keller, A. and Odell, J. A. (1985). The extensibility of macromolecules in solution; a new focus for macromolecular science. *Colloid and Polymer Science*, 263(3):181–201.

[49] Khan, M. B. and Sasmal, C. (2021). Elastic instabilities and bifurcations in flows of wormlike micellar solutions past single and two vertically aligned microcylinders: Effect of blockage and gap ratios. *Physics of Fluids*, 33(3):033109.

[50] Khomami, B. and Moreno, L. D. (1997). Stability of viscoelastic flow around periodic arrays of cylinders. *Rheologica Acta*, 36(4):367–383.

[51] Kumar, M. and Ardekani, A. M. (2021). Elastic instabilities between two cylinders confined in a channel. *Physics of Fluids*, 33(7):074107.

[52] Larson, R. G. (2000). Turbulence without inertia. *Nature*, 405(6782):27–28.

[53] Lee, I. C. Y., Kapur, N., Gaskell, P. H., Savage, M. D., and Homsy, G. M. (2002). Birefringent strands in polymer flows in a co-rotating two-roll mill. *Journal of Non-Newtonian Fluid Mechanics*, 104(1):33–51.

[54] Lester, D. R., Dentz, M., and Le Borgne, T. (2016). Chaotic mixing in three-dimensional porous media. *Journal of Fluid Mechanics*, 803:144–174.

[55] Li, C., Thomases, B., and Guy, R. D. (2019). Orientation dependent elastic stress concentration at tips of slender objects translating in viscoelastic fluids. *Physical Review Fluids*, 4(3):031301.

[56] Liu, A. W., Bornside, D. E., Armstrong, R. C., and Brown, R. A. (1998). Viscoelastic flow of polymer solutions around a periodic, linear array of cylinders: comparisons of predictions for microstructure and flow fields. *Journal of Non-Newtonian Fluid Mechanics*, 77(3):153–190.

[57] Liu, H. L., Wang, J., and Hwang, W. R. (2017). Flow resistance of viscoelastic flows in fibrous porous media. *Journal of Non-Newtonian Fluid Mechanics*, 246:21–30.

[58] Machado, A., Bodiguel, H., Beaumont, J., Clisson, G., and Colin, A. (2016). Extra dissipation and flow uniformization due to elastic instabilities of shear-thinning polymer solutions in model porous media. *Biomicrofluidics*, 10(4):043507.

[59] Mackley, M. R. (1978). Flow singularities, polymer chain extension and hydrodynamic instabilities. *Journal of Non-Newtonian Fluid Mechanics*, 4(1-2):111–136.

[60] Málaga, C. and Rallison, J. M. (2007). A rising bubble in a polymer solution. *Journal of Non-Newtonian Fluid Mechanics*, 141(1):59–78.

[61] Marshall, R. J. and Metzner, A. B. (1967). Flow of viscoelastic fluids through porous media. *Industrial & Engineering Chemistry Fundamentals*, 6(3):393–400.

[62] Miles, M. J. and Keller, A. (1980). Conformational relaxation time in polymer solutions by elongational flow experiments: 2. Preliminaries of further developments: chain retraction; identification of molecular weight fractions in a mixture. *Polymer*, 21(11):1295–1298.

[63] Mitchell, J., Lyons, K., Howe, A. M., and Clarke, A. (2016). Viscoelastic polymer flows and elastic turbulence in three-dimensional porous structures. *Soft Matter*, 12(2):460–468.

[64] Mokhtari, O., Davit, Y., Latché, J.-C., and Quintard, M. (2021). A staggered projection scheme for viscoelastic flows. Working paper or preprint.

[65] Moore, M. N. J. and Shelley, M. J. (2012). A weak-coupling expansion for viscoelastic fluids applied to dynamic settling of a body. *Journal of Non-Newtonian Fluid Mechanics*, 183:25–36.

[66] Müller, A. J., Odell, J. A., and Keller, A. (1988). Elongational flow and rheology of monodisperse polymers in solution. *Journal of Non-Newtonian Fluid Mechanics*, 30(2-3):99–118.

[67] Odell, J. A. and Carrington, S. P. (2006). Extensional flow oscillatory rheometry. *Journal of Non-Newtonian Fluid Mechanics*, 137(1-3):110–120.

[68] Odell, J. A. and Haward, S. J. (2006). Viscosity enhancement in non-Newtonian flow of dilute aqueous polymer solutions through crystallographic and random porous media. *Rheologica Acta*, 45(6):853–863.

[69] Odell, J. A., Müller, A. J., and Keller, A. (1988). Non-newtonian behaviour of hydrolysed polyacrylamide in strong elongational flows: a transient network approach. *Polymer*, 29(7):1179–1190.

[70] Qin, B., Salipante, P. F., Hudson, S. D., and Arratia, P. E. (2019a). Flow resistance and structures in viscoelastic channel flows at low Re. *Physical Review Letters*, 123(19):194501.

[71] Qin, B., Salipante, P. F., Hudson, S. D., and Arratia, P. E. (2019b). Upstream vortex and elastic wave in the viscoelastic flow around a confined cylinder. *Journal of Fluid Mechanics*, 864.

[72] Rallison, J. M. and Hinch, E. J. (1988). Do we understand the physics in the constitutive equation? *Journal of Non-Newtonian Fluid Mechanics*, 29:37–55.

[73] Renardy, M. (1997). High Weissenberg number boundary layers for the upper convected Maxwell fluid. *Journal of Non-Newtonian Fluid Mechanics*, 68(1):125–132.

[74] Renardy, M. (2000). Asymptotic structure of the stress field in flow past a cylinder at high Weissenberg number. *Journal of Non-Newtonian Fluid Mechanics*, 90(1):13–23.

[75] Rothstein, J. P. and McKinley, G. H. (2001). The axisymmetric contraction–expansion: the role of extensional rheology on vortex growth dynamics and the enhanced pressure drop. *Journal of Non-Newtonian Fluid Mechanics*, 98(1):33–63.

[76] Sarti, G. C. and Marrucci, G. (1973). Thermomechanics of dilute polymer solutions: multiple bead-spring model. *Chemical Engineering Science*, 28(4):1053–1059.

[77] Scrivener, O., Berner, C., Cressely, R., Hocquart, R., Sellin, R., and Vlachos, N. S. (1979). Dynamical behaviour of drag-reducing polymer solutions. *Journal of Non-Newtonian Fluid Mechanics*, 5:475–495.

[78] Seybold, H. J., Eberhard, U., Secchi, E., Cisne Jr, R. L. C., Jiménez-Martínez, J., Andrade, R. F. S., Araújo, A. D., Holzner, M., and Andrade Jr, J. S. (2021). Localization in flow of non-newtonian fluids through disordered porous media. *Frontiers in Physics*, 9:5.

[79] Shaqfeh, E. S. G. and Khomami, B. (2021). The Oldroyd-B fluid in elastic instabilities, turbulence and particle suspensions. *Journal of Non-Newtonian Fluid Mechanics*, 298:104672.

[80] Shi, X. and Christopher, G. F. (2016). Growth of viscoelastic instabilities around linear cylinder arrays. *Physics of Fluids*, 28(12):124102.

[81] Skauge, A., Zamani, N., Gausdal Jacobsen, J., Shaker Shiran, B., Al-Shakry, B., and Skauge, T. (2018). Polymer flow in porous media: Relevance to enhanced oil recovery. *Colloids and Interfaces*, 2(3):27.

[82] Snoeijer, J. H., Pandey, A.and Herrada, M. A., and Eggers, J. (2020). The relationship between viscoelasticity and elasticity. *Proceedings of the Royal Society A*, 476(2243):20200419.

[83] Sousa, P. C., Pinho, F. T., Oliveira, M. S. N., and Alves, M. A. (2015). Purely elastic flow instabilities in microscale cross-slot devices. *Soft Matter*, 11(45):8856–8862.

[84] Sun, C.-l. and Huang, H.-Y. (2016). Measurements of flow-induced birefringence in microfluidics. *Biomicrofluidics*, 10(1):011903.

[85] Van Gorder, R. A., Vajravelu, K., and Akyildiz, F. T. (2009). Viscoelastic stresses in the stagnation flow of a dilute polymer solution. *Journal of Non-Newtonian Fluid Mechanics*, 161(1-3):94–100.

[86] Varchanis, S., Hopkins, C. C., Shen, A. Q., Tsamopoulos, J., and Haward, S. J. (2020). Asymmetric flows of complex fluids past confined cylinders: A comprehensive numerical study with experimental validation. *Physics of Fluids*, 32(5):053103.

[87] Varshney, A. and Steinberg, V. (2017). Elastic wake instabilities in a creeping flow between two obstacles. *Physical Review Fluids*, 2(5):051301.

[88] Walkama, D. M., Waisbord, N., and Guasto, J. S. (2020). Disorder suppresses chaos in viscoelastic flows. *Physical Review Letters*, 124(16):164501.

[89] Wall, F. T. (1942). Statistical thermodynamics of rubber. *The Journal of Chemical Physics*, 10(2):132–134.

[90] Wang, G., Yang, F., Wu, K., Ma, Y., Peng, C., Liu, T., and Wang, L.-P. (2021). Estimation of the dissipation rate of turbulent kinetic energy: A review. *Chemical Engineering Science*, 229:116133.

[91] Wapperom, P. and Hulsen, M. A. (1998). Thermodynamics of viscoelastic fluids: the temperature equation. *Journal of Rheology*, 42(5):999–1019.

[92] Wapperom, P. and Renardy, M. (2005). Numerical prediction of the boundary layers in the flow around a cylinder using a fixed velocity field. *Journal of Non-Newtonian Fluid Mechanics*, 125(1):35–48.

[93] Wedgewood, L. E. and Bird, R. B. (1988). From molecular models to the solution of flow problems. *Industrial & Engineering Chemistry Research*, 27(7):1313–1320.

[94] Zamani, N., Bondino, I., Kaufmann, R., and Skauge, A. (2015). Effect of porous media properties on the onset of polymer extensional viscosity. *Journal of Petroleum Science and Engineering*, 133:483–495.

[95] Zami-Pierre, F., de Loubens, R., Quintard, M., and Davit, Y. (2016). Transition in the flow of power-law fluids through isotropic porous media. *Physical Review Retters*, 117(7):074502.

Chapter 4

Les structures de contrainte localisée contrôlent la transition vers le chaos dans les écoulements viscoélastiques à travers un réseau d'obstacles

Nous étudions dans ce Chapitre l'écoulement de fluides viscoélastiques à travers un réseau hexagonal 2D de cylindres.

La mise en évidence du rôle clé des brins biréfringents dans les écoulements viscoélastiques suscite de nombreuses questions. En particulier, dans des treillis ordonnés de cylindres où, en fonction des directions de l'écoulement, il peut ne pas y avoir de chemins d'écoulement préférentiels pré-existants, le mécanisme d'amplification semble prendre une tournure particulière.

Deux récentes études [13] et [32] s'intéressent ainsi l'écoulement de fluides viscoélastiques à travers des réseaux hexagonaux de cylindres qui ont la particularité de présenter de nombreuses symétries. Dans [32], les fluctuations temporelles de la vitesse sont supprimées en modifiant aléatoirement la position de chaque cylindre par rapport à sa position cristalline. L'introduction du désordre semble ainsi supprimer le chaos. Dans [13], considérant la même géométrie mais un angle d'écoulement différent, c'est l'effet inverse qui est observé, le désordre semblant favoriser l'instabilité. L'hypothèse alors émise est que ce n'est pas le désordre mais plutôt les points de stagnation qui contrôlent la transition vers l'instationnaire. Ces observations amènent donc à se demander pourquoi les points de stagnation sont si importants. En particulier, de par leurs interactions avec la structure géométrique, les brins biréfringents pourraient-ils jouer un rôle dans la transition vers le chaos?

Article 3 : Structures of localized stress control the transition to chaos in viscoelastic flows through a lattice of obstacles

O. Mokhtari[1,3], J.-C. Latché[2], M. Quintard[1] and Y. Davit[1]

[1]Institut de Mécanique des Fluides de Toulouse (IMFT), CNRS & Université de Toulouse, France
[2]Institut de Radioprotection et de Sûreté Nucléaire (IRSN), Cadarache, France
[3]TotalEnergies E&P, CSTJF, Pau, France

Article destiné à être soumis à ***Nature Physics***

Abstract

Viscoelastic flows tend to be unstable in the creeping regime and can lead to chaotic temporal fluctuations and elastic turbulence. Recent experiments have studied the flow of polymer solutions past obstacles in microfluidic systems where the inertial effects can be neglected but elasticity is strong. These have revealed complex nonlinear phenomena with spontaneous symmetry breaking and a range of spatiotemporal fluctuations. Here we show that structures of localized stress control the transition to unsteadiness and the route to chaos in viscoelastic flows through a hexagonal lattice of cylindrical obstacles. We found in high performance simulations that the birefringent strands – extremely thin structures of large stress formed at stagnation points and transported in the wake of cylinders – tend to stick to neighboring cylinders through a complex coupling between the channelization of the flow and the transport of the conformation tensor. In the steady base flow, this phenomenon leads to multistability, subcritical bifurcations with the angle of the forcing term and hysteresis. Furthermore, in the staggered configuration, we found that the route to chaos starts with a Hopf bifurcation when increasing the Weissenberg number. This corresponds to the trivial state becoming unstable and self-sustained oscillations that develop with the strands flapping between closest neighbouring cylinders – the other sticky positions in the base flow. When varying the Weissenberg number and the ratio of polymer to solvent viscosities, we evidenced a rich zoology of nonlinear effects with spatiotemporal fluctuations corresponding to travelling wave solutions, slow propagation of defects and puffs of strand movements. For the largest values of Weissenberg number and viscosity ratio, we found that the patterns of localized stress stabilize with persistent pulsatile fluctuations along the strands that exhibit some of the hallmarks of chaos. This last pulsatile regime also develops in the aligned configuration, thus suggesting that it is integral to the transition to chaos. Our study provides a new perspective on the role of localized stress and a framework for understanding many experimental observations. We anticipate that it is an important step forward towards developing a unified theory of the nonlinear dynamics of viscoelastic flows past obstacles.

4.1 Introduction

When a suspension of polymers flows through a porous structure, the flexible chains that are transported undergo strong velocity gradients that change their conformation and generate elastic stress [3, 7, 19, 28]. In turn, this stress modifies the velocity field, leading to a two-way coupling that may induce strong nonlinear effects, such as elastic turbulence [10, 29]. Contrary to the Reynolds number Re, the dimensionless number that captures the relative importance of the elastic effects – the Weissenberg number Wi – scales inversely proportional to the characteristic length so that elastic effects are prominent for the smallest pores [3, 25], not the largest. Modern approaches to exploring viscoelastic flows through porous structures have thus exploited microfluidic technologies with characteristic pore sizes in the range $10-100\ \mu m$ and elastic numbers $El \equiv {}^{Wi}/_{Re} > 1$ [20].

The most recent experiments have used slender cylinders to generate quasi-2D flows with elastic effects that can be visualized using standard optical microscopy [11, 15, 16]. This technology has revealed fascinating physics. Spontaneous symmetry breaking and bistability have been shown to occur in the flow of wormlike micellar or hydrolyzed polyacrylamide solutions past a single cylinder confined in a channel [12, 14, 16]. In the case of two cylinders aligned with the flow, a stagnation zone with counter-rotating recirculation vortices appears between the cylinders [22, 30, 31]. Flows past two side-by-side cylinders have revealed a series of bifurcations depending on both the gap between cylinders and the Weissenberg number with symmetric & asymmetric, converging & diverging, bi- & tri-stable states [17, 21].

Further increasing in complexity, arrays of slender cylinders [13, 32] have been used to explore elastic instabilities and transition to chaos in porous structures. [32] showed that the temporal velocity fluctuations that develop in a staggered hexagonal lattice of cylinders are suppressed by randomly displacing each cylinder from the crystalline position. They used this observation to argue that disorder suppresses chaos. [13] showed that introducing disorder into an aligned hexagonal lattice – the set of points that defines the aligned structure being congruent with the staggered one through a rotation of $\pi/6$ modulo $\pi/3$ – yields the opposite effect, with disorder promoting instability. They hypothesized that the important parameter that controls the flow is not disorder, but rather the number of stagnation points accessible to the polymeric chains, with more stagnation points leading to less stability. They further argued that introducing disorder into the staggered configuration reduces the number of stagnation points, frees flow paths and stabilizes the flow. Inversely, disordering the aligned case increases the number of stagnation points and destabilizes the flow. Naturally, these observations beg the questions of why stagnation points are so important and what the driving mechanism is.

We believe that the answer to these questions lies with the most prominent effects associated with viscoelastic flows past obstacles: the formation of localized structures of large polymeric stresses, also known as birefringent strands. These structures just so happen to originate from stagnation points and essentially act as line distributions of forces that oppose the flow. With this idea, we have shown Chapter 3 that strands explain a variety of experimental observations in steady-state flows: they "cut" the flow in two in the wake of a single cylinder and generate a fore-aft asymmetry; they form an envelope in the case of two aligned cylinders with a zone of stagnation that behaves as a two-sided strands-driven cavity; and they amplify preferential flows in the case of side-by-side cylinders. In arrays of cylinders, we have also shown that strands modify the global flow distribution with an increase of stagnation and channelization. This is associated with a rise of dissipation in the flow channels and of entropy production in the strands that are both integral to the increase in resistance to flow – a phenomenon observed experimentally but not fully understood yet [2, 5, 6, 8, 23, 26]. These evidences that strands are a fundamental component of steady viscoelastic flows in such systems raise important new questions: what is role of strands in the transition to unsteady flows? Could they be the key to a unified theory of the nonlinear dynamics of viscoelastic flows past obstacles?

In this Article, we show that strands indeed control both the steady base flow, the spontaneous transition to unsteady flows and the route to chaos. Our study relies on high-performance simulations of viscoelastic flows through a 2D hexagonal lattice of circles (Fig4.1(**a**)) at zero Reynolds number. We solve incompressible Oldroyd-B, FENE-CR and FENE-P models with an imposed force density in the momentum transport equation and biperiodic boundary conditions. By varying the orientation θ of the forcing term (Fig4.1(**a**)), the Weissenberg number Wi and the ratio of viscosities β (Methods), we explore the physics of strand formation and flow in a variety of configurations including both the aligned and staggered geometries. Starting at steady-state, we first show that the patterns of stress localization control the direction of the average flow in a hexagonal lattice and yield preferential directions. We evidence a succession of subcritical

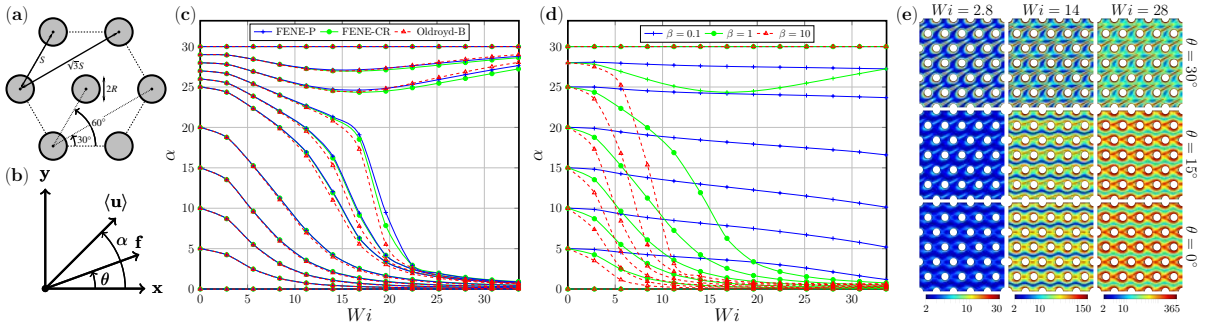

Fig. 4.1 Viscoelastic flows through a hexagonal lattice. (**a**) Geometry of the crystalline structure with a hexagonal lattice of circles of radius R in the aligned configuration used in [13]. The shortest distance between centers of circles S and the second shortest is $\sqrt{3}S$. (**b**) System of axes and definition of the different angles. $\mathbf{f}$ is the unit vector forming an angle θ with $\mathbf{x}$ and representing the dimensionless force density in the momentum transport equation (Methods). $\langle\mathbf{u}\rangle$ is the intrinsic average of the velocity field $\langle\mathbf{u}\rangle = {}^1\!/\!_{|\Omega|}\int_\Omega \mathbf{u} d\Omega$ forming an angle α with $\mathbf{x}$. (**c**) Plots of the angle α as a function of the Weissenberg number Wi for a ratio of polymer to solvent viscosities $\beta = 1$ (Methods), different values of θ and the FENE-P, FENE-CR and Oldroyd-B models. Each curve is obtained by fixing the angle and progressively increasing the Weissenberg number, starting from $Wi = 0$. The graph is limited to the range $\theta \in [0, 30°]$ because of the 6-fold rotational symmetry combined with the reflection symmetry about the $\mathbf{x}$ axis. Points are actual computations and lines are just guides for the eyes. (**d**) Plots of the angle α as a function of the Weissenberg number for the Oldroyd-B model and different values of θ and β. Points are actual computations and lines are just guides for the eyes. (**e**) Fields of polymer stretching – the trace of the conformation tensor, $\mathrm{tr}\,(\mathbf{c})$ (Methods) – for $\beta = 1$ and different values of Wi and θ.

bifurcations with the angle of the forcing term leading to multistability and hysteresis. We then focus on the transition to unsteadiness, focusing on the – more interesting – staggered case. We find a rich zoology of nonlinear behaviors when varying the Weissenberg number Wi and the ratio of viscosities β, including self-sustained flapping oscillations, travelling wave solutions, strand coalescence, slow propagation of defects, puffs and persistent pulsatile fluctuations that exhibit some of the hallmarks of chaos. Our study provides a new perspective on the role of localized stress in viscoelastic flows past obstacles, which we believe is an important step forward towards understanding transition to chaos in such systems and a unified nonlinear theory.

We start our analysis with steady-state solutions in the aligned configuration. Our first objective is to better grasp the pattern of localized stress and the role of the strands on base flow. Since strands are known to delineate flow channels within the porous structure (see Chapter 3) and thus define the orientation of the flow, our idea is to use the angle α between the average velocity field $\langle \mathbf{u} \rangle$ and the $\mathbf{x}$ axis (Fig4.1(**b**)) as a proxy for the orientation of the strands. In our simulations, we proceeded by fixing the angle θ and progressively increasing the Weissenberg number, starting from $Wi = 0$. The limit $Wi = 0$ corresponds to the Newtonian case, so that the observed flow angle is the same as the angle of the imposed force density, $\alpha = \theta$. Upon increasing Wi, results in Fig4.1(**c**) show the formation of two clear preferential flow directions at $\theta = 0°$ and $\theta = 30°$ for all constitutive relations (Oldroyd-B, FENE-P and FENE-CR). The strands that form in the wake of each circle appear as if they are sticking to other circles, either to the closest neighbors at 0° and 60° or to the second closest at 30° (Fig4.1(**e**)).

We hypothesize that the mechanism that makes strands sticky is a feedback between the transport of the conformation tensor and the flow, which is reminiscent of the amplification mechanism of preferential flow paths in the case of side-by-side circles (detail in Chapter 3). Consider for example the case $\theta = 25°$. Initially, the strands tend to form an angle of 25° in the wake of each circle, such that the distance with the circle immediately below is smaller than the distance with the circle above. The flow path of least resistance is above the strands with a positive feedback loop that tends to curve the streamlines towards the path of lowest flow rate and thus displace the strands further down, until enventually the path below is completely closed, see also Movie1. To further test this hypothesis, we study next the behavior of the strands for different values of the parameter β that controls the feedback of the strands upon the flow. Fig4.1(**d**) shows that for $\beta = 0.1$, the preferential flow directions almost completely vanish and the strands do not appear to stick to other circles. When $\beta = 10$, however, the mechanism gets stronger and appears for even smaller Weissenberg numbers.

The fact that the Oldroyd-B, FENE-P and FENE-CR models yield similar results shows that the effect is robust across constitutive laws, thus suggesting that it is integral to viscoelastic fluids in general. These three models indeed describe slightly different physics. The Oldroyd-B model is based upon an affine relation between τ_p and $\mathbf{c}$ that can be interpreted as a Hookean entropic spring description in a molecular dumbbell representation. The trace of the conformation tensor – the stretching od the chains of polymers – and its gradients can become extremely large, which is the essence of the High Weissenber Number Problem and at the core of numerical difficulties associated with such problems. FENE models bound the trace of the conformation tensor, thus limiting the maximum stretching of the chains. FENE-CR and FENE-P models differ in their response to shear flow, with the FENE-CR essentially representing a Boger fluid and the FENE-P being shear-thinning.

We next studied the variations of α when varying the angle of the forcing term θ for fixed values of the Weissenberg number. Fig4.2 shows in blue how α evolves when progressively increasing θ from 0 to 60°. In the limit of small Weissenberg numbers, we observe a linear behavior that is characteristic of the Newtonian case. For a moderate value of the Weissenberg number ($Wi = 8.4$), the evolution of the blue curve resembles a sigmoid, which is a signature of

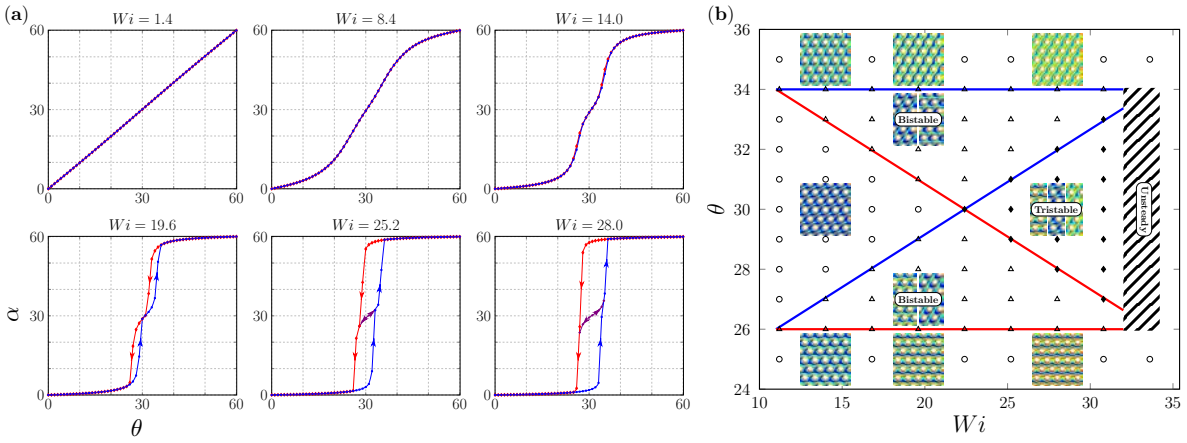

Fig. 4.2 Multistability and hysteresis for the Oldroyd-B model and $\beta = 1$. (**a**) Bifurcation diagrams with the angle θ of the force density. In blue, we plotted the results obtained when increasing θ from 0 to 60°. The red curves correspond to the decrease from 60° to 0 and the purple curves are obtained either by decreasing θ from a point at $\alpha \simeq 45°$ on the blue curve or increasing θ from a point at $\alpha \simeq 15°$ on the red curve. Points are actual computations and lines are just guides for the eyes. (**b**) (θ, Wi) phase diagram with the different stability domains. Insets show the corresponding polymer stretching fields with the position of the strands. The blue and red limits correspond respectively to the cases of an increasing and decreasing angle. (○) indicates a single stable state, (▵) bistability and (♦) tristability.

strands interacting with the closest circles (distance S at 0° and 60°). For $Wi = 14$, the shape of the blue curve changes for $\theta \simeq 30°$ with strands that are long enough to reach the second closest circle (distance $\sqrt{3}S$ at 30°) , thus creating a preferential flow direction with an intermediary plateau at $\alpha \simeq 30°$. The width of this zone evolves non-monotonically with the Weissenberg number, with only a kink in the blue curve for $Wi = 8.4$, a clear preferential direction at $Wi = 14$ and $Wi = 19.6$ and then a decrease with a complete disappearance for $Wi = 28$. This decrease for larger Wi numbers occurs as the interactions of the horizontal strands with closest circles at $\alpha \simeq 0°$ get stronger, so that ultimately detachment from the horizontal position occurs for $\theta > 30°$ and the strands switch from 0 to $\theta = 60°$ with no intermediary value. It also corresponds to a change in the topology of the strands with the formation of an envelope around the circles, which is evidently the most stable configuration.

The threshold effect with strands sticking to closest neighbors yields a subcritical bifurcation and hysteresis. Fig4.2 shows in red the path obtained when decreasing θ starting from $\theta = 60°$. Symmetrically, the strands are now stuck to the closest neighbors at 60° and the transition occurs for lower values of θ compared to the blue curve. We can also recover an intermediary plateau at 30° – in purple in Fig4.2 – by either decreasing θ from a point at $\alpha \simeq 45°$ on the blue curve or increasing θ from a point at $\alpha \simeq 15°$ on the red curve. As described above, this plateau corresponds to strands sticking to the second closest neighbors but can only be obtained when the strands are not initially stuck to the closest neighbors. We further observe two hysteresis regimes with the Weissenberg number. For $Wi = 19.6$, we have two separate hysteretic loops featuring bistability around $\theta = 0°$ and 30° or around $\theta = 30°$ and 60°. These loops then meet to yield tristability around $\theta = 0°$, 30° and 60°.=, see Movie2. The (θ, Wi) phase diagram in Fig4.2 summarizes the different regimes and shows insets of the corresponding stretching field.

Upon further increasing the Weissenberg number, we observed spontaneous transition to unsteady flows. To study this transition, we chose to use the FENE-CR model to avoid

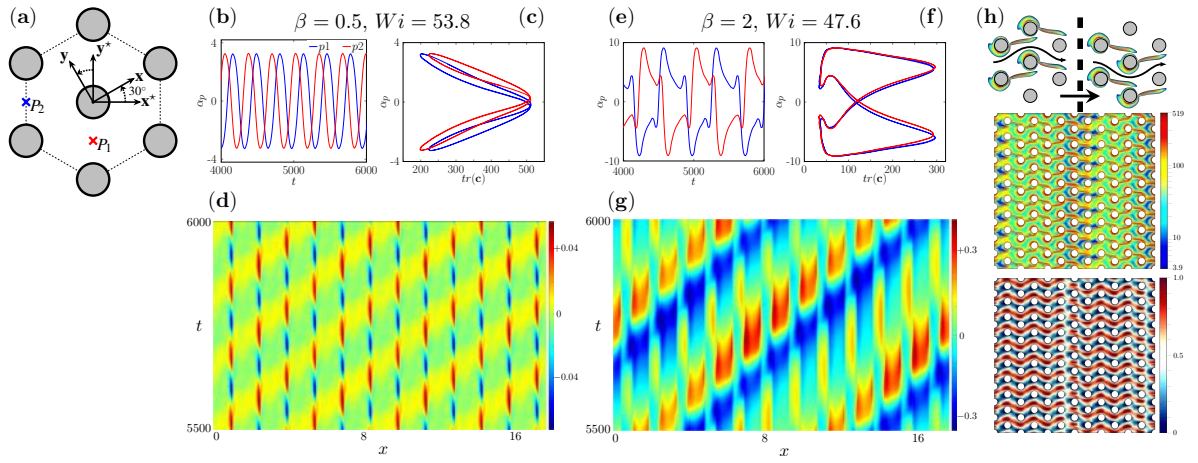

Fig. 4.3 Oscillations and travelling wave solutions in the cases ($\beta = 0.5$, $Wi = 53.8$) and ($\beta = 2$, $Wi = 47.6$) for the FENE-CR model with $b = 1000$ (Methods). (**a**) Schematics of the staggered configuration used in [32] with the correponding reference frame ($\mathbf{x}^\star$,$\mathbf{y}^\star$). It be obtained by a simple rotation of the reference frame ($\mathbf{x}$,$\mathbf{y}$) corresponding to the aligned case. This figure also shows two points of interest, P_1 and P_2. (**b**, **e**) Time variations of the local velocity angle α_P at the two points P_1 and P_2. (**c**, **f**) Phase diagrams with α_P as a function of the local trace of the conformation tensor at P_1 and P_2. (**d**, **g**) Kymographs of the Helmholtz free energy averaged over the vertical direction, normalized by its the time average (Methods). (**h**) Example of a travelling wave in the domain. The schematic diagram on the top illustrates the two equivalent strand configurations with a travelling front corresponding to strands switching side. The fields below show results of the simulations for the trace of the conformation tensor and the corresponding velocity field for the case ($\beta = 2$, $Wi = 47.6$).

complications associated with shear-thinning (FENE-P) and to maximize accuracy (Oldroyd-B). Since multistability occurs for $\theta \simeq 30°$, we also chose to focus on the staggered configuration, placing ourselves in the $(\mathbf{x}^\star, \mathbf{y}^\star)$ frame of reference (Methods). In all cases where we observed unsteadiness, the strands initially form along the direction of the force and then destabilize spontaneously. Within some range of β and Wi, oscillations develop about the direction of the force density with a supercritical Hopf bifurcation and out-of-phase flapping oscillations from one row to the next (Fig4.3b and Movie3). The power spectrum for ($\beta = 0.5,\ Wi = 47.6$) in Fig4.4 shows a dominant frequency at $f \simeq 10^{-1}$ with distinct oscillations on the global flow angle α in Fig4.5. For ($\beta = 0.5,\ Wi = 53.8$), orbits in Fig4.3c, time averaged field of $\mathrm{tr}\,(\mathbf{c})$ and root mean square variations in Fig4.4 show that the oscillations occur about the base flow configuration. There is also a collective effect with signal propagation in the direction as the force density, as evident in the kymographs of the Helmholtz free energy in Fig4.3. This is because strands interact hydrodynamically with each other through the quasi-Newtonian flow channels.

When the strands start sticking to closest neighbors at $\pm 30°$, whether through increasing β or Wi, they still periodically change position with a distinct frequency in the power spectrum, Fig4.4 ($\beta = 2,\ Wi = 47.6$). However, orbits in Fig4.3f, time averaged field of $\mathrm{tr}\,(\mathbf{c})$ and root mean square variations in Fig4.4 show that they do not oscillate about the base flow configuration. Rather, strands stick to one side or the other with clear travelling wave solutions (Movie4). This phenomenon is a stronger manifestation of the collective motion of the strands, which we can think of as follows. Each strand may be roughly understood as a gate allowing or preventing flow through a given pore throat. These gates have a limited number of accessible positions. They are either stuck to one or the other neighbor and in so doing allow or prevent flow in given channels. Globally, strands also have to arrange in a way that maintains flow through the structure, this leading to a set of possible configurations. Fig4.3h presents possible solutions with strands successively sticking up and down so as to form tortuous "zigzag" channels in the x direction. It also shows that two topologically equivalent configurations are possible for the same zigzag channels. Some of the observed travelling wave solutions consist of vertically invariant zones of one of these two configurations with a propagating front corresponding to strands switching side (Movie4).

In another range of dimensionless numbers, we observed the formation of longer strands that are associated with completely different behaviors. The initial flapping oscillations disappeared and were replaced by low frequency/large amplitude temporal fluctuations (Fig4.5(**IV**) and (**V**)). We observed mixed patterns of zigzag channels and envelope patterns along the $\pm 30°$ degree angle – e.g. in Fig4.4 ($\beta = 5,\ Wi = 70$). Fig4.4 ($\beta = 10,\ Wi = 58.8$) illustrates a case with envelop formation throughout the entire lattice with a pattern of localized stress that is reminiscent of the aligned configuration Fig4.1e. We hypothesized that this is the consequence of the intrinsic stability of the envelope pattern. To test this hypothesis, we performed calculations in the aligned case to further assess the stability of this pattern. Results (extended) show a much simpler dynamics with none of the bifurcations observed in the staggered case. We initially have a single strand that transforms into an envelope upon increasing Wi and stays stable over a wide range of β and Wi.

When the strands strongly interact with neighbors and form envelopes, we observed rather regular patterns of strands but also defects that delineate zones with configurations that are mutually incompatible. These defects were either stable in a given position, as shown in Fig4.4 ($\beta = 5,\ Wi = 70$), or moved through the lattice of obstacles. Movement occurred in various ways ranging from a slow propagation from neighbor to neighbor or large puffs of rapid strand movements, as illustrated in Fig4.4 ($\beta = 5,\ Wi = 42$). In many instances, the defects were only ephemerous and ultimately disappeared, leading to a stable pattern of strands. This suggests

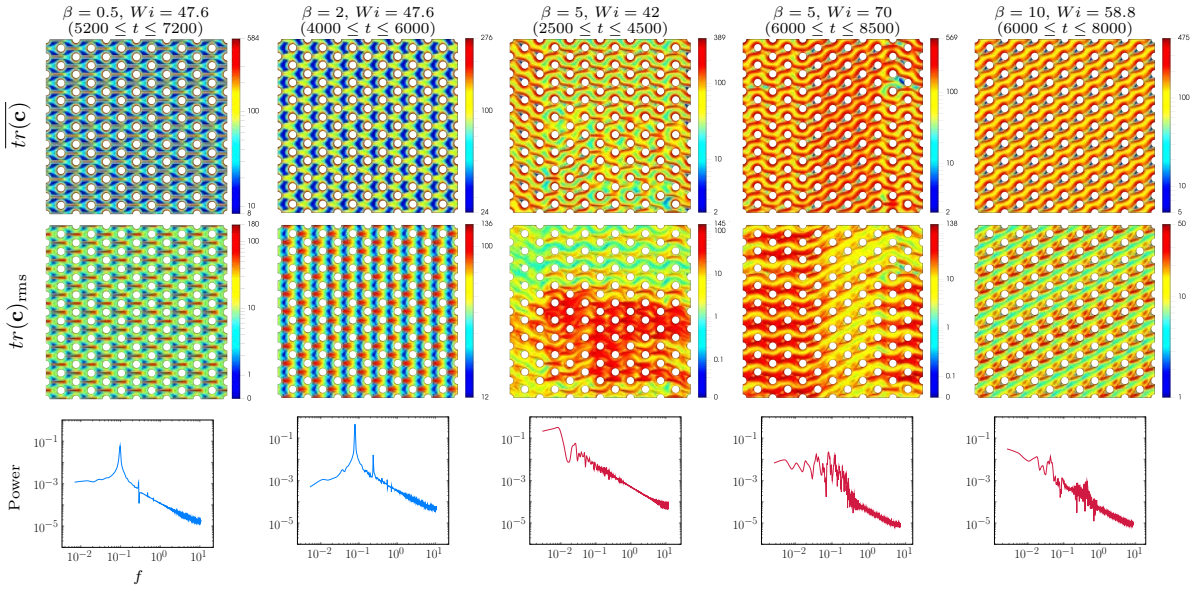

Fig. 4.4 Examples of unsteady flows obtained for the FENE-CR model with $b = 1000$ (Methods). Each column corresponds to a different set of dimensionless numbers with results presented in different time intervals. The first and second lines show the time-averaged fields of the trace of the conformation tensor and the corresponding root mean square variations, respectively (methods). The power spectral density associated with the temporal fluctuation of α are plotted in the third line. The case ($\beta = 0.5,\ Wi = 47.6$) corresponds to regime (**I**) and ($\beta = 2,\ Wi = 47.6$) to regime (**II**). ($\beta = 5,\ Wi = 42$), ($\beta = 5,\ Wi = 70$) and ($\beta = 10,\ Wi = 58.8$) belong to regime (**V**). The color code in the plots of the power spectrum corresponds to that of Fig4.5 with blue correspond to short oscillating strands and red to long strands with envelope formation.

defect propagation is integral to the dynamics of the flow when strands interact strongly with obstacles.

Lastly, we observed a pulsatile movement along the strands at long times (Movie5 and Movie6-b). This movement is visible on the $\mathrm{tr}(\mathbf{c})_{\mathrm{rms}}$ fields in Fig4.4 at both $\beta = 5$ and $\beta = 10$ and on the average flow angle α in Fig4.5 in the case $\beta = 10$. Pulsations in this case are very different in nature from previous oscillations. They feature a more complex temporal response with a power spectrum (Fig4.4) that has no distinct frequency, but rather some of the signatures of chaos [10, 29]. Calculations in the aligned case also show a pulsatile regime, which represents the unique unsteady bifurcation in this case. This suggests that this regime is universal, as opposed to both the Hopf bifurcation with short strands and defect dynamics with long strands that are absent in the aligned case.

For the staggered case, we propose a classification of these different regimes, which are summarized in Figure4.5. We use a color code that corresponds to relatively short strands without envelope formation (blue) and longer strands with envelope formation (red). In blue, we have of course the trivial steady-state solution before transition to unsteady flows. In the unsteady regime, we have

(**I**) **Oscillations** about base flow following a supercritical Hopf bifurcation.

(**II**) **Travelling fronts** separating zones with different configurations of the strands.

(**III**) An **intermediary** regime with subcritical Hopf bifurcation and large amplitude/low frequency fluctuations.

(**IV**) A **quasi-steady** regime with no oscillations and large amplitude/low frequency fluctuations leading to a steady-state.

(**V**) A **pulsating** regime with high-frequency fluctuations over a range of frequencies that suggests a transition towards chaos.

Our results are consistent with recent microfluidic experiments, which is particularly remarkable given the complexity of the problem and fundamental differences – e.g. a variety of perturbations in the experiments that are not present in the simulations or biperiodic boundary conditions in the simulations that have no equivalent in the experiments. Steady flow fields in [32] (Fig 1 and Movie S1) show similar profiles to that in extended Fig4.6 ($\beta = 0.5$, $Wi = 42$). We see that strands are aligned with the pressure gradient and cut the flow field in two in the wake of each circle. Fig 3 and Movie S3 in [13] show two strands per cylinder in the aligned case and the formation of an envelope of polymeric stress. In the oscillation regime, $\overline{\mathrm{tr}(\mathbf{c})}$ and $\mathrm{tr}(\mathbf{c})_{\mathrm{rms}}$ in Fig4.4 share similarities with the retardation in Fig 3 in [13] for the lowest Weissenberg numbers – note that we use colorbars in log scale to facilitate the visualization so that the comparison is not entirely straightforward. The most striking proof for the existence of self-sustained oscillations is in Movie S1 in [13], which clearly shows strands flapping from one side to the other. This is directly comparable to our simulations in Movie3. Movie S1 in [13] also shows the temporary formation of structure that are similar to our zigzag channels. Movies S2 and S3 in [32] also show travelling fronts that delineate zones with different strand configurations. Finally, movies S2 and S4 in [13] show stable patterns of retardation that seem to exhibit some of the pulsatile fluctuations that we observed in our simulations (Movie5 and Movie6-b).

Our analysis further allows us to propose a novel interpretation of some of the results in [13]. Authors showed that the spatially averaged retardation fluctuations varies non-monotonically with the Weissenberg number. In the staggered case, they observe a large increase followed by a sudden decrease and then a smoother increase similar to that of the aligned case. We propose

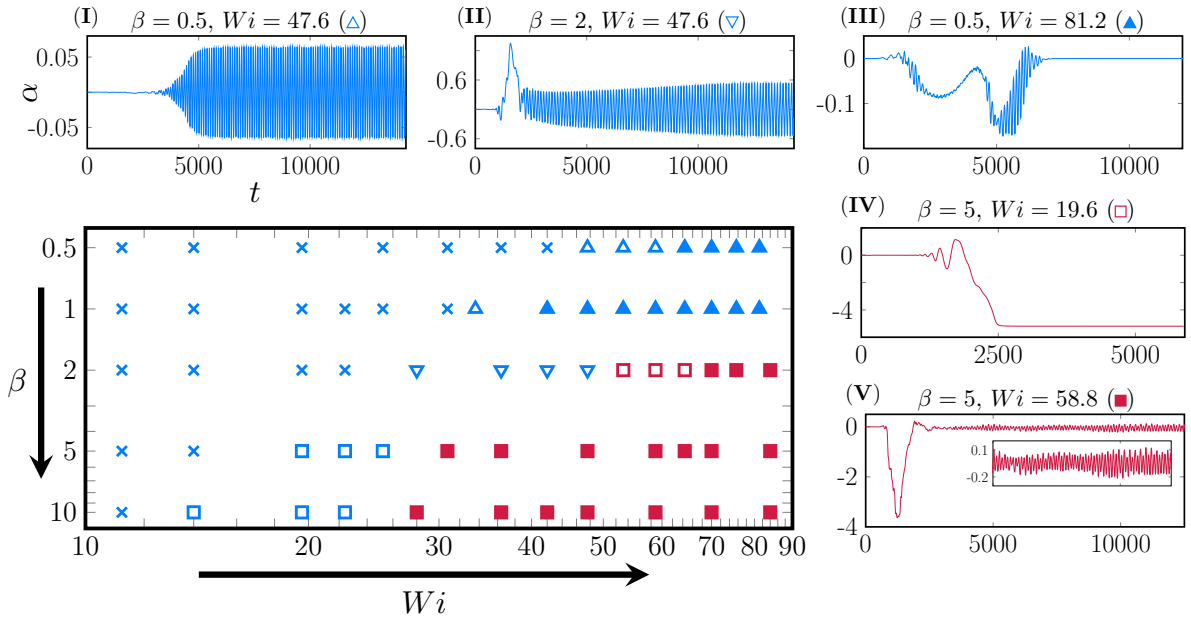

Fig. 4.5 Diagram of the different regimes obtained for the FENE-CR with $b = 1000$ (Methods). The main graph shows the different regimes as a function of β and Wi. The other plots are examples of time evolutions of α for each regime. (×) corresponds to the trivial steady solution, (△) to oscillations (**I**), (▽) to travelling fronts (**II**), (▲) to the intermediary regime (**III**), (□) to the quasi-steady regime (**IV**) and (■) to the pulsating regime (**V**).

that the increase occurs when reaching the Hopf bifurcation and self-sustained oscillations. Upon further increasing Wi, the interaction of the strands with other obstacles gets stronger, which stabilizes the pattern of localized stress and leads a decrease in the temporal fluctuations. In our simulations, we even obtain regimes with steady-states in the long time limit – e.g. the quasi-steady regime. Finally, we also hypothesize that second increase is the consequence of the pulsatile regime whereby we observe an increase in fluctuations that is very similar in nature to that of the aligned case.

Contrary to [13], however, we found that stagnation points only play an indirect role in the dynamics of the flow. They are important in the sense that they create birefringent strands, but the key to understanding the dynamics of the system really is the pattern of localized polymeric stress, not the stagnation points. This pattern is the consequence of a complex coupling between the flow, the transport of the conformation tensor and the obstacles. Our interpretation in terms of birefringent strands provides a unified theory for explaining a wide range of different experimental observations in such systems. Our previous work showed, in particular, that they explain recent results for steady flows with one or two cylindric obstacles and offer a new perspective on dissipation through arrays of cylinders. Here, we showed that the patterns of localized stress can also be used to explain many aspects of the transition to unsteady flows in hexagonal lattices of obstacles. We believe that this idea will prove to be the key to a unified theory of the nonlinear dynamics of viscoelastic flows past obstacles and through ordered, disordered and even three-dimensional stuctures.

4.2 Methods

Bulk flow models We consider an incompressible flow with $\operatorname{div}\mathbf{u}=0$ and steady momentum transport given by

$$0=-\nabla\mathfrak{p}+\operatorname{div}\left(\tau_s+\tau_p\right)+\mathfrak{F}, \tag{4.1}$$

with $\mathbf{u}$ the velocity, $\mathfrak{p}$ the pressure, τ_s the solvent stress tensor, τ_p the polymeric stress tensor and $\mathfrak{F}$ an imposed force density. The flow through the obstacles results solely from the imposed force density $\mathfrak{F}$ in the momentum transport equation. The constitutive stress relation for the solvent is $\tau_s=\eta_s\left(\nabla\mathbf{u}+(\nabla\mathbf{u})^{\mathsf{T}}\right)$ with η_s the viscosity. For the polymeric stress, we consider the Oldroyd-B, FENE-CR and FENE-P models. The stress tensor is given by $\tau_p=\frac{\eta_p}{\lambda}g(\mathbf{c})\mathbf{c}-h(\mathbf{c})\mathbf{I}_d$ with η_p the polymeric viscosity, λ a characteristic time for polymer relaxation and $\mathbf{c}$ the conformation tensor. We have $g(\mathbf{c})=h(\mathbf{c})=1$ for the Oldroyd-B, $g(\mathbf{c})=h(\mathbf{c})=\frac{b}{b-\operatorname{tr}(\mathbf{c})}$ for the FENE-CR and $g(\mathbf{c})=\frac{b}{b-\operatorname{tr}(\mathbf{c})}$, $h(\mathbf{c})=\frac{b}{b-\operatorname{tr}(\mathbf{I}_d)}$ for the FENE-P. In both FENE models, b is the parameter that controls the maximum stretching of the polymers with $\operatorname{tr}(\mathbf{c})<b$. The other important ingredient is the constitutive transport equation for the conformation tensor, which reads

$$\partial_t\mathbf{c}+(\mathbf{u}\cdot\nabla)\mathbf{c}=\nabla\mathbf{u}\,\mathbf{c}+\mathbf{c}\,(\nabla\mathbf{u})^{\mathsf{T}}-\frac{1}{\eta_p}\tau_p. \tag{4.2}$$

Domain, boundary conditions and non-dimensionalization We consider a simulation domain that is a rectangle with biperiodic left/right and top/bottom conditions and a no-slip/no-penetration ($\mathbf{u}=0$) condition on the boundaries of the obstacles. These obstacles consist of an array of circles, as presented in Fig4.1(**a**). We consider two geometries. The first one, which is used for the study of multistability, consists of 10×6 circles in the aligned configuration. The second one, which is used to study unsteady flows, consists of 12×20 circles in the staggered configuration.

The mesh is structured and uniform. It consists of quadrilateral cells with circles obtained by making holes into the uniform mesh and circles boundaries approximated as stair-steps. In studying the transition to unsteady flows, we took care of working with Cartesian meshes that were symmetric about the horizontal configuration of the strands corresponding to base flow at steady-state. We used a constant mesh size of $0.04R$, where R is the circle radius. This corresponds to about $3\cdot10^5$ of cells for the aligned geometry and about 1.2 million of cells for the staggered configuration.

To non-dimensionalize the problem, we used the minimum distance between two circles $H=S-2R$ as a characteristic length, $U=\frac{H^2}{\eta_s+\eta_p}\|\mathfrak{F}\|$ as the reference velocity and H/U with as a characteristic time. The final dimensionless equation for momentum transport reads

$$0=-\nabla p+\nabla^2\mathbf{u}+\frac{\beta}{Wi}\operatorname{div}\left(g(\mathbf{c})\mathbf{c}-h(\mathbf{c})\mathbf{I}_d\right)+(1+\beta)\ \mathbf{f}, \tag{4.3}$$

$$0=\operatorname{div}\mathbf{u}, \tag{4.4}$$

$$\partial_t\mathbf{c}+(\mathbf{u}\cdot\nabla)\mathbf{c}=\nabla\mathbf{u}\,\mathbf{c}+\mathbf{c}\,(\nabla\mathbf{u})^{\mathsf{T}}-\frac{1}{Wi}\left(g(\mathbf{c})\mathbf{c}-h(\mathbf{c})\mathbf{I}_d\right), \tag{4.5}$$

with the Weissenberg number defined as

$$Wi=\frac{\lambda U}{H} \tag{4.6}$$

and the viscosity ratio as

$$\beta=\frac{\eta_p}{\eta_s}. \tag{4.7}$$

Numerical scheme A detailed presentation of the numerical scheme is available in [24]. The flow problem is solved using a staggered projection-correction scheme with p, $\mathbf{c}$ evaluated at the center of mesh elements and $\mathbf{u}$ at the center of faces. The transport of the conformation tensor is done using a Strang operator splitting combined with a log transform in the hyperbolic transport equation. The spatial discretization for the momentum transport equation is based on Rannacher-Turek finite elements, while we use finite volumes for the transport of $\mathbf{c}$.

HPC implementation The solver is implemented as a specific module in CALIF^{3}S [4]. The calculations were performed on TotalEnergies' supercomputer Pangea II. Parallel computations were carried out using a domain decomposition approach based on the METIS (4.0.3) graph partitioner [18] and the OpenMPI (3.1.5) library [9]. As an example to illustrate the cost of the calculations, one point in the stationnary case required about 10^3 core $\times\, h$ while the case $\beta = 10$, $Wi = 84$ alone required about 10^5 core $\times\, h$.

Helmoltz free energy The Helmoltz free energy [1, 27, 34, 35] is given by

$$\psi = \frac{\beta}{2Wi}\mathrm{tr}\left(\mathbf{c} - \mathbf{I}_d + \ln\left(\mathbf{c}\right)\right), \tag{4.8}$$

the term in $\mathrm{tr}\left(\mathbf{c} - \mathbf{I}_d\right)$ and $\mathrm{tr}\left(\ln\left(\mathbf{c}\right)\right)$ is entropic [33]. For the kymographs, the free energy is averaged along the vertical direction by $\bar{\psi}^y = \frac{1}{L_y}\int_0^{L_y}\psi\left(x,y\right)dy$, where L_y corresponds to the domain height. This spatial average is then normalized by the time average by $\frac{\bar{\psi}^y - \left\langle\bar{\psi}^y\right\rangle_t}{\left\langle\bar{\psi}^y\right\rangle_t}$.

Time averaging and rms The time-averaged value of a variable ξ over the interval $[t_1, t_2]$ is defined as

$$\bar{\xi} = \frac{1}{t_2 - t_1}\int_{t_1}^{t_2}\xi\left(\tau\right)d\tau \tag{4.9}$$

and the corresponding rms is defined by

$$\xi_{rms} = \sqrt{\overline{\left(\xi - \bar{\xi}\right)^2}}. \tag{4.10}$$

Power spectral density The power spectral density of $S(f)$ corresponding to a discrete-time signal ξ is given by the discrete Fourier transform of its autocorrelation function $R(k)$ through

$$S(f) = \sum_{k=1}^{N} R(k)\exp(-2\pi i f k),$$

with

$$R(k) = \frac{1}{N}\sum_{n=1}^{N} x(n)x(n-k).$$

4.3 Extended figures

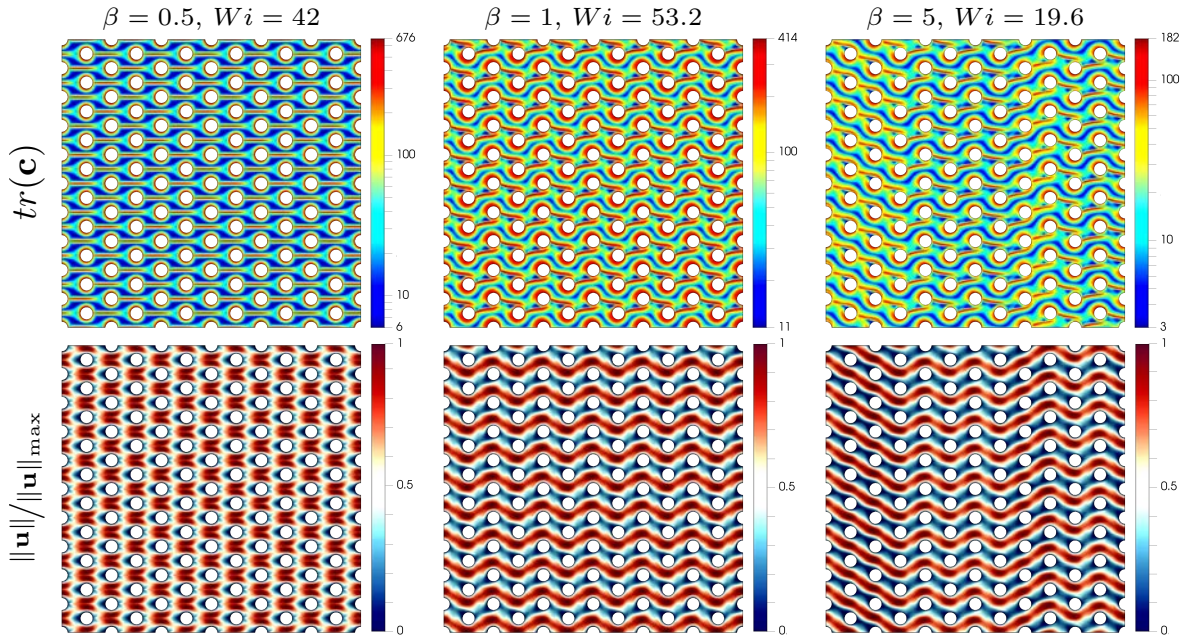

Fig. 4.6 Examples of steady-state fields for $\mathrm{tr}\,(\mathbf{c})$ and the corresponding normalized amplitude of the velocity.

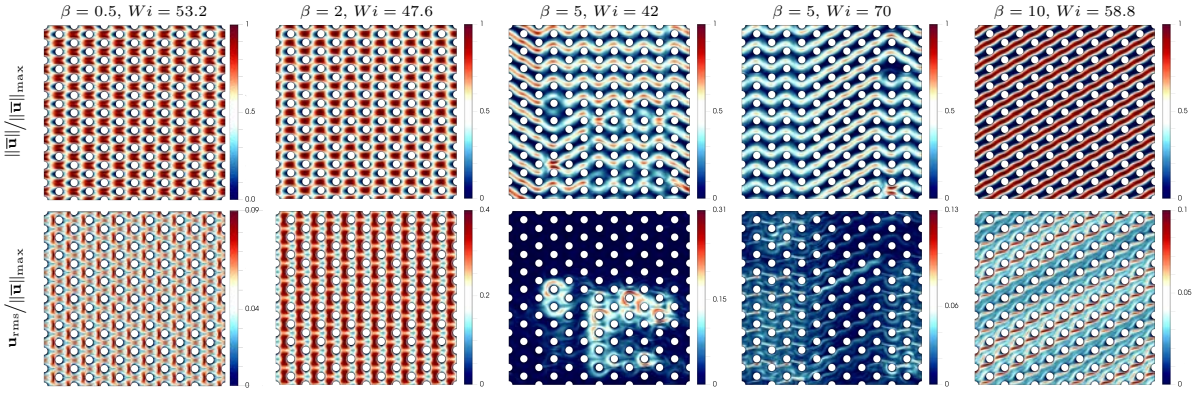

Fig. 4.7 Velocity fields corresponding to Fig4.4.

Références

[1] Booij, H. C. (1984). The energy storage in the Rouse model in an arbitrary flow field. *The Journal of Chemical Physics*, 80(9):4571–4572.

[2] Browne, C. A. and Datta, S. S. (2021). Elastic turbulence generates anomalous flow resistance in porous media. *Science Advances*, 7(45):eabj2619.

[3] Browne, C. A., Shih, A., and Datta, S. S. (2020). Pore-scale flow characterization of polymer solutions in microfluidic porous media. *Small*, 16(9):1903944.

[4] CALIF3S (2021). A Computational Fluid Dynamics software based on Pelicans. https://gforge.irsn.fr/gf/project/calif3s.

[5] Clarke, A., Howe, A. M., Mitchell, J., Staniland, J., Hawkes, L., and Leeper, K. (2015). Mechanism of anomalously increased oil displacement with aqueous viscoelastic polymer solutions. *Soft Matter*, 11(18):3536–3541.

[6] Clarke, A., Howe, A. M., Mitchell, J., Staniland, J., and Hawkes, L. A. (2016). How viscoelastic-polymer flooding enhances displacement efficiency. *SPE Journal*, 21(03):0675–0687.

[7] Dauben, D. L. and Menzie, D. E. (1967). Flow of polymer solutions through porous media. *Journal of Petroleum Technology*, 19(08):1065–1073.

[8] Galindo-Rosales, F. J., Campo-Deano, L., Pinho, F. T., Van Bokhorst, E., Hamersma, P. J., Oliveira, M. S. N., and Alves, M. A. (2012). Microfluidic systems for the analysis of viscoelastic fluid flow phenomena in porous media. *Microfluidics and Nanofluidics*, 12(1-4):485–498.

[9] Graham, R. L., Woodall, T. S., and Squyres, J. M. (2005). Open MPI: A flexible high performance MPI. In *International Conference on Parallel Processing and Applied Mathematics*, pages 228–239. Springer.

[10] Groisman, A. and Steinberg, V. (2000). Elastic turbulence in a polymer solution flow. *Nature*, 405(6782):53–55.

[11] Haward, S., Hopkins, C. C., Varchanis, S., and Shen, A. Q. (2021a). Bifurcations in flows of complex fluids around microfluidic cylinders. *Lab on a Chip*, 21:4041–4059.

[12] Haward, S. J., Hopkins, C. C., and Shen, A. Q. (2020). Asymmetric flow of polymer solutions around microfluidic cylinders: Interaction between shear-thinning and viscoelasticity. *Journal of Non-Newtonian Fluid Mechanics*, 278:104250.

[13] Haward, S. J., Hopkins, C. C., and Shen, A. Q. (2021b). Stagnation points control chaotic fluctuations in viscoelastic porous media flow. *Proceedings of the National Academy of Sciences*, 118(38).

[14] Haward, S. J., Kitajima, N., Toda-Peters, K., Takahashi, T., and Shen, A. Q. (2019). Flow of wormlike micellar solutions around microfluidic cylinders with high aspect ratio and low blockage ratio. *Soft Matter*, 15(9):1927–1941.

[15] Haward, S. J., Toda-Peters, K., and Shen, A. Q. (2018). Steady viscoelastic flow around high-aspect-ratio, low-blockage-ratio microfluidic cylinders. *Journal of Non-Newtonian Fluid Mechanics*, 254:23–35.

[16] Hopkins, C. C., Haward, S. J., and Shen, A. Q. (2020). Microfluidics: Purely elastic fluid–structure interactions in microfluidics: Implications for mucociliary flows. *Small*, 16(9):2070047.

[17] Hopkins, C. C., Haward, S. J., and Shen, A. Q. (2021). Tristability in viscoelastic flow past side-by-side microcylinders. *Physical Review Letters*, 126(5):054501.

[18] Karypis, G. and Kumar, V. (1998). A fast and high quality multilevel scheme for partitioning irregular graphs. *SIAM Journal on Scientific Computing*, 20(1):359–392.

[19] Kawale, D., Bouwman, G., Sachdev, S., Zitha, P. L. J., Kreutzer, M. T., Rossen, W. R., and Boukany, P. E. (2017a). Polymer conformation during flow in porous media. *Soft Matter*, 13(46):8745–8755.

[20] Kawale, D., Marques, E., Zitha, P. L. J., Kreutzer, M. T., Rossen, W. R., and Boukany, P. E. (2017b). Elastic instabilities during the flow of hydrolyzed polyacrylamide solution in porous media: effect of pore-shape and salt. *Soft Matter*, 13(4):765–775.

[21] Khan, M. B. and Sasmal, C. (2021). Elastic instabilities and bifurcations in flows of wormlike micellar solutions past single and two vertically aligned microcylinders: Effect of blockage and gap ratios. *Physics of Fluids*, 33(3):033109.

[22] Kumar, M. and Ardekani, A. M. (2021). Elastic instabilities between two cylinders confined in a channel. *Physics of Fluids*, 33(7):074107.

[23] Mitchell, J., Lyons, K., Howe, A. M., and Clarke, A. (2016). Viscoelastic polymer flows and elastic turbulence in three-dimensional porous structures. *Soft Matter*, 12(2):460–468.

[24] Mokhtari, O., Davit, Y., Latché, J.-C., and Quintard, M. (2021). A staggered projection scheme for viscoelastic flows. Working paper or preprint.

[25] Poole, R. J. (2019). Three-dimensional viscoelastic instabilities in microchannels. *Journal of Fluid Mechanics*, 870:1–4.

[26] Qin, B., Salipante, P. F., Hudson, S. D., and Arratia, P. E. (2019). Flow resistance and structures in viscoelastic channel flows at low Re. *Physical Review Letters*, 123(19):194501.

[27] Sarti, G. C. and Marrucci, G. (1973). Thermomechanics of dilute polymer solutions: multiple bead-spring model. *Chemical Engineering Science*, 28(4):1053–1059.

[28] Seright, R. S., Fan, T., Wavrik, K., and de Carvalho Balaban, R. (2011). New insights into polymer rheology in porous media. *SPE Journal*, 16(01):35–42.

[29] Steinberg, V. (2021). Elastic turbulence: An experimental view on inertialess random flow. *Annual Review of Fluid Mechanics*, 53:27–58.

[30] Varshney, A. and Steinberg, V. (2017). Elastic wake instabilities in a creeping flow between two obstacles. *Physical Review Fluids*, 2(5):051301.

[31] Varshney, A. and Steinberg, V. (2019). Elastic alfven waves in elastic turbulence. *Nature communications*, 10(1):1–7.

[32] Walkama, D. M., Waisbord, N., and Guasto, J. S. (2020). Disorder suppresses chaos in viscoelastic flows. *Physical Review Letters*, 124(16):164501.

[33] Wall, F. T. (1942). Statistical thermodynamics of rubber. *The Journal of Chemical Physics*, 10(2):132–134.

[34] Wapperom, P. and Hulsen, M. A. (1998). Thermodynamics of viscoelastic fluids: the temperature equation. *Journal of Rheology*, 42(5):999–1019.

[35] Wedgewood, L. E. and Bird, R. B. (1988). From molecular models to the solution of flow problems. *Industrial & Engineering Chemistry Research*, 27(7):1313–1320.

Chapter 5

Loi de Darcy modifiée pour les écoulements viscoélastiques de solutions polymères très diluées à travers des milieux poreux

Nous dérivons dans ce Chapitre une forme moyennée du modèle Oldroyd-B à l'échelle de Darcy.

Ayant mis en évidence le rôle important des zones de forte contrainte sur l'écoulement, leur prise en compte dans la dérivation d'un modèle à l'échelle macroscopique devient nécessaire. Or, les quelques dérivations que l'on trouve à ce jour dans la littérature [6, 16] proposent de linéariser le problème en négligeant les termes de production $\nabla \mathbf{u}\,\mathbf{c} + \mathbf{c}(\nabla \mathbf{u})^{\mathsf{T}}$ présents dans l'équation constitutive, ce qui permet de découpler l'équation de conservation de la quantité de mouvement de l'équation de transport de la conformation mais, ce faisant, ne permet pas de capturer la formation des brins birefringents. La question est donc de savoir comment linéariser le problème tout en capturant les filaments et leur effet sur l'écoulement moyen. Une des pistes, proposée ici, est donc de considérer le régime très dilué, $\beta \ll 1$, qui permet de découpler le système tout en prenant en compte les termes de production de conformation, nécessaires à la formation des brins.

Article 4 : A modified Darcy's law for viscoelastic flows of highly dilute polymer solutions through porous media

O. Mokhtari[1,3], J.-C. Latché[2], M. Quintard[1] and Y. Davit[1]

[1]Institut de Mécanique des Fluides de Toulouse (IMFT), CNRS & Université de Toulouse, France
[2]Institut de Radioprotection et de Sûreté Nucléaire (IRSN), Cadarache, France
[3]TotalEnergies E&P, CSTJF, Pau, France

Article destiné à être soumis à ***Journal of Non-Newtonian Fluid Mechanics***

Abstract

Viscoelastic flows of polymer solutions in complex geometries can generate a strong localization of stress within small regions of the fluid with, in particular, the formation of birefringent strands. In porous media, these localized structures of stress can drive preferential flow paths and increase global dissipation. Modeling the impact of such effects at Darcy or larger scales is a daunting task – one of the reasons being the lack of approaches using homogenization theories to help figure out both the correct form of the averaged transport equations and the relevant set of effective parameters. Here we homogenize the Oldroyd-B equations at zero Reynolds number to obtain a model that captures the effect of localized polymeric stress. This homogenized model consists of an advection-reaction transport equation for the average conformation tensor along with a form of Darcy's law that contains an additional drag term associated with structures of localized stress. The derivation is based upon a limit of high dilution, a regime where the Oldroyd-B model can be transformed into a sequence of linear problems using asymptotic developments. We validate our approach in test cases corresponding to flows in a channel and through arrays of circles. Besides providing a new model for viscoelastic flows in porous media, our work also shows that modelling viscoelastic flows through porous media is not simply a matter of determining an apparent permeability tensor – the homogenized model cannot be easily reduced to a simple form of Darcy's law – but rather requires the development of specific homogenized models that capture the coupling between the transport of the polymeric stress and momentum.

5.1 Introduction

Modeling the flow of non-Newtonian fluids through porous media, in particular viscoelastic polymer solutions, is a problem of interest in a number of engineering applications including soil remediation processes or enhanced oil recovery. Solving viscoelastic flows at pore-scale in complex structures is challenging, even for moderate Weissenberg numbers – the dimensionless number that measures the relative importance of elastic effects. This issue is often referred to as the High Weissenberg Number Problem (HWNP) and stems from a strong localization of the polymeric stress in small regions of the domain where the conformation tensor can reach extremely high values. The archetypal example is the birefringent strand observed past a single cylinder [11, 13, 25] or in cross-slot devices [17, 20, 23]. This HWNP strongly constrains the simulations with strong limits upon accessible Weissenberg numbers and upon the extent of the simulation domains. Deriving average formulations that do not require the detailed description at pore-scale, but rather capture small-scale phenomena through effective parameters at larger scale, is an interesting fundamental problem and would also be a useful tool in engineering applications.

A few computations of apparent permeabilities are available in the literature. However, there is a very limited amount of literature attempting to perform any sort of direct upscaling of

viscoelastic flows through porous media and, in so doing, to question the form of the macroscale equations and the relevant set of effective parameters. Khuzhayorov et al. [16] used formal multiple scale asymptotics and De Haro et al. [6] used volume averaging to derive a form of dynamic Darcy's law. Unfortunately, the homogenization in both these works is limited to a linear form of viscoelasticity with a constitutive equation that is not frame indifferent and that does not capture transport of the polymeric stress – it is simialr to a low Weissenberg approximation. In particular, this eliminates right away terms that can actually generate the birefringent strands, in particular the part of the upper-convected derivative with the velocity gradient in the constitutive equation of the Oldroyd-B model. Slattery [24] proposes a generalization of the resistance tensor for several fluids, including a Noll simple fluid of memory fluids, but without performing the homogenization of the constitutive equation.

In this work, we use volume averaging to derive a homogenized model starting from the incompressible Oldroyd-B equations at low Reynolds number,

$$0 = -\nabla p + \Delta \mathbf{u} + \frac{\beta}{Wi}\nabla \cdot \mathbf{c} + \mathbf{F}, \tag{5.1a}$$

$$0 = \nabla \cdot \mathbf{u}, \tag{5.1b}$$

$$\partial_t \mathbf{c} + \mathbf{u} \cdot \nabla \mathbf{c} = \nabla \mathbf{u} \cdot \mathbf{c} + \mathbf{c} \cdot \nabla \mathbf{u}^{\mathsf{T}} - \frac{1}{Wi}(\mathbf{c} - \mathbf{I}_d), \tag{5.1c}$$

with a no-slip and no-penetration boundary condition for fluid/solid interfaces. Here p is a dimensionless pressure, $\mathbf{u}$ a dimensionless velocity, $\mathbf{c}$ the conformation tensor, $\mathbf{I}_d$ the identity in dimension $d = 2$ or 3 and $\mathbf{F}$ a constant/uniform dimensionless force density vector field. $\beta \overset{\text{def}}{=} \eta_p/\eta_s$ is the ratio of polymeric to solvent viscosities and $Wi \overset{\text{def}}{=} \lambda U/H$ is the Weissenberg number with λ the relaxation time of the polymer, U a reference velocity and H a caracteristic lengthscale.

Our idea is to perform the homogenization in a limit that allows us to derive a linearized form of the problem but that still captures the stress localization. $Wi \ll 1$ is frequently used for the linearization but does not capture the stress localization that appears for moderate Weissenberg numbers. Instead, we proceed by considering the limit $\beta \ll 1$ that can be thought of as a limit of large dilution for polymer solutions (η_p small and thus β small). In this case, the leading order for the velocity is simply the Newtonian field with viscosity η_s and the leading order for the conformation tensor corresponds to the transport in Eq 5.1c with the Newtonian velocity, therefore transforming the problem into a sequence of linear problems with one-way couplings. This makes it possible to treat cases with relatively large Wi numbers and thus to derive a form of Darcy's law that captures some of the fundamental features of viscoelastic flows, such as birefringent strands.

The paper is organized as follows. In Section 5.2, we detail the non-dimensionalization of the problem, reformulate the Oldroyd-B model in terms of a conformation vector, rather than a matrix, and derive the sequence of problems in the limit $\beta \ll 1$. We then proceed in Section 5.3 to averaging the partial differential equations at each order in the asymptotic developments and to deriving the corresponding average model. To finish, we study Section 5.4 the behaviour of our model for three 2D test cases in simple geometries (channel, crystalline and amorphous periodic structure of circles).

5.2 Reformulation of the flow problem

5.2.1 Non-dimensionalization

In the Introduction, Eq 5.1 is a dimensionless form fo the Oldroyd-B problem. Here we show how to derive this form starting from the dimensional form of the Oldroyd-B problem

$$0 = -\nabla \mathfrak{p} + \eta_s \Delta \mathfrak{u} + \frac{\eta_p}{\lambda} \nabla \cdot \mathbf{c} + \mathfrak{F}, \tag{5.2a}$$

$$0 = \nabla \cdot \mathfrak{u}, \tag{5.2b}$$

$$\partial_t \mathbf{c} + \mathfrak{u} \cdot \nabla \mathbf{c} = \nabla \mathfrak{u} \cdot \mathbf{c} + \mathbf{c} \cdot \nabla \mathfrak{u}^{\mathsf{T}} - \frac{1}{\lambda} (\mathbf{c} - \mathbf{I}_d). \tag{5.2c}$$

$\mathfrak{u}$ and $\mathfrak{p}$ are the velocity and pressure, respectively. $\mathfrak{F}$ is the dimensional force density vector field that we take constant and uniform. η_s and η_p are solvent and polymeric viscosities, respectively. λ is a characteristic time associated with the relaxation of the polymers. This problem may be written in dimensionless form as

$$0 = -\nabla p + \Delta \mathbf{u} + \frac{\beta}{Wi} \nabla \cdot \mathbf{c} + \mathbf{F}, \tag{5.3a}$$

$$0 = \nabla \cdot \mathbf{u}, \tag{5.3b}$$

$$\partial_t \mathbf{c} + \mathbf{u} \cdot \nabla \mathbf{c} = \nabla \mathbf{u} \cdot \mathbf{c} + \mathbf{c} \cdot \nabla \mathbf{u}^{\mathsf{T}} - \frac{1}{Wi} (\mathbf{c} - \mathbf{I}_d), \tag{5.3c}$$

with

$$\mathbf{x} \overset{\text{def}}{=} \frac{\mathfrak{x}}{H}, \quad t \overset{\text{def}}{=} \frac{\|\mathfrak{F}\| H}{\eta_s} \mathfrak{t}, \quad p \overset{\text{def}}{=} \frac{\mathfrak{p}}{\|\mathfrak{F}\| H}, \quad \mathbf{F} \overset{\text{def}}{=} \frac{\mathfrak{F}}{\|\mathfrak{F}\|}, \quad \beta \overset{\text{def}}{=} \frac{\eta_p}{\eta_s}, \quad Wi \overset{\text{def}}{=} \frac{\lambda \|\mathfrak{F}\| H}{\eta_s}.$$

5.2.2 Vector form of the transport equations

The transport equation for the conformation tensor in the fluid domain Ω_f is

$$\partial_t \mathbf{c} + \mathbf{u} \cdot \nabla \mathbf{c} = \nabla \mathbf{u} \cdot \mathbf{c} + \mathbf{c} \cdot \nabla \mathbf{u}^{\mathsf{T}} - \frac{1}{Wi} (\mathbf{c} - \mathbf{I}_d), \tag{5.4}$$

with $\mathbf{c}(\mathbf{x}, t) \in \mathbb{R}^{d \times d}_{S,>0}$ a symmetric (S) positive (>0) $d \times d$ matrix with $d = 2$ or 3. Dealing with the transport of a matrix in the homogenization procedure is tedious. Closure relationships for $\mathbf{c}$ would involve tensors of at least rank 4, with complex symmetries and the process would be extremely cumbersome. The homogenization procedure can be greatly simplified with a reformulation of the problem in terms of a vector, $\mathbf{c}(\mathbf{x}, t) \in \mathbb{R}^{\frac{d(d+1)}{2}}$, defined such that $\mathbf{c} \overset{\text{def}}{=} \begin{pmatrix} C_{xx} & C_{yy} & C_{xy} \end{pmatrix}^{\mathsf{T}}$ in 2D and $\mathbf{c} \overset{\text{def}}{=} \begin{pmatrix} C_{xx} & C_{yy} & C_{zz} & C_{yz} & C_{xz} & C_{xy} \end{pmatrix}^{\mathsf{T}}$ in 3D. This approach is reminiscent of the Voigt and Mandel notation often used in linear elasticity . The new transport equation can be written as

$$\partial_t \mathbf{c} + \mathbf{u} \cdot \nabla \mathbf{c} = (D\mathbf{u}) \cdot \mathbf{c} - \frac{1}{Wi} (\mathbf{c} - \mathbf{i}) \tag{5.5}$$

with

$$D\mathbf{u} \overset{\text{def}}{=} \begin{pmatrix} 2\partial_x u_x & 0 & 2\partial_y u_x \\ 0 & 2\partial_y u_y & 2\partial_x u_y \\ \partial_x u_y & \partial_y u_x & 0 \end{pmatrix} \text{ for } d = 2, \tag{5.6}$$

and

$$D\mathbf{u} \stackrel{\text{def}}{=} \begin{pmatrix} 2\partial_x u_x & 0 & 0 & 0 & 2\partial_z u_x & 2\partial_y u_x \\ 0 & 2\partial_y u_y & 0 & 2\partial_z u_y & 0 & 2\partial_x u_y \\ 0 & 0 & 2\partial_z u_z & 2\partial_y u_z & 2\partial_x u_z & 0 \\ 0 & \partial_y u_z & \partial_z u_y & \partial_y u_y + \partial_z u_z & \partial_x u_y & \partial_x u_z \\ \partial_x u_y & \partial_y u_x & 0 & \partial_z u_x & \partial_z u_y & \partial_x u_x + \partial_y u_y \\ \partial_x u_z & 0 & \partial_z u_x & \partial_y u_x & \partial_x u_x + \partial_z u_z & \partial_y u_z \end{pmatrix} \text{ for } d = 3, \quad (5.7)$$

and

$$\mathbf{i} \stackrel{\text{def}}{=} \begin{pmatrix} 1 \\ 1 \\ 0 \end{pmatrix} \text{ for } d = 2 \text{ and } \mathbf{i} \stackrel{\text{def}}{=} \begin{pmatrix} 1 \\ 1 \\ 1 \\ 0 \\ 0 \\ 0 \end{pmatrix} \text{ for } d = 3. \quad (5.8)$$

Note in particular that $D\mathbf{u} \cdot \mathbf{i} = \nabla \mathbf{u} + (\nabla \mathbf{u})^{\mathsf{T}}$.

For the momentum transport equation, we rewrite this as

$$0 = -\nabla p + \Delta \mathbf{u} + \frac{\beta}{Wi} \nabla_c \cdot \boldsymbol{c} \quad (5.9)$$

with

$$\nabla_c \stackrel{\text{def}}{=} \begin{pmatrix} \partial_x & 0 & \partial_y \\ 0 & \partial_y & \partial_x \end{pmatrix} \text{ for } d = 2 \text{ and } \nabla_c \stackrel{\text{def}}{=} \begin{pmatrix} \partial_x & 0 & 0 & 0 & \partial_z & \partial_y \\ 0 & \partial_y & 0 & \partial_z & 0 & \partial_x \\ 0 & 0 & \partial_z & \partial_y & \partial_x & 0 \end{pmatrix} \text{ for } d = 3. \quad (5.10)$$

Note in particular that $(\nabla_c \cdot D\mathbf{u}) \cdot \mathbf{i} = \Delta \mathbf{u}$.

The final form of the system of equations is thus

$$0 = -\nabla p + \Delta \mathbf{u} + \frac{\beta}{Wi} \nabla_c \cdot \boldsymbol{c} + \mathbf{F}, \quad (5.11a)$$

$$0 = \nabla \cdot \mathbf{u}, \quad (5.11b)$$

$$\partial_t \mathbf{c} + \mathbf{u} \cdot \nabla \mathbf{c} = (D\mathbf{u})\,\mathbf{c} - \frac{1}{Wi}(\mathbf{c} - \mathbf{i}). \quad (5.11c)$$

5.2.3 Approximate form of transport through β asymptotics

To perform the asymptotic development, we use the standard mathematical approach that consists in scaling the dimensionless parameters as a function of a small parameter, ε, and searching for solutions in the form of series of ε. The limit $Wi = O(\varepsilon^n)$ with $n \geq 1$ is trivial (see e.g. detailed asymptotics in [1, 19]), yielding a standard Darcy's law with a viscosity $1 + \beta$ at leading-order. This case does not require considering asymptotics in β. Our interest is in the case $Wi = O(1)$ and $\beta = O(\epsilon)$ where strands start forming. Cases of large Weissenberg numbers can also be treated following a similar strategy, but the most interesting case is actually $Wi = O(1)$ because it maintains a competition between stretching and relaxation in the transport equation for the conformation tensor.

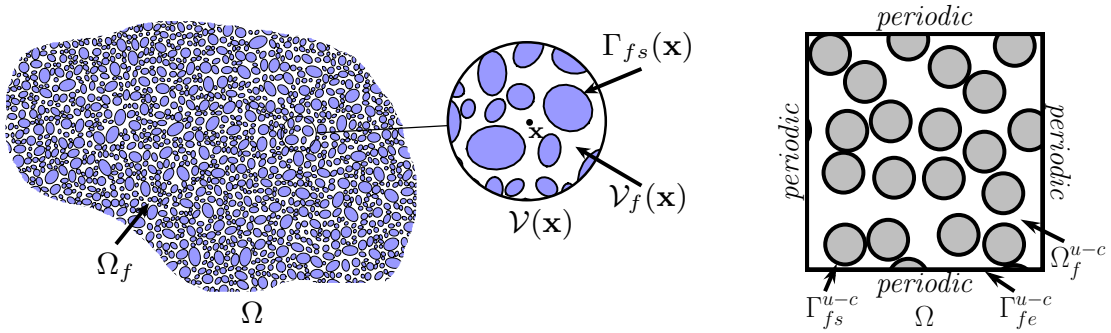

(a) Large scale domain and averaging volume

(b) Unit-cell

Fig. 5.1 Schematics of the volume averaging procedure with (a) the large scale domain, magnifications for the averaging volume at point $\mathbf{x}$ and notations for the sets considered; and (b) a unit-cell with corresponding notations.

For $Wi = O(1)$ and $\beta = O(\epsilon)$, we write $\beta = \varepsilon\beta^\star$ and have

$$0 = -\nabla p + \Delta\mathbf{u} + \varepsilon\frac{\beta^\star}{Wi}\nabla_c \cdot \boldsymbol{c} + \mathbf{F}, \tag{5.12a}$$

$$0 = \nabla \cdot \mathbf{u}, \tag{5.12b}$$

$$\partial_t \mathbf{c} + \mathbf{u}\cdot\nabla\mathbf{c} = (D\mathbf{u})\,\mathbf{c} - \frac{1}{Wi}(\mathbf{c} - \mathbf{i}). \tag{5.12c}$$

We are looking for a solution in the form

$$p = p^{(0)} + \varepsilon p^{(1)}, \tag{5.13a}$$

$$\mathbf{u} = \mathbf{u}^{(0)} + \varepsilon\mathbf{u}^{(1)}, \tag{5.13b}$$

$$\mathbf{c} = \mathbf{c}^{(0)}, \tag{5.13c}$$

in order to obtain a sequence of problem corresponding to the different orders. At leading order for the momentum transport and mass conservation, we have

$$0 = -\nabla p^{(0)} + \Delta\mathbf{u}^{(0)} + \mathbf{F}, \tag{5.14a}$$

$$0 = \nabla \cdot \mathbf{u}^{(0)}, \tag{5.14b}$$

and for the transport of the conformation tensor

$$\partial_t \mathbf{c}^{(0)} + \mathbf{u}^{(0)}\cdot\nabla\mathbf{c}^{(0)} = D\mathbf{u}^{(0)}\mathbf{c}^{(0)} - \frac{1}{Wi}\left(\mathbf{c}^{(0)} - \mathbf{i}\right). \tag{5.15}$$

At first order for momentum and mass conservation, we have

$$0 = -\nabla p^{(1)} + \Delta\mathbf{u}^{(1)} + \frac{\beta^\star}{Wi}\nabla_c \cdot \mathbf{c}^{(0)}, \tag{5.16a}$$

$$0 = \nabla \cdot \mathbf{u}^{(1)}. \tag{5.16b}$$

5.3 Homogenization through volume averaging

5.3.1 Definitions

We define the intrinsic average operator as

$$\langle \chi \rangle (\mathbf{x}) = \frac{\int_{\mathcal{V}_f(\mathbf{x})} \chi \, dV}{\int_{\mathcal{V}_f(\mathbf{x})} dV}. \tag{5.17}$$

The porosity ϕ is defined as

$$\phi = \frac{\int_{\mathcal{V}_f(\mathbf{x})} dV}{\int_{\mathcal{V}(\mathbf{x})} dV}. \tag{5.18}$$

To simplify the developments, we also consider a porous structure such that $\int_{\mathcal{V}_f} dV$ and the porosity are uniform and constant. Important notations for the averaging procedure are summarized in Fig 5.1.

Note that in this paper, $\langle \chi \rangle$ refers to the intrinsic average of χ, which is not the most standard notation in the volume averaging literature (usually we use $\langle \rangle^{\text{fluid}}$ or similar) but is more compact and simpler when the porosity is constant and uniform.

5.3.2 Volume averaging for the transport of $\mathbf{u}^{(0)}$

We indicate key steps here as the technique is described in details in many works (see for instance Whitaker [27, 26], Davit et al. [5]). First, we average

$$0 = -\nabla p^{(0)} + \Delta \mathbf{u}^{(0)} + \mathbf{F}, \qquad \text{in } \Omega_f \tag{5.19a}$$

$$0 = \nabla \cdot \mathbf{u}^{(0)}, \qquad \text{in } \Omega_f \tag{5.19b}$$

$$\mathbf{u}^{(0)} = 0, \qquad \text{on } \Gamma_{fs} \tag{5.19c}$$

considering a no-slip/no-penetration boundary condition on the fluid/solid interface Γ_{fs}. We then use the average plus perturbation decomposition

$$p^{(0)} = \left\langle p^{(0)} \right\rangle + \tilde{p}^{(0)}, \tag{5.20a}$$

$$\mathbf{u}^{(0)} = \left\langle \mathbf{u}^{(0)} \right\rangle + \tilde{\mathbf{u}}^{(0)}, \tag{5.20b}$$

to obtain

$$0 = -\nabla \left\langle p^{(0)} \right\rangle + \left\langle -\nabla \tilde{p}^{(0)} + \Delta \tilde{\mathbf{u}}^{(0)} \right\rangle + \mathbf{F}, \tag{5.21a}$$

$$0 = \nabla \cdot \left\langle \mathbf{u}^{(0)} \right\rangle, \tag{5.21b}$$

where the Brinkman term $\Delta \left\langle \mathbf{u}^{(0)} \right\rangle$ has been removed as is standard. The perturbation equation reads

$$0 = -\nabla \tilde{p}^{(0)} + \Delta \tilde{\mathbf{u}}^{(0)} - \left\langle -\nabla \tilde{p}^{(0)} + \Delta \tilde{\mathbf{u}}^{(0)} \right\rangle \qquad \text{in } \Omega_f \tag{5.22a}$$

$$0 = \nabla \cdot \tilde{\mathbf{u}}^{(0)} \qquad \text{in } \Omega_f \tag{5.22b}$$

$$\tilde{\mathbf{u}}^{(0)} = -\left\langle \mathbf{u}^{(0)} \right\rangle \qquad \text{on } \Gamma_{fs} \tag{5.22c}$$

and is simply obtained by subtracting Eqs 5.21a and 5.21b from Eqs 5.19a and 5.19b, respectively. Because of the linearity of the problem, we may seek a solution of the problem in the form

$$\tilde{p}^{(0)} = -\mathbf{b}^{(0)} \cdot \left\langle \mathbf{u}^{(0)} \right\rangle, \tag{5.23a}$$

$$\tilde{\mathbf{u}}^{(0)} = -\mathbf{B}^{(0)} \cdot \left\langle \mathbf{u}^{(0)} \right\rangle, \tag{5.23b}$$

with the corresponding closure problem

$$0 = -\nabla \mathbf{b}^{(0)} + \Delta \mathbf{B}^{(0)} - \left\langle -\nabla \mathbf{b}^{(0)} + \Delta \mathbf{B}^{(0)} \right\rangle \quad \text{in } \Omega_f^{\text{u-c}} \tag{5.24a}$$

$$0 = \nabla \cdot \mathbf{B}^{(0)} \quad \text{in } \Omega_f^{\text{u-c}} \tag{5.24b}$$

$$\mathbf{B}^{(0)} = \mathbf{I}_d \quad \text{on } \Gamma_{fs}^{\text{u-c}} \tag{5.24c}$$

$$\text{Periodicity} \quad \text{on } \Gamma_{fe}^{\text{u-c}} \tag{5.24d}$$

$$\text{Averages } \left\langle \mathbf{b}^{(0)} \right\rangle = 0 \text{ and } \left\langle \mathbf{B}^{(0)} \right\rangle = 0 \tag{5.24e}$$

This problem is used to calculate the effective parameters appearing in the macroscale equations. The periodicity on boundary conditions for the outside of the unit-cell ($\Gamma_{fe}^{\text{u-c}}$) is the standard approach.

The macroscale equation is obtained by introducing the closure relations into Eq 5.21a to obtain

$$0 = -\nabla \left\langle p^{(0)} \right\rangle - \left\langle -\nabla \mathbf{b}^{(0)} + \Delta \mathbf{B}^{(0)} \right\rangle \cdot \left\langle \mathbf{u}^{(0)} \right\rangle, \tag{5.25a}$$

$$0 = \nabla \cdot \left\langle \mathbf{u}^{(0)} \right\rangle. \tag{5.25b}$$

We further define the Darcy velocity

$$\left\langle \mathbf{u}^{(0)} \right\rangle^D \stackrel{\text{def}}{=} \phi \left\langle \mathbf{u}^{(0)} \right\rangle \tag{5.26}$$

and

$$\mathbf{K}^{-1} \stackrel{\text{def}}{=} \phi^{-1} \left\langle -\nabla \mathbf{b}^{(0)} + \Delta \mathbf{B}^{(0)} \right\rangle, \tag{5.27}$$

assuming that $\mathbf{K}$ is invertible. We then obtain Darcy's law

$$\left\langle \mathbf{u}^{(0)} \right\rangle^D = \mathbf{K} \cdot \left(-\nabla \left\langle p^{(0)} \right\rangle + \mathbf{F} \right). \tag{5.28}$$

Note that we can reformulate the problem for $\mathbf{b}^{(0)}$ and $\mathbf{B}^{(0)}$ using the change of unknown functions

$$\mathbf{b}^{(0)} = \mathbf{g} \cdot \phi \mathbf{K}^{-1} \tag{5.29}$$

$$\mathbf{B}^{(0)} = \mathbf{I}_d + \mathbf{G} \cdot \phi \mathbf{K}^{-1} \tag{5.30}$$

with

$$0 = -\nabla \mathbf{g} + \Delta \mathbf{G} - \mathbf{I}_d \qquad \text{in } \Omega_f^{\text{u-c}} \tag{5.31a}$$

$$0 = \nabla \cdot \mathbf{G} \qquad \text{in } \Omega_f^{\text{u-c}} \tag{5.31b}$$

$$\mathbf{G} = 0 \qquad \text{on } \Gamma_{fs}^{\text{u-c}} \tag{5.31c}$$

$$\text{Periodicity} \qquad \text{on } \Gamma_{fe}^{\text{u-c}} \tag{5.31d}$$

$$\text{Average } \langle \mathbf{g} \rangle = 0 \tag{5.31e}$$

$\left\langle \mathbf{b}^{(0)} \right\rangle = 0$ implies that $\langle \mathbf{g} \rangle = 0$ and $\left\langle \mathbf{B}^{(0)} \right\rangle = 0$ leads to $\mathbf{I}_d + \langle \mathbf{G} \rangle \cdot \phi \mathbf{K}^{-1} = 0$ and thus

$$\mathbf{K} = -\phi \langle \mathbf{G} \rangle . \tag{5.32}$$

The advantage of solving the problem for $(\mathbf{g},\ \mathbf{G})$ rather than the one for $\left(\mathbf{b}^{(0)},\ \mathbf{B}^{(0)}\right)$ is that it is differential and not integro-differential.

5.3.3 Volume averaging for the transport of the conformation tensor

We now proceed to averaging the transport equation for the conformation tensor at leading order

$$\partial_t \mathbf{c}^{(0)} + \mathbf{u}^{(0)} \cdot \nabla \mathbf{c}^{(0)} = D\mathbf{u}^{(0)} \mathbf{c}^{(0)} - \frac{1}{Wi} \left(\mathbf{c}^{(0)} - \mathbf{i} \right). \tag{5.33}$$

We use the average plus perturbation decomposition

$$\mathbf{c}^{(0)} = \left\langle \mathbf{c}^{(0)} \right\rangle + \widetilde{\mathbf{c}}^{(0)} \tag{5.34}$$

We have $\left\langle \partial_t \mathbf{c}^{(0)} \right\rangle = \partial_t \left\langle \mathbf{c}^{(0)} \right\rangle$ since there is no time variation of the geometry. We also have

$$\left\langle \mathbf{u}^{(0)} \cdot \nabla \mathbf{c}^{(0)} \right\rangle = \left\langle \mathbf{u}^{(0)} \right\rangle \cdot \nabla \left\langle \mathbf{c}^{(0)} \right\rangle + \left\langle \mathbf{u}^{(0)} \cdot \nabla \widetilde{\mathbf{c}}^{(0)} \right\rangle, \tag{5.35}$$

$$\left\langle D\mathbf{u}^{(0)} \cdot \mathbf{c}^{(0)} \right\rangle^f = \left\langle D\mathbf{u}^{(0)} \right\rangle \cdot \left\langle \mathbf{c}^{(0)} \right\rangle + \left\langle D\mathbf{u}^{(0)} \cdot \widetilde{\mathbf{c}}^{(0)} \right\rangle. \tag{5.36}$$

Averaging thus leads to

$$\begin{aligned} \partial_t \left\langle \mathbf{c}^{(0)} \right\rangle + \left\langle \mathbf{u}^{(0)} \right\rangle \cdot \nabla \left\langle \mathbf{c}^{(0)} \right\rangle = \left\langle D\mathbf{u}^{(0)} \right\rangle \cdot \left\langle \mathbf{c}^{(0)} \right\rangle - \frac{1}{Wi} \left(\left\langle \mathbf{c}^{(0)} \right\rangle - \mathbf{i} \right) \\ - \left\langle \mathbf{u}^{(0)} \cdot \nabla \widetilde{\mathbf{c}}^{(0)} \right\rangle + \left\langle D\mathbf{u}^{(0)} \cdot \widetilde{\mathbf{c}}^{(0)} \right\rangle \end{aligned} \tag{5.37}$$

Upon neglecting terms in $\nabla \left\langle \mathbf{c}^{(0)} \right\rangle$ (leading order in $\left\langle \mathbf{c}^{(0)} \right\rangle$) and assuming quasi-stationarity, the perturbation equation reads

$$\mathbf{u}^{(0)} \cdot \nabla \widetilde{\mathbf{c}}^{(0)} - \left\langle \mathbf{u}^{(0)} \cdot \nabla \widetilde{\mathbf{c}}^{(0)} \right\rangle = \left(D\mathbf{u}^{(0)} \cdot \widetilde{\mathbf{c}}^{(0)} - \left\langle D\mathbf{u}^{(0)} \cdot \widetilde{\mathbf{c}}^{(0)} \right\rangle \right) - \frac{1}{Wi} \widetilde{\mathbf{c}}^{(0)} + \widetilde{D}\mathbf{u}^{(0)} \cdot \left\langle \mathbf{c}^{(0)} \right\rangle, \tag{5.38}$$

which is obtained by subtracting Eq 5.37 from Eq 5.33. Because of the linearity, we write a closure in the form

$$\widetilde{\mathbf{c}}^{(0)} = \mathbf{A} \cdot \left\langle \mathbf{c}^{(0)} \right\rangle, \tag{5.39}$$

so that

$$\mathbf{u}^{(0)}\cdot\nabla\mathbf{A} = D\mathbf{u}^{(0)}\cdot\mathbf{A} - \frac{1}{We}\mathbf{A} + D\mathbf{u}^{(0)} - \mathbf{B} \qquad \text{in } \Omega_f^{\text{u-c}} \tag{5.40a}$$

$$\text{with } \langle\mathbf{A}\rangle = 0, \tag{5.40b}$$

$$\text{and } \mathbf{B} = \left\langle D\mathbf{u}^{(0)}\cdot\left(\mathbf{I}_{\frac{d(d+1)}{2}} + \mathbf{A}\right)\right\rangle - \left\langle \mathbf{u}^{(0)}\cdot\nabla\mathbf{A}\right\rangle, \tag{5.40c}$$

$$\text{and periodicity} \qquad \text{on } \Gamma_{fe}^{\text{u-c}} \tag{5.40d}$$

Again this equation is integro-differential but can be simplified through the decomposition

$$\mathbf{A} = \left(\mathbf{M} - \mathbf{I}_{\frac{d(d+1)}{2}}\right) - Wi\ \mathbf{M}\cdot\mathbf{B} \tag{5.41}$$

with $\mathbf{M}$ solution of

$$\mathbf{u}^{(0)}\cdot\nabla\mathbf{M} = D\mathbf{u}^{(0)}\cdot\mathbf{M} - \frac{1}{Wi}\left(\mathbf{M} - \mathbf{I}_{\frac{d(d+1)}{2}}\right) \qquad \text{in } \Omega_f^{\text{u-c}} \tag{5.42a}$$

$$\text{Periodicity} \qquad \text{on } \Gamma_{fe}^{\text{u-c}} \tag{5.42b}$$

$\langle\mathbf{A}\rangle = 0$ implies that

$$\mathbf{B} = Wi^{-1}\left(\mathbf{I}_{\frac{d(d+1)}{2}} - \langle\mathbf{M}\rangle^{-1}\right). \tag{5.43}$$

Also note that $\mathbf{A} = \mathbf{M}\cdot\langle\mathbf{M}\rangle^{-1} - \mathbf{I}_{\frac{d(d+1)}{2}}$ so that

$$\mathbf{c}^{(0)} = \mathbf{M}\cdot\langle\mathbf{M}\rangle^{-1}\cdot\left\langle\mathbf{c}^{(0)}\right\rangle. \tag{5.44}$$

The macroscopic equation reads

$$\partial_t\left\langle\mathbf{c}^{(0)}\right\rangle + \left\langle\mathbf{u}^{(0)}\right\rangle\cdot\nabla\left\langle\mathbf{c}^{(0)}\right\rangle = \mathbf{B}\cdot\left\langle\mathbf{c}^{(0)}\right\rangle - \frac{1}{Wi}\left(\left\langle\mathbf{c}^{(0)}\right\rangle - \mathbf{i}\right). \tag{5.45}$$

5.3.4 Volume averaging for the transport of $\mathbf{u}^{(1)}$

At first order, we have

$$0 = -\nabla p^{(1)} + \Delta\mathbf{u}^{(1)} + \frac{\beta^\star}{Wi}\nabla_c\cdot\mathbf{c}^{(0)}, \qquad \text{in } \Omega_f \tag{5.46a}$$

$$0 = \nabla\cdot\mathbf{u}^{(1)}, \qquad \text{in } \Omega_f \tag{5.46b}$$

$$\mathbf{u}^{(1)} = 0 \qquad \text{on } \Gamma_{fs} \tag{5.46c}$$

that we average as

$$0 = -\nabla\left\langle p^{(1)}\right\rangle + \Delta\left\langle\mathbf{u}^{(1)}\right\rangle + \frac{\beta^\star}{Wi}\nabla_c\cdot\left\langle\mathbf{c}^{(0)}\right\rangle + \left\langle -\nabla\tilde{p}^{(1)} + \Delta\tilde{\mathbf{u}}^{(1)} + \frac{\beta^\star}{Wi}\nabla_c\cdot\tilde{\mathbf{c}}^{(0)}\right\rangle, \tag{5.47a}$$

$$0 = \nabla\cdot\left\langle\mathbf{u}^{(1)}\right\rangle. \tag{5.47b}$$

The perturbation equation is

$$0 = -\nabla\tilde{p}^{(1)} + \Delta\tilde{\mathbf{u}}^{(1)} + \frac{\beta^\star}{Wi}\nabla_c\cdot\widetilde{\mathbf{c}}^{(0)} - \left\langle -\nabla\tilde{p}^{(1)} + \Delta\tilde{\mathbf{u}}^{(1)} + \frac{\beta^\star}{Wi}\nabla_c\cdot\widetilde{\mathbf{c}}^{(0)}\right\rangle \qquad \text{in } \Omega_f \tag{5.48a}$$

$$0 = \nabla\cdot\tilde{\mathbf{u}}^{(1)} \qquad \text{in } \Omega_f \tag{5.48b}$$

$$\tilde{\mathbf{u}}^{(1)} = -\left\langle \mathbf{u}^{(1)}\right\rangle \qquad \text{on } \Gamma_{fs} \tag{5.48c}$$

Upon using

$$\widetilde{\mathbf{c}}^{(0)} = \left(\mathbf{M}\cdot\langle\mathbf{M}\rangle^{-1} - \mathbf{I}_{\frac{d(d+1)}{2}}\right)\cdot\left\langle\mathbf{c}^{(0)}\right\rangle, \tag{5.49}$$

we have

$$\nabla_c\cdot\widetilde{\mathbf{c}}^{(0)} = \nabla_c\cdot\left(\mathbf{M}\cdot\langle\mathbf{M}\rangle^{-1}\right)\cdot\left\langle\mathbf{c}^{(0)}\right\rangle \tag{5.50}$$

so that

$$\begin{aligned} 0 = &-\nabla\tilde{p}^{(1)} + \Delta\tilde{\mathbf{u}}^{(1)} - \left\langle -\nabla\tilde{p}^{(1)} + \Delta\tilde{\mathbf{u}}^{(1)}\right\rangle \qquad \text{in } \Omega_f \\ &+ \frac{\beta^\star}{Wi}\nabla_c\cdot\left(\mathbf{M}\cdot\langle\mathbf{M}\rangle^{-1}\right)\cdot\left\langle\mathbf{c}^{(0)}\right\rangle - \frac{\beta^\star}{Wi}\left\langle\nabla_c\cdot\left(\mathbf{M}\cdot\langle\mathbf{M}\rangle^{-1}\right)\right\rangle\cdot\left\langle\mathbf{c}^{(0)}\right\rangle \end{aligned} \tag{5.51a}$$

$$0 = \nabla\cdot\tilde{\mathbf{u}}^{(1)} \qquad \text{in } \Omega_f \tag{5.51b}$$

$$\tilde{\mathbf{u}}^{(1)} = -\left\langle \mathbf{u}^{(1)}\right\rangle \qquad \text{on } \Gamma_{fs} \tag{5.51c}$$

We have the following closure

$$\tilde{p}^{(1)} = -\mathbf{b}^{(0)}\cdot\left\langle\mathbf{u}^{(1)}\right\rangle - \frac{\beta^\star}{Wi}\boldsymbol{P}^{(1)}\cdot\left\langle\mathbf{c}^{(0)}\right\rangle \tag{5.52a}$$

$$\tilde{\mathbf{u}}^{(1)} = -\mathbf{B}^{(0)}\cdot\left\langle\mathbf{u}^{(1)}\right\rangle - \frac{\beta^\star}{Wi}\mathbf{U}^{(1)}\cdot\left\langle\mathbf{c}^{(0)}\right\rangle \tag{5.52b}$$

with $\left(\boldsymbol{P}^{(1)},\ \mathbf{U}^{(1)}\right)$ solution of

$$0 = -\nabla\boldsymbol{P}^{(1)} + \Delta\mathbf{U}^{(1)} - \nabla_c\cdot\left(\mathbf{M}\cdot\langle\mathbf{M}\rangle^{-1}\right) - \mathbf{N} \qquad \text{in } \Omega_f^{\text{u-c}} \tag{5.53a}$$

$$0 = \nabla\cdot\mathbf{U}^{(1)} \qquad \text{in } \Omega_f^{\text{u-c}} \tag{5.53b}$$

$$\mathbf{U}^{(1)} = 0 \qquad \text{on } \Gamma_{fs}^{\text{u-c}} \tag{5.53c}$$

$$\text{Periodicity} \qquad \text{on } \Gamma_{fe}^{\text{u-c}} \tag{5.53d}$$

$$\text{Averages } \left\langle\boldsymbol{P}^{(1)}\right\rangle = 0 \text{ and } \left\langle\mathbf{U}^{(1)}\right\rangle = 0 \tag{5.53e}$$

with

$$\mathbf{N} \overset{\text{def}}{=} \left\langle -\nabla\boldsymbol{P}^{(1)} + \Delta\mathbf{U}^{(1)} - \nabla_c\cdot\left(\mathbf{M}\cdot\langle\mathbf{M}\rangle^{-1}\right)\right\rangle. \tag{5.54}$$

As usual, this system is integro-differential (here because of $\mathbf{N}$) and we can simplify it using the decomposition

$$\boldsymbol{P}^{(1)} = \boldsymbol{P}^{(1)*} + \mathbf{g}\cdot\mathbf{N} \tag{5.55a}$$

$$\mathbf{U}^{(1)} = \mathbf{U}^{(1)*} + \mathbf{G}\cdot\mathbf{N} \tag{5.55b}$$

with $(\mathbf{g},\ \mathbf{G})$ solving Eqs 5.31a and $\left(\boldsymbol{P}^{(1)*},\ \mathbf{U}^{(1)*}\right)$ solving

$$0 = -\nabla \boldsymbol{P}^{(1)*} + \Delta \mathbf{U}^{(1)*} - \nabla_c \cdot \left(\mathbf{M} \cdot \langle \mathbf{M} \rangle^{-1}\right) \qquad \text{in } \Omega_f^{\text{u-c}} \tag{5.56a}$$

$$0 = \nabla \cdot \mathbf{U}^{(1)*} \qquad \text{in } \Omega_f^{\text{u-c}} \tag{5.56b}$$

$$\mathbf{U}^{(1)*} = 0 \qquad \text{on } \Gamma_{fs}^{\text{u-c}} \tag{5.56c}$$

$$\text{Periodicity} \qquad \text{on } \Gamma_{fe}^{\text{u-c}} \tag{5.56d}$$

$$\text{Average } \left\langle \boldsymbol{P}^{(1)*} \right\rangle = 0 \tag{5.56e}$$

Using $\left\langle \mathbf{U}^{(1)} \right\rangle = 0$, we have that

$$\mathbf{N} = -\langle \mathbf{G} \rangle^{-1} \cdot \left\langle \mathbf{U}^{(1)*} \right\rangle. \tag{5.57}$$

We also define $\mathbf{N}^*$ as

$$\mathbf{N}^* \overset{\text{def}}{=} -\phi \langle \mathbf{G} \rangle \cdot \mathbf{N} = \mathbf{K} \cdot \mathbf{N} = \phi \left\langle \mathbf{U}^{(1)*} \right\rangle \tag{5.58}$$

Introducing Eq 5.52 into Eq 5.47, we obtain the macroscale equation

$$\left\langle \mathbf{u}^{(1)} \right\rangle^D = \mathbf{K} \cdot \left(-\nabla \left\langle p^{(1)} \right\rangle + \frac{\beta^\star}{Wi} \nabla_c \cdot \left\langle \mathbf{c}^{(0)} \right\rangle \right) - \frac{\beta^\star}{Wi} \mathbf{N}^* \cdot \left\langle \mathbf{c}^{(0)} \right\rangle. \tag{5.59}$$

5.3.5 Summary

Summing up the equations for momentum transport at different orders, considering the leading order transport for the conformation tensor and removing the ε for simplicity, we get

$$\langle \mathbf{u} \rangle^D = \mathbf{K} \cdot \left(-\nabla \langle p \rangle^f + \mathbf{F} + \frac{\beta}{Wi} \nabla_c \cdot \left\langle \mathbf{c}^{(0)} \right\rangle \right) - \frac{\beta}{Wi} \mathbf{N}^* \cdot \left\langle \mathbf{c}^{(0)} \right\rangle \tag{5.60a}$$

$$\left\langle \mathbf{u}^{(0)} \right\rangle^D = \mathbf{K} \cdot \left(-\nabla \left\langle p^{(0)} \right\rangle + \mathbf{F} \right) \tag{5.60b}$$

$$\nabla \cdot \langle \mathbf{u} \rangle^D = \nabla \cdot \left\langle \mathbf{u}^{(0)} \right\rangle^D = 0 \tag{5.60c}$$

$$\partial_t \left\langle \mathbf{c}^{(0)} \right\rangle + \phi^{-1} \left\langle \mathbf{u}^{(0)} \right\rangle^D \cdot \nabla \left\langle \mathbf{c}^{(0)} \right\rangle = \mathbf{B} \cdot \left\langle \mathbf{c}^{(0)} \right\rangle - \frac{1}{Wi} \left(\left\langle \mathbf{c}^{(0)} \right\rangle - \mathbf{i} \right) \tag{5.60d}$$

with

$$\mathbf{K} = -\phi \langle \mathbf{G} \rangle, \tag{5.61a}$$

$$\mathbf{N}^* = \phi \left\langle \mathbf{U}^{(1)*} \right\rangle, \tag{5.61b}$$

$$\mathbf{B} = \frac{1}{Wi} \left(\mathbf{I}_{\frac{d(d+1)}{2}} - \langle \mathbf{M} \rangle^{-1} \right). \tag{5.61c}$$

The corresponding closure problems are

$$0 = -\nabla \mathbf{g} + \Delta \mathbf{G} - \mathbf{I}_d \qquad \text{in } \Omega_f^{\text{u-c}} \tag{5.62a}$$
$$0 = \nabla \cdot \mathbf{G} \qquad \text{in } \Omega_f^{\text{u-c}} \tag{5.62b}$$
$$\mathbf{G} = 0 \qquad \text{on } \Gamma_{fs}^{\text{u-c}} \tag{5.62c}$$
$$\text{Periodicity} \qquad \text{on } \Gamma_{fe}^{\text{u-c}} \tag{5.62d}$$
$$\text{Average } \langle \mathbf{g} \rangle = 0 \tag{5.62e}$$

and

$$\mathbf{u}^{(0)} \cdot \nabla \mathbf{M} = D\mathbf{u}^{(0)} \cdot \mathbf{M} - \frac{1}{Wi}\left(\mathbf{M} - \mathbf{I}_{\frac{d(d+1)}{2}}\right) \qquad \text{in } \Omega_f^{\text{u-c}} \tag{5.63a}$$
$$\text{Periodicity} \qquad \text{on } \Gamma_{fe}^{\text{u-c}} \tag{5.63b}$$

and

$$0 = -\nabla \boldsymbol{P}^{(1)*} + \Delta \mathbf{U}^{(1)*} - \nabla_c \cdot \left(\mathbf{M} \cdot \langle \mathbf{M} \rangle^{-1}\right) \qquad \text{in } \Omega_f^{\text{u-c}} \tag{5.64a}$$
$$0 = \nabla \cdot \mathbf{U}^{(1)*} \qquad \text{in } \Omega_f^{\text{u-c}} \tag{5.64b}$$
$$\mathbf{U}^{(1)*} = 0 \qquad \text{on } \Gamma_{fs}^{\text{u-c}} \tag{5.64c}$$
$$\text{Periodicity} \qquad \text{on } \Gamma_{fe}^{\text{u-c}} \tag{5.64d}$$
$$\text{Average } \left\langle \boldsymbol{P}^{(1)*} \right\rangle = 0 \tag{5.64e}$$

5.4 Test cases

In this section, we study two test cases corresponding to flows in a channel and through arrays of cylinders. We aim at validating our approach by comparison with either analytical solutions in the case of channel flow or direct numerical simulations in the case of the cylinders. We also use these test cases to evaluate further the model, for instance by calculating how the effective parameters vary with the Weissenberg number.

5.4.1 Channel flow

Let us consider a steady two-dimensional flow between the two lines $y = 0$ and $y = 1$ with no-slip boundary conditions. We further suppose that the flow is periodic in the x direction and is imposed through a force $\mathbf{F} = \begin{pmatrix} 1 & 0 \end{pmatrix}^\mathsf{T}$. The reference analytical solution of this problem is given by

$$\mathbf{u}_{\text{ref}} = \begin{pmatrix} \frac{1}{2}\frac{y(1-y)}{(1+\beta)} \\ 0 \end{pmatrix} \tag{5.65}$$

and

$$\mathbf{c}_{\text{ref}} = \begin{pmatrix} 1 + \frac{Wi^2}{2}\frac{(1-2y)^2}{(1+\beta)^2} \\ 1 \\ \frac{Wi}{2}\frac{(1-2y)}{1+\beta} \end{pmatrix}. \tag{5.66}$$

Through asymptotics in β, we then have

$$\mathbf{u}_{\text{ref}}^{(0)} = \begin{pmatrix} \frac{1}{2}y(1-y) \\ 0 \end{pmatrix} \tag{5.67}$$

and

$$\mathbf{u}_{\text{ref}}^{(1)} = \beta \begin{pmatrix} -\frac{1}{2}y(1-y) \\ 0 \end{pmatrix} \tag{5.68}$$

and

$$\mathbf{c}_{\text{ref}}^{(0)} = \begin{pmatrix} 1+\frac{Wi^2}{2}(1-2y)^2 \\ 1 \\ \frac{Wi}{2}(1-2y) \end{pmatrix} \tag{5.69}$$

Averaging these equations, we obtain

$$\left\langle \mathbf{u}_{\text{ref}}^{(0)} \right\rangle = \begin{pmatrix} 1/12 \\ 0 \end{pmatrix}, \tag{5.70}$$

and

$$\left\langle \mathbf{u}_{\text{ref}}^{(1)} \right\rangle = \beta \begin{pmatrix} -1/12 \\ 0 \end{pmatrix}, \tag{5.71}$$

and

$$\left\langle \mathbf{c}_{\text{ref}}^{(0)} \right\rangle = \begin{pmatrix} 1+\frac{1}{6}Wi^2 \\ 1 \\ 0 \end{pmatrix}. \tag{5.72}$$

Solution of the homogenized formulation Now that we have reference analytical solutions, we proceed to calculating the result of our homogenized formulation. $\mathbf{G}$ solves Eq 5.62 and can be easily calculated as

$$\mathbf{G} = \begin{pmatrix} -\frac{1}{2}y(1-y) & 0 \\ 0 & 0 \end{pmatrix}. \tag{5.73}$$

We then have

$$\mathbf{K} = -\langle \mathbf{G} \rangle = \begin{pmatrix} 1/12 & 0 \\ 0 & 0 \end{pmatrix} \tag{5.74}$$

and $\left\langle \mathbf{u}^{(0)} \right\rangle = \mathbf{K} \cdot \mathbf{F}$ leading to

$$\left\langle \mathbf{u}^{(0)} \right\rangle = \begin{pmatrix} 1/12 \\ 0 \end{pmatrix} = \left\langle \mathbf{u}_{\text{ref}}^{(0)} \right\rangle. \tag{5.75}$$

We thus recover the correct average velocity.

For the conformation tensor, the problem for $\mathbf{M}$ is

$$0 = D\mathbf{u}^{(0)} \cdot \mathbf{M} - \frac{1}{Wi}\left(\mathbf{M} - \mathbf{I}_{\frac{d(d+1)}{2}}\right) \tag{5.76}$$

so that

$$\mathbf{M} = \left(\mathbf{I}_{\frac{d(d+1)}{2}} - Wi\ D\mathbf{u}^{(0)}\right)^{-1} = \begin{pmatrix} 1 & \frac{1}{2}Wi^2(1-2y)^2 & Wi(1-2y) \\ 0 & 1 & 0 \\ 0 & \frac{1}{2}Wi(1-2y) & 1 \end{pmatrix}. \tag{5.77}$$

By averaging, we obtain

$$\langle \mathbf{M} \rangle = \begin{pmatrix} 1 & \frac{1}{6}Wi^2 & 0 \\ 0 & 1 & 0 \\ 0 & 0 & 1 \end{pmatrix} \tag{5.78}$$

and thus

$$\langle \mathbf{M} \rangle^{-1} = \begin{pmatrix} 1 & -\frac{1}{6}Wi^2 & 0 \\ 0 & 1 & 0 \\ 0 & 0 & 1 \end{pmatrix}. \tag{5.79}$$

We finally have

$$\mathbf{B} = Wi^{-1}\left(\mathbf{I}_{\frac{d(d+1)}{2}} - \langle \mathbf{M} \rangle^{-1}\right) = \begin{pmatrix} 0 & \frac{1}{6}Wi & 0 \\ 0 & 0 & 0 \\ 0 & 0 & 0 \end{pmatrix}, \tag{5.80}$$

and $\left\langle \mathbf{c}^{(0)} \right\rangle$ is given by

$$\left\langle \mathbf{c}^{(0)} \right\rangle = \left(\mathbf{I}_{\frac{d(d+1)}{2}} - Wi\mathbf{B}\right)^{-1} \cdot \mathbf{i}. \tag{5.81}$$

We further have

$$\left(\mathbf{I}_{\frac{d(d+1)}{2}} - Wi\mathbf{B}\right)^{-1} = \begin{pmatrix} 1 & \frac{1}{6}Wi^2 & 0 \\ 0 & 1 & 0 \\ 0 & 0 & 1 \end{pmatrix} \tag{5.82}$$

so that

$$\left\langle \mathbf{c}^{(0)} \right\rangle = \begin{pmatrix} 1+\frac{1}{6}Wi^2 \\ 1 \\ 0 \end{pmatrix} = \left\langle \mathbf{c}^{(0)}_{\text{ref}} \right\rangle, \tag{5.83}$$

and we also recover the exact solution.

Let us now consider the first-order correction to the velocity. We want to solve Eq 5.64 so that we first need to evlaluate $\mathbf{M} \cdot \langle \mathbf{M} \rangle^{-1}$. Using Eqs 5.78 and 5.79, we have

$$\mathbf{M} \cdot \langle \mathbf{M} \rangle^{-1} = \begin{pmatrix} 1 & -\frac{1}{6}Wi^2 + \frac{1}{2}Wi^2(1-2y)^2 & Wi(1-2y) \\ 0 & 1 & 0 \\ 0 & \frac{1}{2}Wi(1-2y) & 1 \end{pmatrix} \tag{5.84}$$

We can then calculate

$$-\nabla_c \cdot \left(\mathbf{M} \cdot \langle \mathbf{M} \rangle^{-1}\right) = \begin{pmatrix} 0 & Wi & 0 \\ 0 & 0 & 0 \end{pmatrix} \tag{5.85}$$

Solving Eq 5.64, then leads to

$$\mathbf{U}^{(1)*} = \begin{pmatrix} 0 & \frac{1}{2}y(1-y)Wi & 0 \\ 0 & 0 & 0 \end{pmatrix} \tag{5.86}$$

By averaging, we have

$$\left\langle \mathbf{U}^{(1)*} \right\rangle = \mathbf{N}^* = \begin{pmatrix} 0 & \frac{1}{12}Wi & 0 \\ 0 & 0 & 0 \end{pmatrix} \tag{5.87}$$

Finally, Eq 5.59

$$\left\langle \mathbf{u}^{(1)} \right\rangle = \frac{\beta}{We}\mathbf{K} \cdot \left(\nabla_c \cdot \left\langle \mathbf{c}^{(0)} \right\rangle\right) - \frac{\beta}{Wi}\mathbf{N}^* \cdot \left\langle \mathbf{c}^{(0)} \right\rangle \tag{5.88}$$

with

$$\nabla_c \cdot \left\langle \mathbf{c}^{(0)} \right\rangle = \begin{pmatrix} 0 \\ 0 \end{pmatrix} \tag{5.89}$$

and

$$-\mathbf{N}^* \cdot \left\langle \mathbf{c}^{(0)} \right\rangle = \begin{pmatrix} -\frac{1}{12} Wi \\ 0 \end{pmatrix} \tag{5.90}$$

leads to

$$\left\langle \mathbf{u}^{(1)} \right\rangle = \beta \begin{pmatrix} -\frac{1}{12} \\ 0 \end{pmatrix} = \left\langle \mathbf{u}^{(1)}_{\text{ref}} \right\rangle. \tag{5.91}$$

5.4.2 Flow through biperiodic arrays of cylinders

We now turn to arrays of cylinders with both crystalline and amorphous structures – amorphous structures generated by randomly displacing cylinders from the crystalline structure, as detailed in Fig 5.2. We consider steady biperiodic flow. We can eliminate gradients of average quantities because of the periodicity and the macroscale model simply boils down to

$$\frac{\langle \mathbf{u} \rangle^D - \left\langle \mathbf{u}^{(0)} \right\rangle^D}{\beta} = -\frac{1}{Wi} \mathbf{N}^* \cdot \left\langle \mathbf{c}^{(0)} \right\rangle \tag{5.92a}$$

$$0 = \mathbf{B} \cdot \left\langle \mathbf{c}^{(0)} \right\rangle - \frac{1}{Wi} \left(\left\langle \mathbf{c}^{(0)} \right\rangle - \mathbf{i} \right) \tag{5.92b}$$

Calculating $\left\langle \mathbf{c}^{(0)} \right\rangle = \left(\mathbf{I}_{\frac{d(d+1)}{2}} - Wi\mathbf{B} \right)^{-1} \cdot \mathbf{i}$ from the second equation and injecting it in the first one, we further get

$$\frac{\langle \mathbf{u} \rangle^D - \left\langle \mathbf{u}^{(0)} \right\rangle^D}{\beta} = -\mathbf{N}^* \cdot \left(Wi \ \mathbf{I}_{\frac{d(d+1)}{2}} - Wi^2 \mathbf{B} \right)^{-1} \cdot \mathbf{i}, \tag{5.93}$$

that can also be written as

$$\frac{\langle \mathbf{u} \rangle^D - \left\langle \mathbf{u}^{(0)} \right\rangle^D}{\beta} = -\frac{1}{Wi} \mathbf{N}^* \cdot \langle \mathbf{M} \rangle \cdot \mathbf{i}. \tag{5.94}$$

The caracteristic lengthscale used to determine the Wi number is $H = P - 2R$, which corresponds to the smallest distance between the surfaces of two successive circles.

5.4.2.1 Numerical methods

The aim is to solve both the Oldroyd-B problem Eq 5.3 and the closure problems Eqs 5.62, 5.63 and 5.64. Our numerical approach follows that developed and detailed in [18]. The space discretization relies on a partition of the domain with quadrilateral cells and consists in a staggered approximation of the unknowns with nonconforming low-order finite elements, namely the Rannacher and Turek (RT) element. The discrete unknowns of $\mathbf{u}$, $\mathbf{G}$ and $\mathbf{U}^{(1)*}$ are located at the center of the faces of the mesh while the discrete unknowns of $\mathbf{c}$ and $\mathbf{M}$ are associated with the cells of the mesh. $\mathbf{c}$ and $\mathbf{M}$ are discretized as piecewise constant and the corresponding transport equations are then solved using a finite-volume scheme.

We use a mesh that is structured and uniform, consisting of $N \times N$ square cells of equal size. Circles are approximated as "stair steps" by making holes into the mesh. In order to keep the geometry unchanged, mesh refinement is obtained by cutting each face into 2 equal parts and

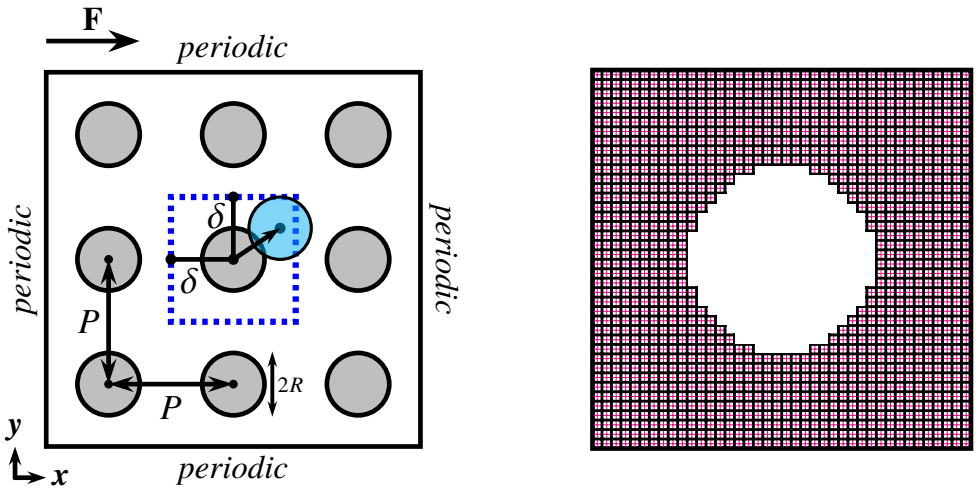

(a) Geometry (b) Mesh

Fig. 5.2 Geometry and mesh for simulations through biperiodic arrays. The crystalline structure corresponds to the grey circles of radius R with distance P between the centers of the circles. *The amorphous structures* are obtained by randomly displacing each circle. Each component of the displacement vector is obtained by uniform random sampling of the interval $[0, \varepsilon]$. The mesh is Cartesian and consists of $N \times N$ square cells of equal size. The cells are taken as holes if they are cut by the cylinder. An example of a mesh for a single cylinder is given in (b) in the case $N = 40$. This mesh is refined by splitting each face into 2 equal parts, which amounts to splitting each cell into 4 parts.

each cell into 2×2 parts. An exemple of the mesh for a single circle is given Fig 5.2 in the case $N = 40$. We used a constant mesh size with $N = 100$, corresponding to a characteristic cell size of $1/50$ radius of a circle. In all the computations, steady-state is obtained by running a transient computation until the solution stabilizes in time. The time step is monitored to ensure time convergence towards steady-state solutions.

Decoupling of the Oldroyd-B problem The scheme is based upon a fractional step approach. Hydrodynamics equations (i.e. mass and momentum balance equations) are decoupled from the constitutive equation by using a beginning-of-step approximation $\mathbf{c}^n$ of the conformation tensor in the momentum balance equation. The problem then consists of iteratively solving a Stokes system

$$0 = -\nabla p + \Delta \mathbf{u} + \frac{\beta}{Wi} \nabla_c \cdot \mathbf{c}^n + \mathbf{F}, \tag{5.95a}$$

$$0 = \nabla \cdot \mathbf{u}, \tag{5.95b}$$

with no-slip/no-penetration boundary conditions on solid interfaces and a transport equation of the conformation tensor

$$\partial_t \mathbf{c}^{n+1} + \mathbf{u} \cdot \nabla \mathbf{c}^{n+1} = \nabla \mathbf{u} \cdot \mathbf{c}^{n+1} + \mathbf{c}^{n+1} \cdot \nabla (\mathbf{u})^{\mathsf{T}} - \frac{1}{Wi} \left(\mathbf{c}^{n+1} - \mathbf{I}_d \right). \tag{5.96}$$

Solution of the Stokes problems Systems 5.95, 5.62, and 5.64 can all be written as a Stokes problem

$$0 = -\nabla h + \Delta \mathbf{H} + \mathbf{S}, \tag{5.97a}$$
$$0 = \nabla \cdot \mathbf{H}, \tag{5.97b}$$

with the scalar h and the vector $\mathbf{H}$ as unknowns and the vector $\mathbf{S}$ as (volumic) source term. These systems are solved in an iterative manner. A standard projection scheme is used to decouple the momentum balance equation from the divergence constraint, thus making it possible to avoid solving a discrete saddle point problem. The solution is obtained by the following algorithm

$$\begin{aligned}
&\text{While } \|\mathbf{H}^{k+1} - \mathbf{H}^k\|_\infty > tol : \\
&\quad \textbf{Prediction step} - \text{Solve for } \tilde{\mathbf{H}}^{k+1} : \\
&\quad \frac{1}{dt}\left(\tilde{\mathbf{H}}^{k+1} - \mathbf{H}^k\right) + \nabla h^k - \nabla \cdot \left(\nabla \tilde{\mathbf{H}}^{k+1} + \left(\nabla \tilde{\mathbf{H}}^{k+1}\right)^{\mathsf{T}}\right) + \mathbf{S} = 0. \\
&\quad \textbf{Correction step} - \text{Solve for } h^{k+1} \text{ and } \mathbf{H}^{k+1} : \\
&\quad \frac{1}{dt}\left(\mathbf{H}^{k+1} - \tilde{\mathbf{H}}^{k+1}\right) + \nabla\left(h^{k+1} - h^k\right) = 0, \\
&\quad \nabla \cdot \mathbf{H}^{k+1} = 0,
\end{aligned}$$

where dt is the time step and the tolerance tol is fixed here to 10^{-06}.

Solution of the transport problems The time discretization of the conformation transport $\mathbf{c}$ is performed using a Strang-type decoupling. A half-step of homogeneous transport of $\mathbf{c}$ is first performed. Then we treat the reaction terms, and finish by the second half-step of transport of $\mathbf{c}$. For precision, we introduce a log transformation of the conformation tensor (see [7, 14]) that is applied to the transport equation. The scheme reads

$$\begin{aligned}
&\textbf{Advection I} - \text{Solve for } \mathbf{c}^{n+\frac{1}{3}} : \\
&\quad \frac{1}{dt/2}\left(\log \mathbf{c}^{n+\frac{1}{3}} - \log \mathbf{c}^n\right) + \nabla \cdot \left(\boldsymbol{u}^{n+1} \log \mathbf{c}^{n+\frac{1}{3}}\right) = 0. \\
&\textbf{ODE} - \text{Set } \mathbf{c}(t_n) = \mathbf{c}^{n+\frac{1}{3}} \text{ and solve for } \mathbf{c}^{n+\frac{2}{3}} = \mathbf{c}(t_n + dt) : \\
&\quad \dot{\mathbf{c}} - \left(\nabla \boldsymbol{u}^{n+1}\right)\mathbf{c} - \mathbf{c}^{\mathsf{T}}\left(\nabla \boldsymbol{u}^{n+1}\right)^{\mathsf{T}} + \frac{1}{Wi}\left(\mathbf{c} - \mathbf{I}\right) = 0. \\
&\textbf{Advection II} - \text{Solve for } \mathbf{c}^{n+1} : \\
&\quad \frac{1}{dt/2}\left(\log \mathbf{c}^{n+1} - \log \mathbf{c}^{n+\frac{2}{3}}\right) + \nabla \cdot \left(\boldsymbol{u}^{n+1} \log \mathbf{c}^{n+1}\right) = 0.
\end{aligned}$$

The matrix $\mathbf{c}$ being symmetric positive definite, there exists an invertible matrix $\boldsymbol{P} \in \mathbb{R}^{d\times d}$ and $\lambda_1, \ldots, \lambda_d \in \mathbb{R}^{+*}$ such that $\mathbf{c} = \boldsymbol{P}^{-1} diag(\lambda_1, \ldots, \lambda_d)\boldsymbol{P}$. The log transformation of $\mathbf{c}$ is then defined by $\log \mathbf{c} = \boldsymbol{P}^{-1} diag\left(\log(\lambda_1), \ldots, \log(\lambda_d)\right)\boldsymbol{P}$.

The local ODE is solved using a first-order implicit Euler scheme

$$\begin{cases} \mathbf{c}_0 & = \mathbf{c}^n, \\ \frac{1}{\delta t}\left(\mathbf{c}_{k+1} - \mathbf{c}_k\right) & = \nabla \boldsymbol{u}^{n+1}\ \mathbf{c}_{k+1} + \left(\mathbf{c}_{k+1}\right)^{\mathsf{T}}\left(\nabla \boldsymbol{u}^{n+1}\right)^{\mathsf{T}} - \frac{1}{Wi}\left(\mathbf{c}_{k+1} - \mathbf{I}\right), \end{cases}$$

where δt is a local time-step for the solution of the ODE on each mesh element. To preserve the positive definiteness of the conformation tensor, this local time-step for the solution of the

ODE is set to $\delta t = {}^{dt}/_{n}$ with n the smallest integer number such that $\delta t \leq 1/\left(100\|\nabla u^{n+1}\|_\infty\right)$, see [18].

For $\mathbf{M}$, we proceed exactly as for $\mathbf{c}$ by considering the unsteady form of the transport problem Eq 5.63

$$\partial_t \mathbf{M} + \mathbf{u}^{(0)} \cdot \nabla \mathbf{M} = D\mathbf{u}^{(0)} \cdot \mathbf{M} - \frac{1}{We}\left(\mathbf{M} - \mathbf{I}_{\frac{d(d+1)}{2}}\right) \tag{5.98a}$$

$$\mathbf{M}_{(t=0)} = \mathbf{I}_{\frac{d(d+1)}{2}} \tag{5.98b}$$

and wait until steady-state is reached. The matrix is no longer symmetric but remains positive definite. The computation of the logarithm is then done by a block diagonalization which consists in computing the Schur form and to eliminate off-diagonal blocks by solving Sylvester equations [4].

Implementation and high performance computing The solvers are implemented as specific modules of the CALIF^{3}S platform [2] developed at the French Institut de Radioprotection et de Sûreté Nucléaire (IRSN). Parallel computations were carried out on TotalEnergies' group supercomputer Pangea II through a domain decomposition approach using the OpenMPI (3.1.5) library [8] and the METIS (4.0.3) graph partitioner [15]. All the linear systems are preconditionned by a Block-Jacobi preconditioner. The linear systems coming from the prediction steps and the transport problems are solved using the GMRES method [22]. The projection steps are solved using a classical conjugate gradient method. The log transformation of the conformation tensor is done by diagonalizing $\mathbf{c}$, using a QR decomposition. The log transformation of $\mathbf{M}$ is carried out using the Eigen (3.4.0) library [9]. Finally, the linear systems coming from the local ODE are solved using a direct LU method.

5.4.2.2 Results

We plotted in Fig 5.3a and Fig 5.3b the components of the matrices $\mathbf{B}$ and $\mathbf{N}^*$ for the crystalline case. The dominant terms are B_{12} and N^*_{12}, which is similar to the channel flow. This is because of the structure of the birefringent strands and the flow in this case. As discussed in Harlen [10], Rallison and Hinch [21] + JFM , the strands follow streamlines and can be thought of as a line distribution of forces in an otherwise Newtonian fluid. In the crystalline case, strands connect the circles on both sides and a large channel flow develops between lines of circles, see Fig 5.4. Because of this structure, the situation is actually close to the channel flow and dominant terms in the $\mathbf{B}$ and $\mathbf{N}^*$ are the same. It is also important to note that, although B_{11} is much smaller, it still is important with the increase in $C^{(0)}_{xx}$ being controlled by $B_{11}C^{(0)}_{xx} + B_{12}C^{(0)}_{yy}$. Similarly, the additional drag due to viscoelasticity is primarily determined by both N^*_{11} and N^*_{12} .

To assess the validity of our approach and its limits, we plotted in Figs 5.3c and 5.3d the normalized trace of the conformation tensor and the average velocity for both the homogenized model and the average results of the direct numerical simulations for different values of β. We see that the homogenized model is, as expected, valid in the limit $\beta \ll 1$ with our approach providing a reasonable approximation up to $\beta \simeq 10^{-1}$. Beyond $\beta \simeq 10^{-1}$, the overall trend is similar but the feedback of the strands upon the flow field becomes too important and higher-order terms would be needed to obtain a more accurate representation.

We now turn to the case of a flow in an amorphous structure, with example fields for the conformation tensor and the velocity shown in Fig 5.5 at different values of β. The strands show clearly in the wake of each circle at $\beta = 10^{-2}$ and $\beta = 10^{-1}$. $\beta = 1$ is associated with a stronger couplings between momentum and transport of the conformation tensor with both a decrease

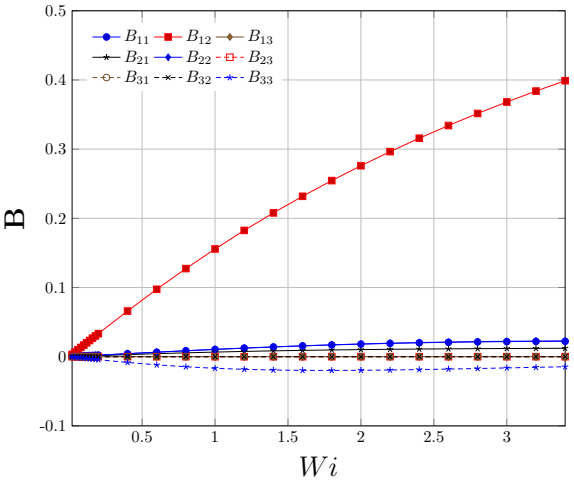

(a) $\mathbf{B}$ as a function of Wi

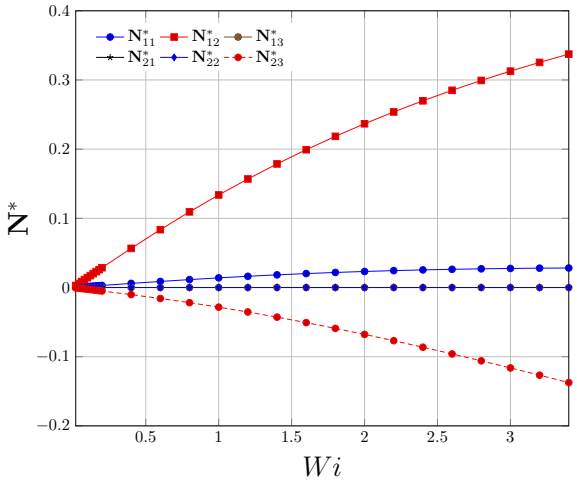

(b) $\mathbf{N}^*$ as a function of Wi

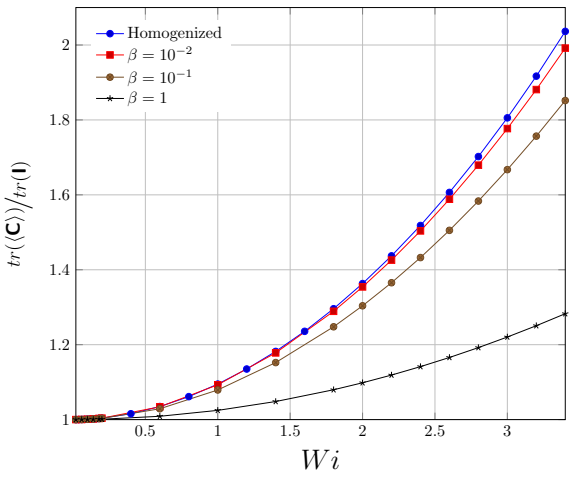

(c) Normalized trace of $\mathbf{c}$ as a function of Wi

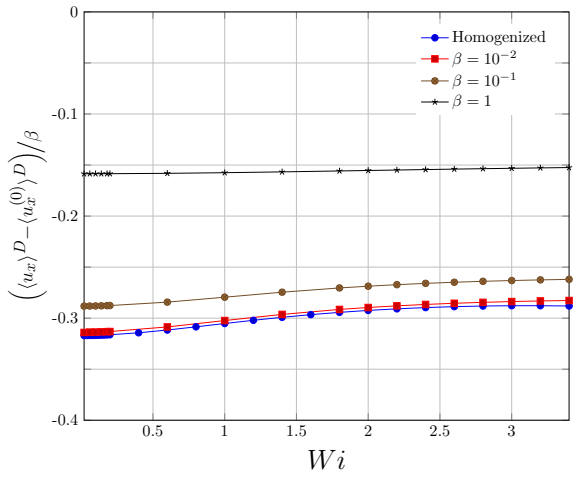

(d) Normalized velocity as a function of Wi

Fig. 5.3 Crystalline structure: components of the effective matrices in the homogenized models and comparison between homogenized and direct numerical simulations for different values of β.

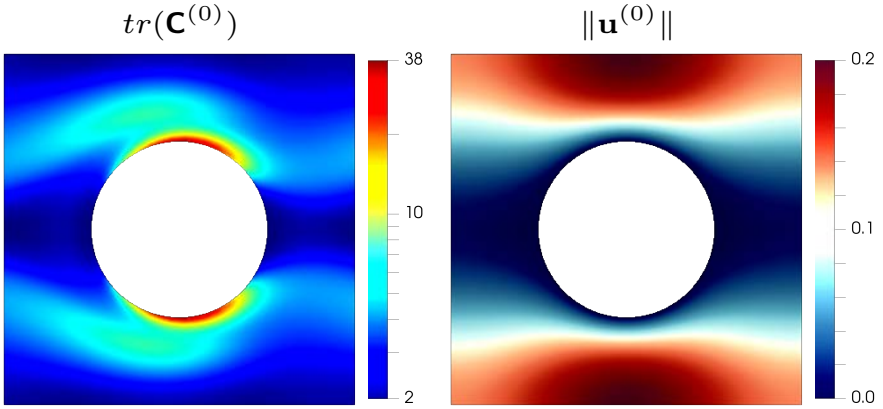

Fig. 5.4 Example of fields obtained for $tr\left(\mathbf{C}^{(0)}\right)$ and $\left\|\mathbf{u}^{(0)}\right\|$ in the crystalline structure at $Wi = 3.4$.

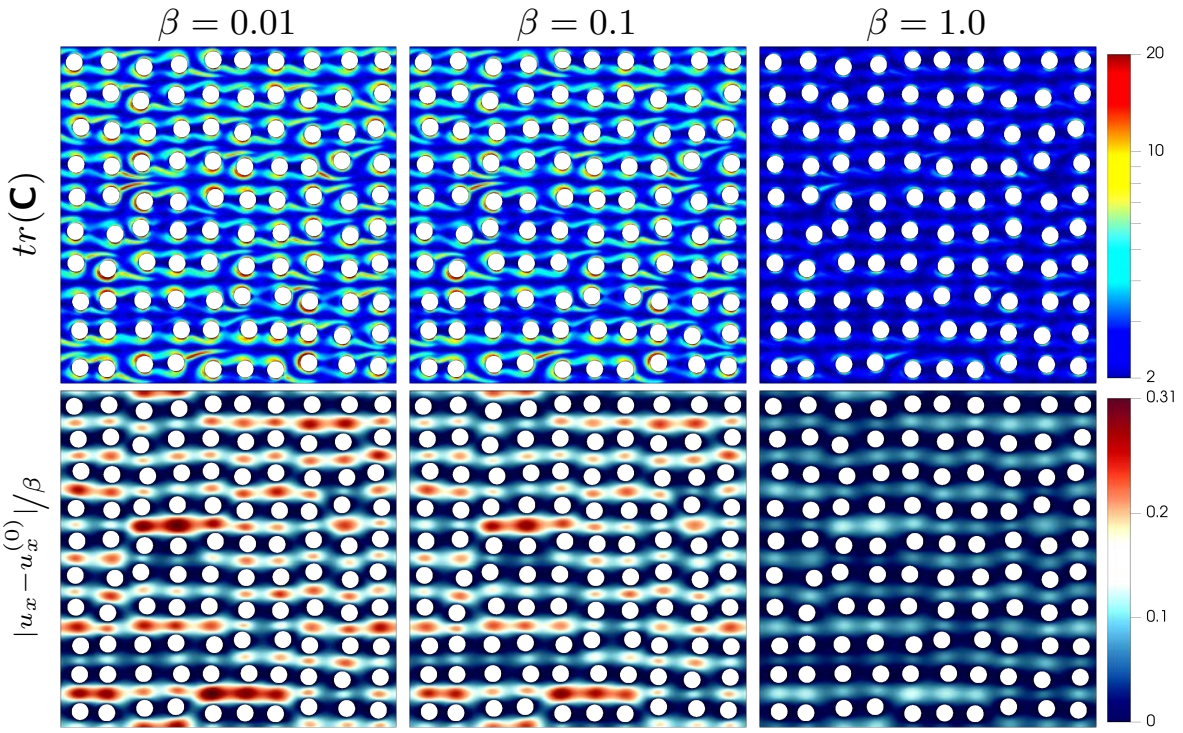

Fig. 5.5 Trace of the conformation tensor and velocity fields for the amorphous structure ($\delta = 0.5$) at $Wi = 3.4$.

in the intensity of the strands and the velocity magnitude. In Figs 5.6a and 5.6b, we plotted the components of matrices $\mathbf{B}$ and $\mathbf{N}^*$. Again, B_{12} and N^*_{12} are the dominant components but are relatively weaker compared to the crystalline case. We further compare direct numerical simulations of the Oldroyd-B model with the homogenized model in Figs 5.6c and 5.6d. These results show again that our approach yields a reasonable appoximation up to $\beta \simeq 10^{-1}$. We also see that the behaviour of the velocity difference is non-monotonic with the Weissenberg number. Such apparent thinning, followed by apparent thickening, is a known phenomenon in the flow of polymer solutions through porous media [3, 12]. We have hypothesized in JFM that, for steady flows, this is due to the presence of the birefringent strands. Interestingly, our homogenized model is able to capture this phenomenon.

Figs 5.7a and 5.7b show the xx and yy components of the conformation tensor for the solution of the homogenized model in all the different structure. Remarkably, we recover a solution for $C^{(0)}_{xx}$ that is very close to the channel flow in all different structures, even though the components of $\mathbf{B}$ vary significantly (see Figs 5.7c). The primary difference is for $C^{(0)}_{yy}$. $C^{(0)}_{yy} = 0$ for the channel case but is non-zero for all other cases and seems to increase with the "disorder" in the structure.

5.5 Conclusions

We have developed a homogenized model for the flow of an Oldroyd-B fluid through porous media. The model consists of an advection-reaction transport equation for the average conformation tensor along with a Darcy's law containing an additional drag generated by viscoleastic stress. It is valid in a limit of high dilutation for polymer suspensions. Our simulations and test cases show that we obtain reasonably accurate solutions for sufficiently dilute suspensions. The

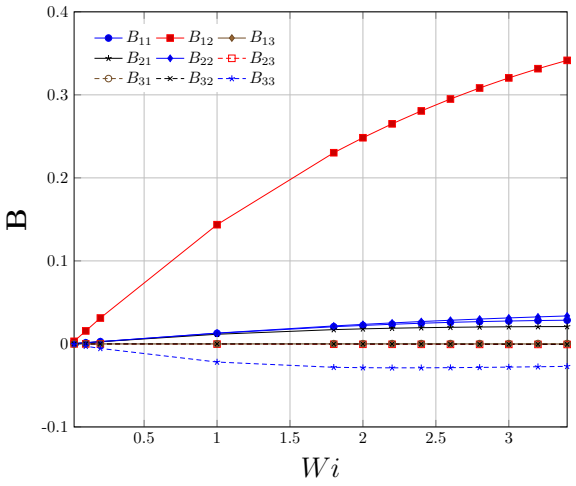

(a) **B** as a function of Wi

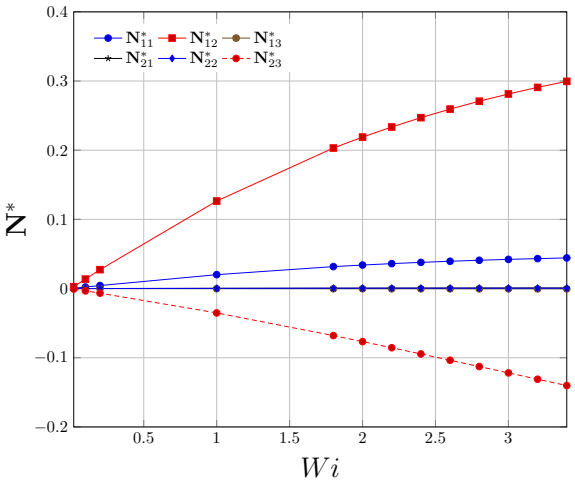

(b) $\mathbf{N}^*$ as a function of Wi

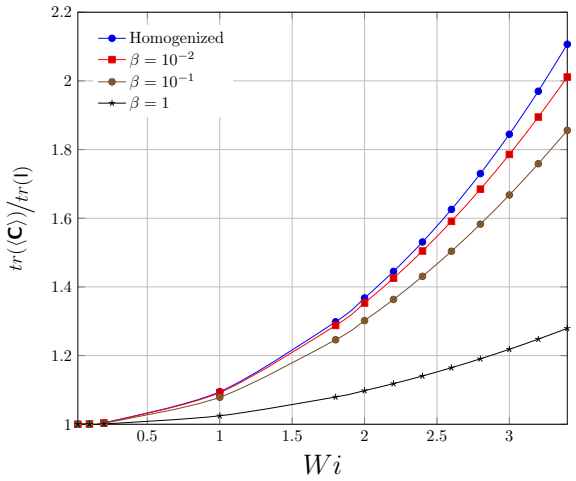

(c) Normalized trace of **c** as a function of Wi

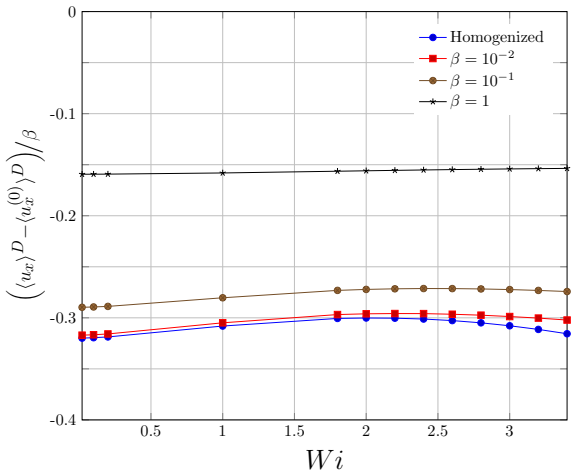

(d) Normalized velocity as a function of Wi

Fig. 5.6 Amorphous structure ($\delta = 0.5$): components of the effective matrices in the homogenized models and comparison between homogenized and direct numerical simulations for different values of β.

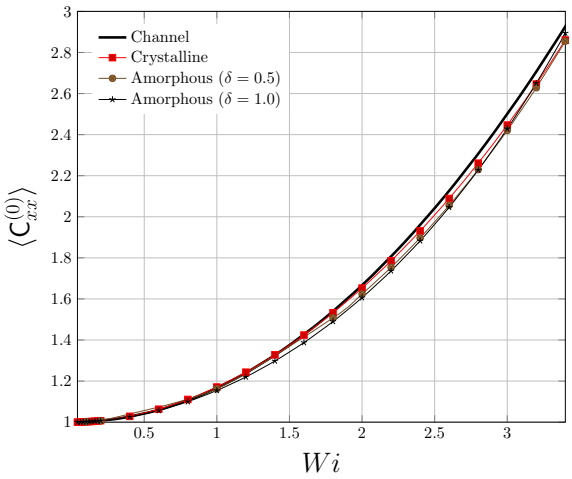

(a) C_{xx} component of the conformation tensor

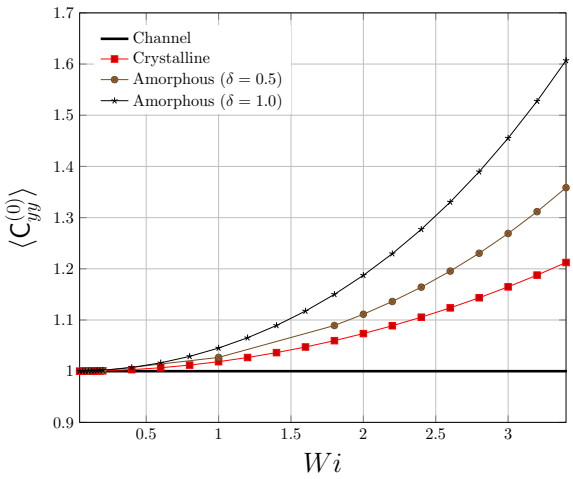

(b) C_{yy} component of the conformation tensor

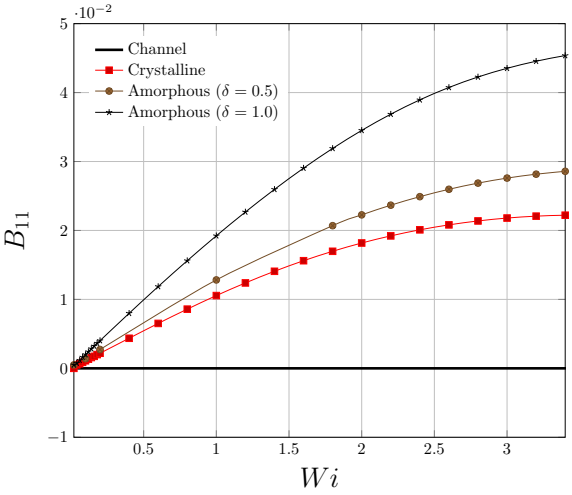

(c) B_{11} as a function of Wi

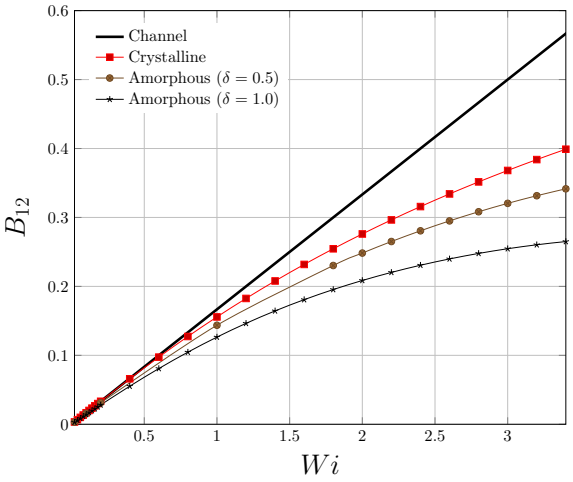

(d) B_{11} as a function of Wi

Fig. 5.7 Comparisons of the conformation tensor and of the dominant components in the matrix **B** for the different structures.

homogenized model can also capture both apparent shear-thinning and shear-thickening, an important property of the flow of polymer solutions through porous media.

Although the case of high dilution is of course limiting, our model is the first proposition of a homogenized model for viscoelastic flows through porous media that can actually capture strong nonlinear effects, such as the development of birefringent strands. Our model shows that modeling viscoelastic flows through porous media cannot be reduced to calculating an apparent permeability in a simple Darcy's law. Our model couples a transport equation for the polymeric stress with a modified form of Darcy's law that features an additional drag term associated with stress localization at pore-scale. This suggests that we need specific models for viscoelastic flows through porous media and not just empirical extensions of Darcy's law. Generalizations of our approach to a wider range of flow regimes may be possible, for instance by considering higher-order asymptotics that can describe the feedback of the strands upon the flow field at pore-scale.

Références

[1] Bresch, D. and Prange, C. (2014). Newtonian limit for weakly viscoelastic fluid flows. *SIAM Journal on Mathematical Analysis*, 46(2):1116–1159.

[2] CALIF3S (2021). A Computational Fluid Dynamics software based on Pelicans. https://gforge.irsn.fr/gf/project/calif3s.

[3] Chauveteau, G. (1981). Molecular interpretation of several different properties of flow of coiled polymer solutions through porous media in oil recovery conditions. In *SPE Annual Technical Conference and Exhibition*. OnePetro.

[4] Davies, P. I. and Higham, N. J. (2003). A schur-parlett algorithm for computing matrix functions. *SIAM Journal on Matrix Analysis and Applications*, 25(2):464–485.

[5] Davit, Y., Bell, C. G., Byrne, H. M., Chapman, L. A. C., Kimpton, L. S., Lang, G. E., Leonard, K. H. L., Oliver, J. M., Pearson, N. C., Shipley, R. J., et al. (2013). Homogenization via formal multiscale asymptotics and volume averaging: How do the two techniques compare? *Advances in Water Resources*, 62:178–206.

[6] De Haro, M. L., Del Río, J. A. P., and Whitaker, S. (1996). Flow of maxwell fluids in porous media. *Transport in Porous Media*, 25(2):167–192.

[7] Fattal, R. and Kupferman, R. (2004). Constitutive laws for the matrix-logarithm of the conformation tensor. *Journal of Non-Newtonian Fluid Mechanics*, 123(2-3):281–285.

[8] Graham, R. L., Woodall, T. S., and Squyres, J. M. (2005). Open MPI: A flexible high performance MPI. In *International Conference on Parallel Processing and Applied Mathematics*, pages 228–239. Springer.

[9] Guennebaud, G., Jacob, B., et al. (2010). Eigen (3.4.0). http://eigen.tuxfamily.org.

[10] Harlen, O. G. (1990). High-deborah-number flow of a dilute polymer solution past a sphere falling along the axis of a cylindrical tube. *Journal of Non-Newtonian Fluid Mechanics*, 37(2-3):157–173.

[11] Haward, S. J., Toda-Peters, K., and Shen, A. Q. (2018). Steady viscoelastic flow around high-aspect-ratio, low-blockage-ratio microfluidic cylinders. *Journal of Non-Newtonian Fluid Mechanics*, 254:23–35.

[12] Hemingway, E. J., Clarke, A., Pearson, J. R. A., and Fielding, S. M. (2018). Thickening of viscoelastic flow in a model porous medium. *Journal of Non-Newtonian Fluid Mechanics*, 251:56–68.

[13] Hopkins, C. C., Haward, S. J., and Shen, A. Q. (2020). Purely elastic fluid–structure interactions in microfluidics: implications for mucociliary flows. *Small*, 16(9):1903872.

[14] Hulsen, M. A., Fattal, R., and Kupferman, R. (2005). Flow of viscoelastic fluids past a cylinder at high Weissenberg number: stabilized simulations using matrix logarithms. *Journal of Non-Newtonian Fluid Mechanics*, 127(1):27–39.

[15] Karypis, G. and Kumar, V. (1998). A fast and high quality multilevel scheme for partitioning irregular graphs. *SIAM Journal on Scientific Computing*, 20(1):359–392.

[16] Khuzhayorov, B., Auriault, J.-L., and Royer, P. (2000). Derivation of macroscopic filtration law for transient linear viscoelastic fluid flow in porous media. *International Journal of Engineering Science*, 38(5):487–504.

[17] Miles, M. J. and Keller, A. (1980). Conformational relaxation time in polymer solutions by elongational flow experiments: 2. preliminaries of further developments: chain retraction; identification of molecular weight fractions in a mixture. *Polymer*, 21(11):1295–1298.

[18] Mokhtari, O., Davit, Y., Latché, J.-C., and Quintard, M. (2021). A staggered projection scheme for viscoelastic flows. Working paper or preprint.

[19] Molinet, L. and Talhouk, R. (2008). Newtonian limit for weakly viscoelastic fluid flows of oldroyd type. *SIAM Journal on Mathematical Analysis*, 39(5):1577–1594.

[20] Odell, J. A. and Carrington, S. P. (2006). Extensional flow oscillatory rheometry. *Journal of non-newtonian fluid mechanics*, 137(1-3):110–120.

[21] Rallison, J. M. and Hinch, E. J. (1988). Do we understand the physics in the constitutive equation? *Journal of Non-Newtonian Fluid Mechanics*, 29:37–55.

[22] Saad, Y. and Schultz, M. H. (1986). GMRES: A generalized minimal residual algorithm for solving nonsymmetric linear systems. *SIAM Journal on scientific and statistical computing*, 7(3):856–869.

[23] Scrivener, O., Berner, C., Cressely, R., Hocquart, R., Sellin, R., and Vlachos, N. S. (1979). Dynamical behaviour of drag-reducing polymer solutions. *Journal of Non-Newtonian Fluid Mechanics*, 5:475–495.

[24] Slattery, J. C. (1967). Flow of viscoelastic fluids through porous media. *AIChE Journal*, 13(6):1066–1071.

[25] Sun, C.-l. and Huang, H.-Y. (2016). Measurements of flow-induced birefringence in microfluidics. *Biomicrofluidics*, 10(1):011903.

[26] Whitaker, S. (1986). Flow in porous media I: A theoretical derivation of Darcy's law. *Transport in Porous Media*, 1(1):3–25.

[27] Whitaker, S. (1999). *The method of volume averaging.* Kluwer Academic Publishers.

Chapter 6

Conclusion et perspectives

Dans ce dernier Chapitre, nous présentons les conclusions générales de ce travail ainsi que ses perspectives.

6.1 Conclusions générales

Au cours de ce travail, nous nous sommes consacrés à l'étude des écoulements viscoélastiques de solutions de polymère en milieu poreux, écoulements qui combinent la complexité de la structure poreuse avec celle de la rhéologie du fluide. De part la présence de longues chaînes polymériques, ces écoulements peuvent présenter des comportements particuliers prenant place sur plusieurs échelles de temps et d'espace, ce qui rend l'interprétation de certaines expériences très difficile. Pour mieux les appréhender, il est donc nécessaire de mieux comprendre la physique ce ces écoulements à l'échelles des pores. Nous avons opté pour une modélisation continue des solutions de polymères, ce qui permet à la fois de capturer, grâce au tenseur de conformation, la configuration des polymères et leur rétroaction sur l'écoulement, tout en gardant un niveau de détail raisonnable pour pouvoir traiter des domaines suffisamment grands. Pour ce faire, nous avons utilisé les modèle d'Oldroyd-B, FENE-CR et FENE-P ; les modèles Oldroyd-B et FENE-CR ayant l'avantage de présenter une viscosité constante en cisaillement.

La première étape, présentée dans le Chapitre 2, était de proposer un schéma numérique pour la résolutions de ces équations, avec le code HPC correspondant. Pour la discrétisation spatiale, nous avons utilisé un schéma à grille décalée d'ordre faible, permettant de considérer un nombre de mailles important sans pour autant nécessiter un nombre trop grand d'inconnues ni l'ajout de termes de stabilisation. Une attention particulière a été portée sur la consistance du schéma, à travers la dissipation de l'énergie libre. Nous avons ainsi proposé une discrétisation qui respecte l'inégalité d'énergie au niveau discret. Néanmoins, ce critère ne suffit pas à garantir ni la stabilité ni la précision du schéma qui passent par un traitement spécifique de l'équation constitutive où les termes de production, faisant intervenir un gradient de vitesse localement élevé, peuvent amener à un profil de conformation qui est difficile à capturer. Le passage au logarithme du tenseur de conformation s'est alors avéré indispensable. Nous avons eu besoin de modifier la discrétisation temporelle, introduisant un fractionnement de l'équation de transport qui permet d'introduire le logarithme de manière judicieuse. Considérant deux cas tests difficiles de la littérature – la cavité entraînée et l'écoulement autour d'un cylindre confiné dans un canal – nous avons montré la capacité de notre schéma à résoudre le problème de manière précise, à traiter des cas pour lesquels les nombres de Weissenberg sont relativement élevés tout en restant stable et à capturer les brins biréfringents pouvant se former dans le sillage d'un cylindre. L'ensemble de ces propriétés font de notre schéma un outil performant pour considérer l'écoulement de fluides viscoélastiques en milieux poreux.

Dans le Chapitre 3, afin de mieux comprendre les mécanismes intervenant à l'échelle du pore, nous nous sommes d'abord focalisés sur deux problèmes modèles, à savoir l'écoulement autour de deux cylindres alignés avec l'écoulement ou placés côte à côte. Bien que très simples, ces deux géométries permettent de mettre en évidence des comportements complexes avec, dans un cas la formation de zones de stagnation et dans l'autre le renforcement de chemins d'écoulement préférentiels. Dans l'optique de comprendre les écoulements dans des milieux plus grands et des géométries plus complexes, ces deux cas tests ont été fondamentaux. C'est ainsi que nous avons pu mettre en évidence le rôle important des brins biréfringents. Ces brins constituent la clé, jusqu'ici manquante, dans la compréhension des écoulements viscoélastiques en général. Du fait de leur rétroaction sur l'écoulement, ces filaments sont responsables de la formation de zones de stagnation, de l'amplification de chemins préférentiels et de la formation de sous-canaux. Dans un milieu poreux, ces mécanismes contribuent à modifier l'écoulement de manière importante. Ces filaments sont ainsi à l'origine de la forte diminution de la perméabilité apparente généralement observée dans l'écoulement de fluides viscoélastiques en milieu poreux. Nous avons montré que cette diminution est due à la fois à une augmentation de la dissipation visqueuse dans les canaux d'écoulement formés par les filaments et à l'augmentation du taux de création d'entropie liée à la formation des brins eux-mêmes. Nous apportons ainsi une explication nouvelle à ce phénomène qui, jusqu'ici, restait mal compris.

Dans des treillis ordonnés de cylindres, le mécanisme d'amplification des chemins d'écoulement préférentiels prend une dimension particulière. De tels agencements, permettent de mettre en évidence la présence de directions d'écoulement privilégiées qui correspondent à des positions stables des filaments. Dans un réseau hexagonal de cylindres, nous mettons ainsi en évidence, Chapitre 4, un couplage complexe entre les canaux d'écoulement et le transport du tenseur de conformation. Ce couplage conduit à une multistabilité, des bifurcations sous-critiques avec l'angle du terme de forçage et une hystérésis. En augmentant le nombre de Weissenberg, l'état trivial devient instable et des oscillations auto-entretenues apparaissent où les brins battent entre les cylindres les plus proches, qui correspondent aux directions d'écoulement privilégiées. En augmentant encore le nombre de Weissenberg et en faisant varier le rapport de viscosité β, nous avons mis en évidence une vaste gamme d'effets non linéaires parmi lesquelles la propagation d'ondes, des bouffées associées aux mouvements de brins et la propagation lente de défauts. Pour des valeurs du nombre de Weissenberg et de β plus élevées, nous avons constaté que les patterns de brins se stabilisent avec, la persistance de fluctuations pulsatiles le long des brins. Cette étude offre ainsi des nouveaux horizons quant au rôle des brins et une clé pour la compréhension de nombreuses observations expérimentales.

Le rôle important des brins biréfringents sur les propriétés de l'écoulement à la grande échelle rend leur prise en compte dans la dérivation de modèles macroscopiques indispensable. Or celle-ci ne peut être obtenue en considérant la limite faible Weissenberg où les brins ne sont pas présents. De ce fait, nous nous sommes plutôt intéressés, au Chapitre 5, à la limite de forte dilution qui permet de découpler l'équation constitutive des équations de conservation tout en capturant les filaments. En utilisant des développements asymptotiques, le modèle d'Oldroyd-B peut être transformé en une séquence de problèmes linéaires. Le modèle homogénéisé consiste finalement en une équation de transport d'advection-réaction pour le tenseur de conformation moyen ainsi qu'en une forme de la loi de Darcy qui contient un terme de traînée supplémentaire associé aux filaments. Cette approche a été validée à la fois par la solution analytique dans un canal mais également sur des écoulements dans des réseaux de cylindres. L'hypothèse de faible dilution reste bien entendu limitante et des généralisations de l'approche à une gamme plus large de régimes d'écoulement peuvent être envisagés, par exemple en considérant des développements d'ordre supérieur. Il s'agit néanmoins de la première proposition d'un modèle homogénéisé pour les écoulements viscoélastiques à travers des milieux poreux qui soit capable de capturer

le développement des brins biréfringents. Notre modèle montre ainsi que la modélisation des écoulements de solutions de polymères dans les milieux poreux ne peut se réduire au calcul d'une perméabilité apparente car le modèle ne prend pas la forme d'une simple loi de Darcy mais nécessite la prise en compte de la conformation des polymères et de leur rétroaction sur l'écoulement.

6.2 Perspectives

Nous avons montré l'importance des brins biréfringents, essentiels dans la compréhension des écoulements viscoélastiques autour d'obstacles et à travers les structures poreuses. Sans vouloir tomber dans le stéréotype de la découverte d'un nouvel outil, on peut se demander quels sont les domaines d'applicabilité et les éventuelles limites de celui-ci. C'est ainsi que l'on peut se poser la question de la généralisation de notre interprétation en terme de brins à d'autres systèmes assez différents tels que les écoulements parallèles. On peut également se demander comment les filaments se comportent dans des écoulements plus complexes tels que les écoulements diphasiques ou multi-constituants. Mais avant tout, se pose la question du rôle de ces brins biréfringents dans des écoulements 3D qui présentent bien des différences avec les écoulement 2D étudiés jusqu'ici.

6.2.1 Empilements 3D de billes

Bien que les structures 2D que nous avons considérées dans ce travail nous ont beaucoup appris sur les écoulements viscoélastiques, les écoulements 2D et 3D sont fondamentalement différents [3]. Dans le cas d'un écoulement autour de deux sphères, par exemple, certaines expériences mettent en évidence la formation à la fois de brins 1D et d'hyperplans 2D [2]. Cela soulève des questions sur la façon dont les écoulements viscoélastiques sont affectés par la dimension du problème. En outre, on peut se demander si les filaments 1D jouent un rôle aussi important dans un écoulement tridimensionnel où la dimension supplémentaire offre par exemple la possibilité de contourner le filament. Dans ce cas, les hyperplans 2D jouent-il un rôle important? Le passage au 3D augmente également les possibilités d'interactions entre les filaments qui peuvent par exemple s'entrecroiser ou, dans un certaines configurations, se replier. Autant de possibilités qui contribuent à la complexité de tels écoulements.

Pour fournir quelques éléments de réponse, nous présentons ici quelques résultats préliminaires. Nous considérons l'écoulement d'un fluide de type Oldroyd-B autour d'une bille de rayon R contenue dans un cube de côté L avec des conditions limites tripériodiques, voir Figure 6.1. L'écoulement est imposé à l'aide d'une force volumique $\mathbf{F}$ normale à l'une des faces du cube et nombre de Weissenberg est alors calculé, à posteriori, par $Wi = \frac{\lambda U}{R}$ où U désigne la norme de la vitesse moyenne et λ le temps de relaxation.

Par périodicité, le cas $L = 2R$ correspond à celui de billes en contact et, en faisant varier L, le rayon R bille restant constant, on peut faire varier la porosité. On étudie alors l'impact de la porosité sur la rhéologie en considérant, comme au Chapitre 2, l'évolution des dissipations de de la traînée avec le nombre de Weissenberg. Dans le cas $L = 2R$, on observe, Figure 6.1(a), un comportement rhéofluidifiant qui s'atténue pour $L = 3$R et disparaît à $L = 4R$. Dans le cas compact ($L = 2R$), on suppose que les zones de forte contrainte polymérique ont plus de mal à se développer, ce qui explique une augmentation relative moins rapide de la dissipation élastique. En éloignant les billes, les zones de forte élongation polymérique peuvent plus facilement se former, ce qui explique que la dissipation élastique relative ne diminue plus. Outre le caractère rhéofluidifiant apparent, on constate également une augmentation plus brutale de la traînée dans le cas $L = 2R$. Ceci pourrait être du à la formation d'une enveloppe englobant les billes et qui

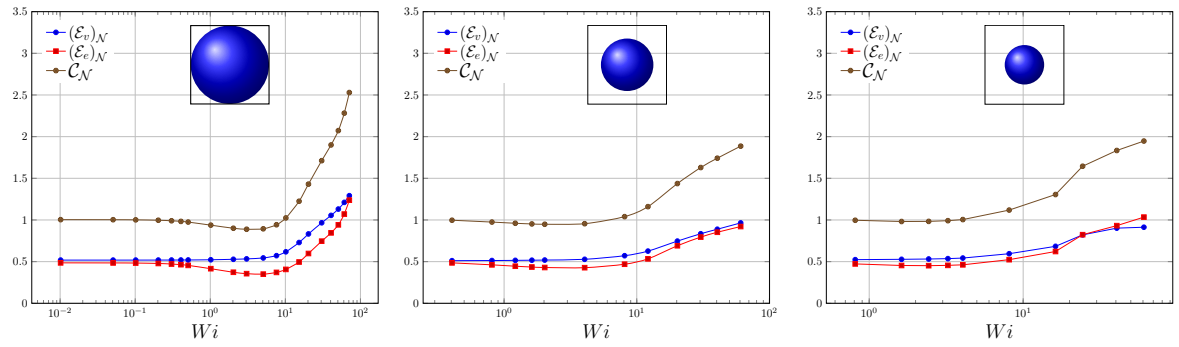

(**a**) (**b**) (**c**)

Fig. 6.1 **Cas d'une bille dans un cube tripériodique.** Évolutions des dissipations et de la traînée dans le cas d'un fluide Oldroyd-B avec $\beta = 1$ pour différentes tailles de domaine. (**a**) $L = 2R$, (**b**) $L = 3R$ et (**c**) $L = 4R$. L'écoulement est imposé à l'aide d'une force volumique $\mathbf{F}$, dont la direction et normale à l'une des faces du cube.

tarde à apparaître dans les cas $L = 3R$ et $L = 4R$, du fait de l'éloignement des billes et d'un nombre de Deborah qui est donc plus faible.

Nous comparons ensuite, Figure 6.2, les résultats obtenus dans le cas $L = 2R$ – qui correspond à un réseau cubique simple – à ceux obtenus pour deux autres réseaux cristallins, à savoir le réseau cubique centré, Figure 6.2 et le réseau cubique face centrée (Figure 6.2(c)). On constate que le comportement rhéofluidifiant est le plus prononcé dans le cas d'un réseau cubique centré qui est aussi celui où l'agencement des billes est le plus compact. Ceci appuie donc l'hypothèse selon laquelle la diminution de la dissipation élastique relative serait due à une possibilité moindre pour les zones de forte élongation polymérique de se développer. Ainsi, dans le réseau face centrée, là où l'agencement de billes est le moins compact, le comportement rhéofluidifiant disparaît. En revanche, après la transition, on constate un comportement inverse à savoir que le rhéoépaississement semble être le plus important là où la géométrie est la moins compacte et où le nombre de Deborah est donc le plus faible. Il se pose donc ici la question de la forme des zones où les polymères sont étirés. On représente ainsi, Figure 6.3(a), les isovolumes correspondants à $tr(\mathbf{c}) > 1000$ et on peut observer que les zones des forte contrainte sont plus développées dans les réseaux les moins compacts. On observe par ailleurs, Figures 6.3(b et c), que les zones de forte contrainte coïncident bien avec une diminution de l'écoulement.

Pour finir, nous nous intéressons à un empilement désordonné de billes de même taille avec, toujours, des conditions tri-périodiques, Figure 6.4. On observe dans ce cas un comportement similaire à ceux observés précédemment à savoir un régime rhéofluidifiant, suivi par une transition caractérisée par une augmentation brutale de la traînée. Une représentation de $tr(\mathbf{c})$ et du le champs de vitesse à différents nombres de Weissenberg est proposée Figure 6.5 où l'on peut voir la formation des zones de forte élongation, accompagnées par une redistribution du champs de vitesse et une augmentation des zones de stagnation.

Cette étude préliminaire confirme donc que les zones de forte contrainte joue également un rôle important dans les écoulements 3D. Néanmoins, la rhéologie semble dépendre de la géométrie de manière bien moins triviale suscitant l'intérêt d'études plus approfondies, à travers notamment des considérations d'ordre topologique.

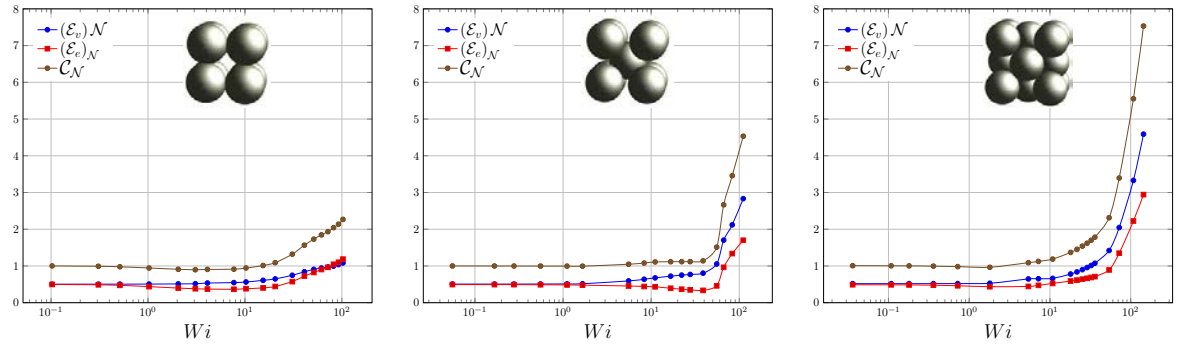

(**a**) (**b**) (**c**)

Fig. 6.2 **Comparaison de différents réseaux cubiques cristallins.** Évolutions des dissipations et de la traînée dans le cas d'un fluide Oldroyd-B avec $\beta = 1$ pour différents réseaux cristallins avec (**a**) cubique simple, (**b**) cubique centré et (**c**) cubiques à faces centrées. L'écoulement est imposé à l'aide d'une force volumique $\mathbf{F}$, dont la direction est normale à l'une des faces du cube caractérisant le réseau.

6.2.2 Zones de stagnation

Dans cette étude, nous avons pu montrer le rôle clé des filaments dans la compréhension des écoulements de fluides viscoélastiques en milieu poreux. Mais ces filaments pourraient également avoir un rôle important dans d'autre types d'écoulement. Nous avons ainsi montré, au Chapitre 3, comment les filaments contribuent à la formation de la zone de stagnation entre deux cylindres alignés. Ce mécanisme pourrait également expliquer l'apparition de vortex observés en amont d'une contraction [1, 9]. Entre autres, le rôle de ces filaments pourrait permettre de comprendre la différence entre une contraction axisymétrique et une contraction planaire [10].

Nous nous intéressons ici à un autre problème qui est celui de l'écoulement autour d'un cylindre 3D unique confiné dans un canal où la formation de zones de recirculation en amont du cylindre a été mise en évidence expérimentalement [8]. Au delà d'un nombre de Weissenberg critique, l'écoulement devient instable, basculant entre deux configurations bistable conduisant à une rupture de symétrie et à la propagation d'une onde élastique relativement loin en amont du cylindre. Nous soupçonnons un rôle important des zones de forte contrainte que ce soit dans l'apparition des zones de recirculation en amont du cylindre mais également dans la transition vers l'instationnaire. Nous avons simulé numériquement cet écoulement qui est de nature hautement tridimensionnelle. L'une des difficultés de cette simulation est la nécessité d'avoir un canal suffisamment long pour que la perturbation générée par le cylindre, en amont ou en aval de celui-ci, ait le temps de relaxer avant de rencontrer les conditions limites imposées en entrée/sortie, ce qui est source de problèmes numériques. Une des possibilités, pour éviter de tels problèmes, est d'imposer des conditions périodiques au niveau des entrées et sorties du canal, ce qui nécessite d'avoir un canal suffisamment long pour s'assurer de l'innocuité de la périodicité. L'écoulement est alors imposé à l'aide d'une force volumique $\mathbf{F}$ parallèle aux parois latérales du canal et le nombre de Weissenberg est alors calculé, à posteriori, par $Wi = \frac{\lambda U}{R}$ où U désigne la norme de la vitesse moyenne et λ le temps de relaxation. Nous présentons, Figures 6.6 et 6.7, les résultats obtenus pour un fluide de type Oldroyd-B dans le cas $Wi = 4$, stationnaire, qui correspond au début de la formation des tourbillons. En observant les différents plans de coupe, on observe, Figure 6.6, la formation d'une enveloppe en amont du cylindre, au niveau du point de stagnation présent à la jonction entre le cylindre et la paroi supérieure. La formation de cette enveloppe correspond à la celle, Figure 6.7, d'une zone de recirculation. La comparaison

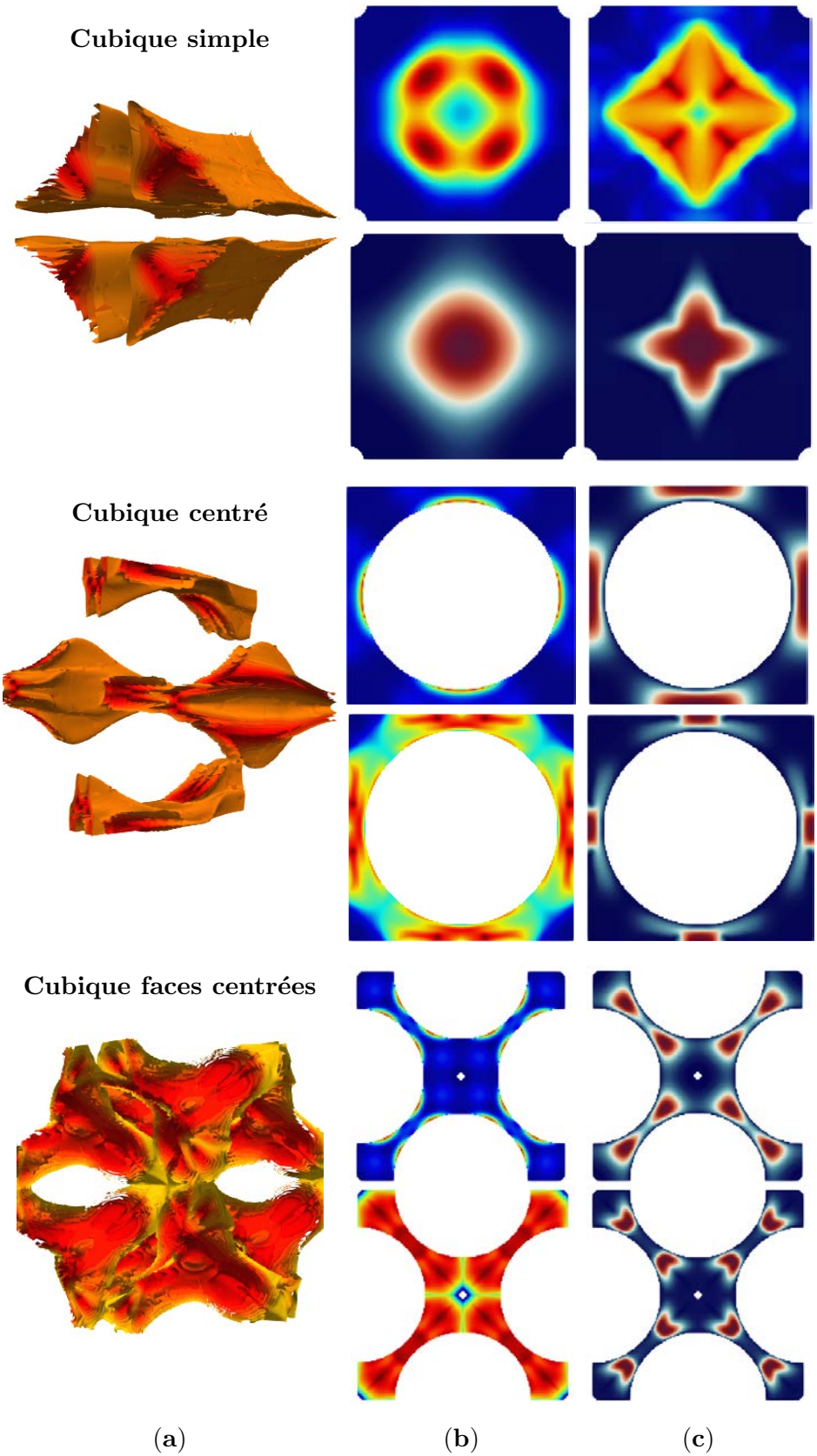

Fig. 6.3 **Représentations dans des cubiques cristallins**. (**a**) Isovolumes correspondants à $tr(\mathbf{c}) > 1000$, (**b** et **c**) Coupes transversales à l'écoulement de $tr(\mathbf{c})$ et de la norme de la vitesse prises au centre de la géométrie dans les cas (**a**) Weissenberg faible et (**b**) Weissenberg élevé.

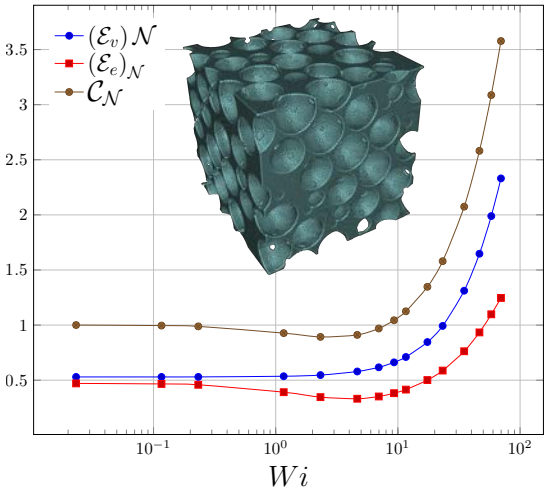

Fig. 6.4 **Exemple d'un empilement désordonné de billes.** Évolutions des dissipations et de la traînée dans le cas d'un fluide Oldroyd-B avec $\beta = 1$. L'écoulement est imposé de la gauche vers la droite à l'aide d'une force volumique $\mathbf{F}$, normale à la face du cube.

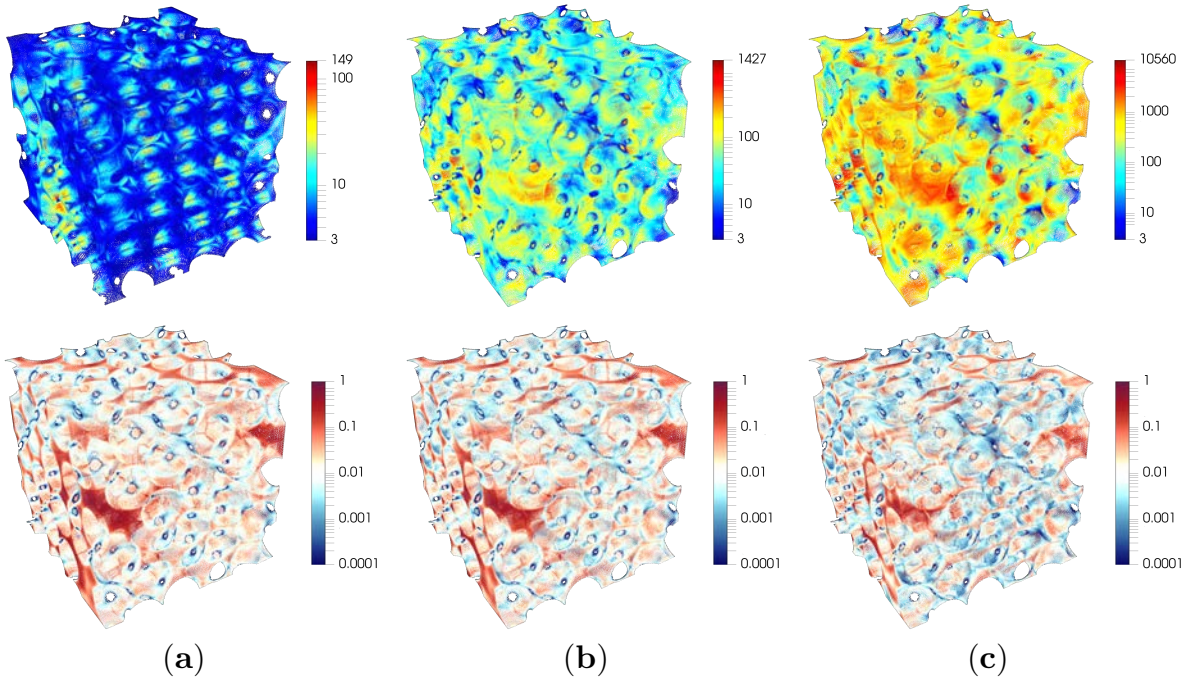

Fig. 6.5 **Empilement désordonné de billes.** Champs de $tr(\mathbf{c})$ et de $\|\mathbf{u}\|/max(\|\mathbf{u}\|)$, dans les cas (**a**) $Wi \simeq 1$, (**b**) $Wi \simeq 5$, et (**c**) $Wi \simeq 30$. L'écoulement est imposé de la gauche vers la droite à l'aide d'une force volumique $\mathbf{F}$, normale à la face du cube.

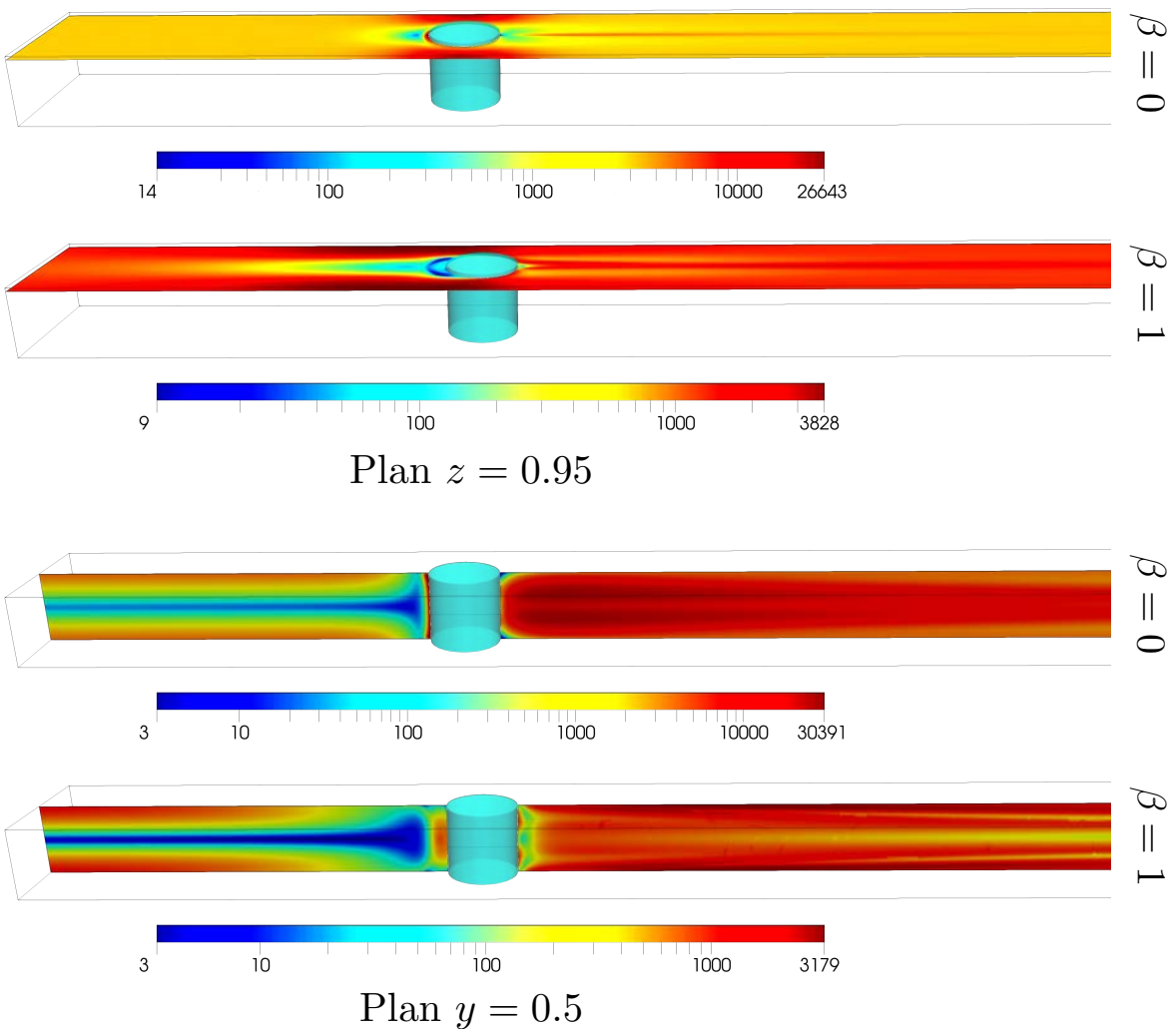

Fig. 6.6 **Cylindre dans un canal 3D.** Plans de coupe correspondants à $z = 0.95$ et $y = 0.5$ pour $tr(\mathbf{c})$ dans les cas $\beta = 0$ et $\beta = 1$. L'écoulement est imposé à l'aide d'une force volumique $\mathbf{F}$, parallèle aux parois latérales du canal.

entre les cas $\beta = 0$ et $\beta = 1$ permet alors d'observer le rôle des zones de forte contrainte qui créent une poche au niveau de l'intersection du cylindre et des plans inférieurs et supérieurs. Nous supposons alors que ces poches vont se développer vers l'amont au fur et à mesure que le nombre de Weissenberg augmente et que la transition vers l'instationnaire prend place au moment où ces poches se rencontrent. Ces simulations sont néanmoins très coûteuses puisque la taille du domaine doit augmenter avec le nombre de Weissenberg, ce qui est très limitant. Un travail sur les conditions limites qui permettent de passer outre cette exigence nous semble ainsi primordial pour permettre un analyse plus poussée de ce problème.

6.2.3 Transition vers l'instationnaire

Nous avons mis en évidence, au Chapitre 4, le rôle des filaments dans l'apparition des oscillations observées dans des treillis ordonnés de cylindres. On peut alors se poser la question de leur rôle dans la transition vers l'instationnaire dans des configurations plus générales. Dans un écoulement présentant une courbure, la transition vers l'instationnaire est supercritique [7] et

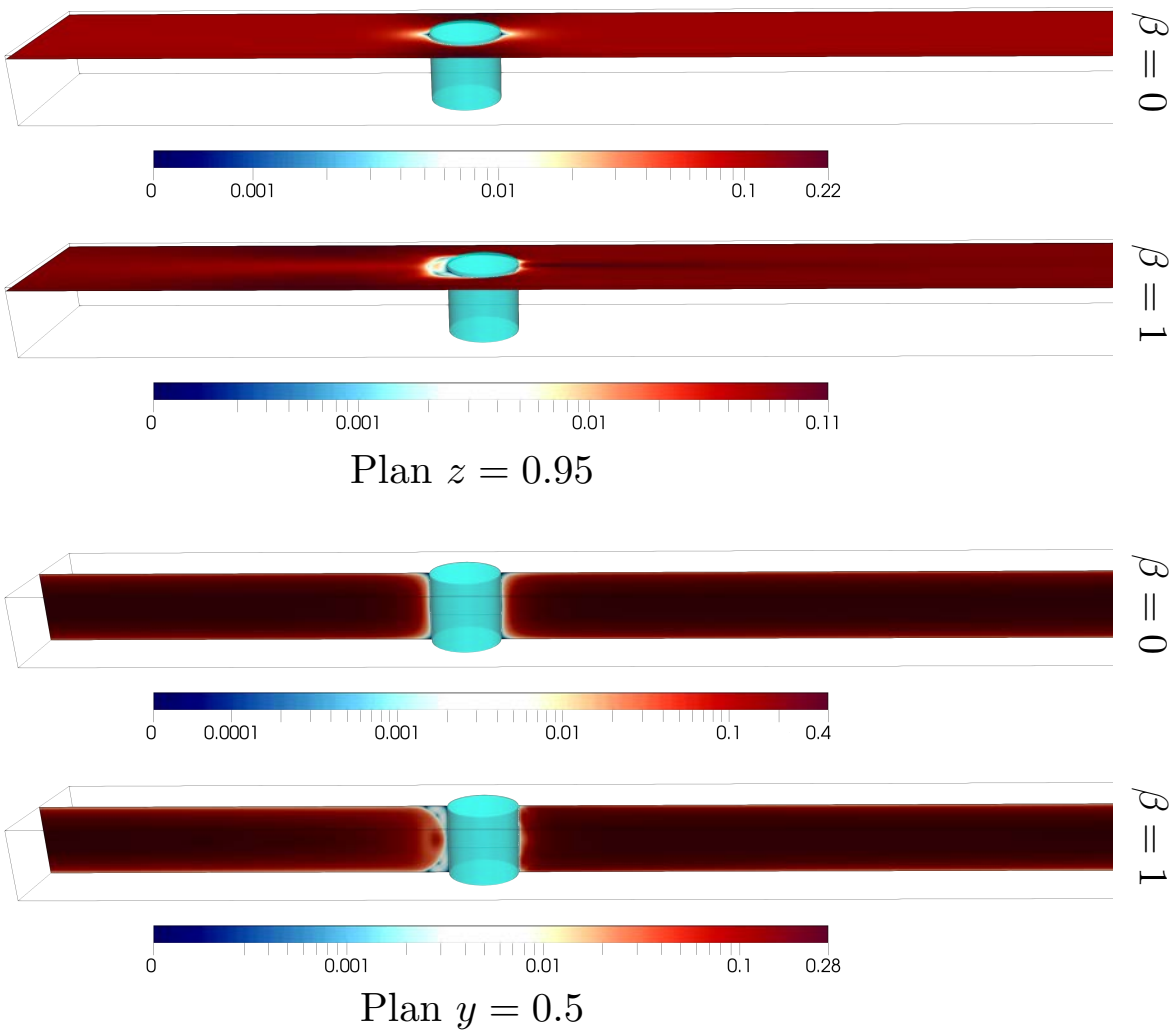

Fig. 6.7 **Cylindre dans un canal 3D.** Plans de coupe correspondants à $z = 0.95$ et $y = 0.5$ pour $\|\mathbf{u}\|/max(\|\mathbf{u}\|)$ dans les cas $\beta = 0$ et $\beta = 1$. L'écoulement est imposé à l'aide d'une force volumique $\mathbf{F}$, parallèle aux plans horizontaux.

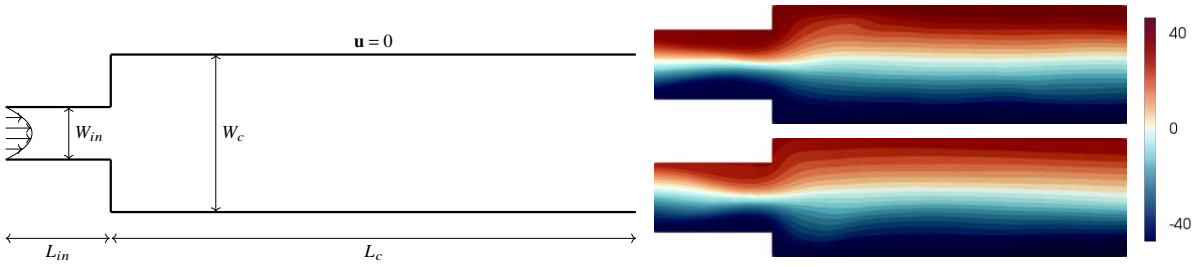

(**a**) (**b**)

Fig. 6.8 **Perturbation générée à l'entrée d'un canal plan.** (**a**) Géométrie utilisée. (**b**) Contours de la fonction de courant à $t = 30$ et $t = 55$. On observe le développement d'une instabilité à l'entrée du grand canal.

peut-être caractérisée par le critère de McKinley [4, 6]

$$\left[\frac{\lambda U}{\mathcal{R}}\frac{\tau_{11}}{\tau_c}\right]^{1/2} \geq M_{crit}, \tag{6.1}$$

où le premier terme représente la contribution de la géométrie à l'étirement du polymère à travers la ligne de courant et le second le rapport entre les contraintes d'extension et de cisaillement. On peut donc se poser ici la question du lien entre ce critère et les filaments. On sait que les filaments correspondent justement à des zones de forte extension. On pourrait donc se demander si cette transition pourrait-être liée à une courbure importante des filaments et comment celle-ci prend alors place.

Dans le cas d'un canal plan, la transition vers l'instationnaire devient sous-critique [5], nécessitant une perturbation initiale pour se développer. Se pose alors la double question de savoir comment on passe de la perturbation initiale à un écoulement instationnaire, interrogation qui, nous semble-t-il rejoint celle précédente sur le critère de McKinley, et, par quels mécanismes, cette instationnarité une foie établie est entretenue. Autant de question auxquelles nous avons tenter de répondre dans le cadre du stage M2R de Clément BRET dont nous présentons, brièvement ici, quelques résultats.

Pour étudier ce problème, nous avons considéré l'écoulement d'un fluide de type Oldroyd-B dans un canal de longueur suffisamment grande $L = 500$ avec des conditions de type entrée/sortie. La perturbation est alors produite en entrée, par un canal d'injection de section plus petite, qui génère une instabilité, voir Figure 6.8, se propageant loin en aval du canal. L'instationnarité présente alors toutes caractéristiques de la turbulence élastique avec une diminution rapide des fréquences élevées de fluctuations, une augmentation de la traînée ainsi que la présence de mélange, Figure 6.9. En observant les champs de vitesse et de vorticité, Figure 6.10, on retrouve qualitativement des résultats très similaires à ceux obtenus par des analyses aux perturbations [5]. De manière intéressante, on observe, Figure 6.11, la formation de filaments se décrochant des proies du canal. Ces filaments pourraient ainsi jouer un rôle important dans l'instationnarité en permettant de l'entretenir. Une étude plus approfondie du décrochage de ces filaments et de leur rétroaction sur l'écoulement nous semble donc nécessaire.

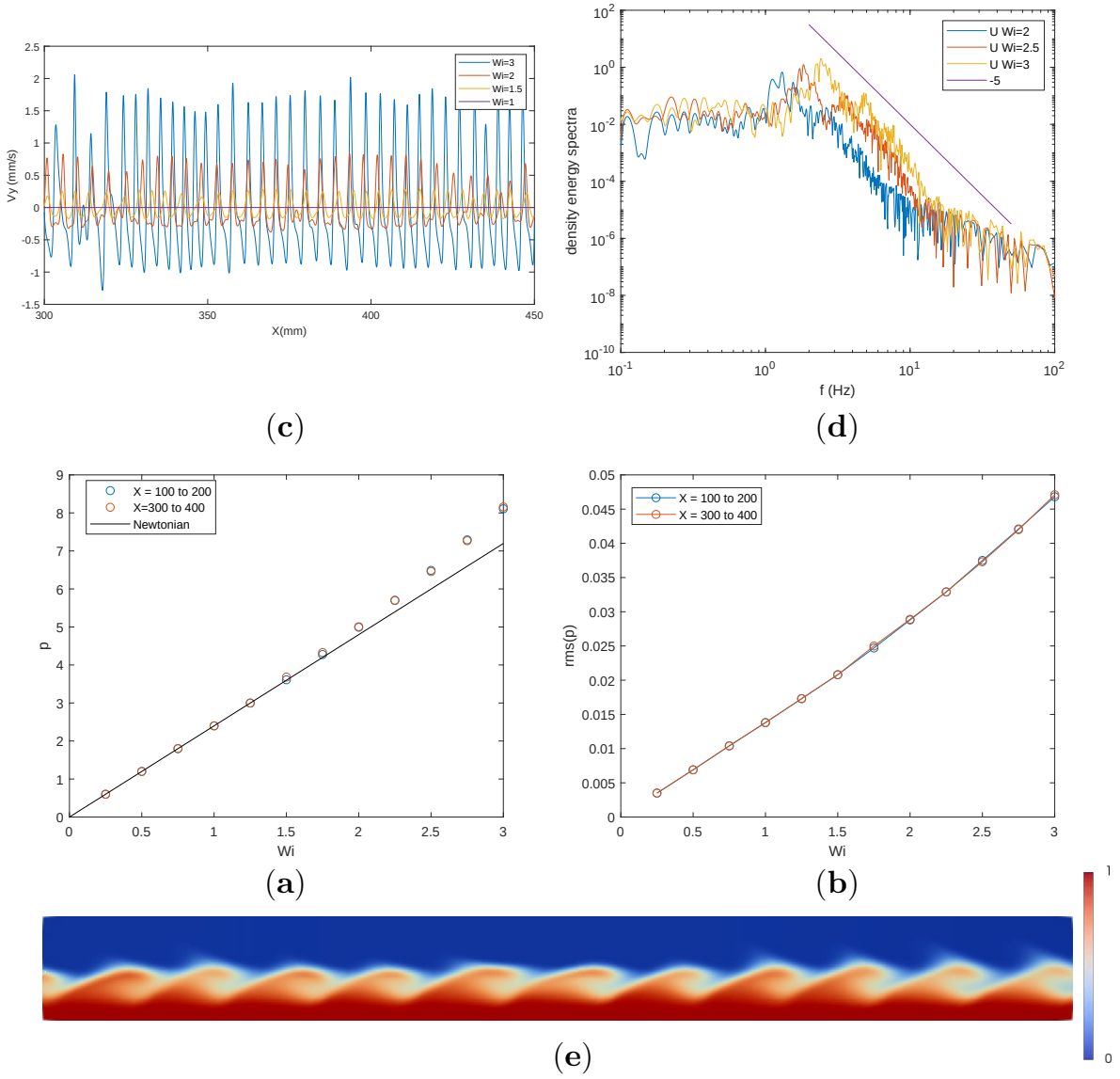

Fig. 6.9 **Caractérisation de l'instationnarité présente dans le canal.** (**a**) Oscillations la la composante verticale de la vitesse entre $x = 300$ et $x = 450$ pour différents nombres de Weissenberg. (**b**) Spectre de fréquence des oscillations pour différentes valeurs du nombre de Weissenberg. (**c**) Évolution de la perte de charge en fonction de Wi sur différents tronçons du canal, à $t = 30$ fixé. (**c**) Moyenne quadratique des fluctuations spatiales de pression pression en fonction du nombre de Wi pour différents tronçons. (**e**) Mise en évidence de la présence de mélange en résolvant une équation de transport scalaire. A l'état initial le canal est rempli au premier quart de la hauteur.

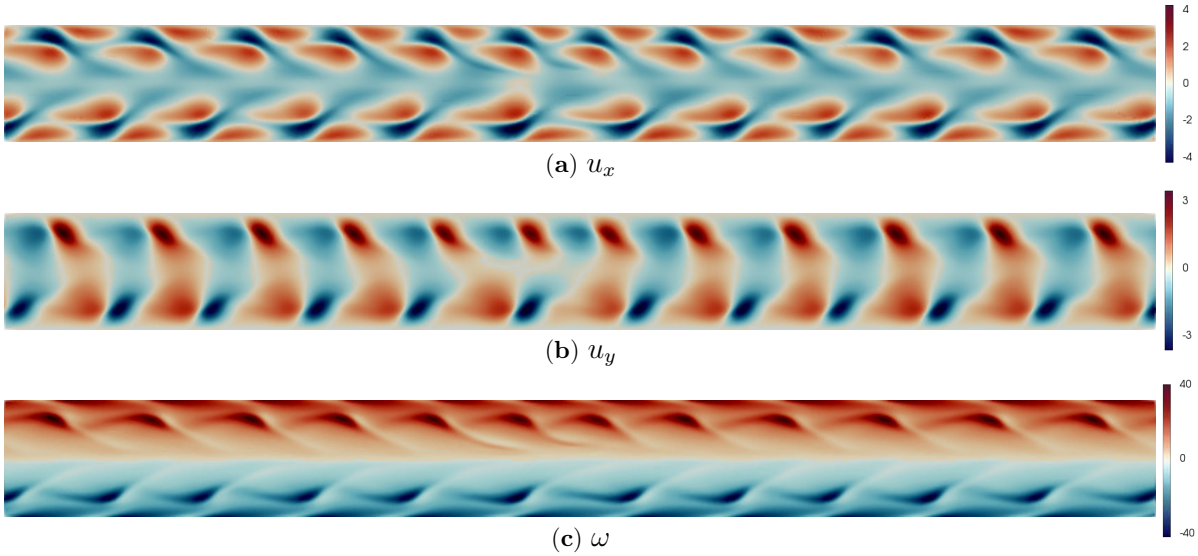

(**a**) u_x

(**b**) u_y

(**c**) ω

Fig. 6.10 **Instabilité dans un canal.** Champs de (**a**) vitesse verticale, (**b**) vitesse horizontale et (**c**) vorticité entre $x = 350$ et $x = 400$.

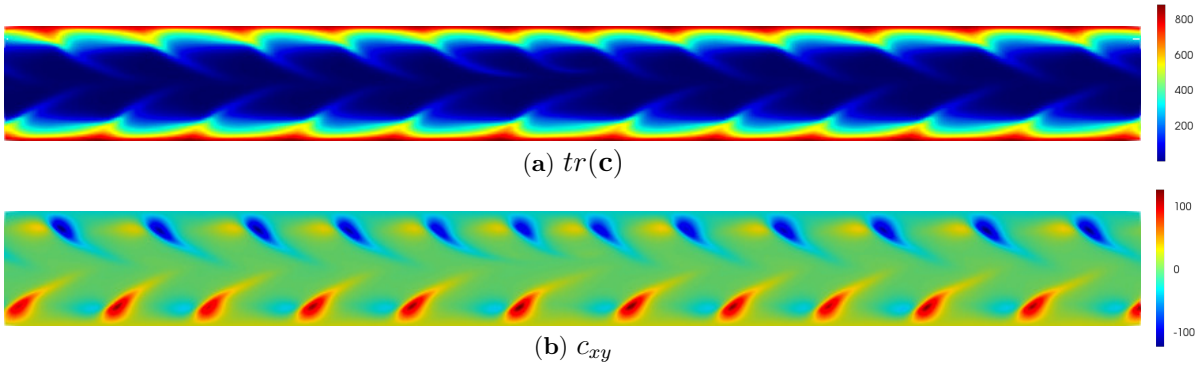

(**a**) $tr(\mathbf{c})$

(**b**) c_{xy}

Fig. 6.11 **Instabilité dans un canal.** Champs de (**a**) $tr(\mathbf{c})$ et (**b**) c_{xy} entre $x = 350$ et $x = 400$.

Références

[1] Boger, D. V. (1987). Viscoelastic flows through contractions. *Annual Review of Fluid Mechanics*, 19(1):157–182.

[2] Haward, S. J. and Odell, J. A. (2004). Molecular orientation in non-Newtonian flow of dilute polymer solutions around spheres. *Rheologica Acta*, 43(4):350–363.

[3] Lester, D. R., Dentz, M., and Le Borgne, T. (2016). Chaotic mixing in three-dimensional porous media. *Journal of Fluid Mechanics*, 803:144–174.

[4] McKinley, G. H., Pakdel, P., and Öztekin, A. (1996). Rheological and geometric scaling of purely elastic flow instabilities. *Journal of Non-Newtonian Fluid Mechanics*, 67:19–47.

[5] Morozov, A. and Van Saarloos, W. (2019). Subcritical instabilities in plane poiseuille flow of an Oldroyd-B fluid. *Journal of Statistical Physics*, 175(3):554–577.

[6] Pakdel, P. and McKinley, G. H. (1996). Elastic instability and curved streamlines. *Physical Review Letters*, 77(12):2459.

[7] Pathak, J. A., Ross, D., and Migler, K. B. (2004). Elastic flow instability, curved streamlines, and mixing in microfluidic flows. *Physics of Fluids*, 16(11):4028–4034.

[8] Qin, B., Salipante, P. F., Hudson, S. D., and Arratia, P. E. (2019). Upstream vortex and elastic wave in the viscoelastic flow around a confined cylinder. *Journal of Fluid Mechanics*, 864.

[9] Rothstein, J. P. and McKinley, G. H. (2001). The axisymmetric contraction–expansion: the role of extensional rheology on vortex growth dynamics and the enhanced pressure drop. *Journal of Non-Newtonian Fluid Mechanics*, 98(1):33–63.

[10] Saramito, P. (2016). *Complex fluids*. Springer.

Communications

Journaux internationaux

O. Mokhtari, J.-C. Latché, M. Quintard, Y. Davit. Birefringent strands drive the flow of viscoelastic fluids through porous media. **Submitted to Journal of Fluid Mechanics**.

O. Mokhtari, Y. Davit, J.-C. Latché, M. Quintard. A staggered projection scheme for viscoelastic flows. **Submitted to Mathematical Modelling and Numerical Analysis**. https://hal.archives-ouvertes.fr/hal-03400727/.

O. Mokhtari, J.-C. Latché, M. Quintard, Y. Davit. Average transport equations for the flow of an Oldroyd-B fluid through porous media. **In preparation**.

O. Mokhtari, J.-C. Latché, M. Quintard, Y. Davit. Multistability and transition to chaos in viscoelastic flows through crystalline porous structures. **In preparation**.

R. Riesco, L. Boyer, S. Blosse, O. Mokhtari, M. Gadelorge, T. Leichle, A. Accardo, Y. Davit, N. Espagnolle, L. Malaquin. Development of a porous PDMS micro-bioreactor to reproduce 3D cellular microenvironments. **In preparation**.

Proceedings

O. Mokhtari, Y. Davit, M. Quintard, J.-C. Latché and R. de Loubens. A Marker-and-Cell scheme for viscoelastic flows on nonuniform grids. **International Conference on Finite Volumes for Complex Applications. Springer, 2020**. https://hal.inria.fr/hal-02950581/.

Conférences internationales

O. Mokhtari, Y. Davit, M. Quintard. The role of birefringent strands on the stability of viscoelastic flows through porous media. **14th Annual InterPore Meeting, Abu Dhabi & Online, May 2022**.

O. Mokhtari, J.-C. Latché, R. de Loubens, Y. Davit, M. Quintard. Viscoelastic Flows Past Arrays of Cylinders: Role of the High-Stress Elastic Filaments. **25th International Congress of Theoretical and Applied Mechanics (ICTAM), Milano, Italy (held Online), Aug. 2021**.

O. Mokhtari, Y. Davit, R. de Loubens, J.-C. Latché, M. Quintard. High-stress elastic filaments control 2D creeping flows of viscoelastic fluids through porous media. **13th Annual InterPore Meeting, Online, Jun. 2021**.

O. Mokhtari, Y. Davit, J.-C. Latché, R. de Loubens, M. Quintard. A Marker-and-Cell scheme for viscoelastic flows on nonuniform grids. **Finite Volumes for Complex Applications IX, Bergen, Norway (held Online), Jun. 2020**.

O. Mokhtari, J.-C. Latché, R. de Loubens, Y. Davit, M. Quintard. Simulation of viscoelastic flows using free-energy-dissipative schemes. **9th International Congress on Industrial and Applied Mathematics (ICIAM), Valencia, Spain, Jul. 2019**.

Conférences nationales

Y. Davit, J.-C. Latché, O. Mokhtari, M. Quintard. Stress localization drives the flow of viscoelastic fluids through porous structures. **Séminaire Mécanique des Fluides Numérique, CEA-SMAI/GAMNI, Institut Henri Poincaré, Paris, Jan. 2022**.

O. Mokhtari, M. Quintard, Y. Davit. On the impact of elastic filaments on viscoelastic flow through porous media. **15èmes Journées d'Etude des Milieux Poreux (JEMP), French Interpore Chapter, Strasbourg, Oct. 2021**.

Workshops

O. Mokhtari, R. de Loubens. Understanding viscoelastic flow in porous media. **CFD@Total, Fev. 2022**.

O. Mokhtari, J.-C. Latché, R. de Loubens, M. Quintard, Y. Davit. Elastic strands drive viscoelastic fluid flows through 2D arrays of cylinders. **GDR SLAMM, Jun. 2021**.

O. Mokhtari, Y. Davit. Viscoelastic fluid flow through porous media. **MPB Group Seminar, Mar. 2021**.

O. Mokhtari, R. de Loubens. Flow of viscoelastic fluids through porous media. **CFD@Total, Nov. 2020**.

A Marker-and-Cell scheme for viscoelastic flows on nonuniform grids

O. Mokhtari[1], Y. Davit[1], J.-C. Latché[2], R. de Loubens[3], M. Quintard[1]

[1]Institut de Mécanique des Fluides de Toulouse (IMFT), Université de Toulouse, France,
[2]Institut de Radioprotection et de Sûreté Nucléaire (IRSN), France,
[3]Total E&P, CSTJF, Pau, France.

Introduction

Abstract We develop a numerical scheme for the solution of the coupled Stokes or Navier-Stokes equations with constitutive equations describing the flow of viscoelastic fluids. In order to obtain consistency, the space discretization of the divergence of the elastic part of the stress tensor in the momentum balance equation is derived using a weak form of the MAC scheme.

Viscoelastic models

The fluid is governed by the following system of equations:

$$\rho(\partial_t \mathbf{u} + \xi \mathbf{u}\cdot\boldsymbol{\nabla}\mathbf{u}) = -\boldsymbol{\nabla} p + \operatorname{div}\boldsymbol{\tau}_s(\mathbf{u}) + \operatorname{div}\frac{\eta_p}{\lambda}\boldsymbol{\tau}_p, \tag{1a}$$

$$\operatorname{div}\mathbf{u} = 0, \tag{1b}$$

$$\partial_t \mathbf{c} + \mathbf{u}\cdot\boldsymbol{\nabla}\mathbf{c} - (\boldsymbol{\nabla}\mathbf{u})\,\mathbf{c} - \mathbf{c}\,(\boldsymbol{\nabla}\mathbf{u})^t + \frac{1}{\lambda}\boldsymbol{\tau}_p = 0. \tag{1c}$$

with ρ, η_p and λ are the fluid density, the polymer viscosity and the polymer retardation time, $\mathbf{u}$ is the velocity and p the pressure. The tensor $\boldsymbol{\tau}_s = \eta_s(\boldsymbol{\nabla}\mathbf{u} + (\boldsymbol{\nabla}\mathbf{u})^t)$ is the solvent stress tensor and $\mathbf{c}$ is the conformation tensor. The polymeric stress tensor $\boldsymbol{\tau}_p$ depends on the model (see [1]):

$$\boldsymbol{\tau}_p = \mathbf{c} - \mathbf{I}_d \qquad \text{Oldroyd-B} \tag{2a}$$

$$\boldsymbol{\tau}_p = \frac{b}{b - \operatorname{tr}(\mathbf{c})}\mathbf{c} - \frac{b}{b-\operatorname{tr}(\mathbf{I}_d)}\mathbf{I}_d \qquad \text{FENE-P} \tag{2b}$$

$$\boldsymbol{\tau}_p = \frac{b}{b-\operatorname{tr}(\mathbf{c})}(\mathbf{c} - \mathbf{I}_d) \qquad \text{FENE-CR} \tag{2c}$$

with $b > d$ (the space dimension), a constant coefficient.

Numerical scheme

The pressure correction scheme

Prediction step – Solve for $\tilde{\mathbf{u}}^{n+1}$:

$$\text{For } 1 \le i \le d,\ \forall \sigma \in \mathcal{E}_S^{(i)},$$
$$\frac{\rho}{\delta t}\left(\tilde{u}^{n+1}_{\sigma,i} - u^n_{\sigma,i}\right) + \xi\,\rho\,\operatorname{div}_\sigma(\tilde{u}^{n+1}_i \mathbf{u}^n) - \operatorname{div}_{\sigma,i}\boldsymbol{\tau}_s(\tilde{\mathbf{u}}^{n+1}) - \operatorname{div}_{\sigma,i}\boldsymbol{\tau}^n_p + \boldsymbol{\nabla}_{\sigma,i}(p^n) = 0. \tag{3a}$$

Correction step – Solve for p^{n+1} and $\mathbf{u}^{n+1}$:

$$\text{For } 1 \le i \le d,\ \forall \sigma \in \mathcal{E}_S^{(i)},$$
$$\frac{\rho}{\delta t}\left(u^{n+1}_{\sigma,i} - \tilde{u}^{n+1}_{\sigma,i}\right) + \boldsymbol{\nabla}_{\sigma,i}(p^{n+1} - p^n) = 0, \tag{3b}$$

$$\forall K \in \mathcal{M},\quad \operatorname{div}_K(\mathbf{u}^{n+1}) = 0. \tag{3c}$$

Constitutive equation discretization

A scalar model problem

We consider the scalar model problem on $I = [-1,1] \times (0,T)$ given by :

$$\partial_t c + \partial_x c = a(x)c \qquad (x,t) \in I \times (0,T), \tag{4a}$$

$$c(x,0) = 1 \qquad x \in I, \tag{4b}$$

$$c(-1,t) = c_L \qquad t \in (0,T). \tag{4c}$$

with a "stiff" source term $a(x)$ given by:

$$a(x) = \begin{cases} -\beta \sin(\frac{\pi}{x_0}x) & x \in (-x_0; x_0), \\ 0 & \textit{elsewhere.} \end{cases} \tag{5}$$

where β and x_0 are the stiffness parameters.

Applying an operator-splitting technique yields:

Advection – Solve for $c^{n+\frac{1}{2}}$:

$$\partial_t c + \partial_x c = 0, \quad (x,t) \in I \times (t^n, t^n + \delta t), \tag{6a}$$

$$c(t^n) = c^n. \qquad x \in I \tag{6b}$$

ODE – Set $c_k(t_n) = c_k^{n+\frac{1}{2}}$, solve for $c^{n+1} = c_k(t_n + \delta t)$:

$$\partial_t c_k(t) = a_k c_k(t), \quad k = 1, \dots, K, \tag{6c}$$

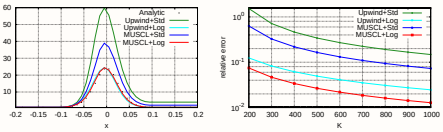

Figure 1: Comparison of the different methods of discretization for the advection step with $\beta = 50$ and $x_0 = 0.1$. Left: Stationary states obtained for $K = 200$. Right: Relative errors (in L^2-norm) with respect to the analytical solution as a function of the mesh size.

The "Strang-log" scheme

Advection I – Solve for $\mathbf{c}^{n+\frac{1}{3}}$:

$$\frac{1}{\delta t/2}\left(\log \mathbf{c}_K^{n+\frac{1}{3}} - \log \mathbf{c}_K^{n}\right) + \operatorname{div}_K(\mathbf{u}^{n+1}\log \mathbf{c}_K^{n+\frac{1}{3}}) = 0, \tag{7a}$$

ODE – Set $\mathbf{c}_K(t_n) = \mathbf{c}_K^{n+\frac{1}{3}}$, solve for $\mathbf{c}^{n+\frac{2}{3}} = \mathbf{c}_K(t_n + \delta t)$:

$$\partial_t \mathbf{c}_K - (\boldsymbol{\nabla}_K \mathbf{u}^{n+1})\,\mathbf{c}_K - \mathbf{c}_K\left(\boldsymbol{\nabla}_K \mathbf{u}^{n+1}\right)^t + \frac{1}{\lambda_K}\boldsymbol{\tau}_{pK} = 0, \tag{7b}$$

Advection II – Solve for $\mathbf{c}^{n+1}$:

$$\frac{1}{\delta t/2}\left(\log \mathbf{c}_K^{n+1} - \log \mathbf{c}_K^{n+\frac{2}{3}}\right) + \operatorname{div}_K(\mathbf{u}^{n+1}\log \mathbf{c}_K^{n+1}) = 0. \tag{7c}$$

The total stress divergence term

How to define the divergence term $\operatorname{div}_{\sigma,i}(\boldsymbol{\tau}_p)$ ***?***

The total Cauchy stress tensor is

$$\mathbf{T}(\tilde{\mathbf{u}}) = -p\mathbf{I}_d + \boldsymbol{\tau}_s(\tilde{\mathbf{u}}) + \boldsymbol{\tau}_p \tag{8}$$

Consistency constraint

We want to satisfy the following :

$$-\sum_{i=1}^{d}\sum_{\sigma\in\mathcal{E}_S^{(i)}} |D_\sigma|\operatorname{div}_{\sigma,i}\mathbf{T}(\tilde{\mathbf{u}})\,u_{\sigma,i} = \sum_{K\in\mathcal{M}} |K|\ (\mathbf{T}(\tilde{\mathbf{u}}) : \boldsymbol{\nabla}\tilde{\mathbf{u}})_K, \tag{9}$$

which is the discrete analogue of the identity:

$$-\int_\Omega \operatorname{div}\mathbf{T}(\mathbf{u})\cdot\mathbf{u} = \int_\Omega \mathbf{T}(\mathbf{u}) : \boldsymbol{\nabla}\mathbf{u}. \tag{10}$$

The discrete velocity gradient (see Figure 2)

❶ $\forall \mathbf{x} \in K_{i,j}$:

$$\partial_x^{\mathcal{M}} u^x(\mathbf{x}) = \frac{u^x_{i+\frac{1}{2},j} - u^x_{i-\frac{1}{2},j}}{h^x_i}. \tag{11}$$

❷ $\forall \mathbf{x} \in K^{xy}_{i-\frac{1}{2},j-\frac{1}{2}}$:

$$\partial_y^{\mathcal{M}} u^x(\mathbf{x}) = \frac{u^x_{i-\frac{1}{2},j} - u^x_{i-\frac{1}{2},j-1}}{h^y_{j-\frac{1}{2}}}. \tag{12}$$

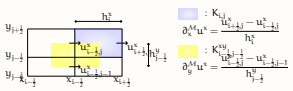

Figure 2: Discrete partial derivatives of the velocity

Finite-volume test functions

We denote by $\boldsymbol{\phi}^{x,(i-\frac{1}{2},j)}$ the test function associated with the degree of freedom of the velocity located at $\mathbf{x}_{i-\frac{1}{2},j}$ and defined by:

$$(\boldsymbol{\phi}^{x,(i-\frac{1}{2},j)})^x_{k-\frac{1}{2},\ell} = \delta^i_k\,\delta^j_\ell,\ \forall (k,\ell) \in \mathcal{I}^x, \tag{13a}$$

$$(\boldsymbol{\phi}^{x,(i-\frac{1}{2},j)})^y_{k,\ell-\frac{1}{2}} = 0,\ \forall (k,\ell) \in \mathcal{I}^y. \tag{13b}$$

Discrete viscous diffusion and pressure gradient

The discrete divergence of the stress tensor is defined by:

$$-(\operatorname{div}\boldsymbol{\tau}_s(\tilde{\mathbf{u}}))^x_{i-\frac{1}{2},j} = \frac{1}{|K^x_{i-\frac{1}{2},j}|}\int_\Omega \boldsymbol{\tau}^{\mathcal{M}}_s(\tilde{\mathbf{u}}) : \boldsymbol{\nabla}^{\mathcal{M}}\boldsymbol{\phi}^{x,(i-\frac{1}{2},j)}. \tag{14}$$

For the pressure gradient, we have:

$$(\boldsymbol{\nabla} p)^x_{i-\frac{1}{2},j} = \frac{-1}{|K^x_{i-\frac{1}{2},j}|}\int_\Omega p\ \partial_x^{\mathcal{M}}\boldsymbol{\phi}^{x,(i-\frac{1}{2},j)} \tag{15}$$

Polymeric stress tensor divergence

Similarly, the discrete divergence of the polymeric stress tensor is defined by:

$$-(\operatorname{div}\boldsymbol{\tau}_p)^x_{i-\frac{1}{2},j} = \frac{1}{|K^x_{i-\frac{1}{2},j}|}\int_\Omega \boldsymbol{\tau}_p : \boldsymbol{\nabla}^{\mathcal{M}}\boldsymbol{\phi}^{x,(i-\frac{1}{2},j)}. \tag{16}$$

What about the fluxes?

Space discretization by the MAC scheme.

- On a vertical face, the flux is given by:

$$\int_\varepsilon (\boldsymbol{\tau}_p\,\mathbf{n}_\varepsilon)^x = \frac{1}{h^y_j}(\boldsymbol{\tau}_p)^{xx}_{i,j} = |\varepsilon^x_{i,j}|(\boldsymbol{\tau}_p)^{xx}_{i,j} \tag{17}$$

- On a horizontal (half) face, the flux is given by:

$$\int_\varepsilon (\boldsymbol{\tau}_p\,\mathbf{n}_\varepsilon)^x = \frac{1}{h^y_{j+\frac{1}{2}}}\left(\frac{|K_{i,j}|}{4}(\boldsymbol{\tau}_p)^{xy}_{i,j} + \frac{|K_{i,j+1}|}{4}(\boldsymbol{\tau}_p)^{xy}_{i,j+1}\right) \tag{18a}$$

$$= |\varepsilon^x_{i-\frac{1}{4},j+\frac{1}{2}}|\left(\alpha\,(\boldsymbol{\tau}_p)^{xy}_{i,j} + (1-\alpha)(\boldsymbol{\tau}_p)^{xy}_{i,j+1}\right), \tag{18b}$$

with: $\alpha = \dfrac{h^y_j}{2h^y_{j+\frac{1}{2}}}$, and $1-\alpha = \dfrac{h^y_{j+1}}{2h^y_{j+\frac{1}{2}}}$.

Numerical results

Lid driven cavity

We present the results for an Oldroyd-B fluid in lid-driven cavity with a Weissenberg number equal to 1.

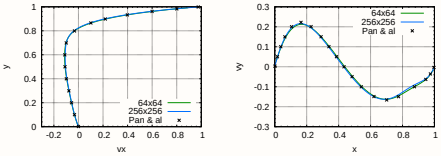

Figure 3: Left: first component of the velocity along the line $x = 0.5$ – Right: second component of the velocity along the line $y = 0.75$.

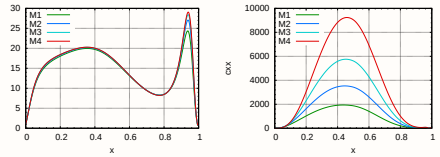

Figure 4: Conformation tensor component c_{xx} along the line $y = 0.975$ (left) and $y = 1$ (right).

Acknowledgements

TOTAL IMFT IRSN INSTITUT DE RADIOPROTECTION ET DE SÛRETÉ NUCLÉAIRE

References

[1] Bird, R.B., Wiest, J.M.: Constitutive Equations for Polymeric Liquids p. 25

[2] CALIF^{3}S: A software components library for the computation of fluid flows. https://gforge.irsn.fr/gf/project/califs

[3] Fattal, R., Kupferman, R.: Time-dependent simulation of viscoelastic flows at high Weissenberg number using the log-conformation representation (2005)

[4] Gallouët, T., Herbin, R., Latché, J.C., Mallem, K.: Convergence of the MAC scheme for the incompressible Navier-Stokes equations. Foundations of Computational Mathematics **18**(1), 249–289 (2018)

[5] Pan, T.W., Hao, J., Glowinski, R.: On the simulation of a time-dependent cavity flow of an Oldroyd-B fluid. International Journal for Numerical Methods in Fluids **60**, 791–808 (2009)

Elastic strands drive viscoelastic fluid flows through 2D arrays of cylinders

O. Mokhtari[1], J.-C. Latché[2], R. de Loubens[3], M. Quintard[1], Y. Davit[1]

[1]Institut de Mécanique des Fluides de Toulouse (IMFT), Université de Toulouse, France,
[2]Institut de Radioprotection et de Sûreté Nucléaire (IRSN), France,
[3]Total E&P, CSTJF, Pau, France.

Introduction

Abstract We study the flow of dilute polymer solutions in model porous media consisting of an array of cylinders. Numerical and experimental studies show that such flows are subject to the intensification of preferential flow paths. We seek to understand the mechanisms of reinforcement of these preferential flow paths. We show that the reinforcement mechanism of the preferential flow paths is linked to the appearance of zones of very large polymer stress that may be understood as elastic filaments strongly interacting with the flow.

Birefringent strand

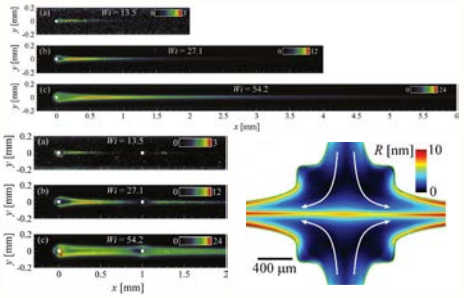

Experimental results, Haward et al. (2013 & 2018)

Viscoelastic models

$$-\boldsymbol{\nabla} p + \operatorname{div} \boldsymbol{\tau}_s(\mathbf{u}) + \operatorname{div} \frac{\eta_p}{\lambda}(\mathbf{c} - \mathbf{I_d}) = 0, \quad (1a)$$

$$\operatorname{div} \mathbf{u} = 0, \quad (1b)$$

$$\partial_t \mathbf{c} + \mathbf{u} \cdot \boldsymbol{\nabla} \mathbf{c} - (\boldsymbol{\nabla} \mathbf{u})\,\mathbf{c} - \mathbf{c}\,(\boldsymbol{\nabla} \mathbf{u})^t + \frac{1}{\lambda} \boldsymbol{\tau}_p = 0. \quad (1c)$$

with η_p the polymer viscosity, and λ the polymer retardation time, $\mathbf{u}$ is the velocity and p the pressure. The tensor $\boldsymbol{\tau}_s = \eta_s(\boldsymbol{\nabla}\mathbf{u} + (\boldsymbol{\nabla}\mathbf{u})^t)$ is the solvent stress tensor and $\mathbf{c}$ is the conformation tensor (see Bird et al. (1995)).

Weissenberg number

$$Wi = \frac{\text{elastic forces}}{\text{viscous forces}} = \lambda\dot{\gamma} = \frac{\lambda\langle U\rangle}{L}$$

Deborah number

$$De = \frac{\text{relaxation time}}{\text{solicitation time}} = \frac{\lambda}{t_c} = \frac{\lambda\langle U\rangle}{D}$$

Numerical scheme

Finite volume staggered grid

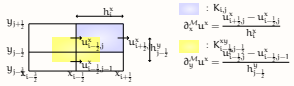

Figure 1: Discrete partial derivatives of the velocity

Pressure correction scheme

Prediction step – Solve for $\tilde{\mathbf{u}}^{n+1}$:

For $1 \le i \le d$, $\forall \sigma \in \mathcal{E}_S^{(i)}$,

$$\frac{\rho}{\delta t}\left(\tilde{u}^{n+1}_{\sigma,i} - u^n_{\sigma,i}\right) + \xi\,\rho \operatorname{div}_\sigma(\tilde{u}^{n+1}_i \mathbf{u}^n) - \operatorname{div}_{\sigma,i} \boldsymbol{\tau}_s(\tilde{\mathbf{u}}^{n+1}) - \operatorname{div}_{\sigma,i} \boldsymbol{\tau}^n_p + \boldsymbol{\nabla}_{\sigma,i}(p^n) = 0.$$

Correction step – Solve for p^{n+1} and $\mathbf{u}^{n+1}$:

For $1 \le i \le d$, $\forall \sigma \in \mathcal{E}_S^{(i)}$,

$$\frac{\rho}{\delta t}\left(u^{n+1}_{\sigma,i} - \tilde{u}^{n+1}_{\sigma,i}\right) + \boldsymbol{\nabla}_{\sigma,i}(p^{n+1} - p^n) = 0,$$

$$\forall K \in \mathcal{M}, \quad \operatorname{div}_K(\mathbf{u}^{n+1}) = 0.$$

Constitutive equation discretization

A scalar model problem

We consider the scalar model problem on $I = [-1, 1] \times (0, T)$ given by :

$$\begin{aligned} &\partial_t c + \partial_x c = a(x)c && (x,t) \in I \times (0,T), \\ &c(x,0) = 1 && x \in I, \\ &c(-1,t) = c_L && t \in (0,T). \end{aligned}$$

with a "stiff" source term $a(x)$.

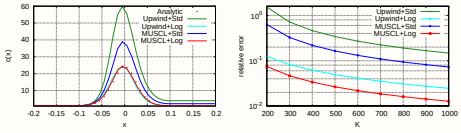

Figure 2: Comparison of different methods of discretization, $\beta = 50$ and $x_0 = 0.1$. Left: Stationary states. Right: Relative errors (in L^2-norm).

The "Strang-log" scheme

Advection I – Solve for $\mathbf{c}^{n+\frac{1}{3}}$:

$$\frac{1}{\delta t/2}\left(\log \mathbf{c}_K^{n+\frac{1}{3}} - \log \mathbf{c}_K^{n}\right) + \operatorname{div}_K(\mathbf{u}^{n+1} \log \mathbf{c}_K^{n+\frac{1}{3}}) = 0,$$

ODE – Set $\mathbf{c}_K(t_n) = \mathbf{c}_K^{n+\frac{1}{3}}$, solve for $\mathbf{c}^{n+\frac{2}{3}} = \mathbf{c}_K(t_n + \delta t)$:

$$\partial_t \mathbf{c}_K - (\boldsymbol{\nabla}_K \mathbf{u}^{n+1})\,\mathbf{c}_K - \mathbf{c}_K\left(\boldsymbol{\nabla}_K \mathbf{u}^{n+1}\right)^t + \frac{1}{\lambda_K}\boldsymbol{\tau}_{pK} = 0,$$

Advection II – Solve for $\mathbf{c}^{n+1}$:

$$\frac{1}{\delta t/2}\left(\log \mathbf{c}_K^{n+1} - \log \mathbf{c}_K^{n+\frac{2}{3}}\right) + \operatorname{div}_K(\mathbf{u}^{n+1} \log \mathbf{c}_K^{n+1}) = 0.$$

Flow Around 2 Cylinders

Aligned cylinders ($D = 9$)

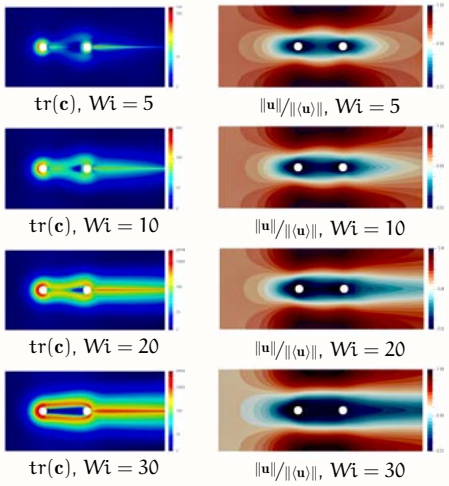

Side-by-side cylinders ($D = 5$)

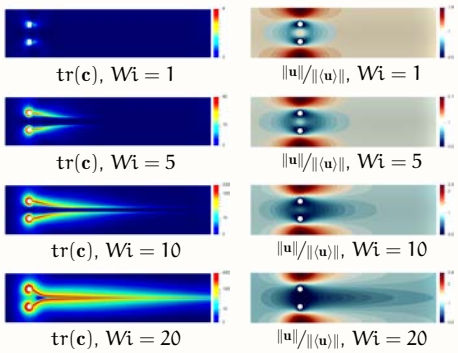

Arrays of Cylinders

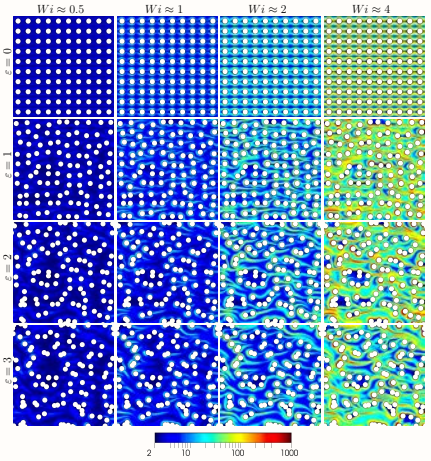

tr(c)

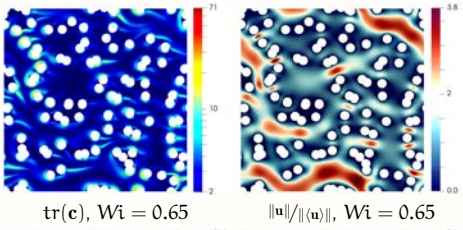

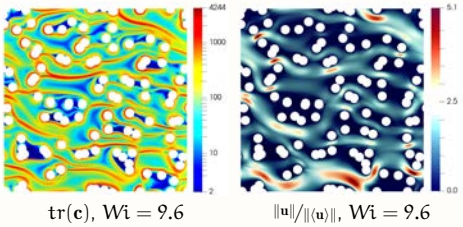

Probability density functions

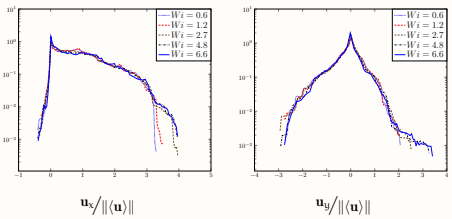

References

[1] M. A. Alves, P. J. Oliveira, and F. T. Pinho. Numerical methods for viscoelastic fluid flows (2021)

[2] R. B. Bird, and J. M. Wiest. Constitutive Equations for Polymeric Liquids (1995)

[3] CALIF^{3}S: A software components library for the computation of fluid flows. https://gforge.irsn.fr/gf/project/califs

[4] S. J. Haward, and G. Mckinley. Instabilities in stagnation point flows of polymer solutions (2013)

[5] Simon J. Haward, T.-P. Kazumi, and A. Q. Shen. Steady viscoelastic flow around high-aspect-ratio, low-blockage-ratio microfluidic cylinders (2018)

[6] O. Mokhtari, Y. Davit, J.-C. Latché, R. de Loubens, and M. Quintard. A staggered projection scheme for viscoelastic flows at high Weissenberg number (in preparation)

[7] O. Mokhtari, J.-C. Latché, M. Quintard, and Y. Davit. High-stress elastic filaments control 2D creeping flows of viscoelastic fluids through porous media (in preparation)